Effects of Fuel Composition on Combustion Stability and NO_X Emissions for Traditional and Alternative Jet Fuels

Shazib Z. Vijlee

A dissertation submitted in partial fulfillment of
the requirements for the degree of

Doctor of Philosophy

University of Washington

2014

Reading Committee:

John C. Kramlich, Chair
Philip C. Malte
Igor V. Novosselov

Program Authorized to Offer Degree:
Department of Mechanical Engineering

University of Washington

Abstract

Effects of Fuel Composition on Combustion Stability and NO_X Emissions for Traditional and Alternative Jet Fuels

Shazib Z. Vijlee

Chair of Supervisory Committee:
Professor John C. Kramlich, Department of Mechanical Engineering

Synthetic jet fuels are studied to help understand their viability as alternatives to traditionally derived jet fuel. Two combustion parameters – flame stability and NO_X emissions – are used to compare these fuels through experiments and models. At its core, this is a fuels study comparing how chemical makeup and behavior relate.

Six 'real', complex fuels are studied in this work – four are synthetic from alternative sources and two are traditional from petroleum sources. Two of the synthetic fuels are derived from natural gas and coal via the Fischer Tropsch catalytic process. The other two are derived from Camelina oil and tallow via hydroprocessing. The traditional military jet fuel, JP8, is used as a baseline as it is derived from petroleum. The sixth fuel is derived from petroleum and is used to study the effects of aromatic content on the synthetic fuels. The synthetic fuels lack aromatic compounds, which are an important class of hydrocarbons necessary for fuel handling systems to function properly.

Several single-component fuels are studied (through models and/or experiments) to facilitate interpretation and understanding. Methane is used for detailed modeling as it has a relatively small and well-understood chemical kinetic mechanism. Toluene, iso-octane, n-

octane, propylcyclohexane, and 1,3,5-trimethylbenzene are included as they are all potential surrogates for jet fuel components.

The flame stability study first compares all the 'real', complex fuels for blowout. A toroidal stirred reactor is used to try and isolate temperature and chemical effects. The reactor has a volume of 250 mL and a residence time of approximately 8.0 ms. The air flow rate is held constant such that the inlet jets are sonic and turbulent mixing is present throughout the reactor. The fuel flow rate (hence equivalence ratio) is slowly lowered until the flame cannot sustain itself and it extinguishes. The results show that there is very little variation in blowout temperature and equivalence ratio for the synthetic fuels when compared to JP8 with low levels (0, 10, and 20%) of the aromatic additive. However, the 100% aromatic fuel behaved significantly differently and showed a lower resistance to blowout (i.e., it blew out at a higher temperature and equivalence ratio).

The modeling study of blowout in the toroidal reactor is the key to understanding any fuel-based differences in blowout behavior. A detailed, reacting CFD model of methane is used to understand how the reactor stabilizes the flame and how that changes as the reactor approaches blowout. A 22 species reduced form of GRI 3.0 is used to model methane chemistry. The model shows that the reactor is quite homogenous at high temperatures, far away from blowout, and the transport of chain-initiating and chain-branching radical species is responsible for stabilizing the flame. Particularly, OH radical is recirculated around the reactor with enough concentration and at a high enough rate such that the radicals interact with the incoming fuel/air and initiate fuel decomposition. However, as equivalence ratio decreases, the reactor begins to behave in a more zonal nature and the radical concentration/location is no longer sufficient to initiate or sustain combustion.

The knowledge of the radical species role is utilized to investigate the differences between a highly aliphatic fuel (surrogated by iso-octane) and a highly aromatic fuel (surrogated by toluene). A perfectly stirred reactor model is used to study the chemical kinetic pathways for these fuels near blowout. The differences in flame stabilization can be attributed to the rate at which these fuels are attacked and destroyed by radical species. The slow disintegration of the aromatic rings reduces the radical pool available for chain-initiating and chain-branching, which ultimately leads to an earlier blowout.

The NO_X study compares JP8, the aromatic additive, the synthetic fuels with and without an aromatic additive, and an aromatic surrogate (1,3,5-trimethylbenzene). A jet stirred reactor is used to try and isolate temperature and chemical effects. The reactor has a volume of 15.8 mL and a residence time of approximately 2.5 ms. The fuel flow rate (hence equivalence ratio) is adjusted to achieve nominally consistent temperatures of 1800, 1850, and 1900K. Small oscillations in fuel flow rate cause the data to appear in bands, which facilitated Arrhenius-type NO_X-temperature correlations for direct comparison between fuels. The fuel comparisons are somewhat inconsistent, especially when the aromatic fuel is blended into the synthetic fuels. In general, the aromatic surrogate (1,3,5-trimethylbenzene) produces the most NO_X, followed by JP8. The synthetic fuels (without aromatic additive) are always in the same ranking order for NO_X production (HP Camelina > FT Coal > FT Natural Gas > HP Tallow). The aromatic additive ranks differently based on the temperature, which appears to indicate that some of the differences in NO_X formation are due to the Zeldovich NO_X formation pathway. The aromatic additive increases NO_X for the HP Tallow and decreases NO_X for the FT Coal. The aromatic additive causes increased NO_X at low temperatures but decreases NO_X at high temperatures for the HP Camelina and FT Natural Gas.

A single perfectly stirred reactor model is used with several chemical kinetic mechanisms to study the effects of fuel (and fuel class) on NO_X formation. The 27 unique NO_X formation reactions from GRI 3.0 are added to published mechanisms for jet fuel surrogates. The investigation first looked at iso-octane and toluene and found that toluene produces more NO_X because of a larger pool of O radical. The O radical concentration was lower for iso-octane because of an increased concentration of methyl (CH_3) radical that consumes O radical readily. Several surrogate fuels (iso-octane, toluene, propylcyclohexane, n-octane, and 1,3,5-trimethylbenzene) are modeled to look for differences in NO_X production. The trend (increased CH_3 → decreased O → decreased NO_X) is consistently true for all surrogate fuels with multiple kinetic mechanisms. It appears that the manner in which the fuel disintegrates and creates methyl radical is an extremely important aspect of how much NO_X a fuel will produce.

“If it’s on fire, it’s on purpose.”

sign found in the UWME Laboratory for Energy and Environmental Combustion
(circa 1998 by Blake Chenevert)

Acknowledgments

As this ends, I get the rare opportunity to thank those that made it what it was.

This work was made possible in part by support from the United States Air Force through the Air Force Research Laboratory at Wright-Patterson Air Force Base in Dayton, Ohio. I can't mention the countless people who helped me, so I will specifically recognize Tim Edwards, David Blunck, Scott Stouffer, and Mike Arstingstall for all of their help. It was also supported in part by the State of Washington JCATI (Joint Center for Aerospace Technology Innovation) program. Several quarters of my time were supported by the Department of Mechanical Engineering at UW through teaching assistantships, fellowships, and interesting projects.

I have worked with outstanding people while at the University of Washington. Most importantly, Professor John Kramlich has been a true mentor and advisor. I appreciate the input and guidance from all of my committee members – Professor Phil Malte, Professor Jim Riley, Professor Ann Mescher, Dr. Igor Novosselov, and Professor Jim Hermanson. My labmates, particularly Boyd Fackler and Megan Karalus, were a huge influence in this work and some of the best people I could ever hope to work with. The UWME Department staff – particularly Maria Hopper, Wanwisa Kisalang, and Bill Kuykendall – found new ways to be helpful every time they were needed. I am also grateful and honored to have worked with dozens of students in many different roles in my time at UW. I must also mention Professor Phil Schmidt and Professor David Bogard at the University of Texas, as their guidance molded me first.

Lastly, I certainly thank my friends and family. Those who were around to enjoy the Pacific Northwest were the best kind of distraction, and those that supported from afar were the best kind of motivation.

Huzzah!

July 15, 2014
Seattle, WA

Table of Contents

List of Figures

<u>Note:</u> Figures are not necessarily drawn to scale.

List of Tables

List of Nomenclature

Acronyms and Abbreviations

Symbol	Description
AFRL	Air Force Research Laboratory
API	American Petroleum Institute
ASTM	American Society for Testing and Materials
C/H	carbon/hydrogen ratio
CEA	Chemical Equilibrium with Applications
CFD	Computational Fluid Dynamics
CL	chemiluminescent
CRM(s)	Chemical Reactor Model(s)
C_mH_n/C_xH_y	generic hydrocarbon
DAq	Data Acquisition
EDC	Eddy Dissipation Concept
FAAE/FAME	Fatty Acid Alkyl/Methyl Ester
FID	Flame Ionization Detector
FT	Fischer Tropsch
GC/GCxGC	Gas Chromatography/ Two-Dimensional Gas Chromatography
GRI	Gas Research Institute
H/C	hydrogen/carbon ratio
HC(s)	Hydrocarbon(s)
HEFA	Hydrogenated Esters and Fatty Acids
HP	Hydroprocessed
HRJ	Hydrotreated Renewable Jet
iso-	isomer
IUPAC	International Union of Pure and Applied Chemistry
JCATI	Joint Center for Aerospace Technology Innovation
JSR	Jet Stirred Reactor
LBO	Lean Blowout
MP	magnetopneumatic
n-	normal
NASA	National Aeronautics and Space Administration
NDIR	Non-Dispersive Infrared

NIST	National Institutes of Standards and Technology
NO_X	Oxides of Nitrogen ($NO + NO_2$)
PaSR	Partially Stirred Reactor
PCH	propylcyclohexane
Pet	petroleum based
PFR	Plug Flow Reactor
PM	Paramagnetic
ppm(v)	parts per million (volume)
premix	premixed fuel and air
PSR	Perfectly Stirred Reactor
R	thermal resistor
RANS	Reynolds Averaged Navier Stokes
RSM	Reynolds Stress Model
SPP	Staged Prevaporizer Premixer
SR	Stirred Reactor
syngas	synthesis gas
THC	total hydrocarbons
TMB	trimethylbenzene
TMP	trimethylpentane
TSR	Toroidal Stirred Reactor
UWME	University of Washington Mechanical Engineering
WPAFB	Wright Patterson Air Force Base

English Symbols

Symbol	Description	Units
A	pre-exponential constant	moles, sec, cm^3
A	exponential curve fit coefficient for NO_X formation	ppm or ppm/ms
A_C	cross-sectional area	mm^2
b	temperature exponent	-
B	exponential curve fit coefficient for NO_X formation	K
$\bar{c}_p$	molar specific heat	J/mol/K
Da	Damköhler number (mixing time/reacting time)	-
D_h	hydraulic diameter	mm

E_A	activation energy	cal/mol
H or h	enthalpy	J or J/mol
h_f	enthalpy of formation	J/mol
I	turbulence intensity	%
k	reaction rate constant	moles, sec, cm^3
k	turbulent kinetic energy	J/kg
Ka	Karlovitz number (reacting time/Kolmogorov time)	-
k_w	statistical deviation factor	-
L	turbulent length scale	mm
L	flame thickness	mm
LHV	Lower Heating Value	MJ/kg
LP	Loading Parameter	mol/L/s/atm$^{1.8}$
$\dot{m}$	mass flow rate	g/s
MW	Molecular Weight	g/mol
$\dot{n}$	molar flow rate	mol/s
p	pressure	atm
p_1 and p_2	exponential curve fit coefficients for NO_X formation	K and ln ppm
P	perimeter	mm
Q	statistical data quality factor	-
$\dot{Q}$ or Q_{loss}	heat loss	W
Q_{max}	statistical rejection coefficient	-
R	universal gas constant	1.987 cal/mol/K
Re	Reynolds number (inertial forces/viscous forces)	-
ROP	Rate of Production	mol/cm^3/s or ppm/ms
s_L	flame speed	m/s
s_w	statistical dispersion	-
t	time	ms
T	temperature	K, ^{o}F, or ^{o}C
t_w	statistical confidence factor	-
u	velocity	m/s
$\forall$	volume	mL
$\dot{\forall}$	volumetric flow rate	mL/min or SLPM
w	statistical range	-
x	generic variable	-

Greek Symbols

Symbol		Description	Units
α	‘alpha’	quantity of air	moles
α	‘alpha’	location of the first carbon in a hydrocarbon chain	-
β	‘beta’	quantity of CO_2	moles or % volume
δ	‘delta’	quantity of CO	moles or % volume
γ	‘gamma’	quantity of H_2O	moles
ϵ	‘epsilon’	quantity of O_2	moles or % volume
ϵ	‘epsilon’	turbulent dissipation rate	m^2/s^3
ζ	‘zeta’	quantity of N_2	moles or % volume
ρ	‘rho’	density	g/mL
ϕ	‘phi’	equivalence ratio	-
χ	‘chi’	quantity of primary fuel	moles
τ	‘tau’	residence time	ms
ω	‘omega’	quantity of fuel	moles
ω	‘omega’	location of the last carbon in a hydrocarbon chain	-

Subscripts, Superscripts, and Annotations

Symbol	Description
298	value at 298 K
∞ ‘infinity’	free stream conditions
A or air	value for air flow
combustion	overall combustion parameter
cond	conduction heat transfer
conv	convection heat transfer
corrected	corrected value (as compared to measured value)
D_h	hydraulic diameter
dry	emissions on a dry basis
exhaust	value based on exhaust conditions
ext or extinction	value at extinction
F or fuel	value for fuel flow
gas	value for the gas
GF	gaseous fuel

in or inlet	value based on inlet conditions
jet ring	jet ring condition
K	value based on Kolmogorov scale
L	value based on turbulent length scale
LF	value for the liquid fuel
m	number of carbon atoms in the fuel (same as x)
max	maximum value in sample
measured	measured value (as compared to corrected value)
min	minimum value in sample
mixing	overall mixing parameter
n	generic index
n	number of hydrogen atoms in the fuel (same as y)
o	integral scale
P	products
PLF	primary liquid fuel
premix	value for the premixed fuel and air
product	value for the combustion products
R	reaction scale
R	reactants
rad	radiation heat transfer
reacting	overall reacting parameter
reactor	value for the parameter inside the reactor
SLF	secondary liquid fuel
stoich	stoichiometric ($\phi = 1$) condition
T	value at temperature T
vaporizing	overall vaporizing parameter
wet	emissions on a wet basis
x	number of carbon atoms in the fuel (same as m)
y	number of hydrogen atoms in the fuel (same as n)

x'	fluctuations
$\dot{x}$	flow rate
$\bar{x}$	average or molar quantity

Chapter 1
Introduction

This work reports on research that compares the combustion characteristics of alternative, synthetic jet fuels with that of traditional, petroleum derived jet fuels. The practical goal is to evaluate the viability of the alternative fuels as replacements for traditional fuels. The chapters of this dissertation discuss the broad background of the problem, describe the fuels, and present and interpret the data from combustion testing. This first chapter provides general background on the problem of alterative jet fuels. This leads to the specific objectives of the present study.

1.1 Motivation

Liquid fuels are extremely important for the transportation, power, and military sectors of society and the global economy. The very high energy density of these fuels makes them the fuel of choice in transportation, where the energy source is generally carried on the vehicle. Thus far, liquid fuels have come almost exclusively from depletable petroleum resources. The reliance of the transportation sector on this single raw energy source, coupled with the scarcity of petroleum relative to other energy sources, has led to both high costs and supply availability issues. Broadening the raw resource supply for transportation fuels has the potential in the long term to (1) reduce supply scarcity, (2) place the sector on a sustainable basis, and (3) possibly reduce costs.

While the alternative jet fuel industry is not yet commercially competitive with petroleum in terms of either quantity or cost, a number of fuel production processes are in various stages of development. Some of these fuels are manufactured from plentiful fossil feedstocks like natural gas or coal which are available domestically, and some come from renewable resources like plant oils, animal fats, or cellulose. These fuels should be manufactured to be 'drop-in' replacements, such that they can function in the same hardware (engines, etc.) with little or no modifications. Aircraft fuel handling and engine systems cannot realistically be redesigned to accommodate an alternative fuel. The use of present candidate alternative fuels does raise some issues that need to be solved. For instance, alternative fuels generally contain little or no aromatic species and these are essential for both the proper operation of current fuel handling systems, and for meeting fuel standards specification testing. Also, carbon chain length and chain isomerization issues affect fuel freeze point, an important problem for wing tanks.

Aviation combustors are designed to process a large amount of fuel in a small volume. In general, the flames in these combustors can be stressed to near their blowout point. Thus, flame stability (i.e., flammability limits and cold start relight performance) is one of the combustion characteristics of these fuels that is of concern. Another concern is emissions, primarily oxides of nitrogen ($NO_X=NO+NO_2$), soot, and unburned hydrocarbons (HCs). In the work presented here, we focus on flame stability (described in Section 1.2.1) and NO_X emission formation (described in Section 1.2.2).

Aircraft combustors are extremely complex devices, involving complicated fluid dynamics, fuel spray vaporization, and chemical kinetics. The post-combustion gases are diluted and surfaces are protected from flame temperatures to avoid material failure. These many complexities make it difficult to understand the relationship between fuels, flame stability, and emissions in real engines. Ideally, the temperature and chemistry should be isolated from any other phenomena present in a combustor to be able understand the reasons behind a given behavior.

The experimental stirred reactor (SR) is intended to serve as the laboratory-scale idealization of the primary zone of a gas turbine combustor, both of which stabilize combustion through large recirculation zones. The stirred reactor is often used to study combustion chemistry in a well-controlled, well-characterized, high-intensity environment. It is helpful to think of a stirred reactor that approaches idealized behavior – perfectly homogenous in species and temperature throughout the reactor volume; this limit is called a *perfectly* stirred reactor (PSR).

The utility of the perfectly stirred reactor method can be seen by first looking to Equation 1.1 for the combustion time. In practical liquid-fueled systems the first step is fuel vaporization, then mixing the fuel and air, and finally the chemical reactions. In a prevaporized, premixed *perfectly* stirred reactor the times for vaporizing and mixing become zero and the overall combustion time simplifies to the chemical reactions time [1].

$$t_{\mathrm{combustion}} = t_{\mathrm{vaporizing}} + t_{\mathrm{mixing}} + t_{\mathrm{reacting}} \quad \text{ms} \tag{1.1}$$

The experimental stirred reactor tries to approach this perfectly stirred reactor method for studying combustion to isolate the reacting chemistry for detailed study. By monitoring temperature and species, the reactor is essentially correlating chemical reactions to temperature and equivalence ratio, which is incredibly informative for studying emissions and stability.

Thus, the motivation is to characterize the viability of synthetic jet fuels as alternative jet fuels by understanding how these fuels behave in terms of flame stability and NO_X emissions. Oxides of nitrogen (NO_X) emissions are reduced at lower combustion temperatures, which is achievable by lowering the ratio of fuel to oxidizer. However, as this ratio decreases, combustion can become unstable and risks extinction. Also, under these conditions, emissions of CO and unburned hydrocarbons tend to increase. Understanding these behaviors, and being able to predict them, makes large-scale use of alternative, synthetic fuels feasible. These synthetic fuels have the potential to replace or supplement fuels derived from petroleum and to become a significant benefit in the overall energy usage spectrum once the stability and emissions behavior are better understood.

1.2 Fundamental Concepts

The two major combustion features that this work addresses are flame stability and NO_X emissions, which are qualitatively described here for reference. In later chapters, these concepts will serve as the basis for comparing fuel composition effects, so a basic understanding of the physical behavior is useful.

1.2.1 Extinction Instability

A large portion of this work deals with the combustion instability leading to extinction or blowout. In general, fuel and air mixtures exist in one of two states: either steady burning or non-burning, with no stable state between these two. This discontinuous behavior is due to the coupling of the principles of conservation of energy and species. The two are non-linearly coupled because the species reaction rate parameters contain an exponential dependency on temperature as shown in the Arrhenius Equation (Equation 1.2).

1.2 $$k = A\,T^{b} \exp\left(-\frac{E_A}{RT}\right)$$ various units

The Damköhler number (Equation 1.3) is a non-dimensional parameter that compares the residence time available for a chemical reaction with the rate of the chemical reaction itself. A low value (Da → 0) implies the reaction time is very long compared to the flow time, so the system is chemically ‘frozen’. A large value (Da → ∞) means the reaction time is infinitesimally small, so the system will be in an equilibrium state. Finite values of Da occur in real systems where reactions occur with finite rates [2].

1.3 $$\mathrm{Da} = \frac{\text{fluid mixing time}}{\text{chemical reacting time}}$$ -

Figure 1.1 shows the relationship between combustor temperature and Da or reactor residence time. This curve is developed by a coupled solution of the species equation and the energy equation. A combustor with a stable flame will be at some point on the upper branch. If we then increase the fuel/air throughput, the residence time will decrease (moving us towards the left). The reduced residence time will mean less of the fuel is burned, and the temperature will correspondingly decrease as shown in the figure. When the combustor arrives at the extinction point labeled on the figure, a further increase in throughput will cause the solution to drop to the lower branch, which in practice is essentially a non-reacting solution. This corresponds to a cold fuel and air mix passing through the reactor. Thus, the extinction point is determined by the point where the flame becomes so stressed that a blowout occurs. For conditions with residence times longer that the extinction state, two solutions are possible, burning or non-burning. Which one prevails is determined by the history of the combustor [2].

Physically, these extinction and ignition points represent states where the chemical reaction rate and the heat transport rate are not balanced. For the lower branch, at Da values above the ignition point, the chemical heat is generated too fast to be steadily transported away. Similarly, for the upper branch, the finite reaction rate means that not all of the available chemical energy can be released during the finite residence time. Extinction occurs when the heat loss from the flame becomes too large to sustain combustion.

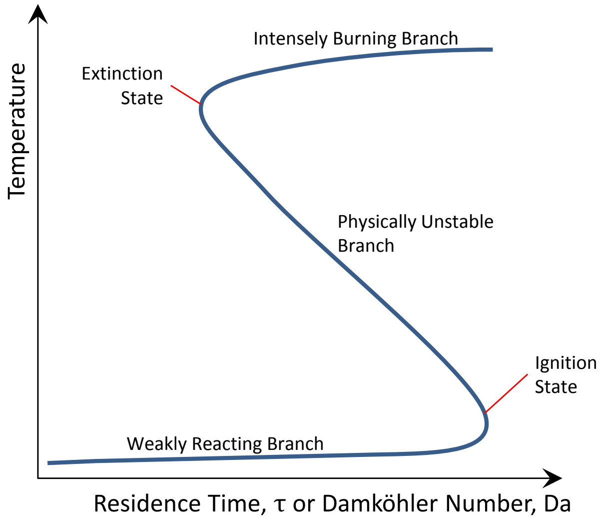

Figure 1.1: Representation of flame stability (s-shaped curve) [2,3]

In this study of extinction (experimentally in Chapter 3 and computationally in Chapter 4), the residence time is held roughly constant, but the fuel flow rate is decreased to decrease the temperature. The decreased temperature reduces reaction rates, which eventually means that all of the chemical energy is not released (because of the finite residence time). Eventually, the temperature and reaction rates are too low for enough chemical energy to be released and converted into heat. In this unsteady process, the heat loss from the flame will be too large, and eventually this imbalance causes extinction [2].

In an ideal system, like a perfectly stirred reactor, the entire volume will extinguish at the same instant. A practical, non-homogenous, system will qualitatively replicate this behavior, but the exact point of extinction will depend on the complex interaction of the flow field and chemistry.

1.2.2 Oxides of Nitrogen

Oxides of Nitrogen (NO_X) emissions collectively refer to the sum of nitric oxide (NO) and nitrogen dioxide (NO_2). These species are formed in high-temperature combustion, and once in the atmosphere are precursors of photochemical smog and acid rain.

NO_X is formed via four major pathways highlighted in each of the four tables below – 1) Zeldovich, 2) Nitrous Oxide (N_2O), 3) NNH, and 4) Fenimore prompt. A fifth pathway involving fuel-bound nitrogen is not relevant to this work. There are a total of 34 reactions, but only 27 unique reactions according to the commonly-used GRI 3.0 mechanism [4]. Seven of the reactions participate in more than one pathway. All of the reactions given below follow the Arrhenius rate constant equation shown previously as Equation 1.2. The reaction rate constant, k, and the pre-exponential constant, A, will generally have units of moles, cm^3, and sec depending on the reaction order. The temperature, T, will be in units of Kelvin and the activation energy, E_A, has units of cal/mol [5]. These values and units are consistent with the widely accepted GRI 3.0 mechanism [4] and in the format for use in the CHEMKIN-PRO kinetic solver [6]. The reactions also show the favored direction under lean, premixed conditions.

Zeldovich NO_X occurs under high-temperature combustion conditions via the reactions from Table 1.1. The Arrhenius parameters for these reactions yield a very strong temperature dependence for the rate constants, which in turn causes these reactions to become important contributors to NO_X emissions at temperatures above 1800K.

Table 1.1: Zeldovich NO_X formation pathway [7]

#	Reactants		Direction	Products		A	b	E_A
1	N	NO	←	N_2	O	2.70E+13	0.00	355
2	N	O_2	→	NO	O	9.00E+09	1.00	6500
3	N	OH	→	NO	H	3.36E+13	0.00	385

1. The units of A are in moles, cm^3, and sec depending on reaction order. The units of E_A are in cal/mol.

The nitrous oxide (N_2O) pathway is active for NO_X formation in high-intensity, lean, premixed combustion. It is given in Table 1.2.

Table 1.2: N_2O NO_X formation pathway [8]

#	Reactants		Direction	Products			A	b	E_A
4	N_2O	O	→	N_2	O_2		1.40E+12	0.00	10810
5	N_2O	O	→	NO	NO		2.90E+13	0.00	23150
6	N_2O	H	→	N_2	OH		3.87E+14	0.00	18880
7	N_2O	OH	→	N_2	HO_2		2.00E+12	0.00	21060
8	N_2O	M	↔	N_2	O	M	7.91E+10	0.00	56020
9	NH	NO	←	N_2O	H		3.65E+14	-0.45	0

1. The units of A are in moles, cm^3, and sec depending on reaction order. The units of E_A are in cal/mol.

The NNH pathway for NO_X is given in Table 1.3. Notice that two of the reactions (2 and 3) are repeated from the Zeldovich pathway above.

Table 1.3: NNH NO_X formation pathway [9]

#	Reactants		Direction	Products			A	b	E_A
10	NNH		←	N_2	H		3.30E+08	0.00	0
11	NNH	M	←	N_2	H	M	1.30E+14	-0.11	4980
12	NNH	O_2	←	HO_2	N_2		5.00E+12	0.00	0
13	NNH	O	←	OH	N_2		2.50E+13	0.00	0
14	NNH	H	←	H_2	N_2		5.00E+13	0.00	0
15	NNH	OH	←	H_2O	N_2		2.00E+13	0.00	0
16	NNH	CH_3	←	CH_4	N_2		2.50E+13	0.00	0
17	NNH	O	→	NH	NO		7.00E+13	0.00	0
18	NH	OH	→	N	H_2O		2.00E+09	1.20	0
19	NH	O	→	NO	H		4.00E+13	0.00	0
20	NH	O_2	→	NO	OH		1.28E+06	1.50	100
2	N	O_2	→	NO	O		9.00E+09	1.00	6500
3	N	OH	→	NO	H		3.36E+13	0.00	385

1. The units of A are in moles, cm^3, and sec depending on reaction order. The units of E_A are in cal/mol.

The Fenimore prompt pathway (Table 1.4) is often called the 'prompt' pathway because the NO is rapidly produced in the flame zone long before there is time for it to form from the Zeldovich mechanism. The HCN and N atoms are believed to quickly oxidize to NO under fuel-lean conditions. Notice that some of the reactions (2-3 from the Zeldovich pathway and 18-20 from the NNH pathway) are repeated from above.

Table 1.4: Fenimore prompt NO$_X$ formation pathway [10]

#	Reactants		Direction	Products			A	b	E_A
21	CH	N2	→	HCN	N		3.12E+09	0.88	20130
22	HCN	O	→	NCO	H		2.03E+04	2.64	4980
23	NCO	O	→	NO	CO		2.35E+13	0.00	0
24	NCO	OH	→	NO	H	CO	2.50E+12	0.00	0
25	NCO	O2	→	NO	CO2		2.00E+12	0.00	20000
26	HCN	O	→	NH	CO		5.07E+03	2.64	4980
27	NCO	H	→	NH	CO		5.40E+13	0.00	0
18	NH	OH	→	N	H2O		2.00E+09	1.20	0
19	NH	O	→	NO	H		4.00E+13	0.00	0
20	NH	O2	→	NO	OH		1.28E+06	1.50	100
2	N	O2	→	NO	O		9.00E+09	1.00	6500
3	N	OH	→	NO	H		3.36E+13	0.00	385

1. The units of A are in moles, cm^3, and sec depending on reaction order. The units of E_A are in cal/mol.

In this study, the overall amount of NO$_X$ formation is measured experimentally and compared for several traditional and alternative jet fuels. Experimentally, the NO$_X$ formation pathway is indeterminable, but Chemical Reactor Models (CRMs) will help identify the kinetic route and the degree to which the various fuel constituents contribute to NO$_X$ formation.

1.3 Literature Review

Ultimately, this effort focuses on how fuel composition affects flame stability and NO$_X$ emissions. The relevant literature can be separated into studies regarding flame stability, detailed reactor modeling, and NO$_X$ emissions.

1.3.1 Flame Stability and Fuel Effects

The flame stability literature is organized into three parts: 1) spherical reactor studies for a historical perspective; 2) toroidal reactor studies relevant to the present effort; and 3) alternative fuel studies on a variety of devices. A fourth part will discuss the potential to provide unique contributions to the understanding of flame stability and fuel effects.

Spherical Stirred Reactor and Flame Stability

The original work focusing on flame stability of premixed combustion in stirred reactors came from Longwell and Weiss [11] who developed the spherical stirred reactor to isolate chemical kinetics and to study the stability of iso-octane fueled flames at several reactor loading values. A short time later, Weiss *et al.* [12] used the same spherical stirred reactor to include many other fuels including hydrogen, and, methane. Those efforts resulted in the 'Longwell curve' for hydrocarbon extinction, which is simplified and shown in Figure 1.2, with equivalence ratio plotted against reactor loading. The conclusion from their work was that all hydrocarbon fuels essentially collapse to a single line while other fuels (i.e., hydrogen) behave differently. Sturgess *et al.* [13] used a propane-fired research step combustor and found that the lean blowout conditions matched the 'Longwell curve'. The present work will investigate how real transportation fuels (with many components) behave in comparison.

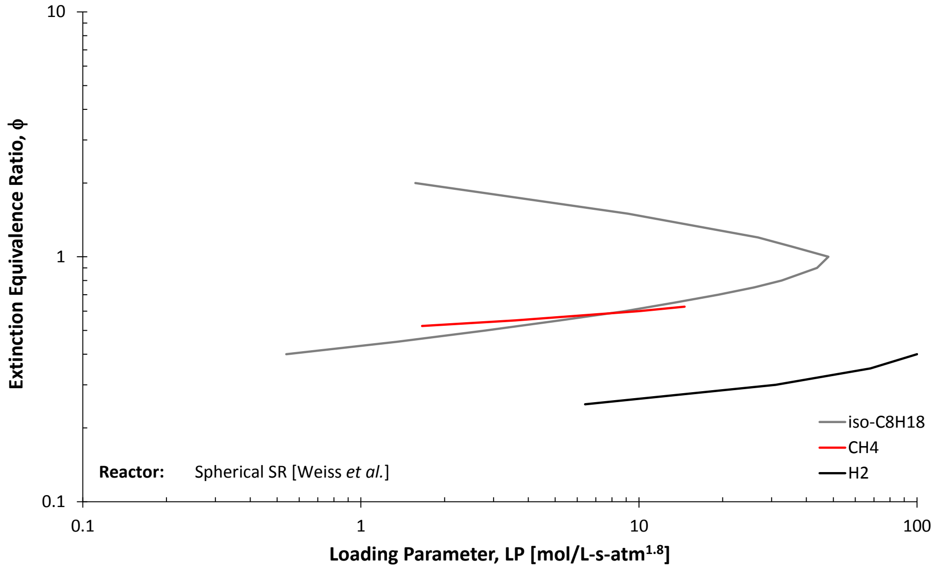

Figure 1.2: Simplified 'Longwell curve' for extinction of various fuels [11,12]

Toroidal Stirred Reactor and Flame Stability

The specific Toroidal Stirred Reactor (TSR) used in this work was developed at Wright Patterson Air Force Base (WPAFB) in Dayton, OH based on the design originally proposed by Nenniger *et al.* [14]. The efforts by Zelina and Ballal [1,15] characterized the reactor and used a propane flame to develop stability loops (ϕ versus reactor loading) compared to the spherical stirred reactor. Their toroidal design operated over a wider range of reactor loading, which they suggest makes it a superior design for stirred reactor stability studies.

Blust *et al.* [16,17] used an earlier version of the TSR to study lean blowout (LBO) and emissions from several fuels including methane, cyclohexane, n-heptane, n-dodecane, toluene, ethylbenzene, and some fuel blends. The authors first characterized the TSR turbulent mixing time to be roughly 19 μs, which compares favorably to the quoted reaction rate times of hydrocarbon reduction (25 μs), CO oxidation (500 μs), and NO_X formation (20 μs), so the reactor is well mixed, particularly for the oxidation reactions. The lean blowout limits for gas turbines are often wider than for the TSR because of incomplete mixing and localized regions of higher flammability. This takes place because mixing limitations produce local regions of higher equivalence ratio. The authors found that many of the fuels exhibited very similar blowout behavior at an equivalence ratio of $\phi = 0.47$. However, methane showed a blowout of $\phi = 0.55$. The most relevant aspect of this work is its characterization of the TSR as a tool for studying LBO for various fuels.

Ballal [18] studied lean blowout of lean premixed propane flames on the toroidal stirred reactor. The study used an earlier version of the stirred reactor that had larger inlets and consequently less turbulent mixing. The study found that the TSR stability limits matched well with both a spherical reactor and a step combustor, which helped validate the TSR as tool for studying lean blowout.

Flame Stability of Complex Fuels

Moses and Roets [19] studied LBO for Jet A, JP5, and a synthetic jet fuel from coal. They worked with a gas turbine combustor, and found that the three fuels behaved in essentially the same way at atmospheric conditions. The three fuels showed some small difference in LBO behavior during altitude tests, but these are attributed to differences in volatility and boiling point distribution.

Ballal [20] and later Stouffer *et al.* [21] used the TSR to study lean blowout of premixed flames using JP8 and a natural gas synthetic jet fuel. The blowout results for the two fuels were nearly identical (approximately 1300K at $\phi = 0.40$) when tested at a single reactor loading. When reactor loading was varied, the equivalence ratio at blowout varied negligibly, but the temperature at blowout increased with increased reactor loading. These two efforts became a foundational work for the current interest in quantifying lean blowout for several synthetic jet fuels with varying compositions.

Some flame stability studies utilized devices other than a stirred reactor, but looked at fuels that are very relevant to this work. The collaborative studies from Kumar *et al.* [22] and Hui *et al.* [23] looked at extinction stretch rates of traditional and alternative jet fuels using a counterflow twin-flame configuration. The studies looked at many fuels including surrogate components, Jet A, as well as synthetic fuels from natural gas, coal, Camelina and tallow. The studies found that the synthetic fuels and normal alkane surrogate fuels are more resistant to extinction than the petroleum jet fuel. The differences between the synthetic fuels are very small. The authors attribute the difference to the aromatic content of Jet A using kinetic models. Specifically, they use found that a slower initial reaction rate of the aromatic hydrocarbons compared to aliphatic hydrocarbons produced an overall slower reaction rate and a reduced resistance to extinction.

In summary, the literature discussed above shows the historical significance of flame stability studies and the use of the stirred reactor in stability characterization. The stirred reactor aims to isolate temperature and kinetics to understand chemically controlled phenomena. Initially, there were some studies of LBO on the TSR for several single-component fuels. In the last 10 years there were a very small number of studies that looked at LBO in the TSR for one traditional and one alternative fuel. The studies of extinction of many synthetic alternatives to jet fuel have focused on a different premixed flame configuration which does not isolate temperature and kinetics in the same way as the TSR.

Potential for Unique Contribution

The void in the previous studies leads to one objective for the present work - a study of the kinetically controlled blowout phenomenon in the stirred reactor for several synthetic alternative jet fuels. Systematically studying the blowout behavior of several alternative jet fuels in the toroidal reactor will provide insight into the behavior of real, multi-component fuels. Characterizing this behavior is crucial to the eventual adoption of these fuels as replacements or supplements of petroleum based jet fuel.

1.3.2 Detailed Stirred Reactor and Stability Modeling

The relevant stirred reactor modeling literature is organized into two parts: 1) stability models of the jet stirred reactor and 2) detailed models of the toroidal stirred reactor even though only one study concerned blowout. A third part will discuss the potential to provide unique contributions to the understanding of flame stability in stirred reactors.

Stability Models of the Jet Stirred Reactor

The Jet Stirred Reactor (JSR) at the University of Washington has been used for experimental studies since it was designed and fabricated by Lee [24]. However, detailed reactor modeling only became feasible relatively recently. Fackler [25] and Fackler *et al.* [26] used detailed Computational Fluid Dynamic (CFD) modeling to understand the internal behavior of the JSR and use it to develop a chemical reactor model (CRM) network. The network model was then used to perform detailed chemical kinetic calculations to predict emissions for various fuel blends.

Karalus *et al.* [27] and Karalus [28] then studied the mechanism of LBO and flame stabilization in the JSR for hydrogen and methane flames using primarily CFD and chemical kinetic calculations. Their CFD analysis found that the flame is effectively stabilized by reacting fluid that recirculates around the reactor and impinges upon the incoming mix of fuel and air. As equivalence ratio, ϕ, decreases the radical pool is not sufficiently large enough nor does it have enough time to develop fully before reaching the incoming jet, thus resulting in a failure to ignite the incoming jet. That insight led to the design of a network of CRMs to conceptualize the physical phenomena inside the reactor. Hydrogen blowout was adequately model with a single plug flow reactor (PFR) with recirculation and heat loss. The model for methane blowout expanded to become two PFRs in parallel that experience turbulent diffusive exchange, heat loss, and recirculation. The more complex model was necessary due to additional steps taking place in methane combustion. Specifically, the methane must first be converted into CO via a process that absorbs free radicals. Then the

CO is oxidized to CO_2 in a process that produces excess free radicals. Stability is determined by the availability of the free radicals from the CO oxidation to facilitate the methane reaction. The additional reactors are needed to simulate the diffusive transport that provides this link between these two zones. Karalus [28] also used the models to show that zones of the JSR occupy the well stirred reactor and reaction sheet regimes of turbulent combustion regime diagram in Figure 1.3. The diagram is described in detail by Law [2] and Peters [29], but a brief explanation is given in Appendix E in relation to some of the results presented in this work. The JSR blowout models helped frame the modeling effort presented in this work for the TSR.

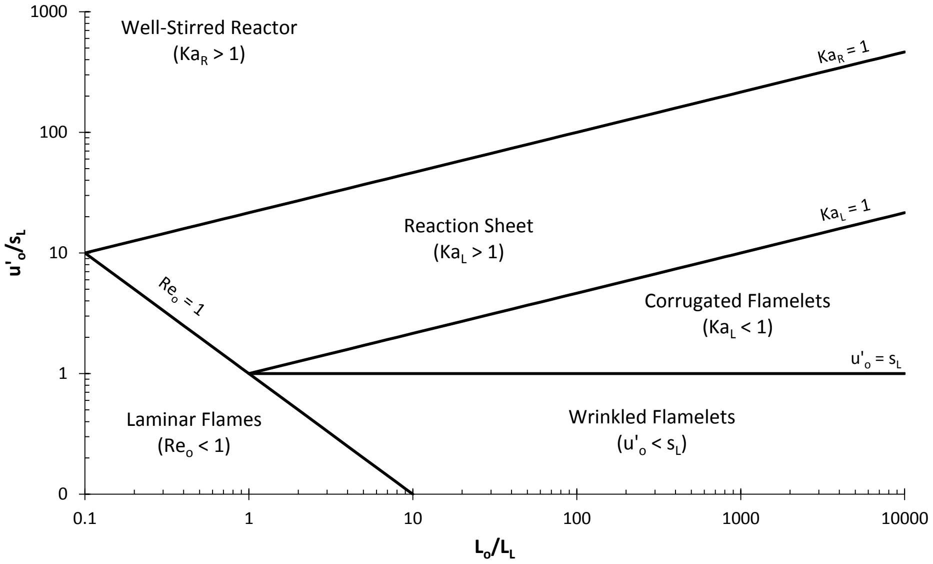

Figure 1.3: Premixed turbulent combustion regime diagram

Models of the Toroidal Stirred Reactor

An early study by Longwell and Bar-Ziv [30] evaluated the mixing behavior inside an earlier version of the TSR based primarily on 0D, 1D, and 2D coalescence-redispersion models. The study looked at mixing in the TSR and how it is affected by mixing frequencies, characteristic times, jet angles, and the number of jets. While that is interesting, the most useful aspect of this work was the extensive characterization of the flow within the reactor. According to the authors, the jets provide zones of shear-generated turbulence that diffuse through the reactor to provide microscale mixing, whereas macroscale mixing is due to the jet and bulk flows. The 20^o angle of the jets which enter the reactor at or near sonic velocity provide the mixing energy and thrust needed to cause the bulk flow to move around the toroid at nearly 200 m/s. The interaction of the jets with the bulk flow create a 'jet in crossflow' mixing system that results in circulating flow with characteristic Reynolds number on the order of 10^5. Each jet is estimated to entrain as much as 50-100 times its mass during a typical residence time. The authors determined that operation is expected to be in the distributed reaction mode based on the mean deformation rates of fluid elements being much larger than the conditions for quenching of laminar strained-flames.

Barat [31] studied the behavior of the TSR near blowout. The author stated that the turbulent premixed feed jets entrain and surround the bulk fluid. The macro-scale turbulent energy diffuses to provide micro-scale turbulent mixing. The turbulent mixing is fast relative to chemical time, so all compositions and temperature gradients are eliminated. At high temperature conditions, the TSR showed PSR like behavior. As the temperature was decreased, temperature and emissions measurement indicated localized combustion instabilities were present even though the reactor was stable in a global sense. The behavior was attributed to a failure of the incoming jet fluid to ignite as it entrained the surrounding bulk gases. The author hypothesized that the reactor volume effectively decreases near blowout due to localized extinction.

Bass and Barat [32] utilized a Partially Stirred Reactor (PaSR) model to predict temperature and species distributions inside the TSR that are impossible with PSR models. They model the TSR using the Interaction by Exchange with the Mean method to handle micro-mixing. The goal was to model the effect of mixing frequency and reaction kinetics on macro- and micro-mixing. Ultimately, it provides information about the distribution within the reactor without needing to perform the much more computationally demanding methods.

To date there is very limited literature discussing detailed reacting CFD analysis of the TSR. The primary work is from Briones *et al.* [33] who set out to 1) characterize the flow and flame structure, 2) investigate the effect of different kinetic models, 3) compare the performance of the TSR model to simpler models. In that effort, the reactor was assumed to be adiabatic.

The reactor model was also assumed periodic in the toroidal direction, based on the eight exhaust ports that existed in a previous version. This resulted in a slice of the reactor that was only 1/8 of the toroid, and only had six inlet jets. The reactor was then also assumed to be symmetric about the midplane, which modeled only ½ of the slice (now effectively only 1/16 of the entire reactor). Three simplified chemical mechanisms were used and compared for ethylene combustion: a one-step global mechanism with five species, a two-step global mechanism with six species, or a 15-step reduced mechanism with 19 species. The study also used the laminar-finite rate model to compute chemistry as it assumed the turbulence is fast enough such that the overall reaction rate is limited by chemistry. The study was primarily intended to be a first step into understanding the TSR and validating it as a tool in the distributed reaction regime. The study also determined that to truly understand the homogeneity of the TSR, comprehensive mechanisms are needed as the global mechanisms were not able to capture the species distributions within the reactor [33].

Potential for Unique Contribution

The simplified geometry and methods of the previous TSR models left a void in the understanding of the mechanism of flame stabilization within the reactor. The present work utilizes the methods developed for the JSR to further understand the fluid mechanics and chemistry inside the TSR by modeling the geometry more completely, with more detailed chemistry, and including the turbulence-chemistry interaction. It is of particular interest to understand the TSR behavior as equivalence ratio is decreased and the reactor approaches blowout.

1.3.3 NO_X Emissions and Fuel Effects

The relevant NO_X emissions literature is organized into two parts: 1) alternative jet fuel studies from gas turbine engines and 2) NO_X studies performed on basic combustion devices. A third part will discuss the potential to provide unique contributions to the understanding of NO_X emissions and fuel effects.

NO_X Emissions from Alternative Jet Fuels in Gas Turbine Engines

The WPAFB partners on this project have extensively studied NO_X emissions from a variety of fuels that are relevant to the present work. However, these tests were almost exclusively performed on a Rolls Royce T63 gas turbine engine used in helicopters. The engine was operated such that combustion temperatures were held roughly constant between fuels. As each study shows, the constant combustion temperatures and real-engine fluid mechanics resulted in virtually no difference in NO_X emissions. Monroig *et al.* [34] tested a synthetic fuel from natural gas with varying amounts of aromatic additive and found almost no difference in NO_X emissions. Cain *et al.* [35] looked at emissions versus engine loading for JP8, a coal-based synthetic fuel, and surrogate blends of n-decane with m-xylene, methyl-cyclohexane, iso-octane, and n-heptane. They found that total NO_X emissions were minimally affected during operation. DeWitt *et al*. [36] looked at the how three classes of petroleum aromatic fuel affected emissions from a natural gas derived synthetic fuel and JP8. The authors found that some emissions (carbon monoxide and unburned hydrocarbons) were increased with aromatics, but the NO_X emissions showed negligible difference. Corporan *et al.* [37] found negligible differences in NO_X emissions from the engine when burning JP8 blended with varying amounts of a synthetic fuel from natural gas at levels between 0% and 100% in increments of 12.5%. In the same study, a swirl stabilized research combustor showed very small effects on gaseous emissions. A later study by Corporan *et al.* [38] investigated many alternative jet fuels derived from various sources (natural gas, coal, blended fats, Camelina, and tallow) and found no appreciable differences in NO_X emissions. Klingshirn *et al.* [39] used the engine to look at the hydroprocessed Camelina and tallow fuels, blends of these fuels with JP8, and the tallow fuel blended with 1,3,5-trimethylbenzene (an aromatic). Once again, the combustion temperatures were held constant, and the authors claim that kept the NO_X emissions the same for each fuel.

In general, the WPAFB studies presented above were unable to find differences in NO_X emissions from the gas turbine engine operating on several fuels. The authors found significant differences in terms of soot, smoke, and particulate production. While interesting, these emissions are not relevant to the present work.

In two studies, Timko *et al.* [40,41] used a gas turbine engine to study emissions from several fuels/blends including JP8/Jet A, synthetic fuels from natural gas, and a biomass derived FAME (fatty acid methyl ester) fuel. When studying JP8 with blends of the natural gas fuel, the authors found small reductions in NO_X at high engine loads, but an increase in NO_X at low engine loads. The authors did experience a small variation in combustion temperature that would explain variations in NO_X emissions. In the second study, the authors found a sizable decrease in NO_X emissions from the FAME fuel blends. The FAME fuel consisted of 12 different oxygenated hydrocarbons. The NO_X differences were attributed to differences in fuel volatility and viscosity, which will effect spray vaporization, mixing, and ultimately, flame structure.

Moses and Roets [19] tested Jet A and a synthetic jet fuel from coal for NO_X emissions from a gas turbine combustor taken over a full landing-takeoff cycle. The NO_X emissions from the coal-based synthetic jet fuel decrease moderately (approximately 4%). Similarly, Lobo *et al.* [42] used an auxiliary power unit and found a 5% reduction in NO_X emissions when using a coal-based synthetic fuel as compared to Jet A. Khandelwal *et al.* [43] investigated NO_X emissions from a small gas turbine engine for Jet A, a synthetic fuel from coal, and a synthetic jet fuel with aromatic additives. The authors found that the 'neat' synthetic fuel produced marginally less NO_X emissions.

It is likely that the aircraft engine diffusion flame burners used in these tests tended to make all the results look the same. Much of the NO_X would have been made at the hot, stoichiometric interface, where the Zeldovich pathway dominates and makes NO_X emissions look similar. Basic combustion experiments (i.e., stirred reactors) would be more representative of land-based lean, premixed combustion systems, where differences between the fuel composition and chemistry might be more apparent.

NO_X Emissions from Basic Combustion Devices

Basic combustion devices are necessary to understand the kinetic pathways for NO_X production. Several studies utilize stirred reactors, counterflow burners, or reactor models to study NO_X emissions.

Blust *et al.* [16,17] presents NO_X versus temperature and carbon to hydrogen (C/H) ratio for many fuels (including methane, n-dodecane, toluene, and others). The authors found the N_2O pathway dominated at temperatures that below 1500K, but at temperatures above 1800K the Extended Zeldovich pathway accounted for NO_X production. They found that hydrocarbon structure and C/H ratio produce different NO_X for temps above 1800K and the same residence time, and that increased residence time increased NO_X production. One important result is that aliphatic fuels produced less NO_X than aromatics and cycloalkanes.

Zelina and Ballal [44,45] as well as Zelina *et al.* [46] used the just-developed TSR to study NO_X emissions from a variety of fuels including methane, ethane, propane, heptane, and JP7. The authors found that emissions increased exponentially with temperature, moderately with equivalence ratio, and peaked slightly on the lean side of stoichiometric. The NO_X emissions were greater for heavier hydrocarbons and increased with C/H ratio.

Ballal [18] burned propane and JP7 in the toroidal stirred reactor (TSR) and compared the results to those obtained from an axial staged combustor and a conventional gas turbine combustor. The primary conclusion from this work is that the stirred reactor reproduces the trends from the other combustors, but the practical systems produce more NO_X. The authors believe that the increased NO_X from practical combustors is due to the unmixedness in practical systems versus the TSR. The unmixedness leads to hot pockets of gas that generate much more NO_X due to the non-linear dependence of NO_X formation on temperature. Later, Ballal [20] presented a single data set of NO emissions versus temperature for JP8 and a synthetic fuel from natural gas. The emissions were measured from the TSR at two air flow rates and several temperatures from approximately 1425K to 1725K and showed a change in NO from approximately 1 ppm to 6 ppm. There is very little difference between these fuels at these temperatures. However, the current effort looks more closely at NO_X emissions from these and other fuels at much higher temperatures.

Meeks *et al.* [47] used a counterflow burner to study NO_X from n-decane and n-dodecane flames. The goal was to develop a set of experiments for kinetic mechanism validation and reduction, particularly for lower temperature NO_X formation where the widely accepted GRI

3.0 mechanism has not been well validated. The authors found that there were almost no differences between n-decane and n-dodecane in terms of NO_X emissions.

Han *et al.* [48] used kinetic models to look at the effect of unsaturated bonds in NO_X production using an n-heptane and 1-heptene triple flame. 1-heptene produced more NO_X in all cases (lean, rich, and non-premixed). The increased NO_X was attributed to higher concentrations of C_2H_2 and CH in the 1-heptene flame. This kinetic interpretation method is similar to one of the tasks in the present work.

Fackler [25] and Fackler *et al.* [26] investigated NO_X formation in the JSR from gaseous fuel alternatives to natural gas. The authors found that: 1) NO_X emissions decrease for methane flames with increasing concentrations of H_2; 2) NO_X emissions increase with the addition of C_2 and C_3 hydrocarbons; 3) adding CO_2 and N_2 diluents to methane flames increases NO_X emissions when stoichiometry was adjusted to maintain the same temperature. The reactor was modeled via CFD to develop a network of CRMs that predict NO_X formation from different zones within the reactor. The CRMs also enabled an analysis that determined the contribution of reactor zones and formation pathways to the overall NO_X production.

Lee *et al.* [49] developed a Staged Prevaporizer-Premixer (SPP) to reduce NO_X emissions and tested the device on several simple fuels, simple fuel blends, and real fuels. The primary effort looked at NO_X production versus air flow rate split (between the two stages), air temperature, residence time, and reactor temperature. Ultimately, the most relevant result is the variation in NO_X with fuel carbon to hydrogen (C/H) ratio that is recreated in Figure 1.4. Notice that there is a linear increase in NO_X production for aliphatic fuels and real fuels, but a different behavior for aromatic fuels. Later, Rutar *et al.* [50] used a network of chemical kinetic models to interpret the experiments. The reactor was divided into zones and each zone modeled with a PSR. Ultimately, the Fenimore prompt and NNH pathways make NO_X in the flame, and the Zeldovich and N_2O pathways make NO_X in the post-flame zone. The NNH, Zeldovich, and N_2O pathways are responsible for the increase of NO_X as a function of C/H ratio. The models show that the NNH pathway produces the largest amount of NO_X from a toluene flame.

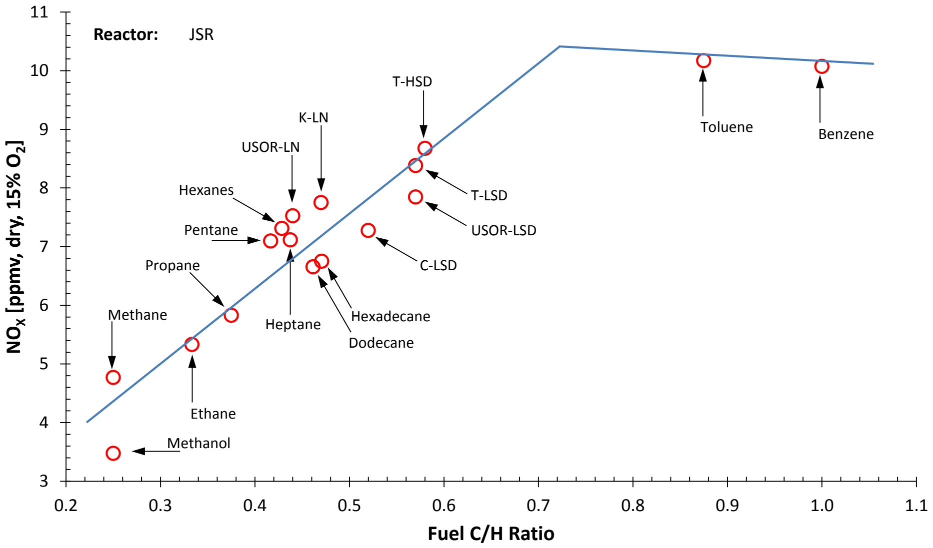

Figure 1.4: NO_X emissions vs. fuel C/H ratio [24,49]

Potential for Unique Contribution

The literature presented above shows that there are very few studies that investigated synthetic alternative jet fuels in a controlled, basic combustion device. This void motivates the present work to focus on studying real, complex jet fuel emissions based on the previous fuel-effects studies from the JSR. Ultimately, the goal will be to compare the new fuels to Figure 1.4 and look into the reasons behind any differences using chemical kinetic models.

1.4 Overview

The overarching goal here is to understand how fuel (especially alternative fuel) composition affects combustion, specifically flame stability and NO_X emissions. The focus is on jet aviation fuels and on stirred reactors, which share similarities with the combustor configuration of jet aircraft engines. A combination of 1) experiments in the stirred reactors with simplified physics and 2) modeling the underlying physical interactions will allow one to interpret experimental data and extrapolate any findings to new situations.

1.4.1 Objectives and Methods

Table 1.5, and the discussion that follows, presents the three objectives for this work with the relevant investigative methods.

Table 1.5: Objectives and methods

#	Objective to Study	Method[1]			Combustor[2]	
		Experiments	CFD	CRM	TSR	JSR
1	Effects of Fuel Composition on Combustion Stability	✓			✓	
2	Mechanism of Flame Stabilization in the Toroidal Reactor	✓	✓	✓	✓	
3	Effects of Fuel Composition on NO_X Emissions	✓		✓		✓

1. CFD = Computational Fluid Dynamics; CRM = Chemical Reactor Models
2. TSR = Toroidal Stirred Reactor; JSR = Jet Stirred Reactor

The first objective is to understand the effect of fuel composition on flame stability. This is approached by performing blowout experiments with several traditional and alternative jet fuels in a toroidal stirred reactor (TSR). The stirred reactor is selected as a good, generic representation of the primary zone of an aircraft gas turbine combustor. The baseline fuel is JP8, the most common military fuel. The first investigation studies the performance of JP8 along with several synthetic JP8 replacements that contain low concentrations of aromatic hydrocarbons. This effectively studies the effect of fuel feedstock. At the same time the study will also look at how higher levels of aromatic concentration affect flame stability by blending aromatic hydrocarbons with a single synthetic jet fuel. Aromatic compounds are necessary for lubricity and seals in fuel handling systems to swell and function properly, and Chapter 2 will show that the synthetic JP8 replacements contain very low concentrations of these important compounds.

The second objective stems from the stability studies using the TSR. There have been very few detailed modeling studies of TSR behavior, especially with the complexities needed to model flame stability. This absence of understanding motivated the work to develop turbulent CFD models that used detailed chemical kinetics for simple fuels, especially in the regime near blowout. These models look first at stable combustion in the TSR to understand the degree of homogeneity and variation of composition/temperature fields present in the reactor. Then the models look at temperature and species behavior as the conditions in the reactor move towards blowout to determine the exact mechanism by which the flame is destabilized. Finally, the CFD results are compared to a truly homogenous system (i.e., a PSR) and a real system (i.e., experiments).

The third objective is to understand how fuel composition effects NO_X emissions. The stirred reactor operates in a near isothermal environment so that NO_X chemistry can be correlated directly to temperature. The goal is to look at a JP8 baseline compared to alternative synthetic fuels and pure aromatic fuels. The kinetic calculations (via CRMs) are used to study how the fuels of different composition and chemical classes produce NO_X via different chemical reactions.

1.4.2 Organization

The remainder of this dissertation is presented in five additional chapters and six appendices. The five chapters are described next with each chapter ending with a discussion of its salient conclusions.

Chapter 2 focuses on the fuels included in this study. Some of the fuels only contain a single species, so their composition and properties are well defined. However, some of the fuels are very complex and a discussion of their composition and properties is necessary. We also discuss how various traditional and alternative jet fuels are made.

Chapter 3 focuses on Objective 1 from Table 1.5. It first presents the experimental system and methods that are used to study blowout for these fuels. It then presents the results of the experimental study. The results show the effects of fuel feedstock and aromatic content on blowout.

Chapter 4 focuses on Objective 2 from Table 1.5. It first presents the methods for modeling the TSR via CFD models and CRMs. It then presents the results of the CFD models. The results look first at stable combustion, and then look at the behavior as the reactor proceeds towards blowout. Finally, the CRMs and experiments are used for comparison and understanding of the blowout behavior.

Chapter 5 focuses on Objective 3 from Table 1.5. It first presents the experimental system and methods that are used to study NO_X for traditional and alternative jet fuels. It then presents the results of the experimental study. Finally, the discussion shifts to CRMs and NO_X formation from various surrogate fuels.

Chapter 6 concludes the dissertation by summarizing each chapter, particularly the conclusions and results from each of the three objectives, along with the impact of this work and directions for future work.

The appendices provide specific details. Appendix A presents details about the fuels. Appendix B presents the complete experimental data from the blowout and NO_X studies. Appendix C presents the analyses used for heat loss from the TSR and JSR, as well as the thermocouple correction analysis. Appendix D describes the details of the experimental data analysis procedures. Appendix E presents additional results from the CFD models. Appendix F provides details on the many chemical kinetic mechanisms used in this study.

Chapter 2
Fuels

This chapter focuses on the jet fuels and their properties. First, we describe how various traditional and alternative jet fuels are produced. Next, we discuss the fuels used in this study, and the properties of these fuels that are expected to be important for their utilization in combustion systems. In general, these fuels are multi-component liquid mixtures. Some of the tests utilize single species liquid fuels as surrogates to help understand the influence of specific chemical structures on combustion phenomena. Methane is used in some cases for comparison and to provide data for a concurrent CFD modeling effort.

2.1 Jet Fuel Production

Jet fuel is traditionally derived from petroleum, but there are several alternative feedstocks that under consideration that can produce very similar fuels. Figure 2.1 shows a simplified diagram of the major feedstocks and processes based primarily on information from Edwards *et al.* [51] and Kinder [52]. In general, jet fuels come from either non-renewable fossil fuel resources (i.e., petroleum, natural gas, and coal) or renewable biomass resources (i.e., lignocellulose, oils/fats, and starches/sugars). Two refining routes are most relevant to this work – Fischer Tropsch and hydroprocessing of fats and oils – so those will be discussed in detail. The other routes will be described briefly.

Each of the refining processes described below is initially used to convert the raw feedstocks into liquid hydrocarbons with carbon chain-lengths in the desired range for jet fuel. Once that is done, the fuels undergo the same processing steps to produce drop-in fuels. The fuels are hydroprocessed (described in detail below) to do three things: 1) remove oxygen and generate almost entirely normal alkanes, 2) 'crack' the chains that are too long for jet fuel, and 3) create branched chains (isomers) to improve low-temperature behavior. Molecules with chain lengths that are too short or too long can be removed via fractional distillation and reprocessed.

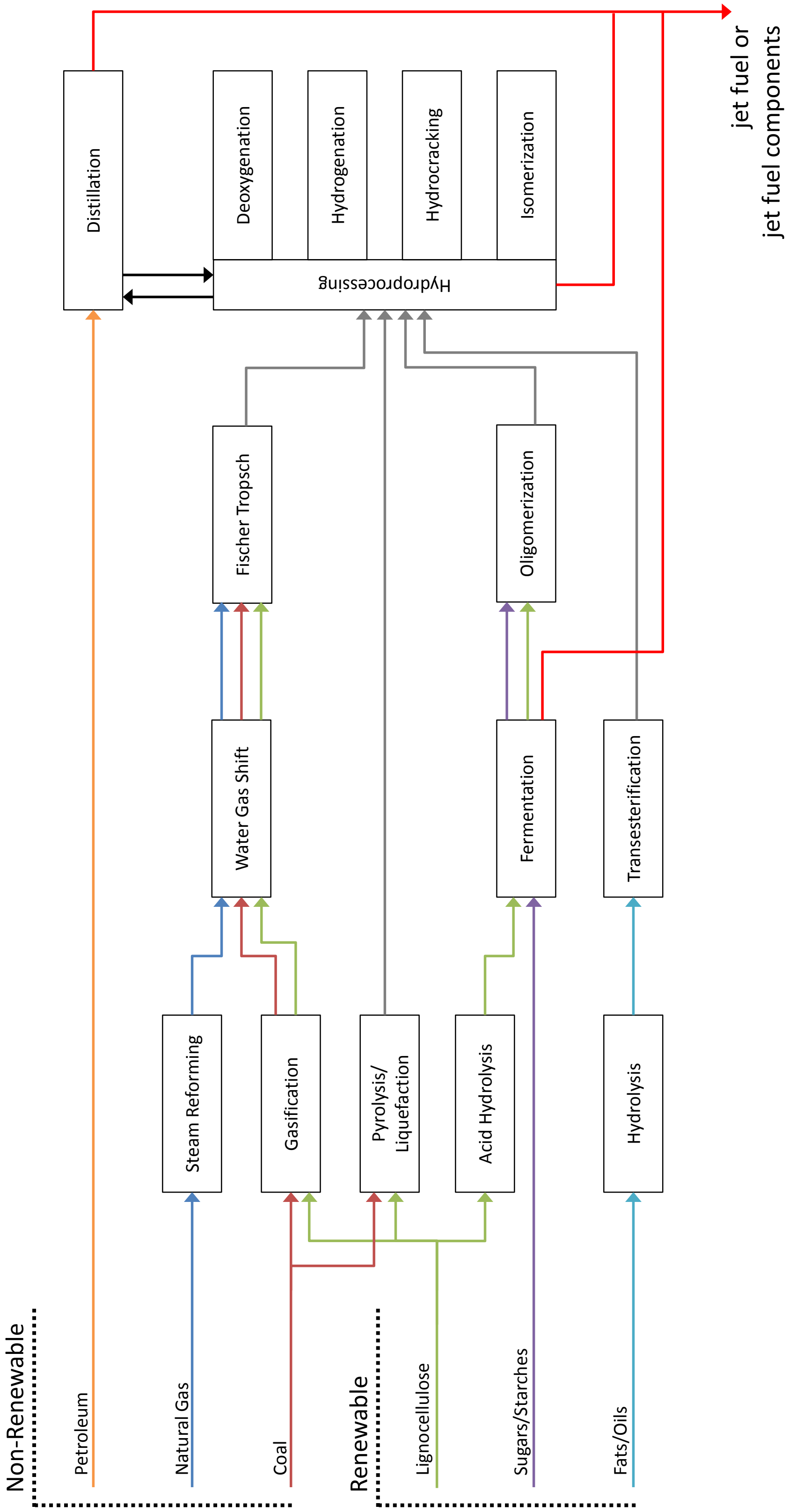

Figure 2.1: Jet fuel production processes [51,52]

2.1.1 From Petroleum via Distillation

Petroleum, or crude oil, comes from the remains of ancient organisms (like zooplankton and algae) that settled in low-oxygen environments among the sediments on lake and sea floors. As layers of sediments settled on top of these remains, temperature and pressure increased and caused the organic material to develop into kerogen (an organic compound prevalent in oil shale) and eventually oil or gas through endothermic reactions. If the temperature was too low the hydrocarbons would remain as kerogen, whereas if it was too high it would undergo thermal decomposition (cracking) to eventually form natural gas.

Traditional jet fuel is made from distillation (or fractionation) of crude petroleum oil. The crude petroleum oil is made up of many hydrocarbon molecules of different chain lengths. A simplified diagram of distillation is shown in Figure 2.2. The crude oil is heated and the different hydrocarbons separate at various temperatures based on ranges of molecular lengths. The lightest range of hydrocarbons is used as liquefied petroleum gas or in the chemical industry. Gasoline for cars is typically from C_5 to C_{10}. The kerosene jet fuel range is generally from C_{10} to C_{17}, which is the relevant range for this work. Diesel fuel used in trucks is roughly from C_{14} to C_{20}. The higher hydrocarbons are used as fuel oils, waxes, or asphalt. Since there is so much demand for transportation fuels, the longer hydrocarbons are 'cracked' to produce shorter hydrocarbons that are more useful in cars, trucks, trains, and planes.

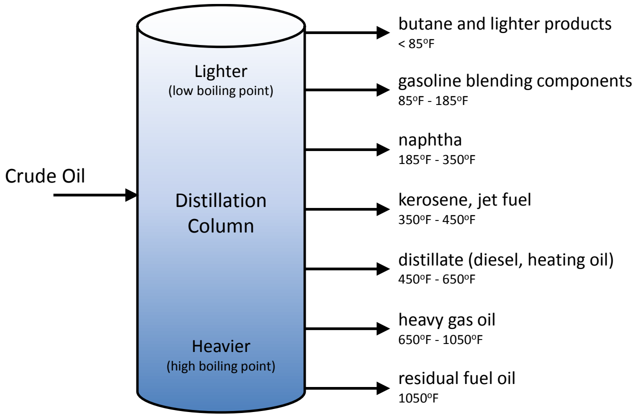

Figure 2.2: Crude oil distillation temperatures [53]

2.1.2 From Natural Gas, Coal, and Lignocellulose via Fischer Tropsch

Natural gas develops in a manner similar to petroleum, but undergoes thermal decomposition from liquids to gases under higher temperatures. Coal comes from woody biomass (plant fibers) that died and were buried under soil and water in an anaerobic environment protected from biodegradation and oxidation. The decaying organic matter experienced high temperature and high pressure over time and slowly converted to coal through various stages. Coal is classified into successive ranks which are indicative of both age and quality: peat, lignite, sub-bituminous, bituminous, and anthracite [54]. Lignocellulose is dry plant matter that is composed of carbohydrate polymers (cellulose and hemicellulose) and an aromatic polymer (lignin) [54]. Lignocellulose is the integral part of plant cell walls and provides the structural element to plants. It can be thought of as the woody/fibrous part of the plant.

The Fischer Tropsch (FT) process was developed by Franz Fischer and Hans Tropsch during the 1920s and provided fuels to German troops during World War II [55]. It is a catalytic reaction of syngas (CO and H_2) to generate liquid hydrocarbons of various carbon chain lengths (see Equation 2.1) [56]. The process is primarily dependent on the ratio of H_2 to CO, the catalyst material, and the residence time in the catalyst.

2.1 $$(2n + 1)H_2 + nCO \longrightarrow C_nH_{2n+2} + nH_2O$$ -

The first step in FT is generating the syngas, whose composition depends on the feedstock. Beginning with a natural gas feedstock, the syngas is typically generated via steam reforming as shown in Reaction 2.2 [56] with natural gas represented as methane. The process is similar for other hydrocarbons.

2.2 $$CH_4 + H_2O \longrightarrow CO + 3H_2$$ -

If coal or lignocellulose is the feedstock, the syngas is generally produced by gasification. Gasification is essentially the partial combustion of carbonaceous material (coal or lignocellulosic biomass) with a controlled amount of oxygen and/or steam. The original fuel undergoes dehydration and pyrolysis to result in char, a fuel that is mostly carbon. The char (shown as ‘C’) undergoes controlled combustion with oxygen to produce carbon dioxide (Reaction 2.3) and subsequently carbon monoxide (Reaction 2.4). In the presence of steam, the carbon and water react to form hydrogen and carbon monoxide (Reaction 2.5).

2.3 $C + O_2 \longrightarrow CO_2$ -

2.4 $CO_2 + C \longrightarrow 2CO$ -

2.5 $C + H_2O \longrightarrow H_2 + CO$ -

The raw syngas has an H_2/CO ratio that is set primarily by the elemental composition of the original fuel. The water-gas shift reaction (Reaction 2.6) is often used to adjust this ratio of H_2 to CO to optimally generate the hydrocarbons desired.

2.6 $CO + H_2O \longrightarrow CO_2 + H_2$ -

Iron, cobalt, nickel, and ruthenium based catalysts [56] are used to convert the syngas into liquid hydrocarbons. The products will be mostly normal alkanes, but there could be unsaturated HCs (α-alkenes) and oxygenates that are handled with further processing.

2.1.3 From Fats and Oils via Hydroprocessing

A second type of biomass (the first being lignocellulose as described above) utilizes the oils from plant seeds or the fats from animal byproducts as the hydrocarbon feedstock for fuel production.

Plant seeds and some fruits contain oils. Many of these oils are used for cooking (olive, sunflower, peanut, etc.), but the compounds in these oils also make good fuels. First, an oil mill is typically used to crush the seeds to make a mixture of oils and solids. The mixture is pressed (or a chemical solvent in used) to separate the oil and solids, with the oils undergoing further processing and the solids (called pomace) often used for fertilizer or animal feed [54,57].

Similarly, animal fat is often used for cooking (i.e., lard or tallow) but the compounds in these fats also make good fuels. After an animal is slaughtered, there will be a significant amount of fat, bone, and tissue left over which will generally not be separated. This material is typically sent to a rendering plant where it will be finely chopped and heated (with or without added steam) and then the liquid fat is centrifugally separated from solids and then subsequently from any water. The process varies slightly based on whether or not the end use of the renderings are for human consumption [54].

The oil extraction and fat rendering processes ultimately result in the same thing – a compound that is almost entirely triglycerides, which will be the feedstock for fuel production. An example triglyceride is shown in Figure 2.3. Triglycerides are esters consisting of glycerol ($C_3H_8O_3$) bonded to three fatty acids which are the aliphatic chains that will be the foundation of the fuel. In the triglyceride image below, the left part is the glycerol and the right parts are palmitic acid ($C_{16}H_{32}O_2$), oleic acid ($C_{18}H_{34}O_2$), α-linolenic acid ($C_{18}H_{30}O_2$) from top to bottom. The hydroxyl (HO-) group on the glycerol bonds with the carboxyl (-COOH) group on the fatty acid to form ester bonds [54].

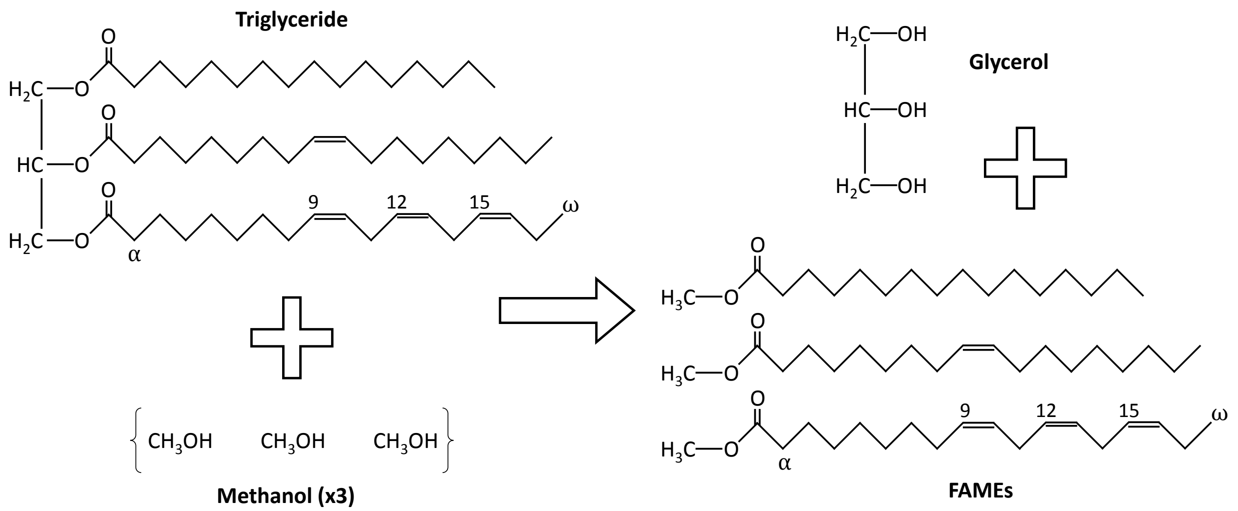

Figure 2.3: Example of a triglyceride and transesterification [54]

The first step in turning a triglyceride to fuel is to react the triglyceride into glycerol and fatty acids. It can be done by hydrolysis (high temperature, high pressure reaction of the triglyceride and water) to create glycerol and fatty acids [58]. Transesterification (also shown in Figure 2.3) transforms the ester to another ester by catalytically reacting the triglyceride with an alcohol (usually methanol), which is often supplied in excess. The free fatty acids (sans the glycerol backbone) will react with the alcohol to form esters which are called Fatty Acid Methyl Esters (FAMEs) or more generically Fatty Acid Alkyl Esters (FAAEs). After transesterification the FAMEs must be separated from the catalyst, excess alcohol, water, and glycerol [57]. At this stage, the fuel is ready to be used as biodiesel, but for use in aircraft, further processing is necessary. Interestingly, different feedstocks have different proportions of fatty-acid carbon chain lengths in the triglyceride [59]. The two triglyceride sources used in this work are Camelina and tallow, with fatty acid profiles as shown in Table 2.1.

Table 2.1: Fatty acid compositions of Camelina and tallow

Oil/Fat	**Fatty Acid[1]**								**Source**
	14:0	**16:0**	**18:0**	**18:1**	**18:2**	**18:3**	**20:1**	**22:1**	
Camelina	-	5.2	2.3	15.0	16.8	35.2	14.2	3.7	[59]
				14-19.5	18.8-24	27-34.7	12-15	4	[54,60]
Tallow	3-6	24-32	20-25	37-43	2-3	-	-	-	[59]

[1] Fatty Acids are designated by XX:Y, where XX is the number of carbons in the chain, and Y is the number of double bonds in the chain

The FAAEs from biodiesel do not have the stability, specific energy, cold-temperature, or blending properties necessary for use as jet fuel. Hydrotreated Renewable Jet (HRJ) is often called Hydrogenated Esters and Fatty Acids (HEFA). The general ‘hydroprocessing’ step turns triglycerides, free fatty acids, alkyl esters, or other compounds into alkanes for use as a jet fuel. Hydroprocessing really includes deoxygenation/hydrogenation, isomerization, and hydrocracking [57].

Deoxygenation is typically a low temperature (approximately 550K) catalytic reaction with a di-metallic catalyst like nickel-molybdenum or cobalt-molybdenum in the presence of hydrogen. Deoxygenating the fatty acids saturates the terminal carbon atoms with hydrogen instead of oxygen. Hydrogenation replaces carbon-carbon double bonds (alkenes) with single bonds (alkanes). The result of deoxygenation and hydrogenation will be saturated hydrocarbons (n-alkanes), water, and carbon dioxide. The n-alkanes remaining will be in the C_{16}-C_{18} range (because of the fatty acids in the triglyceride) and will have poor freezing characteristics which can be improved by isomerization or hydrocracking [57].

Isomerization uses catalytic reaction of n-alkanes with hydrogen at moderate temperatures (roughly 550K) and pressures (roughly 5MPa) to turn the straight-chain hydrocarbons to branched hydrocarbons (isomers). Hydrocracking shortens the chain lengths to the desired range via the catalytic reaction of n-alkanes with hydrogen at high temperatures (roughly 675K) and pressures (7-14MPa). For both isomerization and hydrocracking the catalyst, temperature, and pressure selection will dictate the resultant hydrocarbon range and isomer content. Ultimately, any species that are not in the desired range can be removed (via fractional distillation) and reprocessed to increase the amount of jet fuel produced [57].

2.1.4 From Coal and Lignocellulose via Direct Liquefaction/Pyrolysis

Direct liquefaction can be called 'hydroliquefaction' to distinguish it from pyrolysis [61]. It is the thermochemical conversion of coal or lignocellulose in the presence of hydrogen and a catalyst at relatively low temperatures (525-600K) and high pressures (5-20 MPa). The long-chain compounds in the feedstock are degraded into small molecules using a catalyst or solvent. The small molecules are unstable and reactive so they rearrange through condensation, cyclization, and polymerization leading to new compounds [58].

Pyrolysis and liquefaction are often confused with each other, but the primary difference is the presence of a catalyst and excess hydrogen for liquefaction. Pyrolysis applies high heat (650-800K) and low pressures (0.1-0.5 MPa) with little or no air. It produces char, condensable organic liquids, and other compounds [58].

Direct liquefaction and pyrolysis result in the same thing via slightly different means. The result is liquid organic compounds that can be subjected to further processing (hydrogenation, hydrocracking, isomerization, deoxygenation, polymerization, distillation, etc.) to result in fuels suitable for use in jet engines.

2.1.5 From Lignocellulose and Sugars/Starches via Fermentation

In general, plant sugars consist of sucrose, which includes both glucose ($C_6H_{12}O_6$) and fructose ($C_6H_{12}O_6$) [54,57]. The simple sugars (monosaccharides) are bonded together to form starch. Starch is generally found in the fruit tissues of plants, like kernels of corn [57]. Starch is a ‘simple’ carbohydrate, where the more general term carbohydrate applies in this discussion to very large combinations of mono- and disaccharides.

Fermentation takes sugars and utilizes microorganisms like yeasts, bacteria, or molds [60] to convert monosaccharides like glucose and fructose into alcohols. Reaction 2.7 shows the fermentation conversion of glucose ($C_6H_{12}O_6$) into ethanol (C_2H_5OH) and carbon dioxide [61], which can be more generically described by Equation 2.8.

2.7 $$C_6H_{12}O_6 \longrightarrow 2C_2H_5OH + 2CO_2$$ -

2.8 $$\text{sugars} \xrightarrow{\text{microorganisms}} \text{alcohol} + \text{byproducts}$$ -

All fermentation processes utilize these simple sugars (typically monosaccharides, but sometimes disaccharides) as the reactant, so the complex sugars (polysaccharides) found in carbohydrates (like cellulose and hemicellulose) and starches must first be converted into simple sugars. Both starches and carbohydrates are converted via hydrolysis. Chemical (or acid) hydrolysis is a typical process. Sulfuric acid is common for starch conversion, whereas either sulfuric or hydrochloric acid is common for cellulose/hemicellulose conversion. An alternative to acid-based processes is enzymatic hydrolysis. In practice, cellulose/hemicellulose is converted to simple sugars via first dilute-acid hydrolysis and subsequently enzymatic hydrolysis [60].

The fermentation process is most commonly used to produce ethanol, but other products include methanol, propanol, and butanol [56]. Syngas can be fermented by using a few bacterial strains to produce ethanol and acetic acid [58]. These alcohols are used as the building blocks of jet fuel by performing oligomerization (or polymerization). Oligomerization basically takes the short-chains of alcohols and links them together to form chains of a desired length [57]. Typically, the resultant chain length will be a multiple of the base alcohol (i.e., butanol will produce octane, dodecane, hexadecane, etc.).

New technology utilizes genetic engineering to make organisms that directly ferment the lignocellulosic feedstock to specific hydrocarbons [57].

2.2 Fuels of Interest

2.2.1 Fuels for Experimental Studies

The "complex" fuels used in this study are multi-component liquids at standard temperature and pressure that are candidates for use in jet aircraft. Six fuels of this type were tested, and are described below and in Table 2.2.

Table 2.2: Complex fuels tested

Name	Global Formula[1]	C/H Ratio	Type	Method	Feedstock
FT Natural Gas	$C_{11.9}H_{25.9}$	0.46	Synthetic	Fischer Tropsch Synthesis	Natural Gas
FT Coal	$C_{10.7}H_{22.7}$	0.47			Coal
HP Camelina	$C_{11.3}H_{24.5}$	0.46		Hydroprocessing	Camelina
HP Tallow	$C_{12.3}H_{26.5}$	0.46			Tallow
JP8	$C_{11.9}H_{22.8}$	0.52	Traditional	Distillation	Petroleum
Pet-Aromatic	$C_{9.9}H_{12.9}$	0.77			

[1] Obtained from tests at AFRL [62]

Two of the fuels tested are derived via Fischer Tropsch (FT) synthesis from natural gas and coal. FT Natural Gas is often called S8 for synthetic JP8. It is the standard synthetic fuel used in many studies [21,63,64]. Two of the fuels are derived via hydroprocessing (HP) of biological feedstocks. Camelina (formal binomial name: *Camelina sativa*) is a plant in the cabbage family and tallow is rendered cow fat. The baseline petroleum-based fuel is JP8, which is the standard fuel for United States military aircraft. JP8 is very similar to Jet A (commercial aircraft fuel), but it includes additives to improve lubricity, corrosion, anti-static behavior, and fuel system icing [65]. The sixth fuel, Pet-Aromatic, is a blend of many aromatic compounds and is used to study the effect of aromatic additives to fuel. As will be discussed later, aromatic content is critical for seal-swell in current fuel handling systems. All of these fuels consist of mixtures of a broad range of many hydrocarbons. As such, they do not have a single boiling point, but instead have a distillation curve. More details about all fuels can be found in Appendix A.

Burning these complex fuels follows the same stoichiometry rules that exist for simple hydrocarbons. The stoichiometric, complete combustion reactions for each of the fuels are given below as Reactions 2.9 to 2.14.

$$C_{11.9}H_{25.9} + 18.375[O_2 + 3.76N_2] \longrightarrow 11.9CO_2 + 12.95H_2O + 69.09N_2 \qquad \text{FT Natural Gas} \tag{2.9}$$

$$C_{10.7}H_{22.7} + 16.375[O_2 + 3.76N_2] \longrightarrow 10.7CO_2 + 11.35H_2O + 61.57N_2 \qquad \text{FT Coal} \tag{2.10}$$

$$C_{11.3}H_{24.5} + 17.425[O_2 + 3.76N_2] \longrightarrow 11.3CO_2 + 12.25H_2O + 65.52N_2 \qquad \text{HP Camelina} \tag{2.11}$$

$$C_{12.3}H_{26.5} + 18.925[O_2 + 3.76N_2] \longrightarrow 12.3CO_2 + 13.25H_2O + 71.16N_2 \qquad \text{HP Tallow} \tag{2.12}$$

$$C_{11.9}H_{22.8} + 17.6[O_2 + 3.76N_2] \longrightarrow 11.9CO_2 + 11.4H_2O + 66.176N_2 \qquad \text{JP8} \tag{2.13}$$

$$C_{9.9}H_{12.9} + 13.125[O_2 + 3.76N_2] \longrightarrow 9.9CO_2 + 6.45H_2O + 49.35N_2 \qquad \text{Pet-Aromatic} \tag{2.14}$$

Two “simple” fuels (listed in Table 2.3 and shown in Figure 2.4) were also tested to facilitate modeling and interpretation. One fuel, methane (CH_4), is a gas at room temperature and pressure and is the primary constituent in natural gas. It is included in this study because it is relatively simple to model via detailed chemical kinetics. The other, mesitylene (1,3,5-trimethylbenzene or 135-TMB) is an aromatic composed of a benzene ring with three methyl groups at the first, third, and fifth positions. The specific 135-TMB used here is reported as being derived from a biological feedstock. Ethane and propane were tested briefly (see Appendix B), but were not pursued because they did not fit within the goal of studying and understanding alternatives to jet fuel.

Table 2.3: Simple fuels tested

Type	Name	Molecular Formula	C/H Ratio	IUPAC[1] Name
aliphatic	methane	CH_4	0.25	methane
aromatic	mesitylene/135-TMB	C_9H_{12}	0.75	1,3,5-trimethylbenzene

[1] International Union of Pure and Applied Chemistry

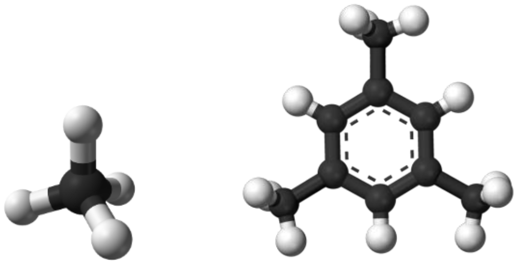

methane 1,3,5-trimethylbenzene

Figure 2.4: Ball-and-stick models for simple fuels [54]

The simple fuels follow the stoichiometric, complete combustion reactions given as Reactions 2.15 and 2.16.

2.15 $$\mathrm{CH_4 + 2[O_2 + 3.76N_2] \longrightarrow CO_2 + 2H_2O + 7.52N_2}$$ methane

2.16 $$\mathrm{C_9H_{12} + 12[O_2 + 3.76N_2] \longrightarrow 9CO_2 + 6H_2O + 45.12N_2}$$ 135-TMB

2.2.2 Fuels for Modeling Studies

Kinetic modeling requires single fuels or surrogate fuels made up of several single fuels. The modeling studies described below utilized fuels based on the kinetic mechanisms available. Firstly, methane and 1,3,5-trimethylbenzene were described above, as they were studied with both experiments and models. Four additional single component fuels were used only for modeling studies. These fuels are shown in Figure 2.5 and Table 2.4.

In general, these fuels were selected because of the kinetic mechanisms available and because they act as representatives for the some of the fuel classes present in the real fuels.

Table 2.4: Simple fuels modeled

Class	Name	Molecular Formula	C/H Ratio	IUPAC[1] Name
normal alkane	methane	CH_4	0.25	methane
	n-octane	C_8H_{18}	0.44	normal octane
iso-alkane	iso-octane	C_8H_{18}	0.44	2,2,4-trimethylpentane
cycloalkane	PCH	C_9H_{18}	0.50	propylcyclohexane
alkylbenzene	toluene	C_7H_8	0.875	methylbenzene
	mesitylene/135-TMB	C_9H_{12}	0.75	1,3,5-trimethylbenzene

1. International Union of Pure and Applied Chemistry

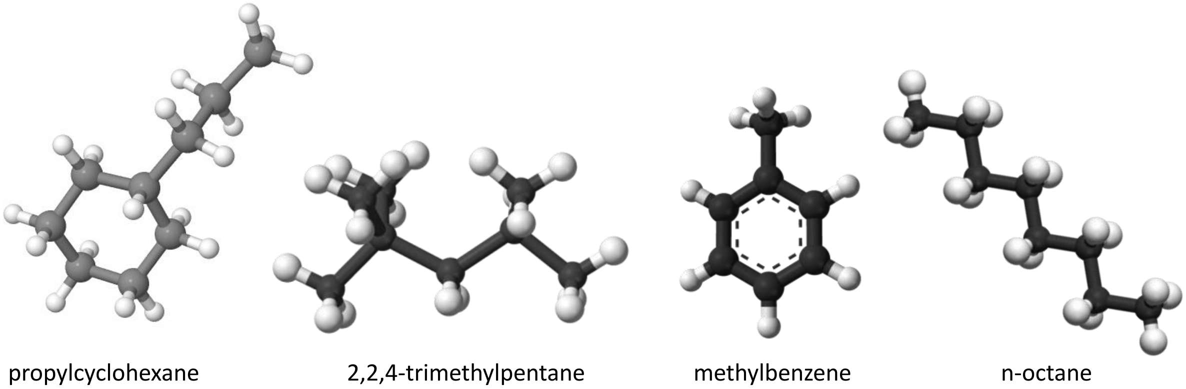

Figure 2.5: Ball-and-stick models for simple modeled fuels [54,66]

2.3 Detailed Fuel Composition

Jet fuel is complex and may consist of thousands of different chemical species. Detailed analysis of these fuels via two-dimensional gas chromatography (GCxGC) testing at AFRL [62] resulted in the raw data chromatograms that are presented below in Figure 2.6. The y-axis is normalized signal amplitude, which are converted to concentrations of specific species as presented later. These traces also suggest some qualitative information about the fuels. Essentially, a few spikes indicate that a few species dominate the composition, whereas many spikes indicate a large distribution. Also, the width of the spiked region indicates fuels with a wide or narrow molecular range.

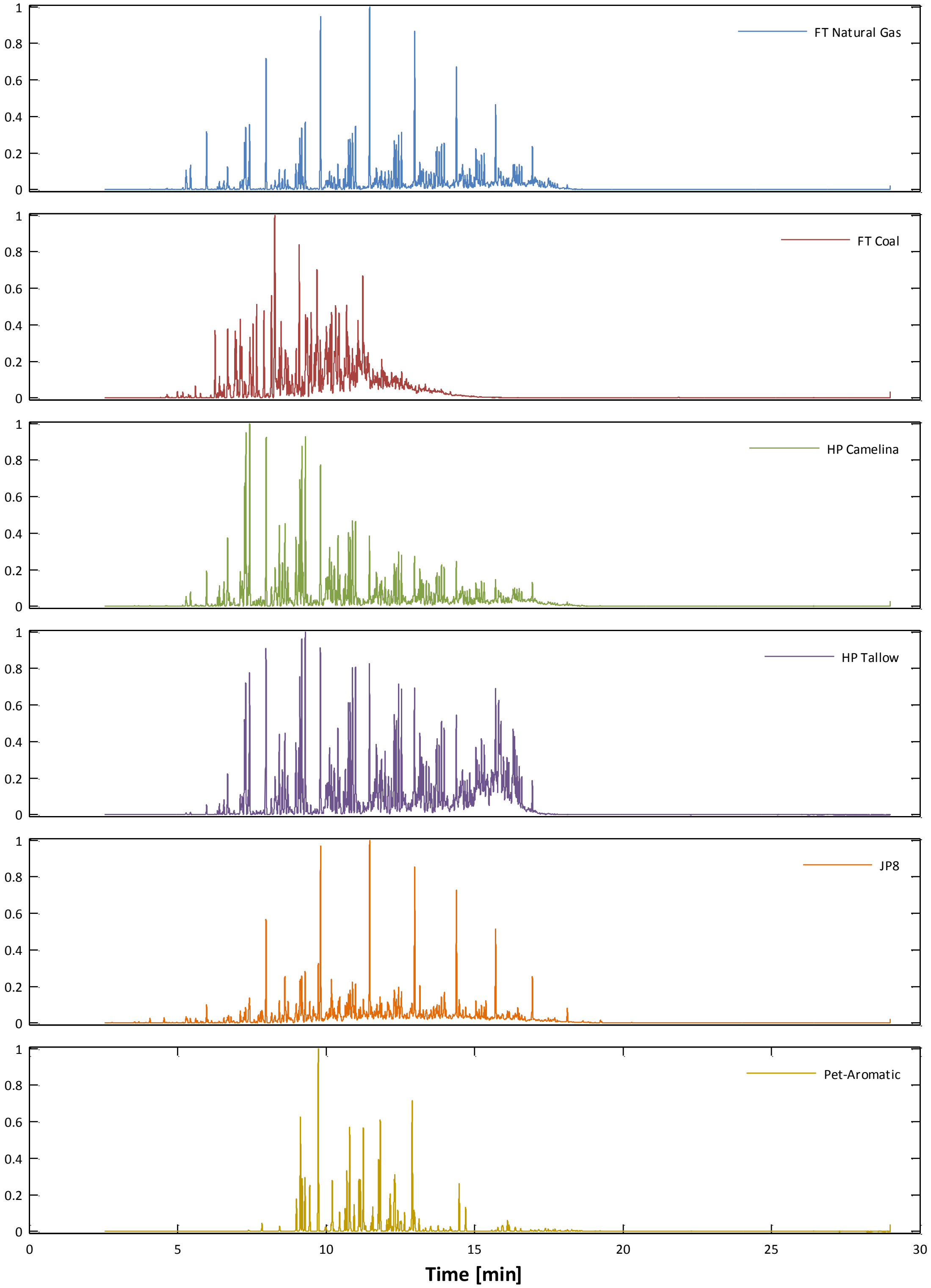

Figure 2.6: Relative abundance chromatograms of complex liquid fuels [62]

The chromatograms can be converted to species concentrations with appropriate calibration curves and standards. The numerical data for the fuel composition are included in Appendix A. The species present in the fuels can be subdivided into various hydrocarbon (HC) categories. The first division splits the fuels into aliphatic HCs versus aromatic HCs, as shown in Figure 2.7. Notice that the four synthetic fuels have almost no aromatic content, which is why the aromatic fuels are added to the synthetic fuels to produce a fuel that is more representative of conventional jet fuel. Aromatic compounds are a necessary element in jet fuel because they are critical to fuel handling systems and lubricity. The fuel system contains several components that utilize o-ring seals and gaskets. These seals swell when used with aromatic fuels and will not work properly in the presence of low or zero aromatic content fuels.

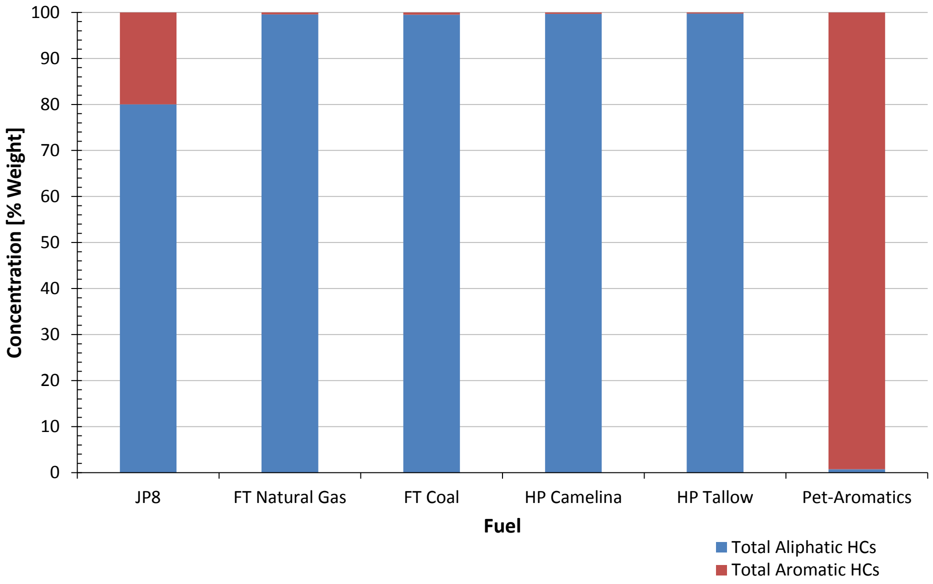

Figure 2.7: Aliphatic and aromatic composition of fuels

The composition can be subdivided into the six categories of Figure 2.8 – three types of aliphatic HCs (normal alkanes, iso-alkanes, and cycloalkanes) and three types of aromatic HCs (alkylbenzenes, indans/tetralins, and alkylnapthalenes). The jet fuel, as expected, contains all six of these types of hydrocarbons.

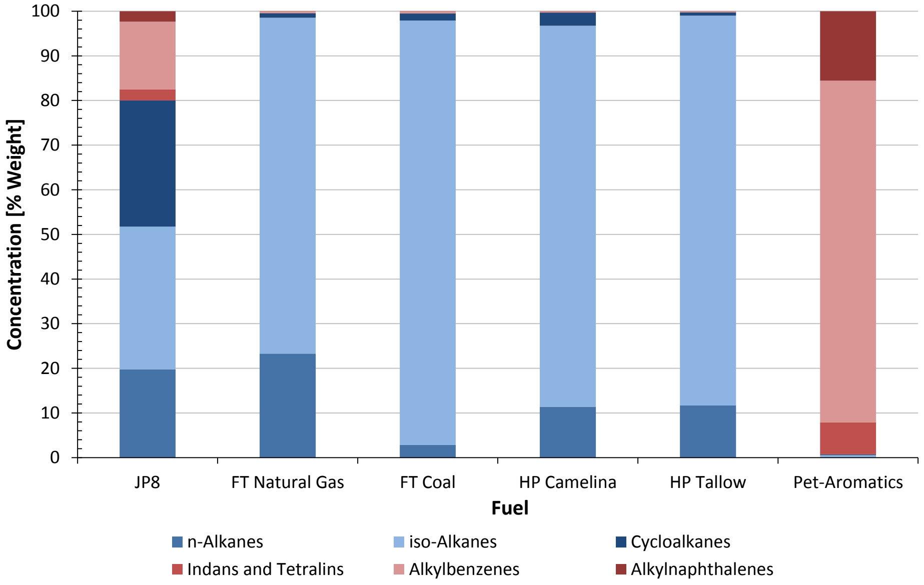

Figure 2.8: Fuel composition in six hydrocarbon classes

Each of the six HC classes can be characterized further from the GCxGC analysis. Looking first at the aliphatic HCs, the fuels contain normal alkanes (Figure 2.9), isomers of alkanes (Figure 2.10), and cycloalkanes (Figure 2.11). Normal alkanes (n-alkane) consists of straight-chain hydrocarbons without any double or triple C-C bonds. Iso-alkanes include any molecular arrangement with a branch group that stems off of the main chain. Both n-alkanes and iso-alkanes follow the general formula of C_nH_{2n+2}. The term isomer is used to distinguish between molecules that have the same atomic makeup, but which have different molecular arrangements. Cycloalkanes are alkanes that contain a ring of at least three carbon atoms. These shown here as mono-cycloalkanes with the general formula of C_nH_{2n} and di-cycloalkanes with the general formula C_nH_{2n-2} [67].

Notice on Figure 2.9, FT Natural Gas has a very high content of n-alkanes with the largest being n-undecane (C_{11}). FT Coal has relatively low n-alkane content with a large amount of n-decane (C_{10}). HP Tallow has a relatively even distribution of n-alkanes.

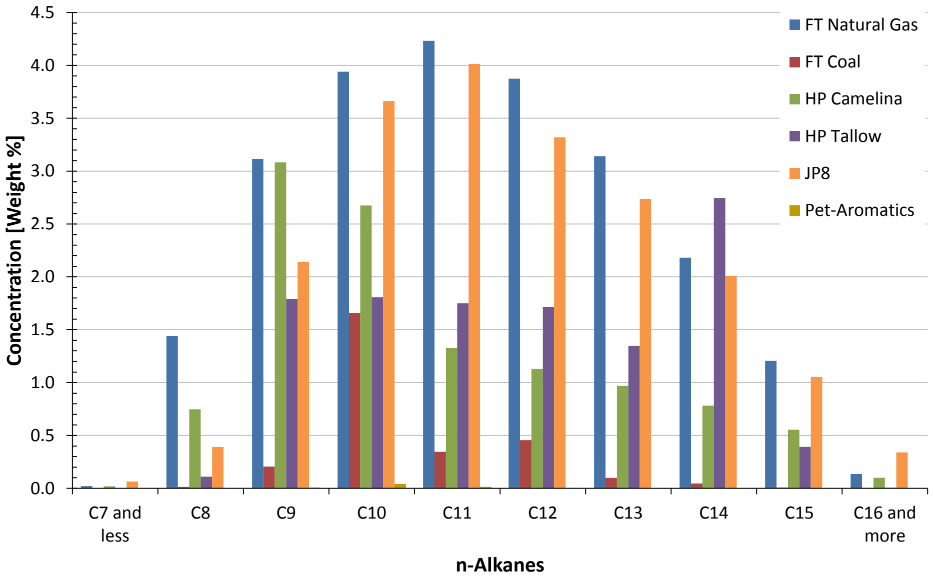

Figure 2.9: n-Alkane concentration in liquid fuels

Notice on Figure 2.10, FT Coal has much larger content of C_9, C_{10}, and C_{11} iso-alkanes than any of the other fuels. In fact the FT Natural Gas, HP Camelina, and HP Tallow fuels have roughly even and similar distributions of iso-alkanes. Lastly, notice on Figure 2.11 that the fuels have very small, yet similar, cycloalkane concentrations.

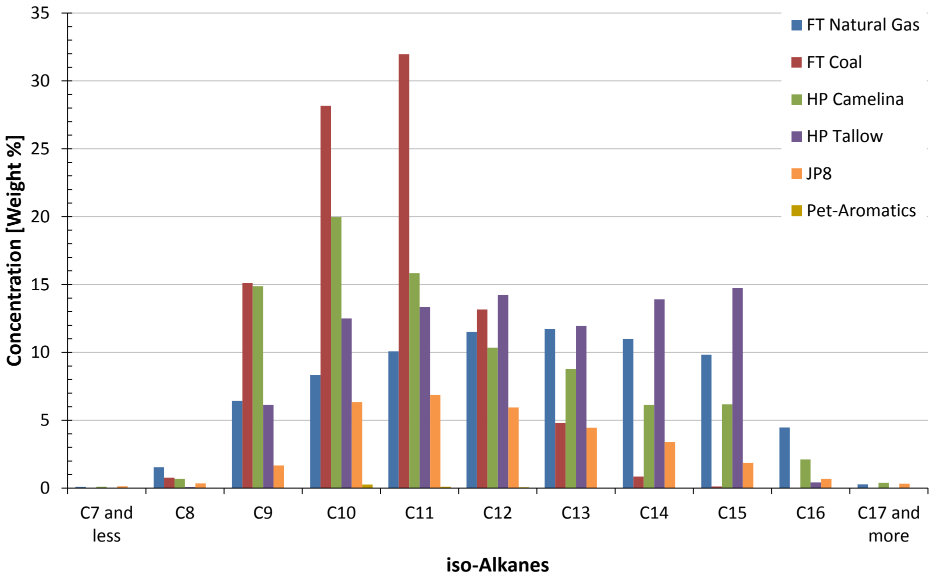

Figure 2.10: iso-Alkane concentration in liquid fuels

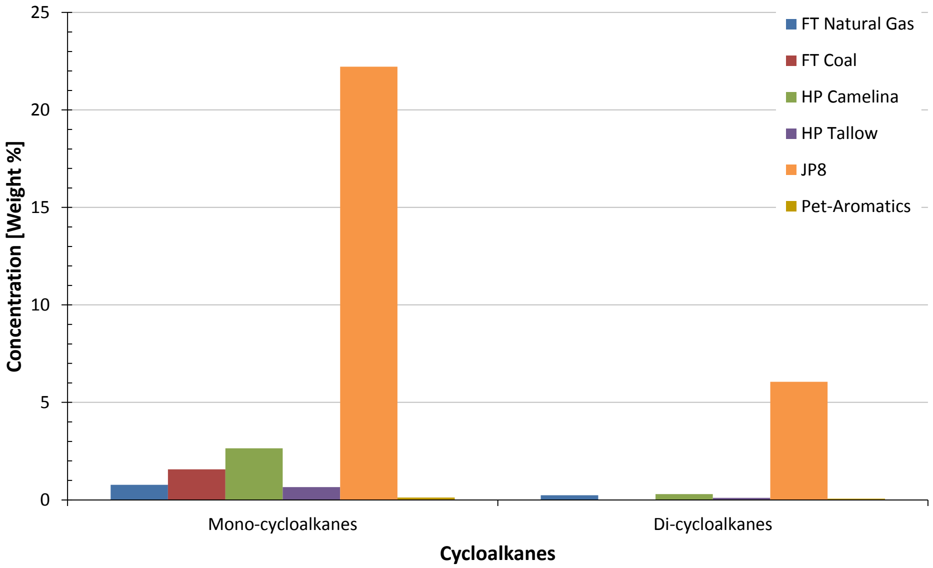

Figure 2.11: Cycloalkane concentration in liquid fuels

The fuels contain aromatic HCs in three forms: alkylbenzenes (Figure 2.12), indans/tetralins (Figure 2.13), and alkylnapthalenes (Figure 2.14). Alkylbenzenes are compounds with the base structure of a benzene (C_6H_6) ring and many potential molecular chains branching off of the carbon atoms. The general formula is C_nH_{2n-6}. Alkylnapthalenes have the base structure of naphthalene (two benzenes fused together to create $C_{10}H_8$) and many potential molecular chains branching off of the carbon atoms. The general formula is C_nH_{2n-12} [67]. Indan and tetralin are benzene based molecules that do not follow the same general formula of other alkylbenzenes. Indan is essentially a benzene molecule fused with a cyclopentane to give the general formula C_9H_{10}. Tetralin is essentially a benzene molecule fused with a cyclohexane to give the general formula $C_{10}H_{12}$.

Notice on Figure 2.12, Pet-Aromatic contains *no* benzene or toluene, and large contents of C_3 and C_4 benzene derivatives. This is the reason 135-TMB is being considered as a potential aromatic component for synthetic jet fuel.

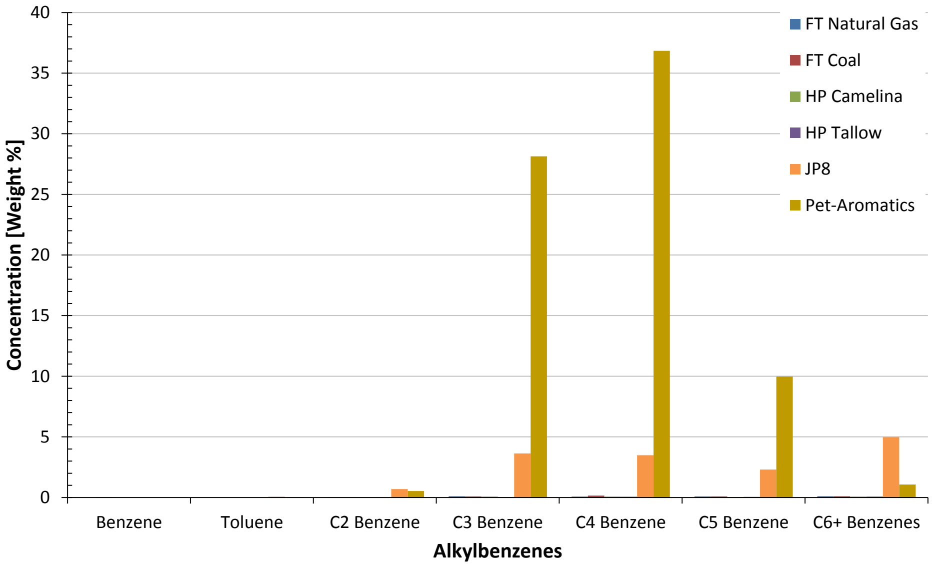

Figure 2.12: Alkylbenzene concentration in liquid fuels

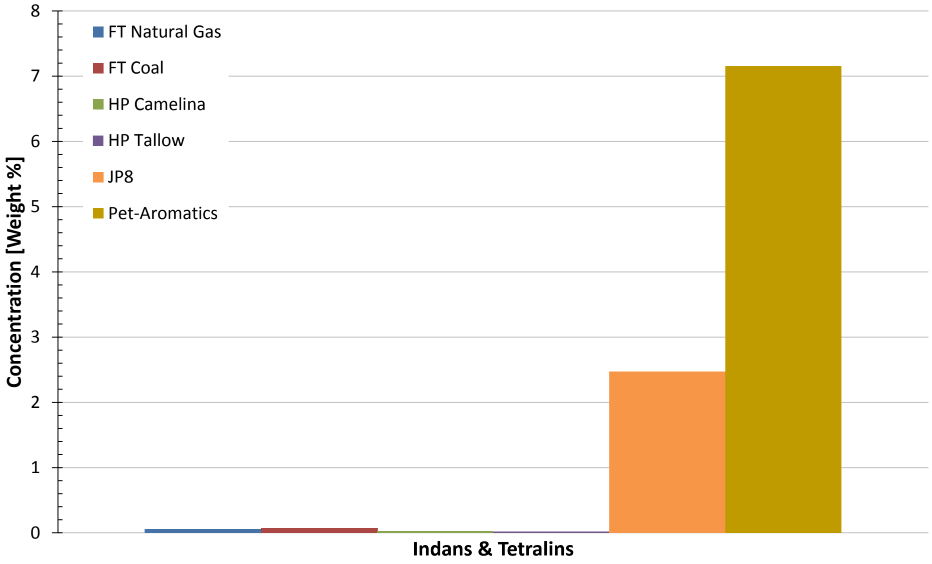

Figure 2.13: Indan and tetralin concentration in liquid fuels

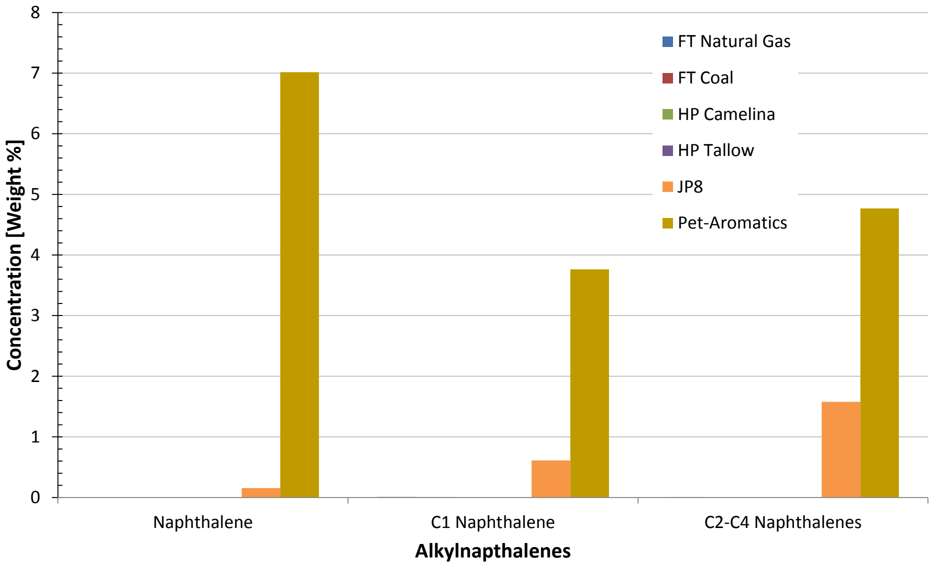

Figure 2.14: Alkylnapthalene concentration in liquid fuels

The JP8 used as a baseline has roughly 20% aromatics by weight (roughly 18.7% by volume [68]), so the first set of tests were limited to that range of aromatic content. Each synthetic fuel is tested in its 'neat' state (without aromatic additives) and with varying content of the Pet-Aromatic fuel.

2.4 Conclusions

So far, we have learned the specific details, properties, and composition of the fuels that are going to be investigated throughout this work. The conclusions that can be drawn so far are as follows:

- The four synthetic fuels contain almost no aromatic compounds.
- The traditional and synthetic jet fuels have very similar C/H ratios.
- The four synthetic fuels have widely varying compositions, but each consist primarily of n-alkanes, iso-alkanes, and cycloalkanes.

Now, let us undertake Objective 1 and investigate how these fuels affect combustion stability.

Chapter 3
Effects of Fuel Composition on Combustion Stability

This chapter focuses on Objective 1 from Table 1.5 in Section 1.4.1, and presents the study into the effects of fuel feedstock and aromatic concentration on extinction behavior and flame stability in the toroidal reactor. The discussion will first cover the experimental methods and then the experimental results. The complete experimental results are available in Appendix B.

3.1 Experimental Methods

The Toroidal Stirred Reactor (TSR) is used for the extinction studies. A system schematic is shown in Figure 3.1 with each of the subsystems highlighted and discussed below in further detail.

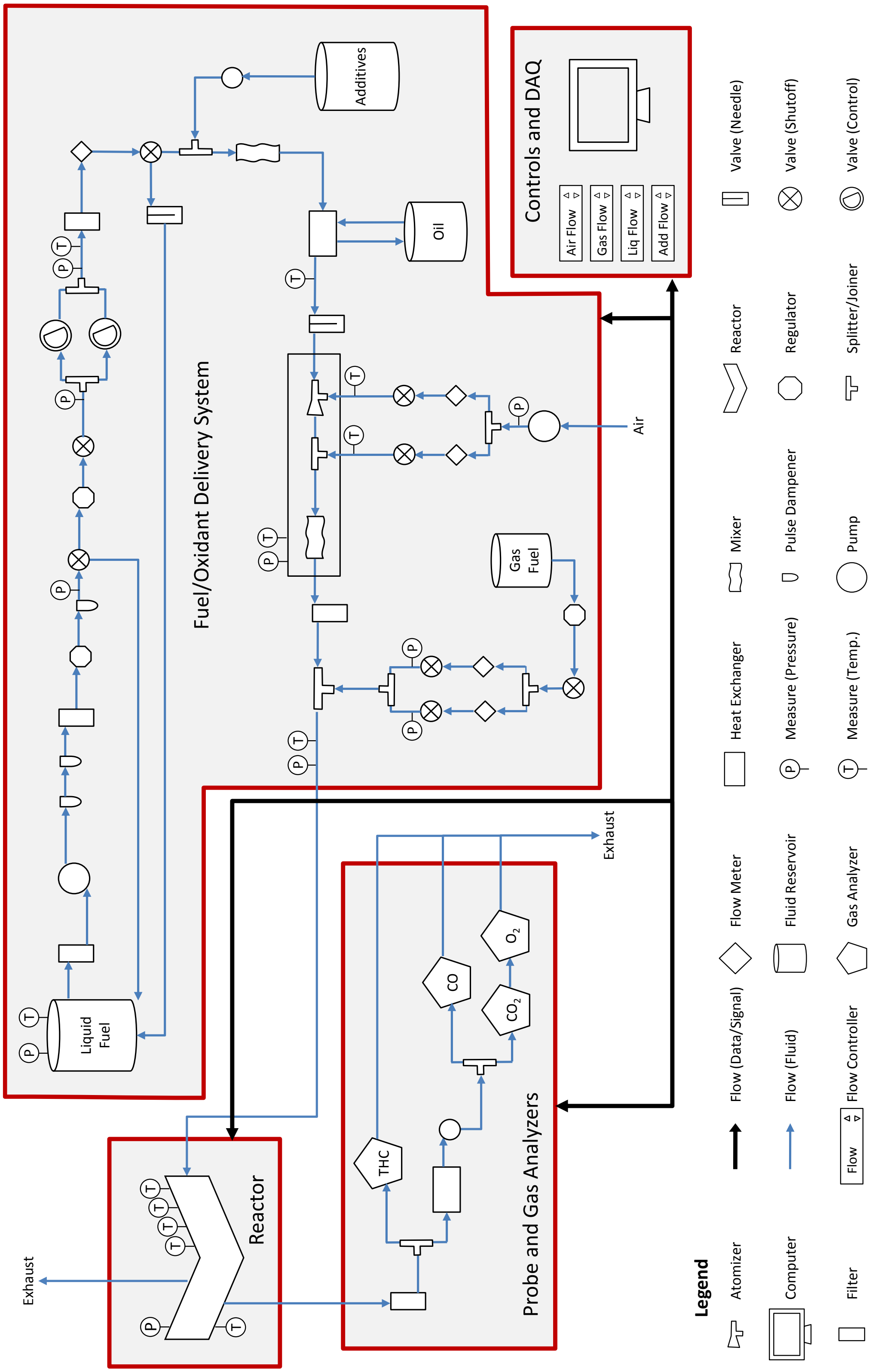

Figure 3.1: TSR system schematic

3.1.1 System Description

The TSR is a stirred reactor that is toroidal in shape based on the original design developed by Nenniger *et al.* [14] and subsequently modified by Zelina [69] and Stouffer *et al.* [21]. The reactor is cast from aluminum oxide (Al_2O_3, alumina) ceramic material. The reactor and jet ring solid model assembly are shown below in Figure 3.2. The most important dimensions of the TSR are shown in Figure 3.3. The reactor volume is 250 cm^3.

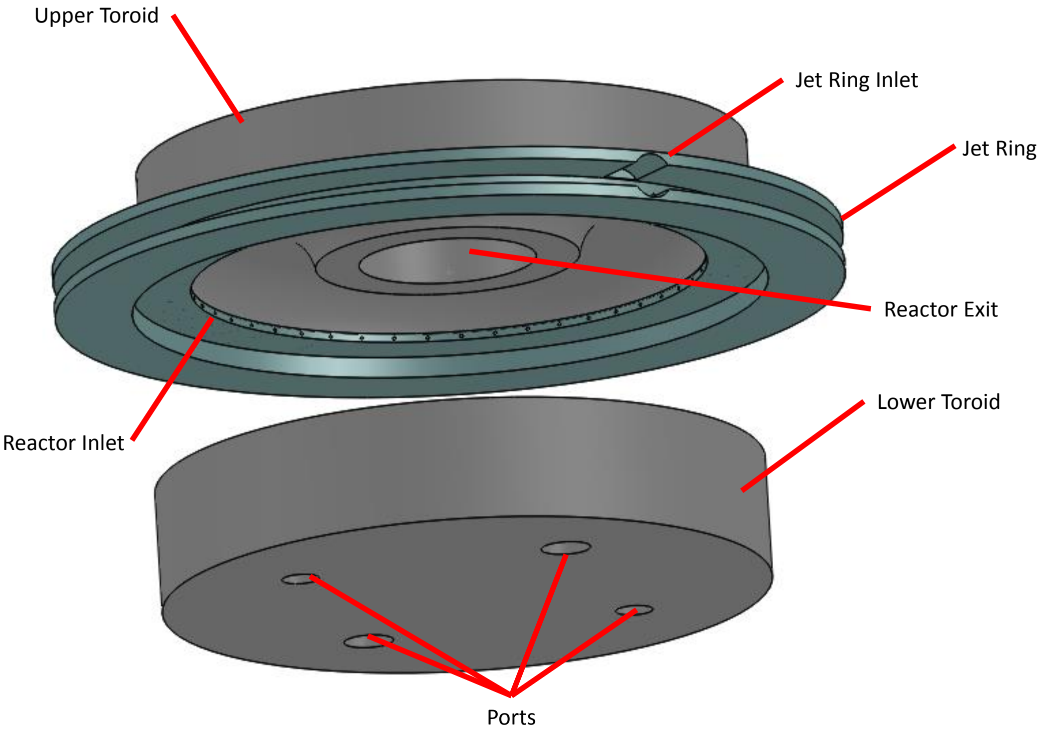

Figure 3.2: TSR solid model

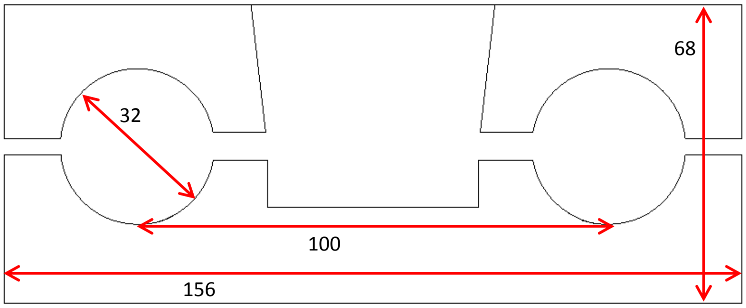

Figure 3.3: Important TSR dimensions (in millimeters)

The premixed fuel and oxidant (henceforth called 'premix') enter the reactor via the Inconel™ jet ring which is monitored for temperature and actively cooled with unmetered gaseous nitrogen if necessary. The jet ring has a single premix inlet that feeds 48 fuel/air jets of 0.86 mm (0.034 inch) diameter that inject premix into the outer radius of the torus. The lower toroid has four ports for the igniter, thermocouple, gas sampling probe, and pressure gauge. The upper half has a large opening for the exhaust.

Inside the TSR, the flow path is inherently three dimensional (3D) as shown in the cross-sectional views of Figure 3.4. In the side view, the premix enters and is ignited by a combination of the recirculating flow and the flow traveling in the toroidal direction. The bulk of the flow follows the toroidal direction coming into and out of the page. The flow into the page is shown as cross-circles and the flow out of the page is shown as dot-circles. The flow exits through a stack. This view also shows location of the Type S thermocouple used to measure temperature inside the reactor at roughly 0.2" (5 mm) from the wall of the lower toroid through one of the ports. The thermocouple bead is coated with ceramic to prevent exothermic catalytic surface reactions. The top view helps illustrate the flow in the clockwise toroidal direction. This view shows the jets angled to move the flow clockwise. The angle is specifically 20° from a radial line. This 3D flow path becomes extremely important in the CFD analysis. For simplicity, all 48 premix jets are not shown in Figure 3.4.

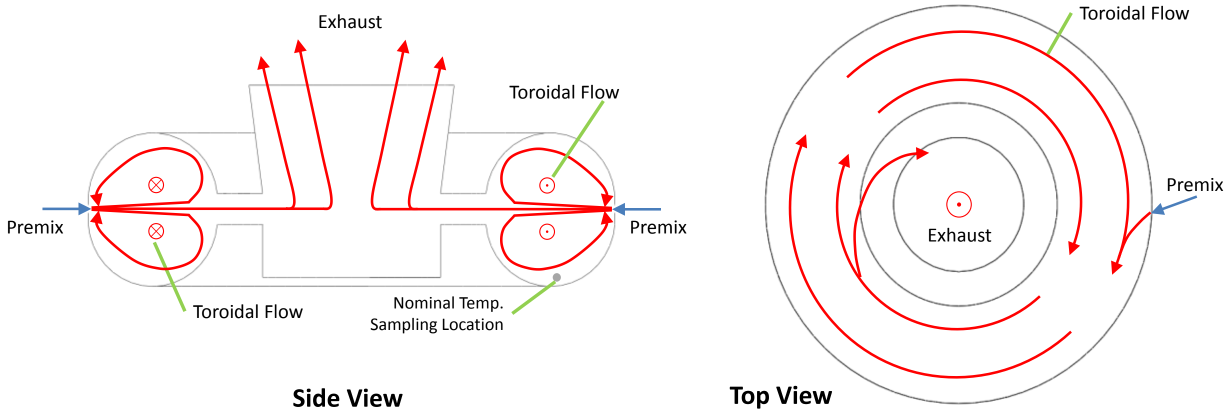

Figure 3.4: TSR cross-sections with generic flow paths

Table 3.1: TSR characteristics

	TSR
Volume [cm^3]	250
Reactor Material	Alumina
Jet Ring Material	Inconel™
Jet Diameter [mm]	0.86
Number of Jets	48
Surface Area to Volume Ratio [1/cm]	1.2
Reactor Mass (kg)	3.3

The remainder of the system deals with delivering fuel/air, sampling, controls/data acquisition, and procedures.

The primary liquid fuel is pumped to two parallel compact precision control valves. One valve provides coarse flow metering, and the second provides more precise flow metering. The secondary liquid fuel is pumped and metered via syringe pumps and mixes with the primary fuel upstream of the atomizer. The liquid fuel mixture is heated by a hot oil heat exchanger to 400K. The fuel mixture is first atomized using a twin-fluid air blast atomizer operating on pressurized air (Delavan Model 30609-2). The atomizing air flow rate is approximately 60 SLPM and reaches the atomizer at 415K. The vaporized fuel is then thoroughly mixed into the combustion air. The compressed (atomizing air and combustion air) air is delivered from facility services. The combustion air flow rate is approximately 340 SLPM and is heated to 515K. In the case of gaseous fuels, the fuel heaters and vaporizer are bypassed and the gaseous fuel mixes with hot air. In all cases, the fuel/air mixture is then filtered before finally entering the jet ring. The temperature of the fuel/air mixture is measured just before the jet ring to be roughly 450K. The TSR system main control panel uses digital controllers to run the flow meters for all fuels and air.

A fully oil-cooled stainless steel probe whose design is based on the work of Blust *et al.* [70] is used to extract samples from the reactor. The probe has a 0.055 inch (1.4 mm) diameter orifice. The sample probe was designed such that the reactions of the exhaust gas are quenched to ensure that the gas analyzers receive a representative sample of the gas at an adequate pressure. The samples are taken flush with the wall of the lower toroid through one of the four ports. The samples are taken from reacting, non-equilibrium zones with significant radical concentrations, so some reactions will continue inside the probe, but the cooled probe aims to minimize these effects according to Blust *et al.* [70]. The sample is sent through a heated line to a heated filter, and then splits into two streams. The first stream remains wet and is analyzed for total hydrocarbons (THC) by a heated flame ionization detector (FID). The second stream passes through a refrigeration device to remove H_2O and is pumped into a sampling unit before passing through three analyzers in series. The CO and CO_2 analyzers are non-dispersive infrared (NDIR) and the O_2 analyzer is magnetopneumatic (MP). Table 3.2 summarizes the TSR gas analyzer system. The THC data are too erratic to be used, but were very helpful during testing as a predictor of incipient blowout.

Table 3.2: Summary of gas analyzer system for TSR

Emission	**Method**	**Analyzer Make/Model**	**Zero Gas [Volume %]**	**Span Gas[1] [Volume %]**
THCs	Heated FID	VIG 20	100% N_2	3.0% C_3H_8 195 ppm C_3H_8
CO	NDIR	Horiba VIA-510 Cal Analytical 603		0.2811% 0.874% 1.90%
CO_2		Horiba VIA-510		9.01% 5.01%
O_2	MP	Horiba MPA-510		18.1%

1. Balance N_2

A National Instruments LabView [71] data acquisition (DAq) system monitors all thermocouples, numerous pressure transducers, flow meters, and gas analyzers. It is also acts as the control for the secondary fuel flow and the thermocouple position. All quantities for the TSR were collected every three seconds. The most important quantities that were recorded for further analysis are listed in Table 3.3.

Table 3.3: Important recorded experimental quantities for extinction tests

Description		Symbol	Units	Used For:
Flow Rates	Primary Liq. Fuel	$\dot{\forall}_{PLF}$	mL/min	Inlet Equivalence Ratio, ϕ_{in} Extinction Equivalence Ratio, ϕ_{ext} Residence Time, τ Loading Parameter, LP
	Secondary Liq. Fuel	$\dot{\forall}_{SLF}$	mL/min	
	Gas Fuel	$\dot{\forall}_{GF}$	SLPM	
	Air	$\dot{\forall}_{A}$	SLPM	
Temperatures	Premix	T_{premix}	^{o}F	Heat Loss, $\dot{Q}_{loss}$ Extinction Temperature, T_{ext}
	Reactor	$T_{reactor}$	^{o}F	
Emissions	CO	-	%V dry	Exhaust Equivalence Ratio, $\phi_{exhaust}$ Heat Loss, $\dot{Q}_{loss}$
	CO_2	-	%V dry	
	O_2	-	%V dry	

Testing for blowout on the TSR begins by heating the reactor with a gaseous fuel until all temperatures reach steady state. During this time the gas analyzers are calibrated. After reaching steady state, the reactor is slowly switched to the test fuel.

Once running on the test fuel, the air flow rate is maintained at a constant value while the fuel flow rate is very slowly lowered until extinction. The fuel flow rate set point is manually reduced by a small value and then the system is allowed to stabilize at the new conditions. For example, the liquid fuel flow rate set point was lowered from 18.00 mL/min to 17.75 mL/min, and then the flow rate was maintained at 17.75 mL/min flow for roughly fifteen minutes. Many observations indicate that fifteen minutes is more than sufficient for the temperature to stabilize at the new condition if the changes are small. The process is then repeated until eventually the fuel flow rate is too low to allow stable combustion and the flame blows out. Immediately following extinction, the reactor is re-lit by lowering the air flow rate, increasing the fuel flow rate, and introducing a spark. The next test is then started. Blust *et al.* [16,17] noted that there is hysteresis in the lean blowout (LBO) limit. If LBO is attempted after the reactor is very hot, the mixture is capable of burning at leaner conditions than if approached from cooler conditions. The authors determined a variance of ±50K in the blowout temperature and ±0.02 in equivalence ratio. Our tests are performed as similarly as possible to minimize this variance, which is quantified using the statistical methods below.

A summary of the experimental conditions for the liquid fuel extinction tests is provided in

Table 3.4. The methane extinction tests are operated at very similar conditions except for the changes in equivalence ratio, product temperature, and residence time that are to be expected. The flow rates used here in conjunction with the reactor/jet ring dimensions are based on the conditions suggested by Stouffer *et al.* [21] to produce sonic velocities for the jets and to ensure turbulent mixing is present throughout the reactor.

Table 3.4: Nominal values of experimental conditions for liquid fuel extinction tests

Parameter	**Nominal Value**		**Units**
	Test Start	**Test End**	
Reactor Pressure	1		atm
Premix Temperature	450		K
Air Flow Rate	8.00		g/s
Fuel Flow Rate	0.25	0.22	g/s
Equivalence Ratio[1]	0.45	0.40	-
Residence Time[1]	7.5	8.0	ms
Loading Parameter[1]	1.112		mole/sec L atm$^{1.8}$
Product Temperature[2]	1500	1360	K

1. Calculated as presented in Section 3.1.2
2. Corrected temperature as described in Appendix C

3.1.2 Data Analysis and Reduction

The blowout data are generally characterized by the corrected temperature and equivalence ratio. Appendix D presents the details of the analysis, but the parameters are briefly mentioned here.

The first step in data analysis is the temperature correction for thermocouple heat loss, which is described in Appendix C. Equation 3.1 presents the correction correlation. The equivalence ratio (Equation 3.2) characterizes the chemistry of the problem.

3.1 $$\mathrm{T_{corrected}} = 1.0621\mathrm{T_{measured}} - 66.55$$ K

3.2 $$\phi_{\mathrm{inlet}} = \frac{\dot{\mathrm{m}}_\mathrm{F}/\dot{\mathrm{m}}_\mathrm{A}|_{\mathrm{inlet}}}{\dot{\mathrm{m}}_\mathrm{F}/\dot{\mathrm{m}}_\mathrm{A}|_{\mathrm{stoich}}}$$ -

The reactor loading is characterized by the Loading Parameter (LP, Equation 3.3) or the residence time (τ, Equation 3.4).

3.3 $$LP = \frac{\dot{n}_A}{\forall p^{1.8}}$$ $\frac{\text{mol}}{\text{s L atm}^{1.8}}$

3.4 $$\tau = \frac{\rho \forall}{\dot{m}}$$ ms

Figure 3.5 shows how the equivalence ratio, ϕ, changes with time during extinction tests. This is specifically for methane, but is representative of all tests. Essentially, the fuel flow rate (hence equivalence ratio) is constant for a single condition, and then lowered until extinction occurs (shown as the red data points).

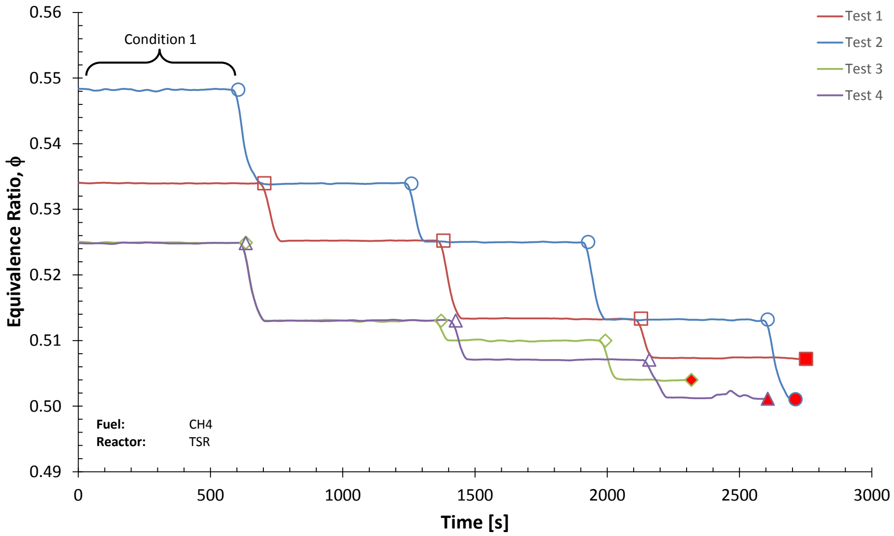

Figure 3.5: Example test conditions (equivalence ratio vs. time)

The equivalence ratio-time history also defines the end-point at a condition, so a condition average can be determined. The conditions leading to extinction were analyzed for methane as it was useful for the modeling effort of Chapter 4. Only the extinction points were analyzed for the liquid fuels. The extinction condition (shown as red in Figure 3.5) warrants a more specific definition. If, for example, each condition is allowed to last for fifteen minutes before changing fuel flow rate, the extinction condition will not last for the full fifteen minutes. By definition, extinction will occur before the fifteen minute condition duration; otherwise, the flow rate would be reduced and a new condition would be started. In some cases, the system will extinguish immediately upon flow rate change. In most cases, the system will last well into the condition before blowing out. The extinction condition is the average for the 30 seconds prior to the precipitous drop in temperature.

3.1.3 Statistical Methods

Since the blowout data points represent a relatively small number of replicates, these require special handling for statistical interpretation (i.e., small sample statistical treatment). Each fuel/blend underwent between three and nine tests, so the analysis results in between three and nine blowout points for each fuel. The small number statistics methods and factors of Dean and Dixon [72] were used to determine confidence intervals. The specific statistical factors are presented in Table 3.5.

Table 3.5: Small sample statistics factors for 95% confidence [72,73]

Number of Samples	$\mathbf{k_w}$	$\mathbf{t_w}$	$\mathbf{Q_{max}}$
2	0.89	6.40	-
3	0.59	1.30	0.970
4	0.49	0.72	0.829
5	0.43	0.51	0.710
6	0.40	0.40	0.625
7	0.37	0.33	0.568
8	0.35	0.29	0.526
9	0.34	0.26	0.493
10	0.33	0.23	0.466

The data are contained in a vector x of length n, sorted from lowest to highest as shown in Equation 3.5. The median is used (instead of the average) as a representative value from a set of data.

3.5 $$x = [x_1, x_2, \ldots x_{n-1}, x_n]$$ -

The measure of dispersion for a small number of observations (s_w) is based on the range (w) and the deviation factor (k_w) as shown in Equations 3.6 and 3.7. The deviation factor (k_w) is tabulated in Dean and Dixon [72] and is dependent on the number of observations in the sample.

3.6 $$w = x_{max} - x_{min} = x_n - x_1$$ -

3.7 $$s_w = w \cdot k_w$$ -

The confidence interval is obtained from the mean ($\bar{x}$) given in Equation 3.8, the range (w), and the confidence factor (t_w) in Equation 3.9. The confidence factor (t_w) is tabulated in Dean and Dixon [72] and is dependent on the number of observations and the desired confidence interval (CI). This work utilizes 95% confidence intervals.

3.8 $$\bar{x} = \frac{\sum x_i}{n}$$ -

3.9 $$\text{confidence limits} = \bar{x} \pm w \cdot t_w$$ -

The statistical analysis presented here is not intended to determine the data quality but instead to quantify the variability in the experimental data set.

The data quality is handled by identifying outliers from a data set. In the set sorted from lowest to highest, the outliers can be determined by comparing Q from Equation 3.10 to the rejection quotient (Q_{max}) tabulated in Rorabacher [73]. If Q is larger than Q_{max} the value can be justifiably rejected.

3.10 $$Q = \frac{x_n - x_{n-1}}{w}$$ -

3.2 Experimental Results

3.2.1 Effect of Base Fuel at Low Aromatics Concentrations

The synthetic fuels were tested in the unmodified or 'neat' states (0% aromatics) as well as with 10% and 20% aromatics. The traditional JP8 fuel is shown in all of the results below as it was used as a baseline, even though it has roughly 18.7% aromatics by volume unmodified.

Unmodified Fuels

The median extinction temperatures are shown in Figure 3.6. The 95% confidence intervals are also included based on the statistical analysis presented previously. The size of these confidence intervals are largely determined by the number of tests performed for each fuel. The interesting result here is that these fuels behave remarkably similar to each other. In fact, the temperature range is only 12K, which is only 0.9% of the median of 1355K.

The second parameter that largely defines extinction is the equivalence ratio at the extinction point, which is shown in Figure 3.7. Once again, the scale is magnified to show the differences, but there actually is very little difference between these fuels. The equivalence ratio range is only 2.3% of the median.

Combining the two previous figures presents the extinction temperature versus extinction equivalence ratio as shown in Figure 3.8.

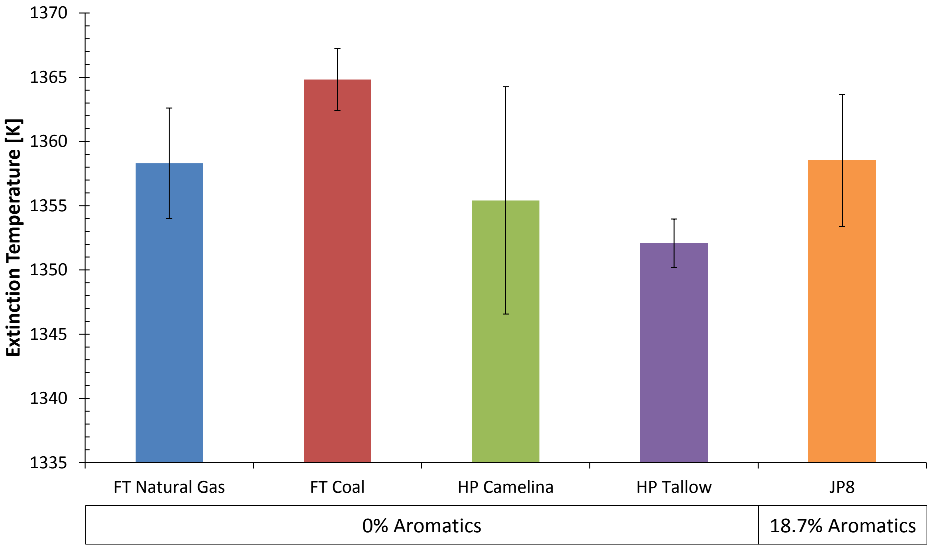

Figure 3.6: T_{ext} for unmodified synthetic fuels and JP8

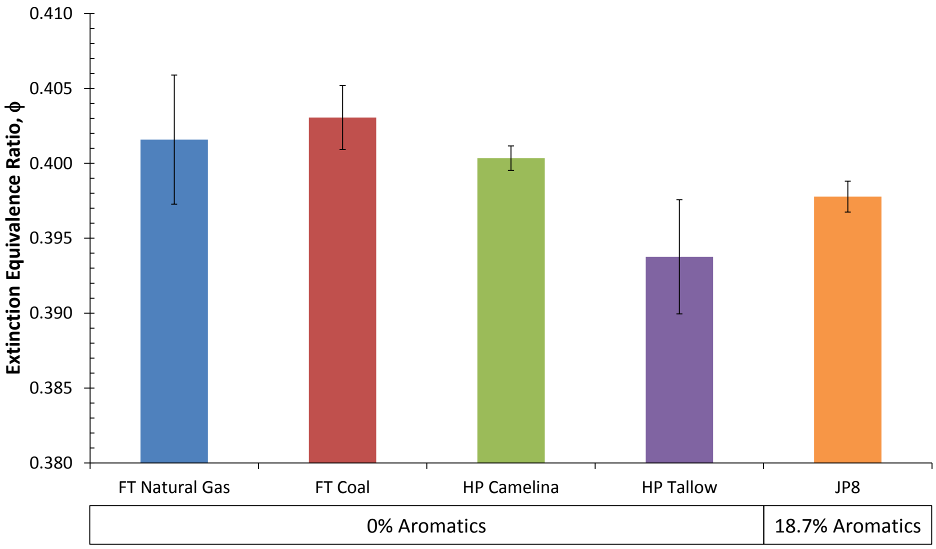

Figure 3.7: ϕ_{ext} for unmodified synthetic fuels and JP8

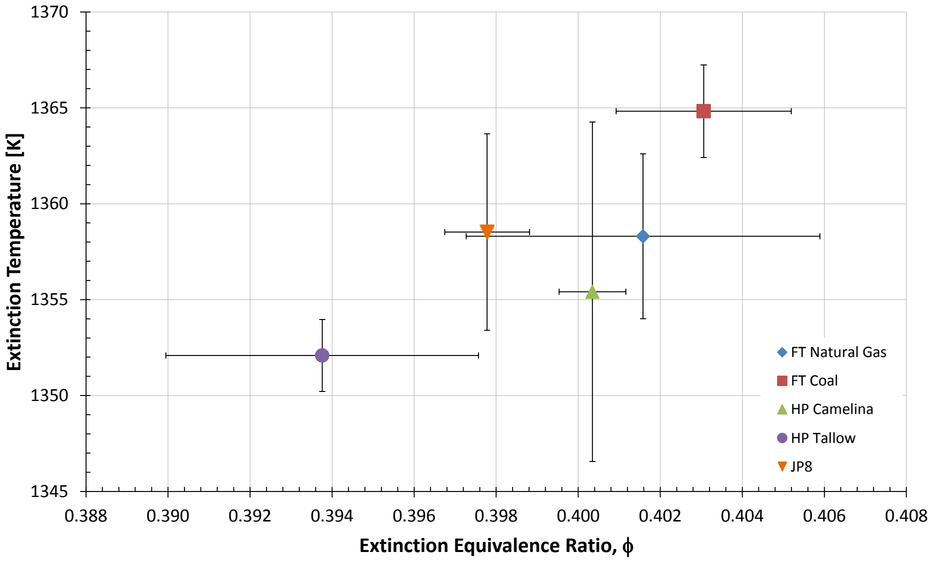

Figure 3.8: T_{ext} vs. ϕ_{ext} for unmodified synthetic fuels and JP8

The conclusion from this first set of results is that extinction behavior does not depend on the fuel feedstock or composition in their unmodified states.

Synthetic Fuels with 10% Aromatics and Unmodified JP8

The second set of results looks at the baseline unmodified JP8 with 18.7% aromatics compared to the synthetic fuels with 10% Pet-Aromatic additive.

The median extinction temperatures are shown in Figure 3.9. Once again the variation of 10K is very small, and only 0.7% relative to the median of 1357K. The equivalence ratio at extinction is shown in Figure 3.10, with a range of only 1.3% of the median.

Combining the two previous figures presents the extinction temperature versus extinction equivalence ratio as shown in Figure 3.11.

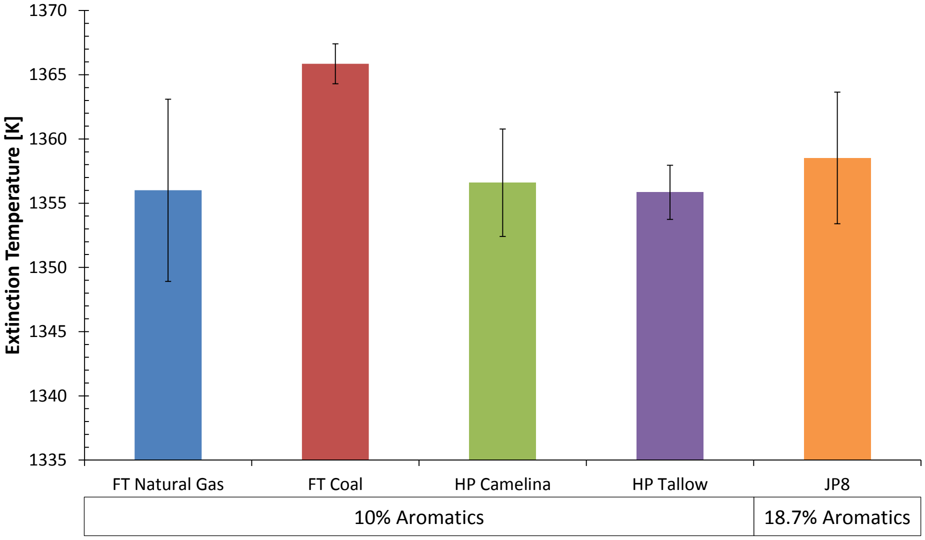

Figure 3.9: T_{ext} for synthetic fuels with 10% Pet-Aromatic and unmodified JP8

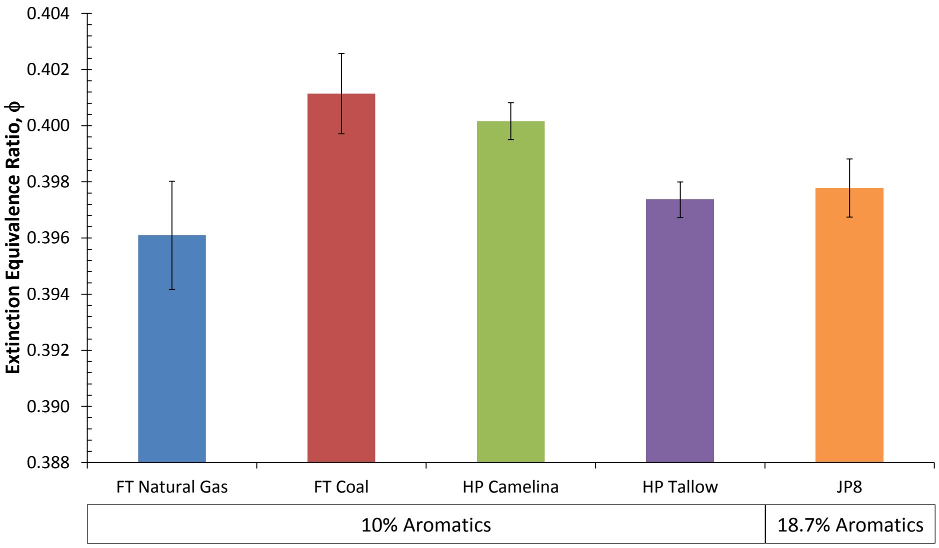

Figure 3.10: ϕ_{ext} for synthetic fuels with 10% Pet-Aromatic and unmodified JP8

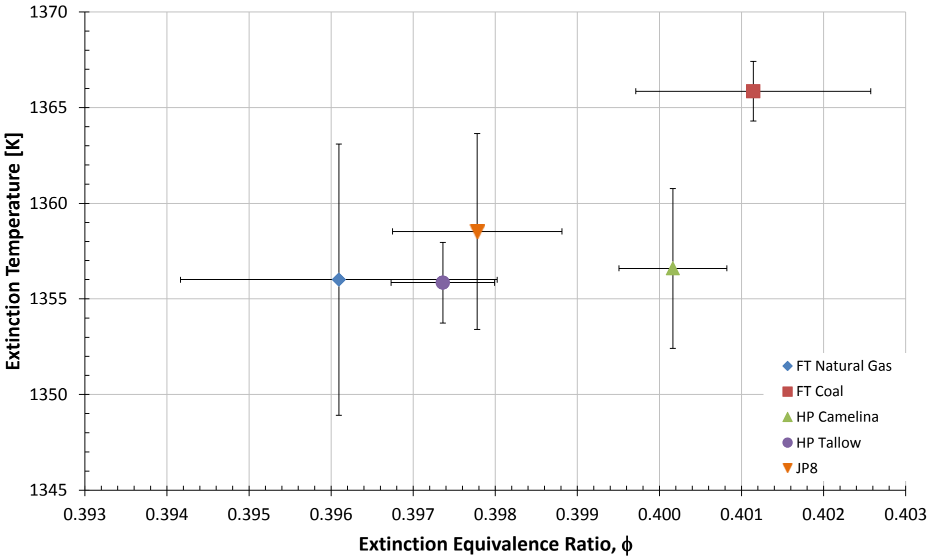

Figure 3.11: T_{ext} vs. ϕ_{ext} for synthetic fuels with 10% Pet-Aromatic and unmodified JP8

The conclusion from this set of results is that extinction behavior does not depend on the fuel feedstock or composition with 10% Pet-Aromatic additive.

Synthetic Fuels with 20% Aromatics and Unmodified JP8

The third set of results looks at the baseline unmodified JP8 with 18.7% aromatics compared to the synthetic fuels with a 20% Pet-Aromatic additive.

The median extinction temperatures are shown in Figure 3.12. Once again the variation of 10K is very small, and only 0.7% relative to the median of 1361K. The equivalence ratio at extinction is shown in Figure 3.13, with a range of only 1% of the median.

Combining the two previous figures presents the extinction temperature versus extinction equivalence ratio as shown in Figure 3.14.

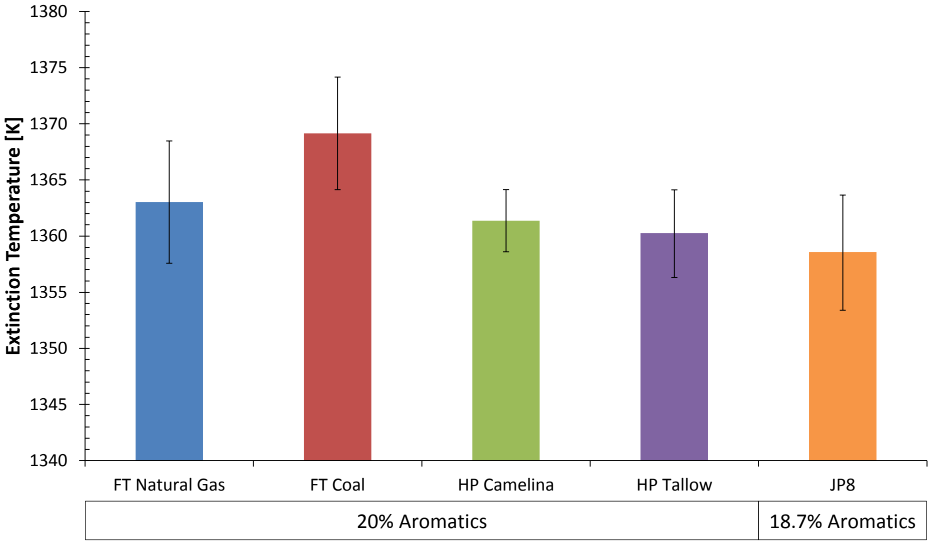

Figure 3.12: T_{ext} for synthetic fuels with 20% Pet-Aromatic and unmodified JP8

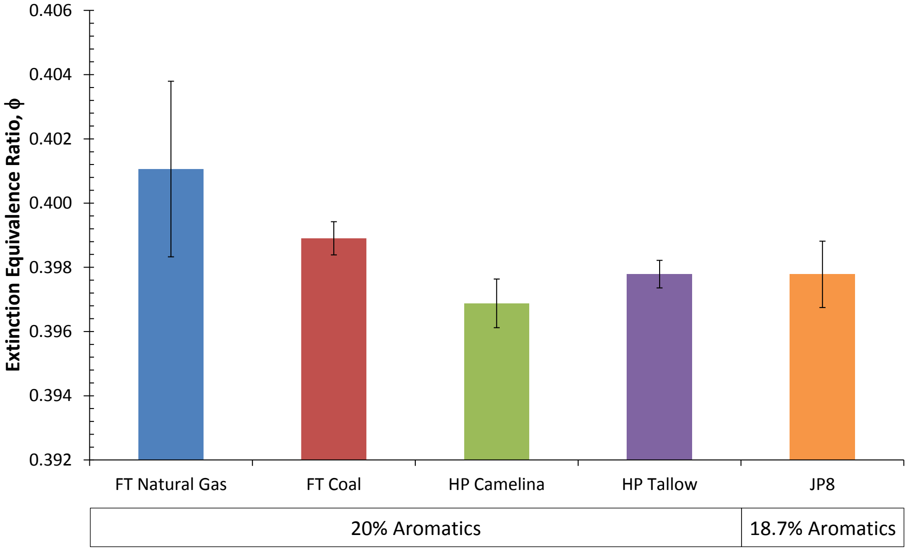

Figure 3.13: ϕ_{ext} for synthetic fuels with 20% Pet-Aromatic and unmodified JP8

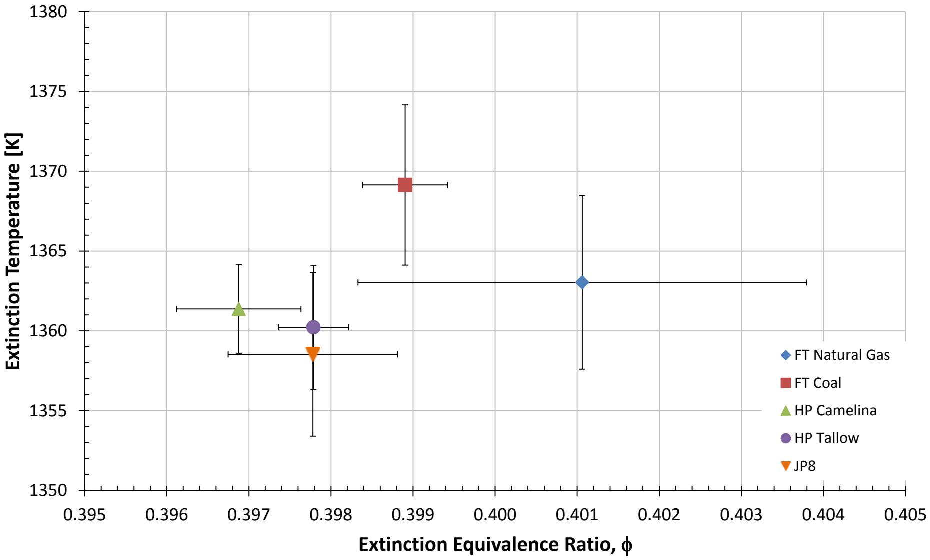

Figure 3.14: T_{ext} vs. ϕ_{ext} for synthetic fuels with 20% Pet-Aromatic and unmodified JP8

The conclusion from this set of results is that extinction behavior does not depend on the fuel feedstock or composition with 20% Pet-Aromatic additive.

3.2.2 Effect of Aromatic Concentration

The previous results showed that blowout behavior does not depend on base fuel type regardless of aromatic concentration between 0% and 20%. However, the blowout behavior of an individual fuel could still depend on aromatic content.

Figures 3.15 and 3.16 show the four synthetic fuels and JP8 with 0%, 10%, and 20% Pet-Aromatic content. The trend with aromatic content is inconsistent, but the variation is extremely small. The temperature varies less than 1% between minimum and maximum aromatic content for all three fuels. The equivalence ratio varies approximately 1% between minimum and maximum aromatic content for all three fuels.

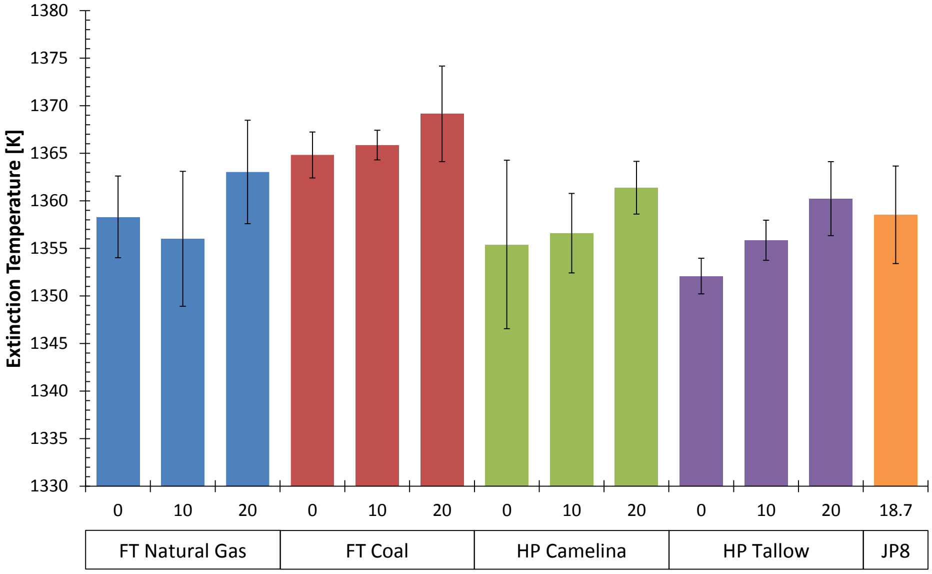

Figure 3.15: T_{ext} for the synthetic fuels with 0-20% aromatic content and JP8

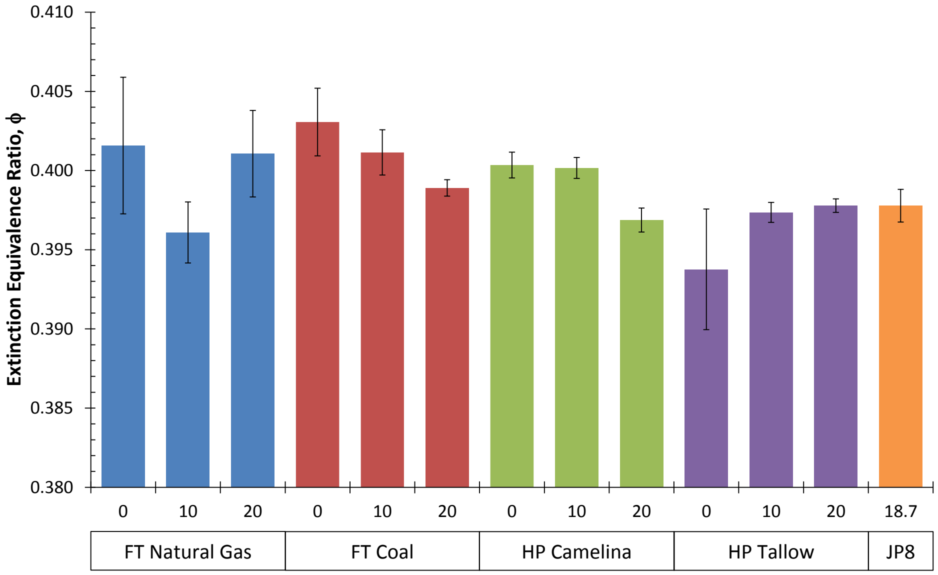

Figure 3.16: ϕ_{ext} for the synthetic fuels with 0-20% aromatic content and JP8

The results above showed little variation between fuel type and low-levels of aromatic content. FT Natural Gas was selected to fully explore the effects of aromatic content. It was tested with 0 to 80% Pet-Aromatic additive content and is compared to the baseline JP8 and the 100% aromatic content fuel (Pet-Aromatic). In general, the majority fuel was delivered from the primary system and the minority fuel was delivered via the secondary system. One test was performed to ensure that the fuel delivery system selection did not significantly affect the results. The first set of tests, performed in 2010, looked at 0, 10, and 20% aromatic content as with the fuels above. Over a year later, in 2011, the system was rebuilt and the tests at 0, 20, 40, 60, and 80% aromatic content were performed. The tests at the same condition were combined into a single sample population for statistical analysis. This explains why the 10% tests are slightly different as it was only taken with the 2010 system.

Figures 3.17 and 3.18 present the extinction temperature and equivalence ratio, respectively. At low aromatic contents (0-20%) there is little to no difference in extinction behavior, which is consistent with the other fuels. However, the Pet-Aromatic (100% aromatic content) fuel shows an obviously different behavior. The results from 40, 60, and 80% aromatic content show an upward trend, but the data are somewhat erratic. During these three high aromatic content tests, which were performed last, the premix delivery system began experiencing inconsistent pressures that generally skewed to be higher than the typical (and preferred) pressures in the system. These higher pressures appear to have an effect on the blowout behavior, which result in the larger confidence intervals for the 40, 60, and 80% aromatic content tests. Upon completion, the system was disassembled and examined. The premix filter and jet ring were found to have a significant amount of deposits that were not present when the system was initially assembled. The increased pressure and deposits in the premix delivery system indicate that there may have been vaporization issues with the high aromatic content fuels. The data are subjected to the 'Q-test' for outliers as described in Section 3.1.3. The 'Q-test' does not indicate the data should be rejected, but the data does have a large spread that creates large confidence intervals.

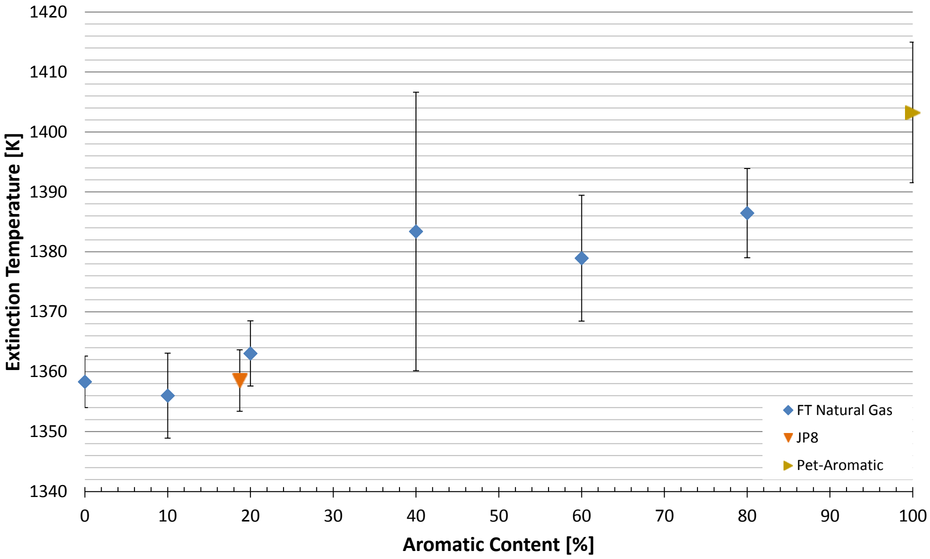

Figure 3.17: T_{ext} for FT Natural Gas with 0-100% Pet-Aromatic and JP8

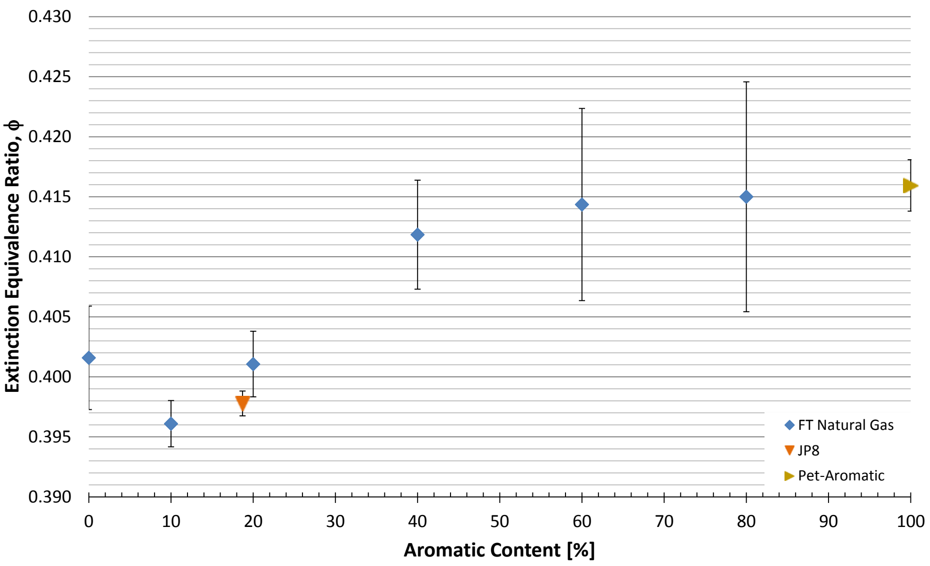

Figure 3.18: ϕ_{ext} for FT Natural Gas with 0-100% Pet-Aromatic and JP8

The conclusion from this set of results is that extinction behavior does not significantly depend on low levels of aromatic content for a single fuel. However, there is a significant change for fuels with high aromatic content, even though the trend between low and high aromatic contents is indiscernible from these tests. Also, using high aromatic content fuels will require special consideration due to increased deposition in the fuel delivery system.

The reasons for the difference between an aromatic fuel and an aliphatic fuel will be addressed in Section 4.3, but the literature does present a hypothesis. According to Hui *et al.* [23] the aromatic compounds contribute to a reduced resistance to extinction (narrower stability limits) due to the slower initial reaction of the aromatic ring and the consequently reduced reactivity of aromatic HCs as compared to aliphatic HCs. The authors base the conclusion on the work of Won *et al.* [74] who show that toluene blended with n-decane dramatically reduces peak OH concentration via H abstraction and radical recombination reactions. The kinetic coupling between the toluene and n-decane mechanisms further accelerated flame extinction. The work of Hui *et al.* [75] and Kumar *et al.* [76] also show that the type of aromatic compound affects the extinction behavior, and that normal and iso-alkanes tend to be more resistant to extinction.

3.2.3 Comparison to Gaseous Fuels and Previous Work

The results from above indicate that the fuels exhibit remarkably similar behavior for blowout in the unmodified state as well as with small amounts of aromatic content. The similarity was so consistent, that one might wonder if there ever are any differences in blowout. The same blowout experiments were performed using the simplest hydrocarbon gaseous fuels (CH_4, C_2H_6, and C_3H_8). Figure 3.19 shows blowout results for JP8, the four synthetic jet fuels, Pet-Aromatic, and methane. Here, significant differences are apparent. The methane data are used as the basis for the computational study of Chapter 4.

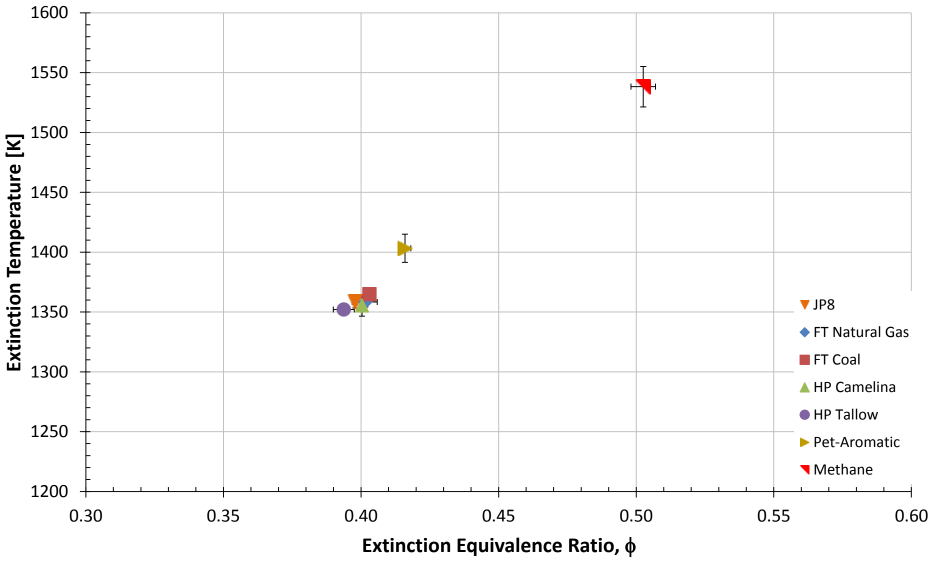

Figure 3.19: T_{ext} versus ϕ_{ext} for jet fuels, Pet-Aromatic, and methane

The original work regarding blowout of hydrocarbons in a stirred reactor was performed in the 1950's, first by Longwell and Weiss [11] and later by Weiss *et al.* [12]. The studies generated a classical curve (colloquially called the 'Longwell curve') of equivalence ratio versus Loading Parameter for both the fuel-lean and fuel-rich regimes as shown in Figure 3.20. A number of fuels were studied, but only iso-octane and methane blowout are shown here. In a sense, that study shows that all hydrocarbons fall onto a single curve in this view. Notice, our simple alkane data agree, suggesting consistency with the earlier data when plotted in this global manner. The jet fuels (traditional and synthetic/alternative) all behave so similarly that they could be collapsed to a single point which falls on the curve as well.

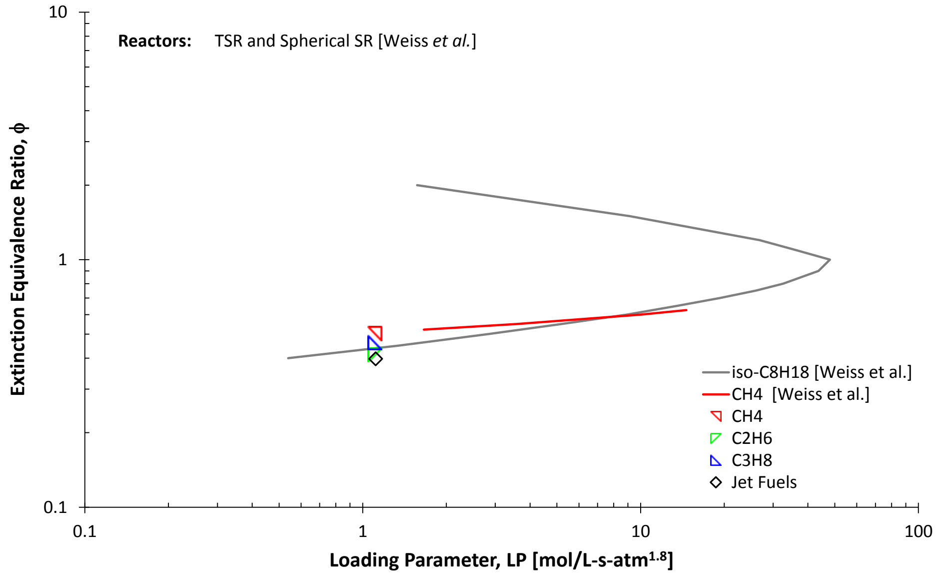

Figure 3.20: Comparison of ϕ_{ext} vs. loading parameter with Weiss *et al.* [12]

More recently, Stouffer *et al.* [21] set the groundwork for the current work, so comparison between these two efforts is warranted. The figures below (Figure 3.21 and Figure 3.22) present the extinction behavior of two of the fuels studied by both Stouffer *et al.* and in this effort. The reactor used by Stouffer *et al.* was essentially the same as the one used here. The primary differences were a different configuration for the exhaust gas exit and a different reactor material. The testing procedures were also slightly different, but in general the agreement between the two studies is good. The goal of this comparison is to show that the current study does reasonably repeat the most similar previous experiments. The Stouffer *et al.* [21] data show that Loading Parameter has a noticeable effect on extinction temperature (decreasing loading will cause combustion to be stable to a lower temperature). However, there is no noticeable relationship between Loading Parameter and extinction equivalence ratio for the conditions investigated.

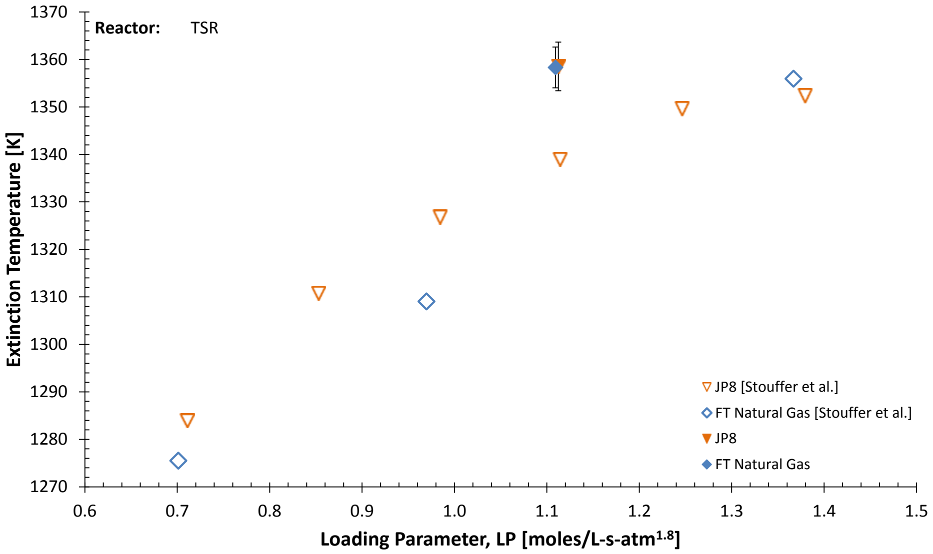

Figure 3.21: Comparison of T_{ext} with Stouffer *et al.* [21]

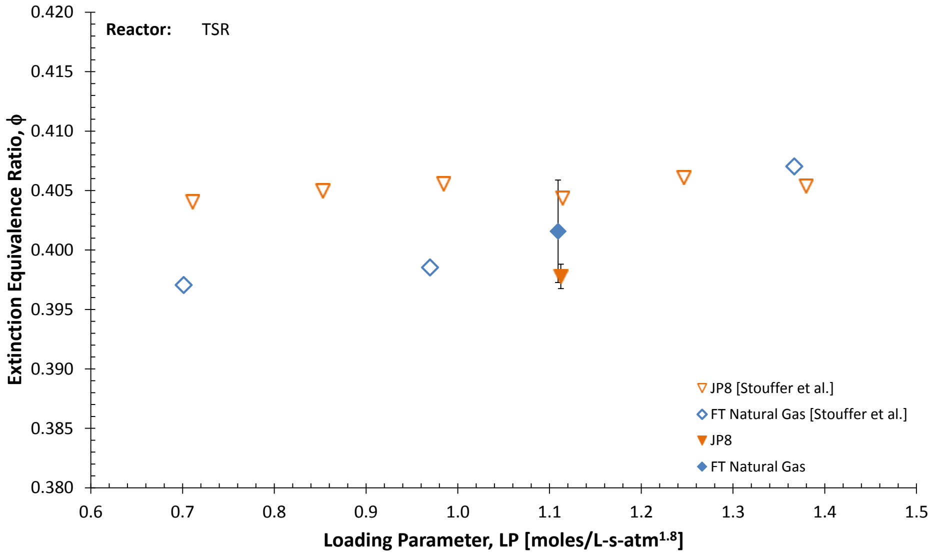

Figure 3.22: Comparison of ϕ_{ext} with Stouffer *et al.* [21]

3.3 Conclusions

The work discussed in this chapter focused on the extinction limits of the various fuels. The principal conclusions drawn from this study are:

- The various base fuels (feedstock) all exhibited statistically identical blowout limits. When these fuels were blended with aromatic species to 0%, 10%, or 20% by volume, the blowout limits remained indistinguishable between all the fuels as a group.

- Aromatic content from 20% to 100% does have a statistically significant effect on blowout behavior for FT Natural Gas, leading to a reduced resistance to blowout at higher aromatic content.

One noteworthy observation is the deposition in the premix filter and jet ring that was experienced during testing with the high aromatic content fuels (40% and above). The deposits, which appeared to be carbon, could be an issue for high aromatic content fuels.

The chemical mechanisms that give rise to the differences in blowout behavior between a highly aromatic and a highly aliphatic fuel are worthy of deeper investigation. This is addressed in Chapter 4.

Chapter 4
Flame Stabilization in the TSR

The experimental work reported in Chapter 3 found a difference in the blowout behavior of a highly aliphatic fuel and a highly aromatic fuel. Models of the reactor, especially chemical kinetic models, should be able to explain the underlying reason for these differences. However, the single PSR model (as described in Section 4.1.3 and shown in Figure 4.1 for methane) predicts blowout poorly as it allows for combustion to continue to much lower temperatures and leaner equivalence ratios than is found in the experiments [31]. Recall from Section 1.2.1 that extinction is the discontinuous change from burning to non-burning, which is due to the non-linear coupling between the species and energy conservation equations.

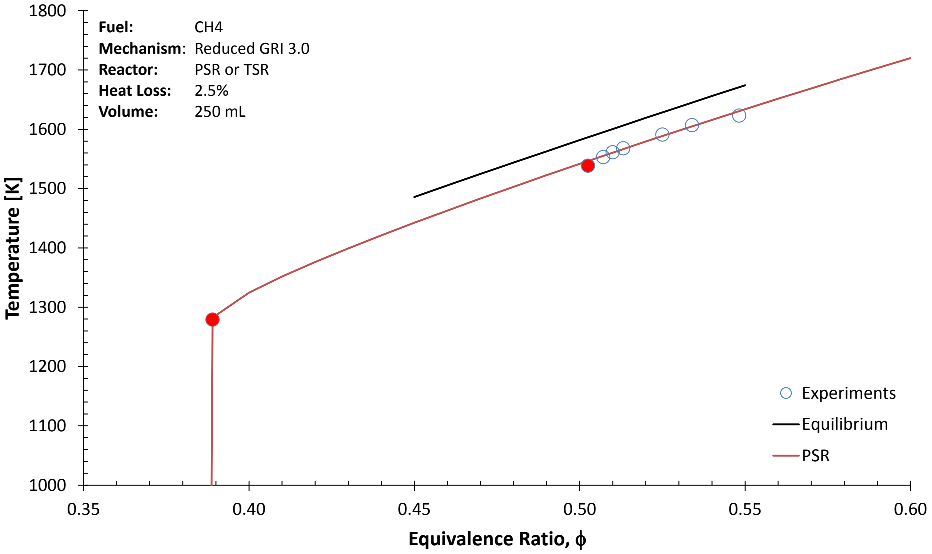

Figure 4.1: T vs. ϕ for methane extinction experiments and PSR model

If the goal is to understand the fuel-based differences in blowout, then the first step is to understand how the reactor behaves as it approaches extinction. The mechanism of blowout in the TSR will be studied with detailed reacting CFD models implemented within ANSYS Fluent 14.5 [77]. Methane is used as it has a relatively small, yet reliable chemical kinetic mechanism. The discussion of the modeling includes geometry and mesh, turbulence and chemistry models, and finally results. This chapter addresses Objective 2 in Table 1.5 from Section 1.4.1 above. Once the mechanism of flame stabilization is understood, it can be applied to understand the differences between the aromatic and aliphatic fuels noted in Chapter 3.

4.1 Methane Model Methods

4.1.1 Chemistry Models

The complete, stoichiometric combustion reaction for methane is given in Reaction 4.1. This overall reaction is accomplished by a series of hundreds of elementary reactions involving approximately 50 species. Chemical kinetic theory and detailed experiments are used to determine the rate constants for each reaction that is involved in the conversion of fuel to heat and products.

4.1 $CH_4 + 2[O_2 + 3.76N_2] \longrightarrow CO_2 + 2H_2O + 7.52N_2$ Methane

The individual chemical reactions are assembled into kinetic mechanisms and used to model the reaction chemistry for various fuels. The Reduced GRI [78] mechanism is used for the methane studies here, and the mechanisms used throughout this work are detailed in Appendix F.

4.1.2 Geometry and Boundary Conditions

The primary fluid domain of the reactor is shown in Figure 4.2. The first half of the figure shows the entire toroid, including all 48 jets. The reactor domain is split into 48 ‘slices’ based on the assumption that the jets will behave periodically in the toroidal direction. The second half of the figure is a single slice of the reactor that only includes 1/48 of the toroid with a single jet at the center of the slice. Each slice of the reactor is 7.5^o segment of the toroid.

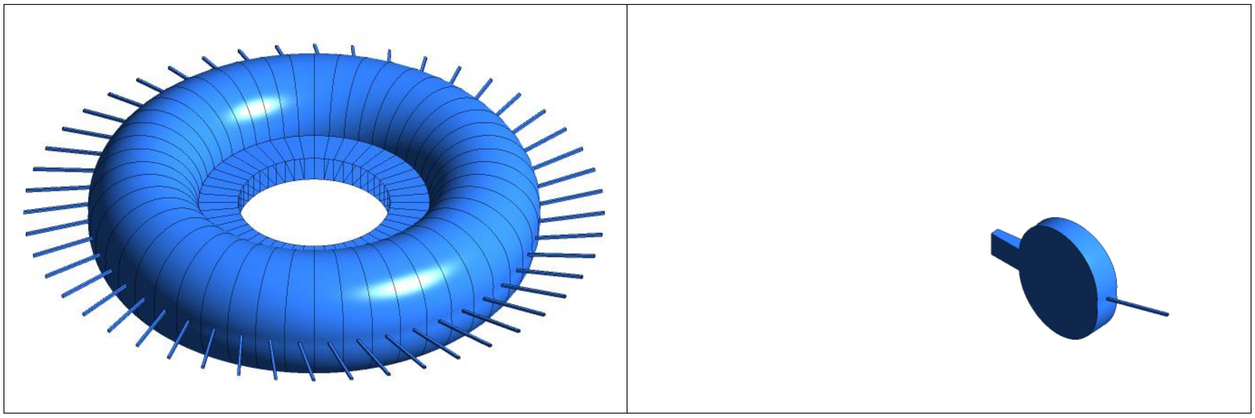

Full Reactor **Reactor Slice**

Figure 4.2: Full reactor and reactor slice

The single slice is the basis for the CFD geometry used in this work, which is shown in Figure 4.3. The previous work by Briones *et al.* [33] assumed symmetry about the midplane, which was not done here as both the upper toroid and the lower toroid of the reactor are included in the domain. The nozzle is angled away from a radial line to generate flow in the toroidal direction. Overall, the reactor has 358,980 elements and 358,933 nodes.

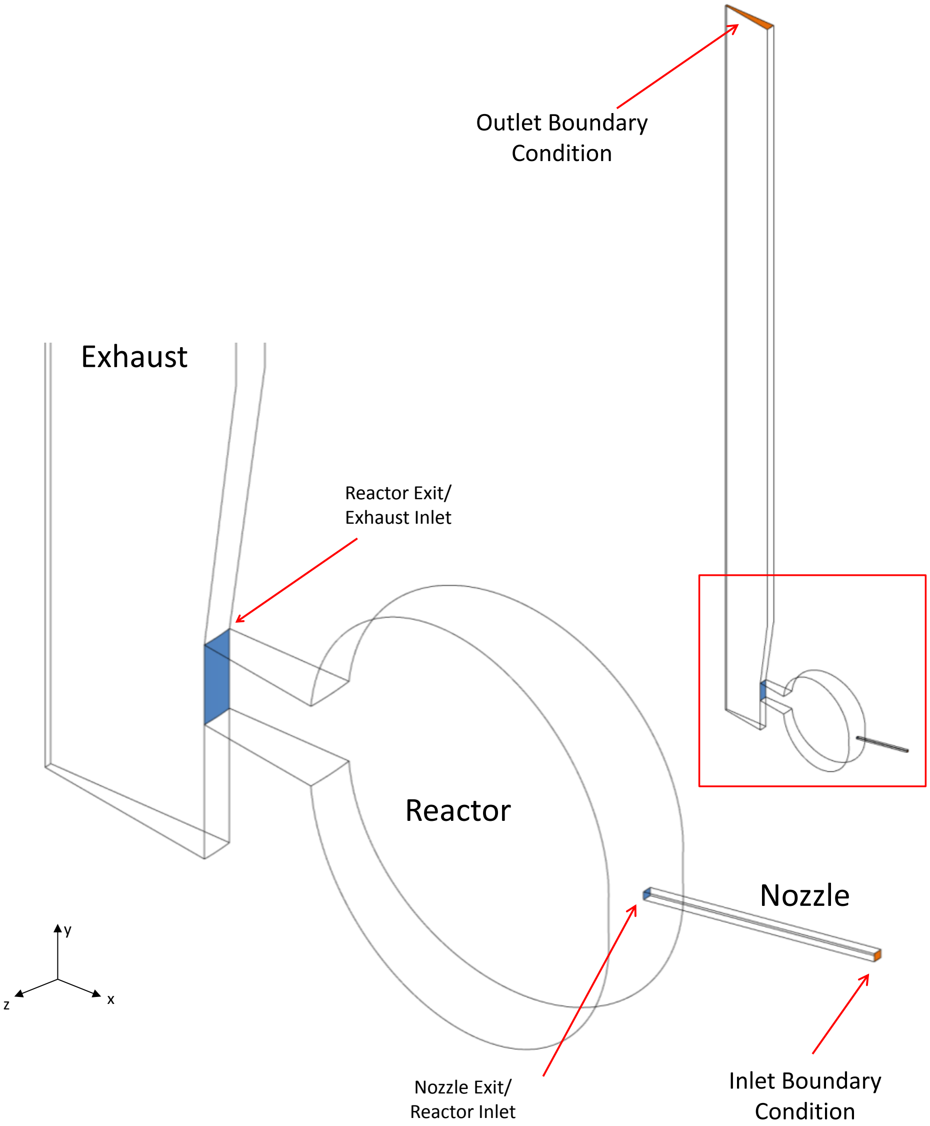

Figure 4.3: Geometry for CFD

The CFD geometry is solely a fluid domain, and is divided into three subdomains: the nozzle, the reactor, and the exhaust. Each domain has its own unique characteristics and features, and will be separately discussed. The flow enters at the nozzle inlet face and exits at the exhaust exit face, which act as the inlet and outlet boundary conditions, respectively (shown in orange). In between the nozzle and exhaust, the flow is in the reactor domain, which is the most important region for interpreting flame stabilization behavior. The top view of Figure 4.4 helps understand the configuration.

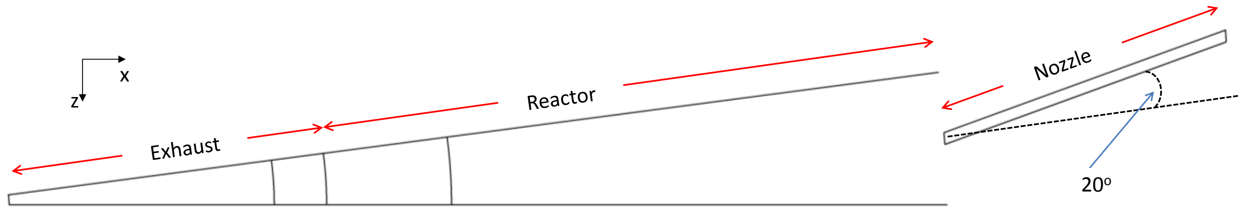

Figure 4.4: Top view of CFD geometry

Nozzle Domain and Inlet Boundary Condition

The top view shows that the nozzle itself is at a 20° angle from a line normal to the toroid perimeter (a radial line from the toroid's center of rotation). The nozzle is very small (0.86 mm diameter) with a high upstream feed pressure to ensure choked flow, but the circular nozzle was replaced with a square duct of the same cross-sectional area. This change improved mesh generation, as circular features make structured meshes difficult. The nozzle is isolated in Figure 4.5 and shown with its mesh. The nozzle region contains 6,400 hexahedron elements with 8,019 nodes. The nozzle domain is 11.1 mm^3 in volume with an average element volume of 0.0017 mm^3. The mesh at the nozzle inlet has an effective area of 0.59 mm^2 with an average element size of 0.0074 mm^2.

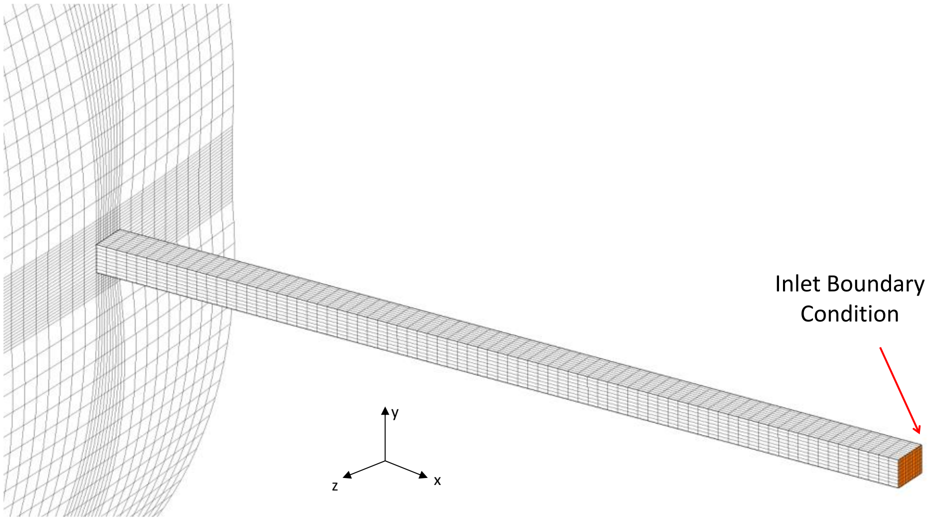

Figure 4.5: Nozzle domain, inlet boundary condition, and mesh

The inlet (shown in orange) is treated as a pressure-based boundary condition, since sonic flow does not behave well with a mass-based boundary condition. The total pressure at this inlet is set to roughly 110 kPa_{gauge} (210 $kPa_{absolute}$). The inlet boundary condition pressure results in a mass flow rate of 0.173 g/s, which is 1/48 of the total mass flow rate through the reactor of 8.3 g/s. The direction of the pressure vector at the inlet is specified via Cartesian coordinates (x = -0.9601, y = 0, z = 0.2798) to give the correct 20^o angle to the flow. The turbulence at the inlet is defined by the turbulence intensity (set to 6%) and turbulent length scale (set to 1 mm). These turbulence parameters are calculated as discussed in the section below. The inlet temperature is set to 450K to match the experiments. The inlet species composition is specified based on the equivalence ratio for the given case (see Table 4.1).

Table 4.1: Mass fractions used for ϕ at inlet

ϕ	**CH_4**	**O_2**
0.55	0.0301	0.22592
0.54	0.0296	0.22604
0.53	0.0290	0.22616
0.52	0.0285	0.22628
0.51	0.0280	0.22640
0.50	0.0275	0.22652
0.49	0.0270	0.22664
0.48	0.0264	0.22676
0.47	0.0259	0.22688
0.46	0.0254	0.22701
0.45	0.0249	0.22713
0.44	0.0243	0.22725

1. Balance N_2

Exhaust Domain and Outlet Boundary Condition

An interesting part of the model domain is the long extension that serves as the exhaust duct. Figure 4.6 shows the entire reactor and emphasizes two noteworthy regions (boxed in blue and green) of the exhaust domain. The first region (boxed in blue) is the reactor exit and is used to define the length of the exhaust region, which is much longer than in the real experiment. The hydraulic diameter at the reactor exit is less than 10 mm, and the exhaust extension is roughly 25 times the hydraulic diameter to encourage fully developed flow conditions. This portion of the domain is not physically realistic. The longer region is included in the model to ensure: 1) computational stability at the exit and 2) the conditions at the exhaust outlet are far enough from the reactor that they will not affect the results inside the reactor. This domain consists of 42,720 hexahedron elements with 51,373 nodes. The exhaust region has a total volume of 12,370 mm^3 with an average element volume of 0.29 mm^3.

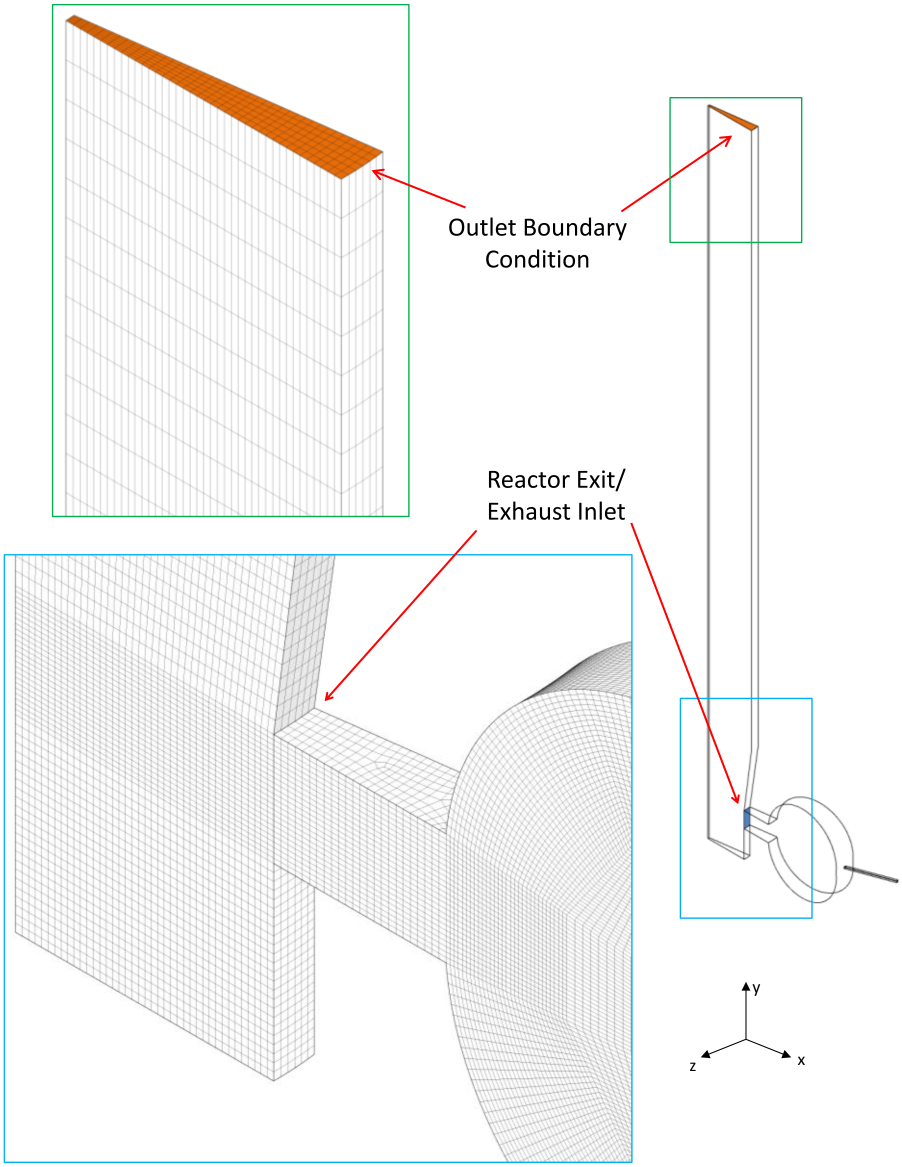

Figure 4.6: Exhaust domain, outlet boundary condition, and mesh

The second region (boxed in green) is the exhaust outlet is also treated as a pressure-based boundary condition. The exhaust leaves the reactor to enter the room at atmospheric conditions, so the total pressure is 0 kPa$_{gauge}$ (100 kPa$_{absolute}$). The inlet pressure discussed above and this outlet pressure result in an agreement on continuity to ensure that mass is conserved at 0.173 g/s. The exhaust outlet face has an area of 41.8 mm^2 with an average element area of 0.17 mm^2. The outlet face is very far downstream from the reactor, so the residence time is large. The boundary condition at this face is set to equilibrium values for temperature and species.

The flow direction at this outlet face requires special handling. In the physical experiment, the swirling nature of the flow leaving the toroid causes a vortex in the exhaust that entrains surrounding flow and causes flow to reverse direction and flow into the exhaust instead of out of the exhaust. This was handled in the experiment by installing a small device that essentially consists of flat plates to straighten the flow. In the model, this was handled by forcing the flow at the exhaust outlet to be only in the y-direction. The direction of the pressure vector at the outlet is specified via Cartesian coordinates (x = 0, y = 1, z = 0) to give the direction to the flow at the outlet. The turbulence at the outlet is defined by the turbulence intensity (set to 6%) and hydraulic diameter (set to 50 mm). These turbulence parameters are calculated as discussed below.

Reactor Domain and Boundary Conditions

The reactor is the third, and most important, domain of the model. The nozzle and exhaust domains dictate what happens inside the reactor, but the reactor domain provides information about flame stabilization.

The reactor domain is shown in Figure 4.7 with the reactor inlet (also the nozzle exit) and the reactor exit (also the exhaust inlet). The majority of the reactor is a structured mesh of hexahedron elements. The entire reactor domain consists of 309,860 elements (280,800 hexahedrons, 2,568 pyramids, and 26,492 tetrahedrons) with 299,541 nodes. Based on the number of elements, the reactor domain is 86% of the entire geometry. The exit channel portion of the reactor (where the reactor domain mesh must adapt to the exhaust domain mesh) is the only portion with the pyramid and tetrahedron elements. The mesh is refined at the reactor midplane and nozzle exit to improve resolution in the region near the jet. The reactor region has an overall volume of 6720 mm^3 with an average element size of 0.022 mm^3.

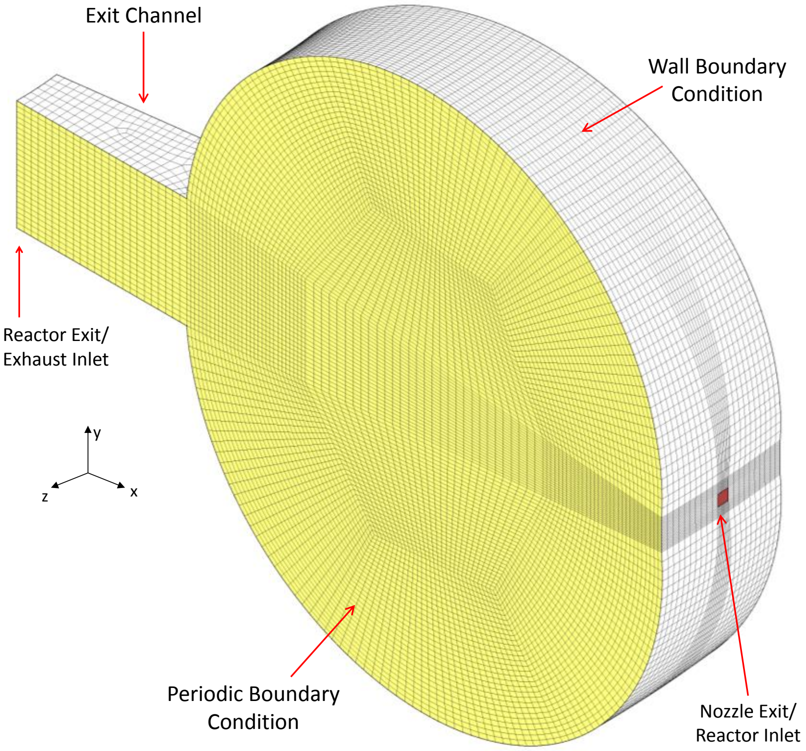

Figure 4.7: Reactor domain, boundary conditions, and mesh

The sliced reactor domain enables the use of the periodic boundary condition. It has two faces in the toroidal direction that should be periodic because each jet configuration is a repeat of its neighbor. One periodic face is shown as yellow in Figure 4.7. The other periodic face is not shown as it is behind the geometry. The periodicity is rotational, since the reactor slice is revolved.

The solid wall boundaries are shown as white in Figure 4.7. These walls utilize a no slip condition, a specified heat flux, and zero diffusive flux. As described in Appendix C, the heat loss is estimated to be 2.5% of energy input based on the fuel flow and higher heating value. For methane, this results in 325 W applied to a total reactor surface area of 295.4 cm^2 which yields a heat flux of 12 kW/m^2. Many previous studies using the toroidal reactor (Blust et al. [16], Barat [31], Nenniger et al. [14], Zelina and Ballal [1]) present similar values.

4.1.3 Models and Solution Methods

The turbulent fluid mechanics inside the reactor require a model to characterize the behavior. Similarly, the turbulence affects the chemistry, so a model is required to characterize the turbulence-chemistry interaction.

Reynolds Stress Model

The turbulent nature of the flow in the toroidal reactor necessitates a model to close the Reynolds-Averaged Navier-Stokes (RANS) equations. Many models for this type of problem utilize one or two equations, but the highly swirling flow in this situation requires more advanced models.

The Reynolds Stress Model (RSM) was originally developed by Launder *et al.* [79]. The model solves transport equations to calculate the individual Reynolds stresses. In order to close the RANS equations for this 3D situation, there are seven additional transport equations including an equation for the dissipation rate.

The transport phenomena for the Reynolds stresses include convection, turbulent diffusion, molecular diffusion, stress production, buoyancy production, pressure strain, dissipation, and rotation. The turbulent diffusion, buoyancy production, pressure strain, and dissipation all require models to close the equations [80]. Of those, the only model with user choice in ANSYS Fluent 14.5 is the pressure strain model. In this work, the Linear Pressure Strain model was selected because it consistently provided convergence and computational stability.

The turbulence modeling requires some parameters to be defined at the nozzle inlet and exhaust outlet. The turbulence intensity and length scale are defined according to the guidelines presented by ANSYS Fluent 14.5 [77,81]. The turbulence intensity (I) is defined as determined in Equation 4.2. The Reynolds number based on the hydraulic diameter is calculated based on the velocity and properties at the respective face. The turbulent length scale (L) is a physical quantity related to the size of the large eddies that contain energy in turbulent flows. The guidelines presented by ANSYS Fluent 14.5 suggest the hydraulic diameter as an acceptable length scale for the inlet and outlet faces (Equation 4.3).

4.2 $$I \equiv \frac{u'}{\bar{u}} = 16\left(Re_{D_h}\right)^{-0.125}$$ %

4.3 $$L = D_h = \frac{4A_c}{P}$$ mm

Species Transport Model

The methane chemistry is modeled with the Reduced GRI mechanism developed by Karalus *et al.* and discussed in Appendix F [78].

The turbulence-chemistry interaction is included by utilizing the built in Eddy Dissipation Concept (EDC) model in ANSYS Fluent 14.5 [77]. The EDC model was developed by Magnussen [82] for turbulent flows only and is capable of modeling the turbulent chemistry interaction with detailed chemical mechanisms.

The EDC model assumes that chemical reactions occur in small turbulent structures called fine scales. These represent the regions where molecular mixing takes place, which is presumed to be required for combustion chemistry to proceed. The size of these turbulent structures depends on the kinematic viscosity, turbulent kinetic energy, and dissipation rate based on the sub-grid scale. Chemical species are assumed to react in these fine scales for some amount of time. The time scale depends on the kinematic viscosity and turbulent dissipation rate. Both the turbulent fine scales and turbulent time scales include constants that are empirical in nature [80].

In practice, the turbulence-chemistry interaction is handled by creating a turbulent stirred reactor with a volume based on the turbulent fine scales and a residence time based on the turbulent time scale. Once the chemistry is defined in this way, the reaction rate parameters are then used to calculate the production/destruction rates of various species. The reaction rates are then used to generate chemical source terms for each species, which are then used in the species conservation equations.

Solution Methods

The selection of solution methods in ANSYS Fluent 14.5 is somewhat subjective and based on results. Certain methods result in convergence and computational stability, while others do not. The selected methods are listed in Table 4.2.

Table 4.2: CFD solution methods

Parameter	Method
Pressure Velocity Coupling	SIMPLE
Gradient	Least Squares Cell Based
Pressure	Standard
Density	First Order Upwind
Momentum	
Turbulent Kinetic Energy	
Turbulent Dissipation Rate	
Reynolds Stresses	
Species	
Energy	

Chemical Reactor Model

Chemical Reactor Models (CRMs) are zero-dimensional (perfectly stirred reactor – PSR) or one-dimensional (plug flow reactor – PFR) volumes used for applying species, momentum, and/or energy conservation principles. These models calculate chemical kinetic behavior for given conditions in order to understand the underlying reasons for chemical differences in fuels. The simplest CRM is the PSR, which we have implemented in CHEMKIN-PRO 15113 from Reaction Design [6] to understand how heat loss, chemistry, and reactor size affect species concentration and temperature with detailed chemical kinetics.

Figure 4.8 shows a schematic of the PSR model. The model inputs are generally based on the experimental conditions of the TSR, but are sometimes based on the results of the CFD models. Methane and air enter the reactor at a given premix temperature (450K). The total flow rate is 8.25 g/s. The PSR model in CHEMKIN-PRO can either be a 'fixed temperature' problem in which the temperature is assumed to be known, or an 'energy equation' problem in which the reactor could experience heat loss and the temperature is then solved from conservation of energy. The Reduced GRI mechanism was used for the detailed kinetics of methane oxidation [78]. The reactor pressure is 1 atm.

Three parameters are used to understand the PSR behavior at/near blowout. The reactor volume was first set to the same as the TSR (250 mL) while the heat loss and equivalence ratio were allowed to vary. Later, the heat loss was fixed at the experimental conditions and the equivalence ratio was set to the value determined from the CFD while the reactor volume was allowed to vary.

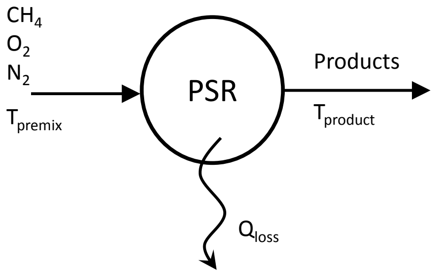

Figure 4.8: PSR schematic for methane CRM analysis

The heat loss is based on the analyses discussed in Appendix C and is limited to three conditions. The first condition, adiabatic, is unrealistic but provides a good bounding comparison. The second condition, 325W heat loss, corresponds to 2.5% of energy input and is roughly the median of the experimental condition. The third condition, 650W heat loss, corresponds to 5.0% of energy input and is roughly the maximum heat loss experienced in the experimental conditions.

The CFD and PSR models are used to understand and interpret the reactor behavior as it approaches blowout. First, the results of the CFD models will be presented and then the results of the PSR models will be presented to help understand the CFD models.

4.2 Methane Model Results

Before reviewing the results, the reader should orient themselves with Figure 4.9 to understand the surfaces used to present the results. The Mid-Plane is at the jet height, slicing the toroid into two hemi-toroids. In the top view, the Toroidal Plane is shown bisecting one segment, but it refers to any plane that rotates with the toroidal direction. In most cases, this plane (at a 3.75° angle) is used. In some cases other Toroidal Planes are used at angles between 0.0° and 7.5°. The Jet Plane is shown covering three segments as it must to show the complete jet.

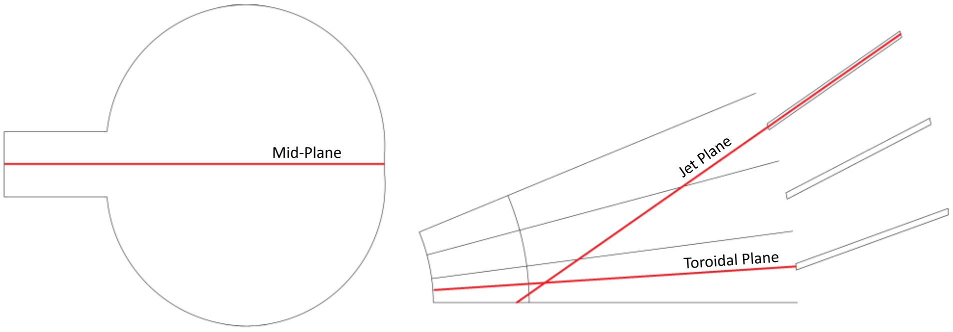

Side View

Top View

Figure 4.9: Planes of interest for CFD results

4.2.1 Results for Stable Combustion (ϕ = 0.55)

The first plots present contours of temperature at a very stable condition (ϕ = 0.55) inside the reactor on various planes of interest. Figure 4.10 shows the temperature on the reactor Mid-Plane (where the upper and lower toroids meet). The periodic boundary is utilized to represent the entire toroid by repeating the modeled slice 48 times. There are two features to note: 1) the jet is somewhat small and 2) there is a slightly colder spot near the center of the domain. Other planes of visualization will help explain these features.

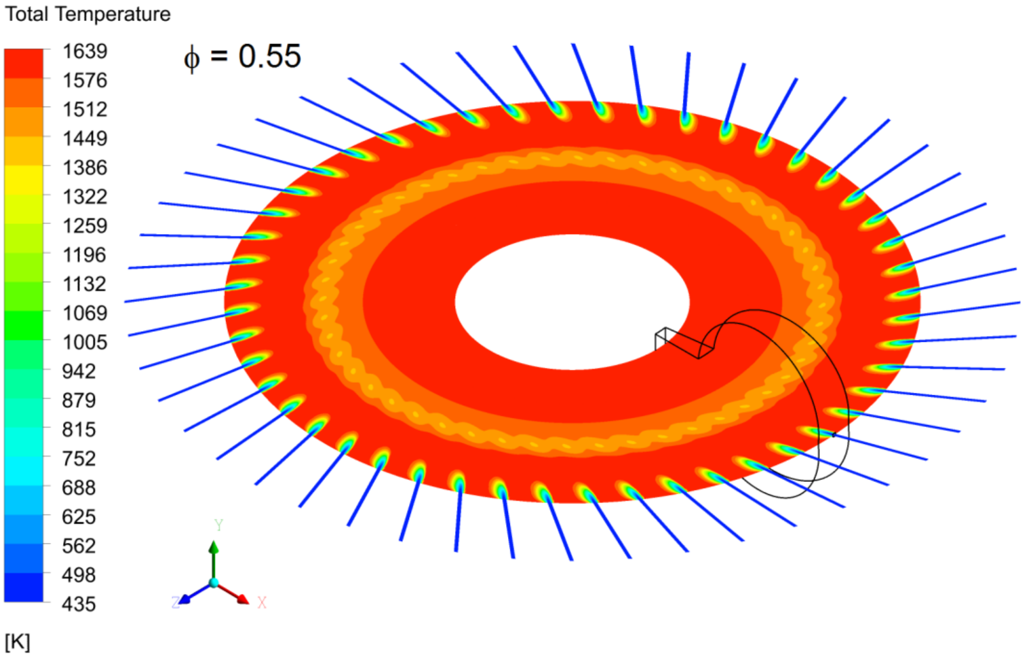

Figure 4.10: Temperature contours on Mid-Plane (ϕ = 0.55)

The temperature is plotted next on the 3.75° Toroidal Plane (Figure 4.11) to show that the jet is still small and seemingly discontinuous, but it explains the jet size and 'cold' spot. The small jet is explained here by noticing that the jet is asymmetric about the Mid-Plane. The previous figure would not capture the full jet since it would be out of that plane of visualization. This asymmetric behavior was ignored in previous models by assuming symmetry about the Mid-Plane [33]. The 'cold' spot is in fact the 'cold' jet penetrating the reactor and expanding.

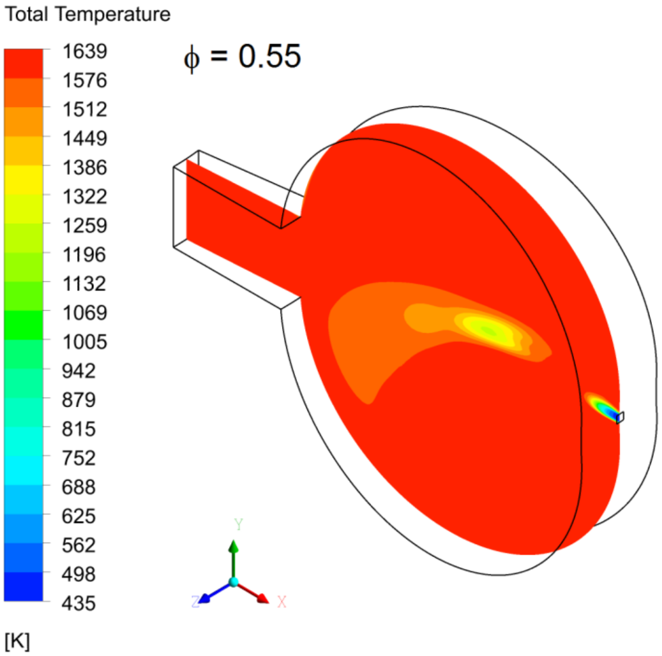

Figure 4.11: Temperature contours on 3.75° Toroidal Plane (ϕ = 0.55)

The discontinuity of the jet is explained by plotting the temperature on the Jet Plane as shown in Figure 4.12. This plane is angled to be coincident with the jet that is two segments before this one (see Figure 4.9) allowing for the entire jet to be visualized. The jet is in fact not discontinuous. Recall that the jets are angled at 20° causing bulk flow in the clockwise toroidal direction. This flow path transports the jet from the upstream reactor segment into this reactor segment, so Figure 4.11 is showing both the jet from this segment and the jets from the previous segments of the reactor. Appendix E presents plots along planes of several angles (between 7.5° and 0.0°) to see how the jet evolves in the toroidal direction.

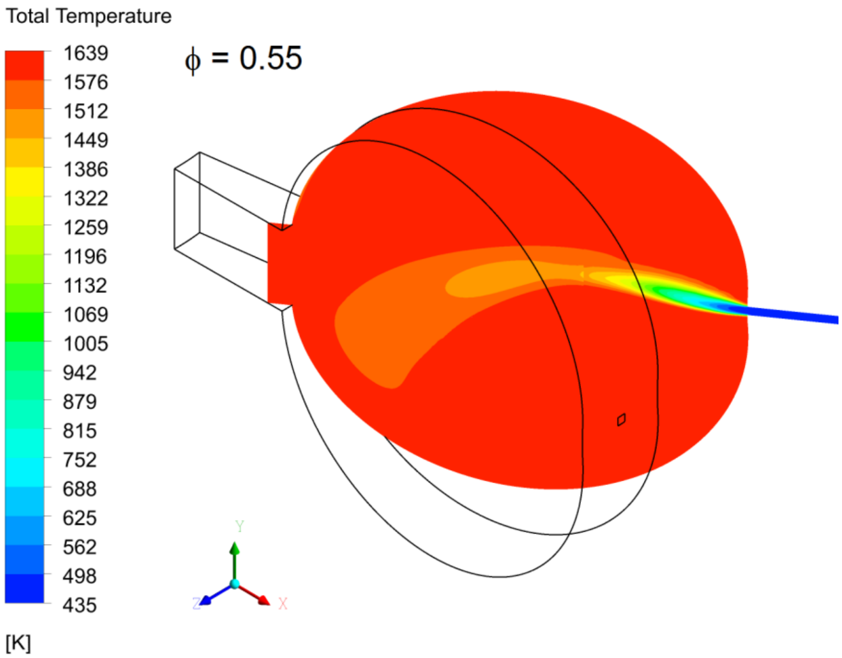

Figure 4.12: Temperature contours on the Jet Plane (ϕ = 0.55)

The CFD results for the temperature inside the reactor appear reasonable, and can be validated. There is very limited ability within the TSR to characterize the behavior at different locations, but Figure 4.13 presents the temperature at various distances along the height of the toroid. The experimental data are at a higher equivalence ratio, but the trend qualitatively matches the model. Note, that the experiment and model both show the dip in temperature at approximately 20 mm, which is slightly above the reactor Mid-Plane. This observation is consistent with the predicted asymmetry of the reactor.

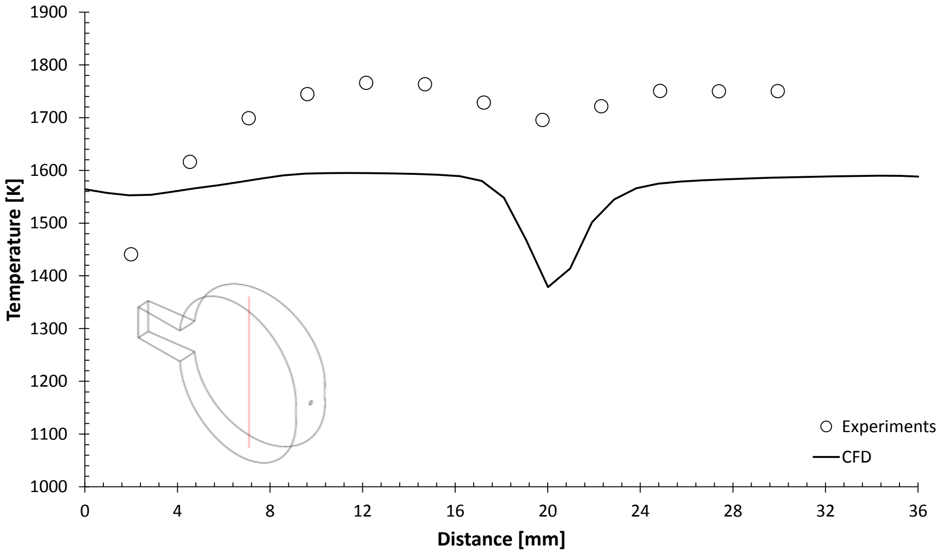

Figure 4.13: Reactor temperature profile (experimental and CFD)

4.2.2 Blowout Results (Variable ϕ)

The primary objective for the use of the CFD models is to understand the behavior of the TSR as it approaches extinction, and in particular how the actual reactor differs in blowout behavior relative to a PSR. The equivalence ratio, ϕ, is set at the inlet boundary condition with a mass fraction of fuel and air. The equivalence ratio is used as a parameter and is slowly decreased until blowout/extinction, which occurs when the model converges upon a non-reacting solution (the temperature inside the reactor is the same as the premix temperature).

The model begins at a stable condition of ϕ = 0.55 and the last reacting condition occurs at ϕ = 0.44. The case of ϕ = 0.43 resulted in a cold-flow solution. Visualizing temperature, species, and reaction rate contours as equivalence ratio decreases helps to understand the mechanism for flame stabilization in the reactor.

Figure 4.14 shows how the temperature varies for selected decreasing equivalence ratios. Not only is the temperature decreasing, but there is a significant temperature variation within the reactor as the equivalence ratio decreases. At ϕ = 0.44 the recirculating jet that is stabilizing combustion is lower in temperature, and the reactor is much less homogeneous than the stable condition of $\phi = 0.55$.

Figure 4.15 shows the methane production/destruction rate for selected decreasing equivalence ratios. Notice that the primary reaction rate occurs in the jet where the incoming methane is being destroyed. Once again, as the equivalence ratio decreases, and the reactor becomes less homogeneous, the region of methane destruction recirculates around and interacts with the incoming jet.

Figure 4.16 shows CO concentration (mole fraction) for selected decreasing equivalence ratios. At the highest equivalence ratio ($\phi = 0.55$) the highest CO concentration is located in a compact region near the center of the reactor and in the jet. As the equivalence ratio decreases, the size and location of the peak CO concentration shifts and recirculates around the reactor. At incipient blowout ($\phi = 0.44$) the peak CO concentration in the reactor is directly in contact with the incoming jet.

Figure 4.17 shows OH concentration (mole fraction) and Figure 4.18 shows OH reaction rate for selected decreasing equivalence ratios. OH is often used as an indicator of the concentration of the free radicals that are necessary to sustain combustion. During stable combustion ($\phi = 0.55$), a high concentration of OH radical is recirculating around and interacting with the incoming jet. As the equivalence ratio decreases, the highest concentration of OH in the reactor moves closer to the incoming jet. At incipient blowout ($\phi = 0.44$) the OH concentration interacting with the jet decreases substantially as the highest concentration has shifted into the center 'eye' of the reactor and the upper toroid of the reactor. The OH concentration that is interacting with the incoming jet is actually very low. At incipient blowout, the highest OH reaction rate is located in a small region between the recirculation region and the 'eye' of the reactor. This region is discussed in detail next as it holds the key to the mechanism of reactor stabilization.

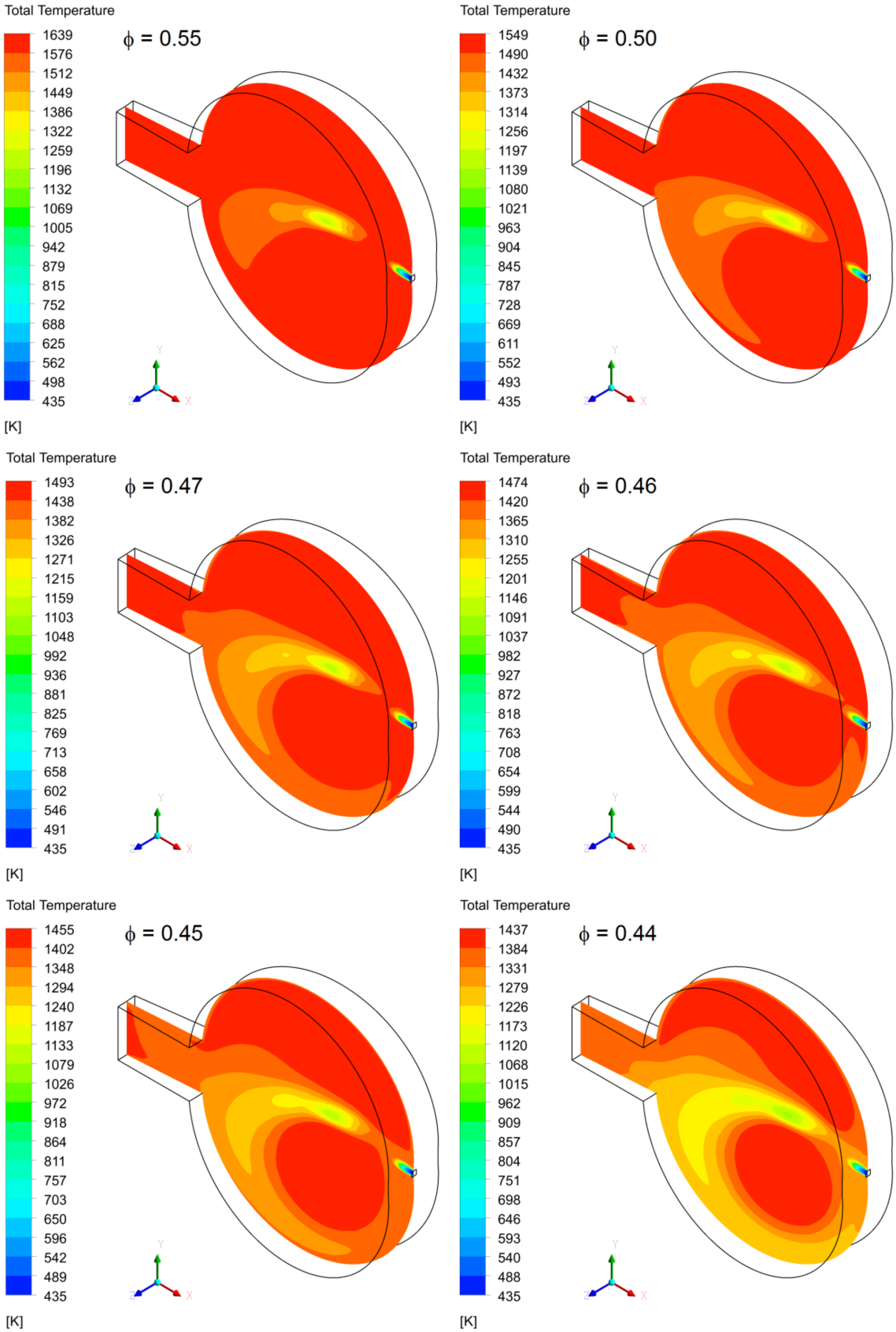

Figure 4.14: Contours of temperature as ϕ varies to extinction

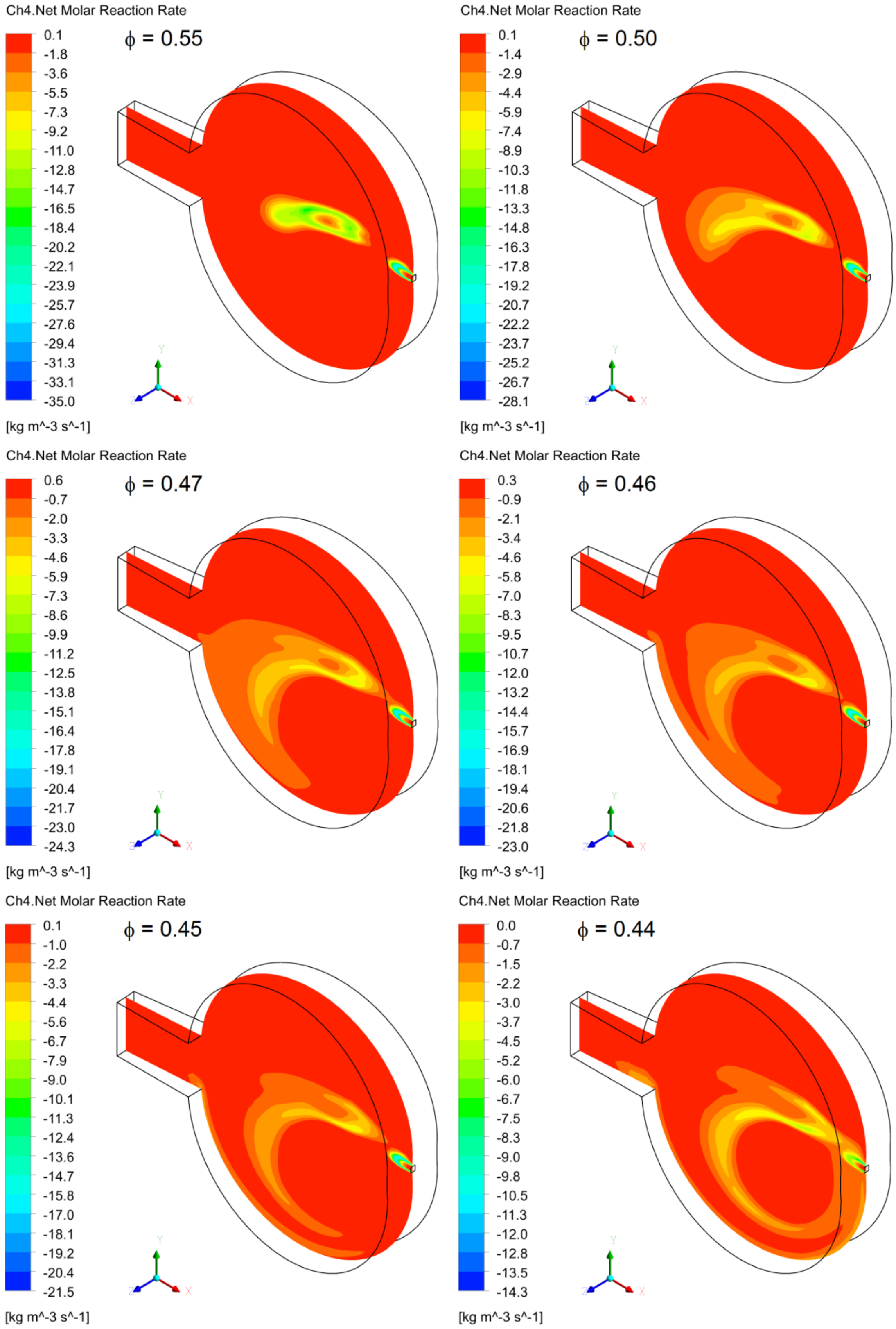

Figure 4.15: Contours of fuel reaction rate as ϕ varies to extinction

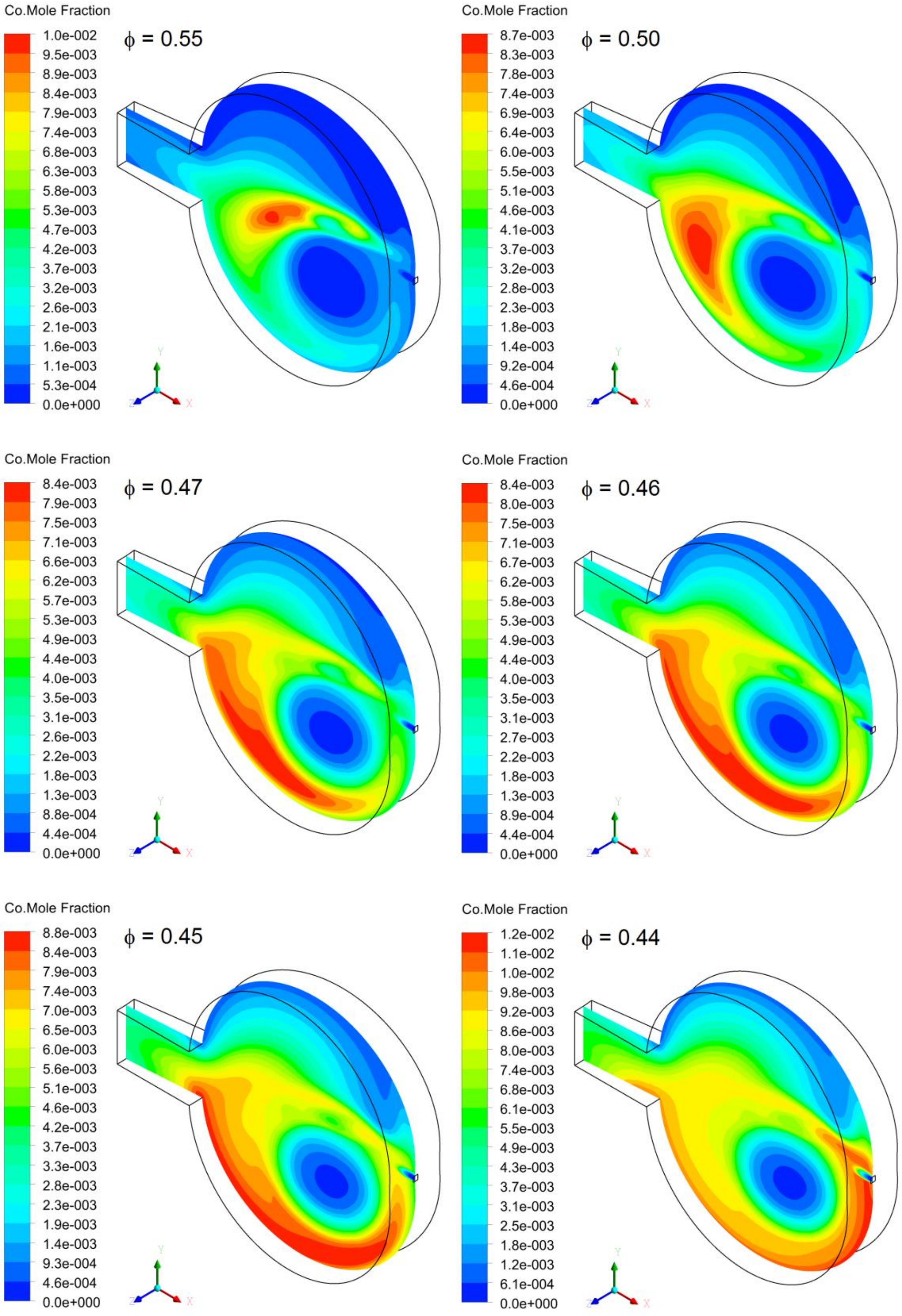

Figure 4.16: Contours of CO mole fraction as ϕ varies to extinction

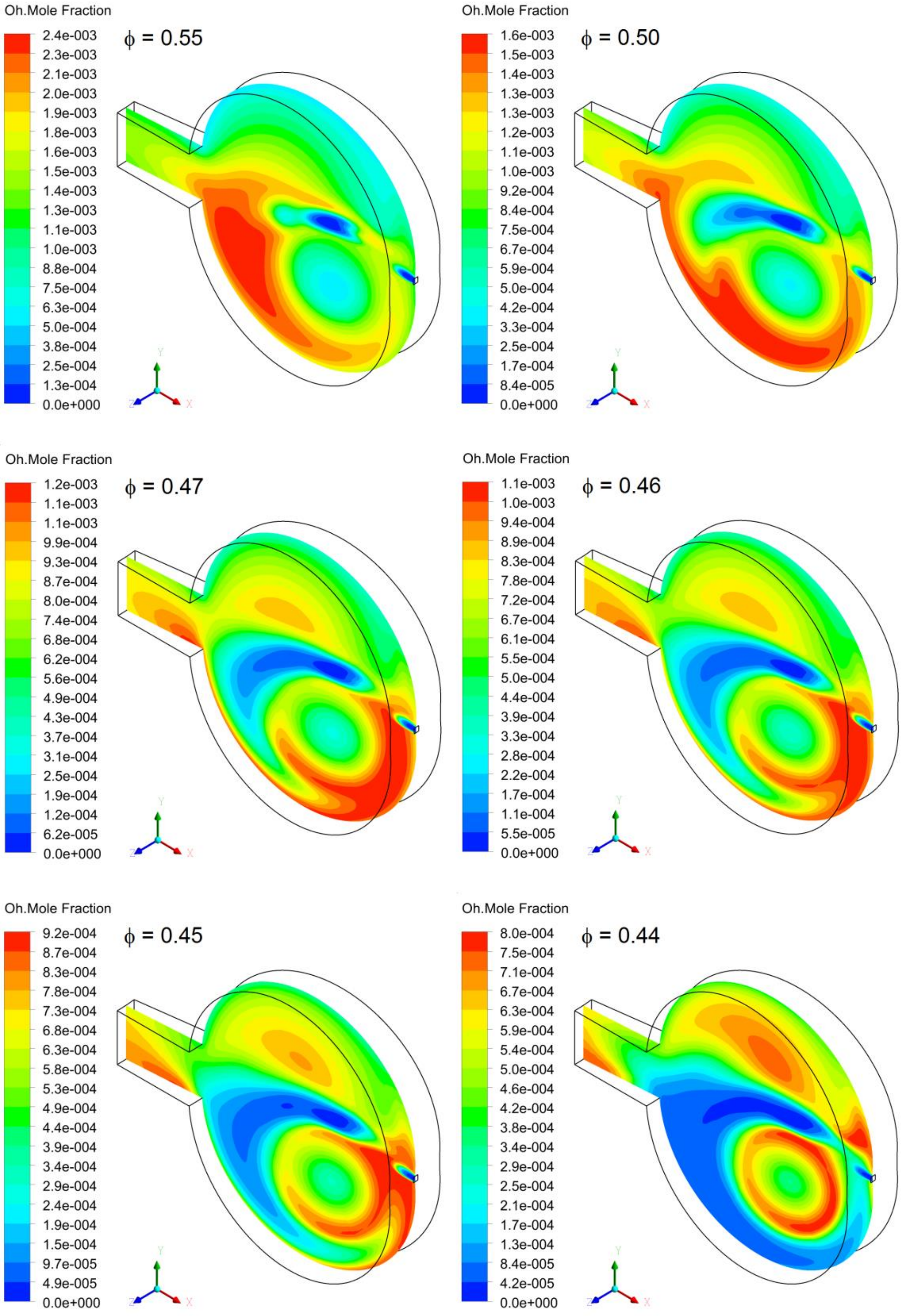

Figure 4.17: Contours of OH mole fraction as ϕ varies to extinction

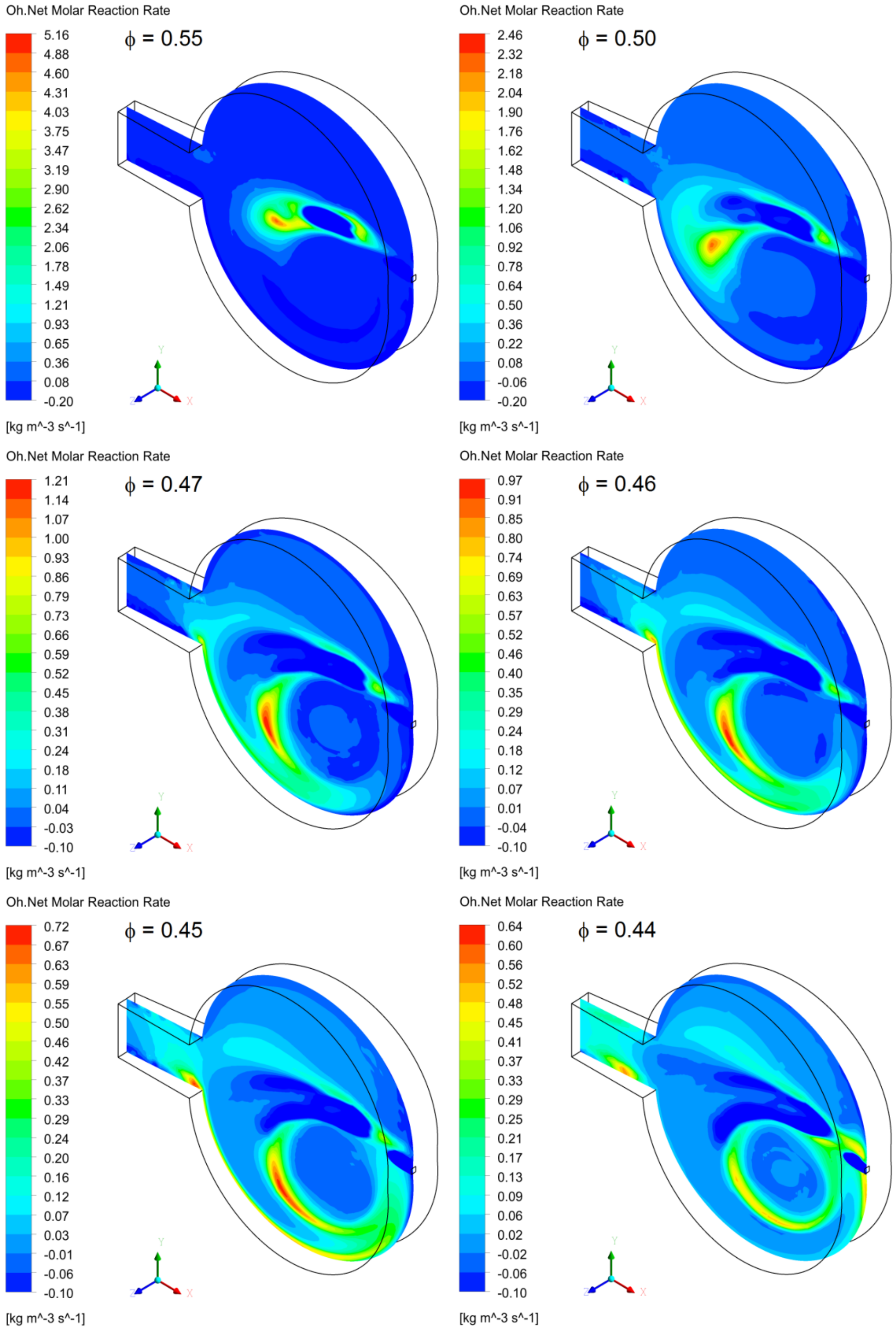

Figure 4.18: Contours of OH reaction rate as ϕ varies to extinction

Figure 4.19 repeats three of the contour plots shown above for direct comparison. The temperature, OH mole fraction, and OH reaction rate contours at ϕ = 0.44 (incipient blowout) show three regions that help us understand flame stabilization. First, there is the 'eye' of the reactor shown as the region of high temperature in the lower toroid. Second, there is the recirculation region, shown as the region of low OH concentration along the wall of the lower toroid. Third, there is a shear region of high OH production which is located at the border of the recirculation and 'eye' regions. These plots also show a black line spanning the height of the reactor, which is used next to see how the temperature, OH concentration, and OH production vary within the reactor.

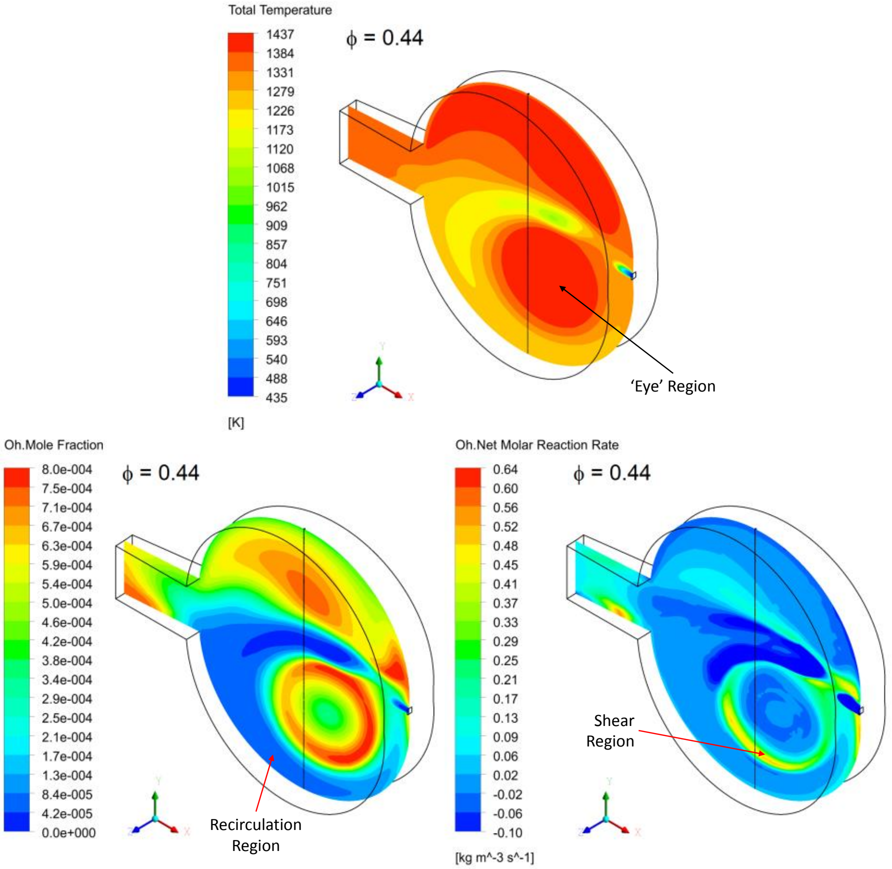

Figure 4.19: Contours of temp., OH mole fraction, and OH reaction rate at ϕ = 0.44

First in Figure 4.20, notice how the temperature and OH concentration vary from the bottom of the lower toroid (0mm distance) to the top of the upper toroid (36mm distance). The temperature is low at the lower toroid wall (recirculation region), then it is highest in the 'eye' of the vortex and low again at the jet location. The OH concentration is also low at the wall in the recirculation region. Focusing on the lower toroid, the OH concentration peaks at two locations that correspond to the boundary between the 'eye' and recirculation regions.

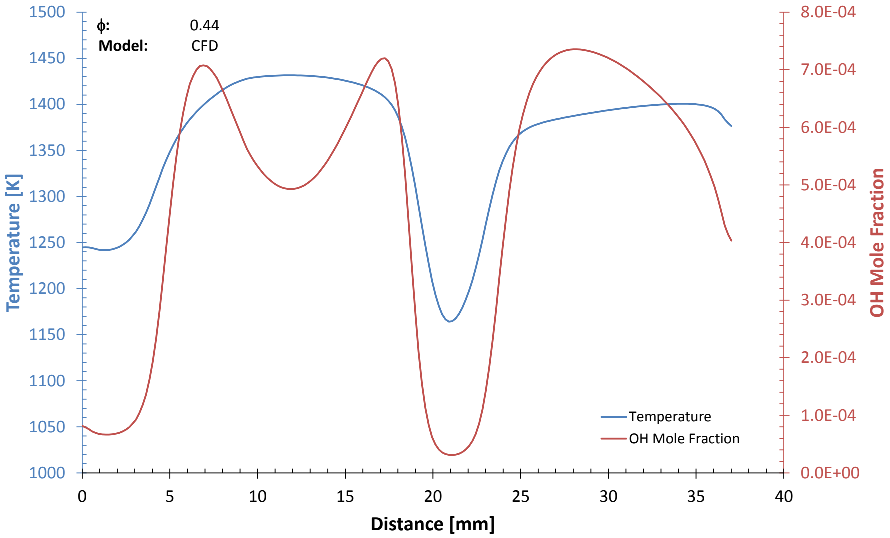

Figure 4.20: Temperature and OH mole fraction reactor profile

The OH concentration and OH reaction rate vary as shown in Figure 4.21. Notice that the highest OH production occurs just outside the 'eye' of the reactor and at the border of the recirculation region.

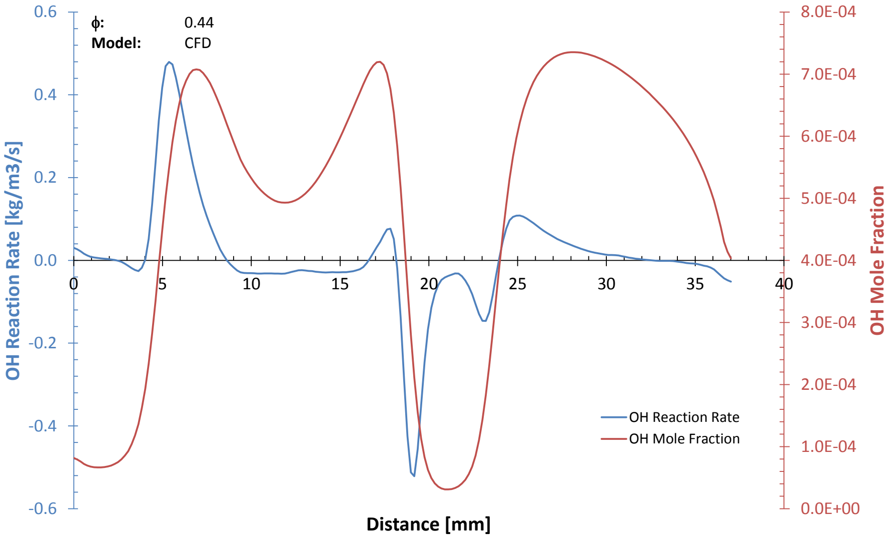

Figure 4.21: OH mole fraction and OH reaction rate reactor profile

The models suggest that the reactor is stabilized by diffusion facilitated processes generating and exchanging OH radical between the recirculation region, 'eye' region, and shear region. In general, the OH is produced in the shear region. The peak OH location then depends on the equivalence ratio and effectively the stability of the flame. Figure 4.22 shows the OH profiles inside the reactor as equivalence ratio decreases toward blowout. During stable combustion the profiles show that the peak OH is diffused into the recirculation region where it is transported around the reactor to interact directly with the incoming premix jet. However, as equivalence ratio decreases and near incipient blowout (ϕ = 0.44), the diffusion process shifts toward the 'eye' of the reactor and the OH radicals are now mostly located at the edges of the 'eye' region with only a small amount that are still recirculating around and directly interacting with the incoming jet.

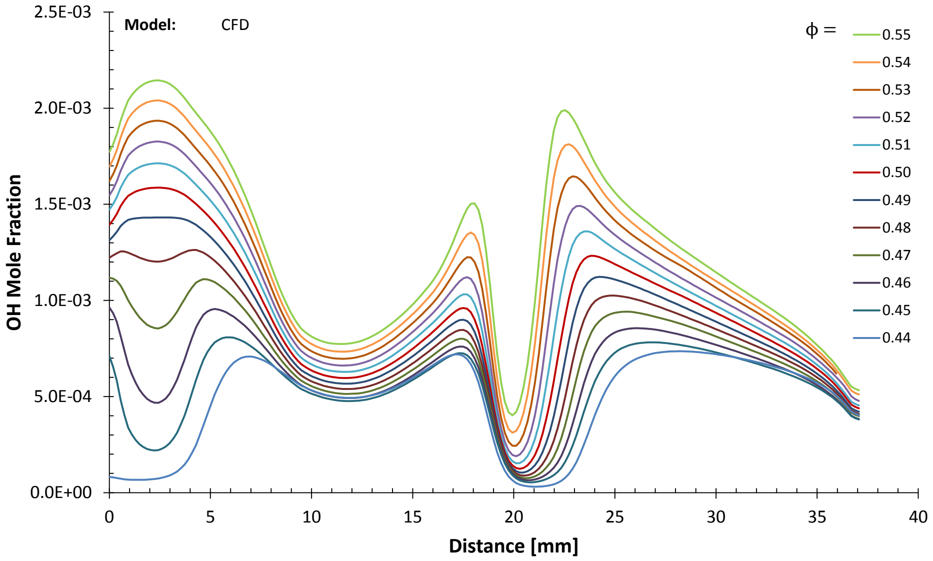

Figure 4.22: OH mole fraction reactor profiles at stable and blowout conditions

The shear rates and velocity in the eye, recirculation, and shear regions will be investigated at a later date to help to understand the behavior within the reactor near blowout.

The CFD models generally agree with the work of Barat [31] who suggests that the reactor becomes less and less homogenous as it approaches blowout. Appendix E presents some contour plots that highlight the change in homogeneity between stable conditions and incipient blowout. This inhomogeneity effectively reduces the reacting volume of the reactor and there is a significant departure from PSR behavior. The CRM described previously will help to interpret the reactor behavior as it approaches blowout.

4.2.3 CRM Interpretation and Experiment Comparison

The simple CRM described in Section 4.1.3, a single PSR, is used to help understand the chemical kinetic behavior near blowout. The first model maintained reactor volume at 250 mL to match the TSR and varied the equivalence ratio and heat loss to look for blowout as shown in Figure 4.23. Notice, first, that the adiabatic condition closely follows the equilibrium condition as expected. Also, notice that the blowout temperature is roughly the same for all three heat loss conditions even though the equivalence ratio at blowout does vary slightly. The median heat loss (2.5% of energy input) case predicted a blowout equivalence ratio of ϕ = 0.39, which is slightly below the CFD prediction of ϕ = 0.44.

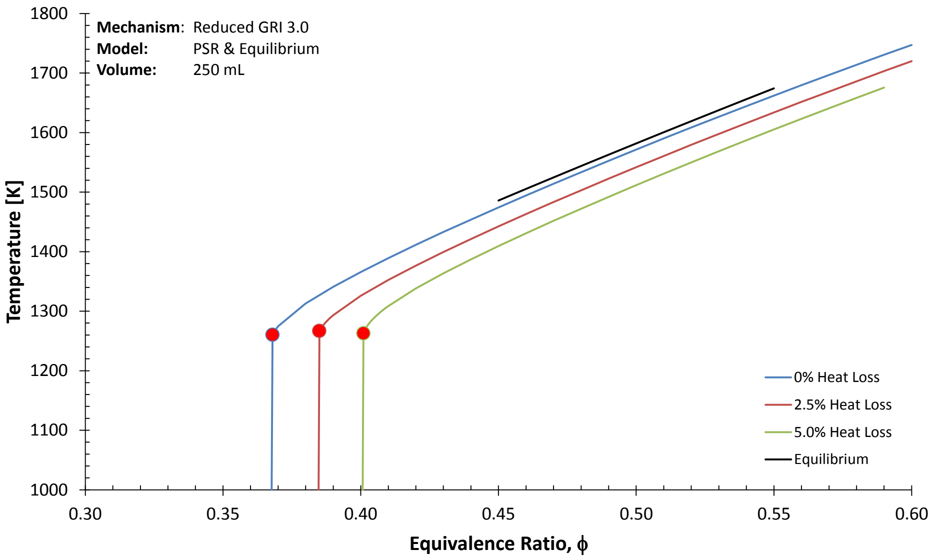

Figure 4.23: PSR model of temperature vs. equivalence ratio and heat loss

The second PSR model fixes heat loss and equivalence ratio to match the CFD models (2.5% and ϕ = 0.44, respectively) at blowout. However, now the volume is allowed to decrease until it (and effectively the residence time) becomes too small to sustain combustion. Figure 4.24 shows that the minimum volume to sustain combustion is 59 mL.

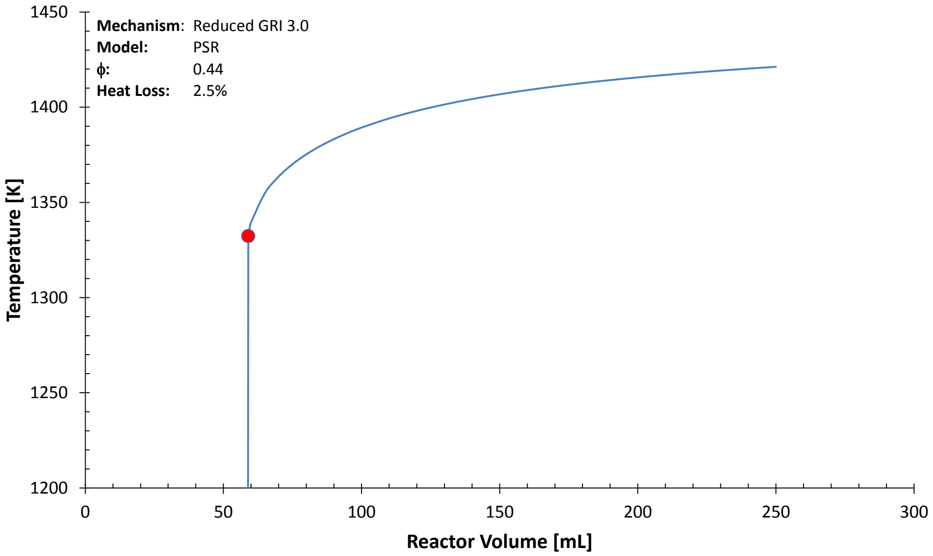

Figure 4.24: Temperature vs. reactor volume for PSR

Figure 4.25 shows the OH concentration and reaction rate as the PSR volume decreases to the blowout volume of 59 mL. The OH reaction rate at blowout is 4.38x10^{-2} kg/m^3/s, which we will use as the minimum reaction rate to define a reacting condition.

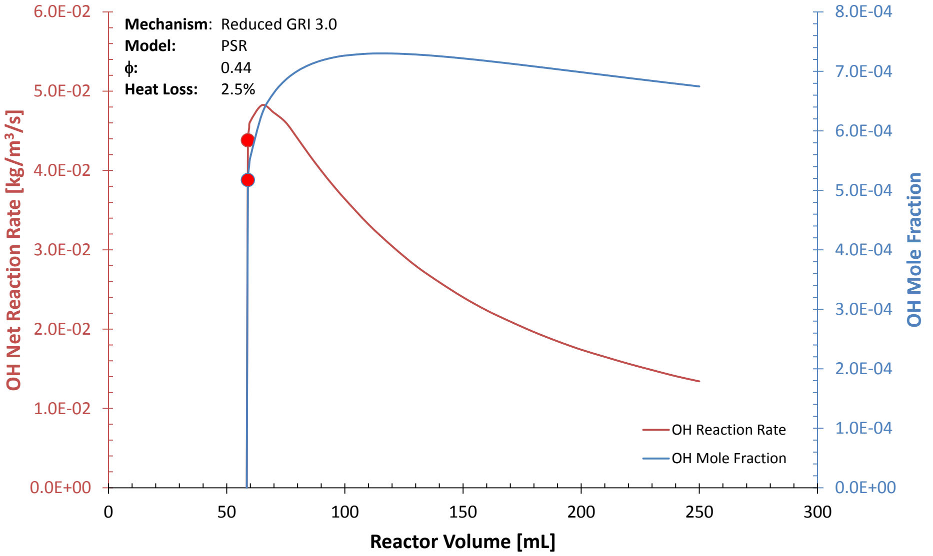

Figure 4.25: OH mole fraction and OH reaction rate vs. reactor volume for PSR

Unlike the PSR, the OH reaction rate from the CFD model varies throughout the reactor. At the same equivalence ratio (ϕ = 0.44) and heat loss (2.5%) as the PSR model, a portion of the

CFD reactor contains cells with OH reaction rates above 4.38x10^{-2} kg/m^3/s (the blowout OH reaction rate from the PSR model). Figure 4.26 shows the volume of the CFD reactor with this minimum OH reaction rate, which can be taken as the reacting volume under these conditions. The total volume of those cells is approximately 63 mL as calculated by ANSYS CFD-Post, which corresponds very well with the independently determined PSR volume at blowout (59 mL).

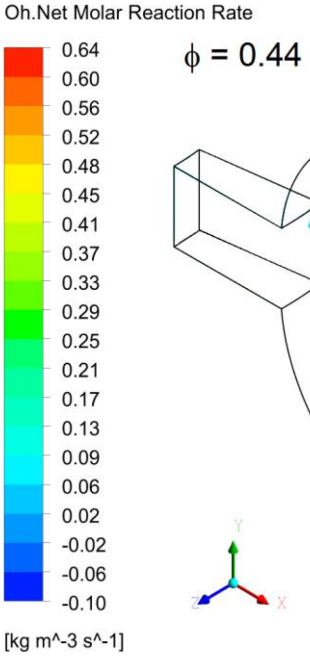

Figure 4.26: Portion of CFD reactor at/above OH reaction rate from PSR model

The last comparison to make is the temperature as equivalence ratio varies, especially at extinction as shown in Figure 4.27. The temperature is measured in the experiments and from the CFD at the same location, which is roughly 5 mm from the bottom of the toroid. The models and experiments agree very well in the stable combustion regime. However, the models are predicting the flame to be stable at lower equivalence ratios than experienced during experiments. Barat [31] also found that the single PSR model predicts blowout poorly as it allows for combustion to continue to much lower temperatures than the experiments. The equilibrium temperature was also determined from the NASA's CEA software program [57] and is included for comparison.

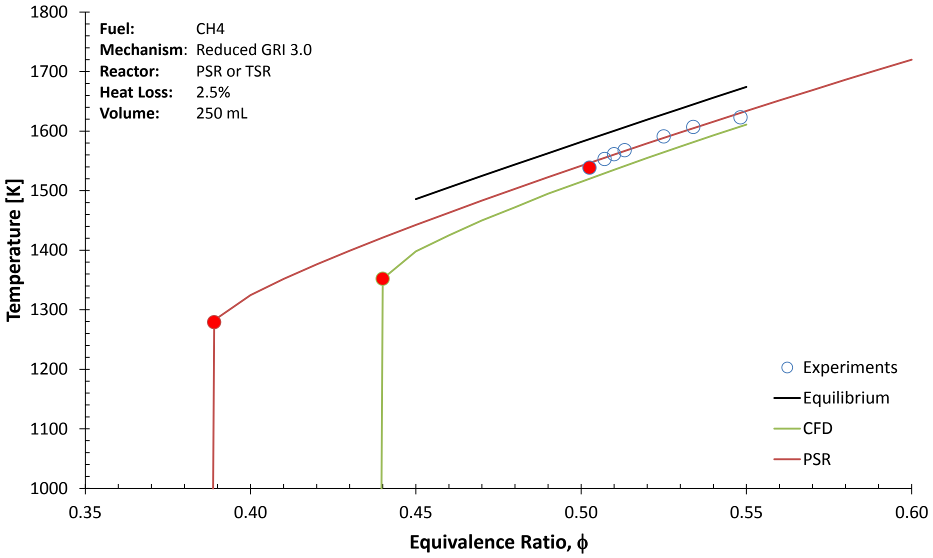

Figure 4.27: T vs. ϕ for methane extinction experiments and models

As mentioned in Section 1.3.2, Karalus *et al.* [27] and Karalus [28] showed that the flame in the jet stirred reactor (JSR) is stabilized for methane flames by two zones (a core region and a recirculation region) within the reactor and by the diffusive exchange between these regions. This is somewhat similar to the mechanism found in the TSR as ultimately, the shear region generating OH radical exists between the recirculation and 'eye' regions and as the reactor approaches blowout the OH transport into these regions is changing.

4.3 Toluene and iso-Octane Model

The newfound understanding of the reactor behavior near blowout can be utilized to rationalize the results from Chapter 3 that showed a difference in blowout between highly aliphatic fuels and highly aromatic fuels. The goal is to understand the fuel-based chemical differences in blowout, but CFD models cannot handle the huge kinetic mechanisms for these fuels. However, the PSR model can use detailed kinetic calculations to provide information about the relative differences in chemical effects by not including the fluid mechanical effects. Since the differences in chemistry are the key to understanding the variation in behavior between the fuels, the compromise here is to use the PSR model which maintains fidelity to the full chemical kinetic mechanisms while sacrificing the details of the reactor structure due to the fluid mechanics.

4.3.1 Model Methods

The model used in this kinetic interpretation is similar to the Chemical Reactor Model described in Section 4.1.3. The PSR is implemented in CHEMKIN-PRO 15113 from Reaction Design [6] to understand how chemistry and reactor size affect species concentration and temperature with detailed chemical kinetics.

Figure 4.28 shows a schematic of the PSR model. The model inputs are generally based on the experimental conditions of the TSR. Fuel (either iso-octane or toluene) and air enter the reactor at a given premix temperature (450K). The total flow rate is 8.25 g/s. The PSR model in CHEMKIN-PRO is an 'energy equation' problem in which the temperature is determined from conservation of energy. Dooley *et al.* [85] published a jet fuel mechanism that contains chemical kinetics for iso-octane and toluene oxidation. The details of this and all the mechanisms used in this work are in Appendix F. The reactor pressure is 1 atm and it experiences no heat loss. The equivalence ratio is held constant for both fuels at $\phi = 0.45$. The reactor volume was the primary parameter and left as a variable in order to find the minimum volume necessary to sustain combustion.

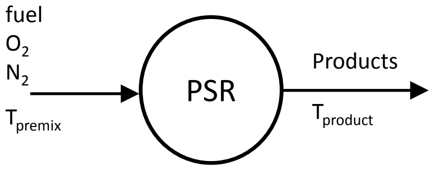

Figure 4.28: PSR schematic for iso-octane and toluene CRM blowout analysis

First, the PSR model will show that there are differences in blowout for iso-octane and toluene. Then the fuel destruction reactions will be analyzed to determine the reason for those differences.

4.3.2 Model Results

The experimental reactor experiences localized extinctions that reduce the reacting volume and ultimately cause blowout. The first step is to look for the minimum volume needed to sustain combustion and how this varies for the different fuels. Figure 4.29 presents the models for iso-octane and toluene and shows a difference in blowout volume. The equilibrium adiabatic flame temperature is also included and explains the reason for the difference in combustion temperature at large reactor volumes. The blowout temperature and volume for toluene are 1405K and 44 mL, respectively. The blowout temperature and volume for iso-octane are 1360K and 38 mL, respectively. This 50K difference in blowout temperature is roughly the same as the difference between the real fuels observed in the experimental studies reported in Chapter 3.

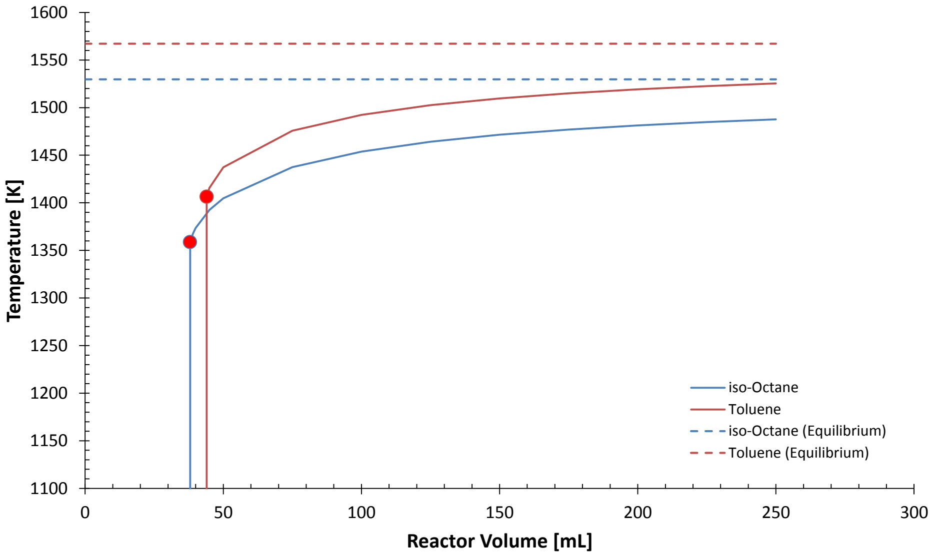

Figure 4.29: Temperature vs. reactor volume for iso-octane and toluene in a PSR

The methane model analysis discussed previously showed that the radical pool is the critical contributor to flame stabilization. Figure 4.30 presents the concentration of hydroxyl (OH) radical for the two fuels. Both fuels have increasing OH concentrations as volume decreases, but experience a sharp decrease just before blowout. Notice that the toluene flame is producing more OH radical during stable combustion, but produces less near blowout.

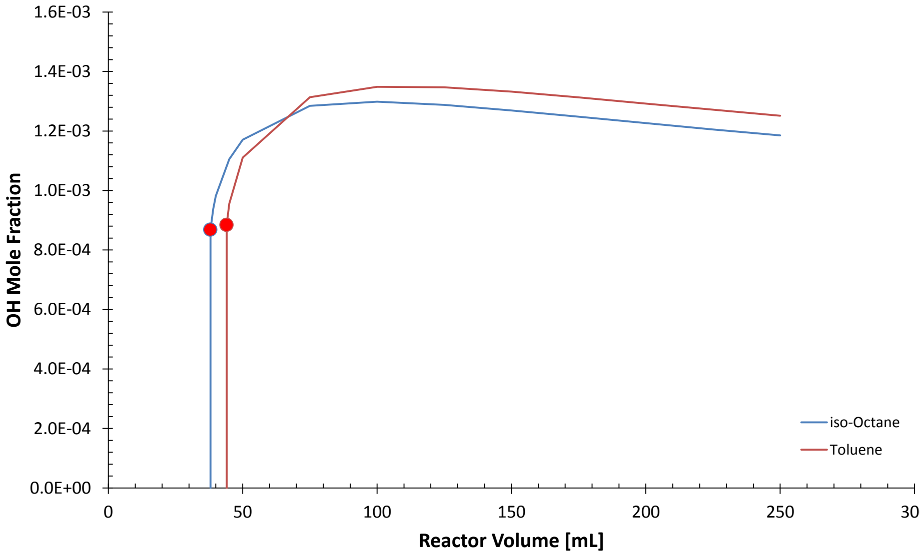

Figure 4.30: OH mole fraction vs. reactor volume for iso-octane and toluene in a PSR

Figure 4.31 shows the net reaction rate of OH radical for the two fuels. Interestingly, both fuels are producing OH at a very similar rate which is increasing with decreasing reactor volume. The production rates peak just before blowout and then drop drastically. Notice that toluene produces OH radical at a lower rate than iso-octane near blowout.

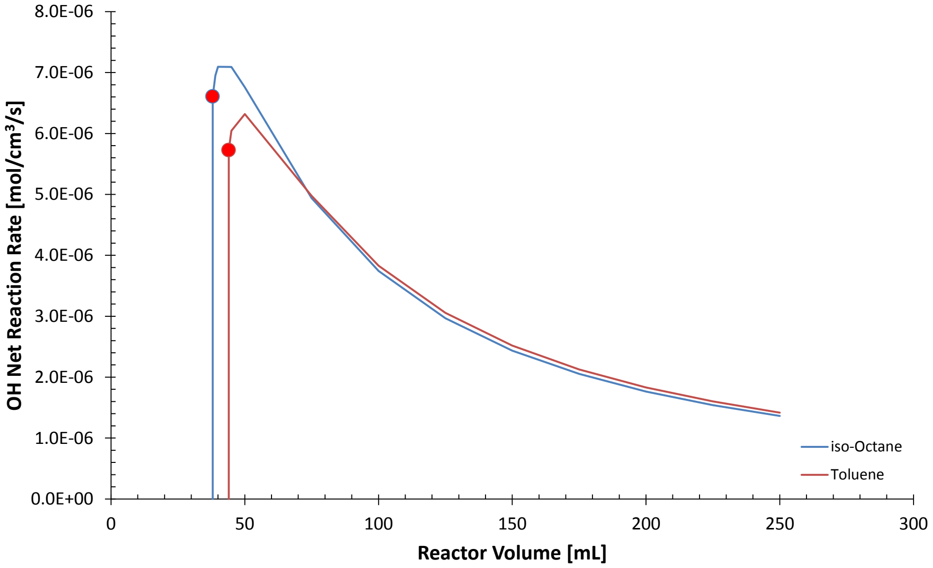

Figure 4.31: OH reaction rate vs. reactor volume for iso-octane and toluene in a PSR

This difference in radical concentration and production rate ultimately stems from a difference in the rate at which the original fuel molecule is being attacked and destroyed by the radical species. The reaction rate parameters for the relevant reactions should be able to quantify this difference. Toluene and iso-octane are destroyed by three radicals: monatomic oxygen (O), monatomic hydrogen (H), and hydroxyl (OH) via the reactions shown in Table 4.3 and Table 4.4, respectively. In general, the reactions indicate the radical is abstracting a hydrogen atom away from the molecule and using it to form a new species.

Notice that the reactions are grouped by reactant, and that all the reactions are second order. Each reaction has three reaction rate parameters (A, b, E_A) that determine a specific reaction rate coefficient, k, at a given temperature (Equation 4.4). In these tables the reaction rate coefficient (k) is calculated at a near blowout temperature of 1410K. Since the temperature is the same for both fuels, the reaction rate coefficient becomes indicative of the rate at which the fuel is being destroyed by the radical species. The reactions with the same reactants are directly comparable, and are combined into a single cumulative reaction rate coefficient ($\sum k$) for each fuel and radical combination.

$$k = A\,T^{b}\exp\left(-\frac{E_A}{RT}\right) \qquad [\mathrm{cm^3/mol/s}] \tag{4.4}$$

Table 4.3: Toluene destruction reactions and rate parameters at 1410K

#	**Reactants**		**Direction**	**Products**		**A [cm^3/mol/s]**	**b**	**E_A [cal/mol]**	**$\sum k$ [cm^3/mol/s]**
6278	$C_6H_5CH_3$	H	→	$C_6H_5CH_2$	H_2	6.5E+00	4.0	3384	8.9E+12
6296			→	$C_6H_4CH_3$	H_2	5.0E+08	1.0	16800	
6303			→	C_6H_6	CH_3	9.5E+05	2.0	944	
6280		O	→	$C_6H_5CH_2$	OH	6.3E+11	0.0	0	5.4E+12
6297			→	$C_6H_4CH_3$	OH	1.7E+13	0.0	14700	
6301			→	$OC_6H_4CH_3$	H	1.7E+13	0.0	3600	
6279		OH	→	$C_6H_5CH_2$	H_2O	1.8E+05	2.4	-602	1.0E+13
6298			→	$C_6H_4CH_3$	H_2O	1.3E+08	1.4	1450	
6302			→	$HOC_6H_4CH_3$	H	1.1E+02	3.2	5590	

Table 4.4: iso-Octane destruction reactions and rate parameters at 1410K

#	**Reactants**		**Direction**	**Products**[1]		**A** **[cm³/mol/s]**	**b**	**E_A** **[cal/mol]**	**∑k** **[cm³/mol/s]**
3564	iC_8H_{18}	H	→	aC_8H_{17}	H_2	7.3E+05	2.8	8147	5.7E+13
3565			→	bC_8H_{17}	H_2	5.7E+05	2.5	4124	
3566			→	cC_8H_{17}	H_2	6.0E+05	2.4	2583	
3567			→	dC_8H_{17}	H_2	1.9E+05	2.8	6280	
3568		O	→	aC_8H_{17}	OH	8.6E+03	3.0	3123	3.0E+13
3569			→	bC_8H_{17}	OH	4.8E+04	2.7	2106	
3570			→	cC_8H_{17}	OH	3.8E+05	2.4	1140	
3571			→	dC_8H_{17}	OH	2.9E+05	2.5	3645	
3572		OH	→	aC_8H_{17}	H_2O	2.6E+07	1.8	1431	1.8E+13
3573			→	bC_8H_{17}	H_2O	9.0E+05	2.0	-1133	
3574			→	cC_8H_{17}	H_2O	1.7E+06	1.9	-1450	
3575			→	dC_8H_{17}	H_2O	1.8E+07	1.8	1431	

1. The iso-octyl radical has four distinct locations (a, b, c, or d) for H-atom abstraction

The cumulative reaction rate coefficients, ∑k, are presented in the last columns of the two tables above and plotted below in Figure 4.32. The important point from the figure is that the cumulative fuel destruction rate coefficients for toluene are much smaller than for iso-octane at the same temperature of 1410K. It does not necessarily indicate that monatomic H is more destructive, as ultimately the individual radical concentrations must be included to determine the actual reaction rate. The difference in blowout for these two fuels is due to the differences in the rates of destruction of the fuel molecules by radical species.

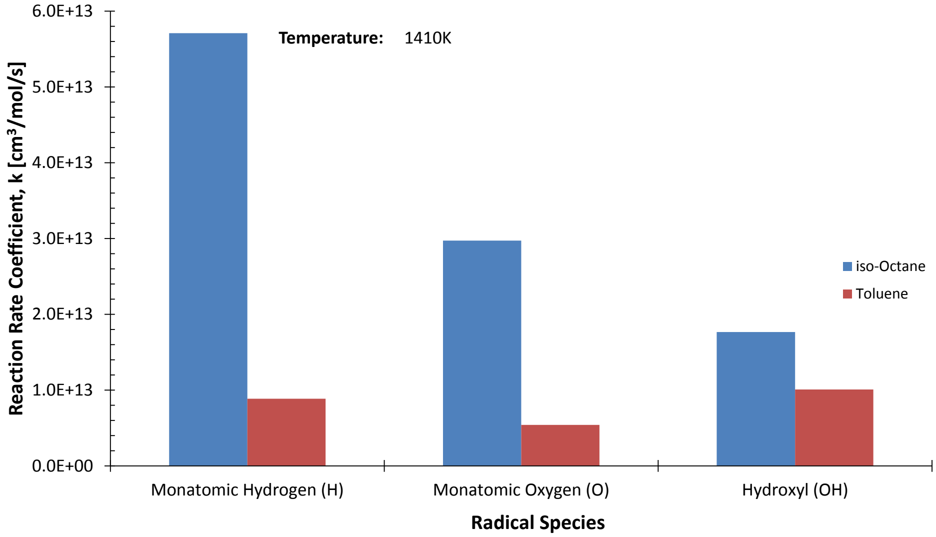

Figure 4.32: Radical reaction rate coefficients for iso-octane and toluene

The PSR and reaction rate coefficient analyses here agree with the experiments that show a difference in blowout behavior for a highly aliphatic fuel when compared to a highly aromatic fuel. Ultimately, the difference can be attributed to the fact that the aromatic fuel is more resistant to radical attack than the aliphatic fuel at the same temperature. The initial destruction reaction rate via H abstraction is slower for the aromatic ring, and that reduced fuel consumption rate subsequently slows the production of additional free radicals via chain branching. This compounded cyclic process reduces fuel consumption and heat release, so the aromatic fuel needs a higher combustion temperature to achieve enough reaction to sustain the flame. Thus, the aromatic fuel has a reduced resistance to extinction.

4.4 Conclusions

This chapter focused on the mechanism by which flames are stabilized inside the toroidal stirred reactor (TSR) using primarily CFD models in conjunction with CRM interpretation and experimental comparison. The conclusions of this work can be summarized as given below:

- The reactor can be separated into segments for each jet, but the jets interact with each other. If we focus on a single segment of the reactor, the jets from the two upstream segments enter the current segment. This flow field creates a bulk flow in the toroidal direction and also plays a role in flame stabilization.

- During stable combustion, the chain-branching radical OH is generated and transported around the reactor in the recirculation zone where it eventually interacts with the incoming jet and initiates combustion.

- As the equivalence ratio is decreased, and blowout becomes imminent, the OH production in the shear region is diffused toward the 'eye' of the reactor instead of the recirculation region. Now, there is a reduced concentration of OH radical that is recirculating around the reactor and interacting with the incoming jet. This effectively causes the reactor to blow out.

- In terms of temperature, the reactor is quite homogeneous at high equivalence ratios, but does experience significant inhomogeneity as it approaches blowout. The reacting volume (and effectively residence time) decreases to a point that cannot sustain combustion. This volume prediction, based on the volume of sufficient OH reaction rate, is similar for the PSR and CFD models.

- The difference in blowout for a highly aliphatic fuel (represented by iso-octane) and a highly aromatic fuel (represented by toluene) can be attributed to the rate at which the fuel is destroyed by radical species. Toluene is destroyed at a slower rate, and ultimately has a lower resistance to extinction (it blows out at a higher temperature and larger volume).

The CFD model helps to understand the mechanism of flame stabilization in the reactor. However, the model could be improved to better match the experimental blowout conditions by expanding the reactor domain to include the alumina solid. The expanded domain would enable a more realistic treatment of heat loss. Currently the model assumes a uniform heat flux out of the reactor wall, but the improved model would be more realistic by calculating any spatial variation in heat loss. This non-uniform heat flux will certainly affect the temperature and species fields inside the reactor, which will likely change the blowout prediction. Essentially, improved heat loss modeling should improve the ability of the model to match the experimental data.

A second item worthy of future effort focuses on a direct comparison of the phenomena at play inside the TSR and JSR that is only possible with this type of detailed modeling. These types of reactor comparisons could lead to correlations that would allow behavior from one reactor to be ‘translated’ to the other and compared.

Chapter 5
Effects of Fuel Composition on NO_X Emissions

The last portion of this work focuses on Objective 3 in Table 1.5 from Section 1.4.1. Specifically, experiments and modeling seek to understand the effects of fuel feedstock, composition, and aromatic content on NO_X behavior in the jet stirred reactor. As mentioned before, the stirred reactor is used as an idealization of the primary zone of a gas turbine combustor. The complete experimental results are available in Appendix B.

5.1 Experimental Methods

The Jet Stirred Reactor (JSR) is used for the NO_X studies. A system schematic is shown in Figure 5.1 with each of the subsystems highlighted and discussed below in further detail.

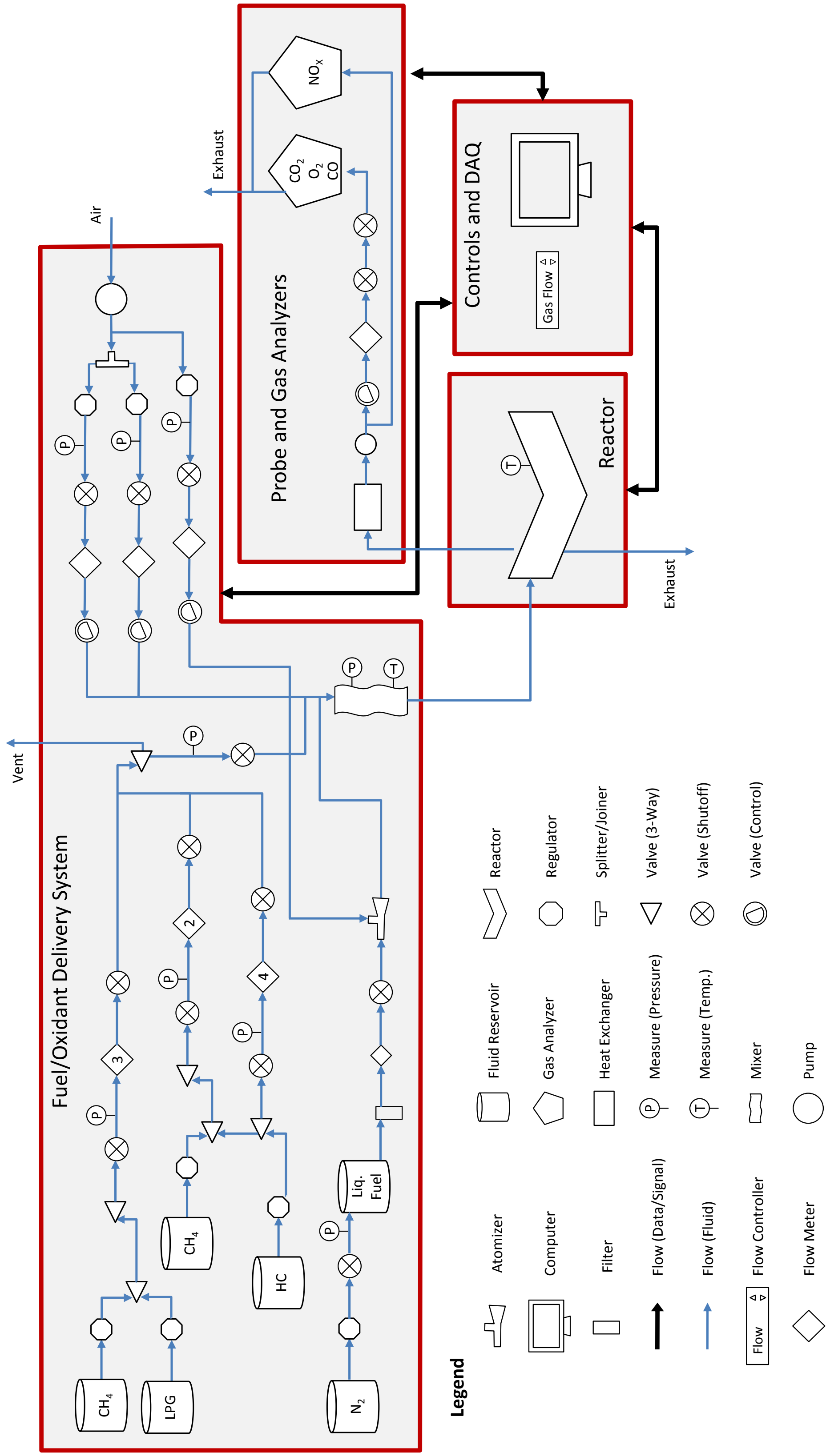

Figure 5.1: JSR system schematic

5.1.1 System Description

The JSR is a single-jet stirred reactor in the shape of a truncated cone. It was designed and fabricated by Lee [24]. The reactor walls are cast from aluminum oxide (Al_2O_3, alumina) ceramic material. The reactor solid model assembly (section view) is shown in Figure 5.2. The most important dimensions of the JSR are shown in Figure 5.3. The reactor volume is 15.8 cm^3. Full dimensional drawings are available in the work of Lee [24].

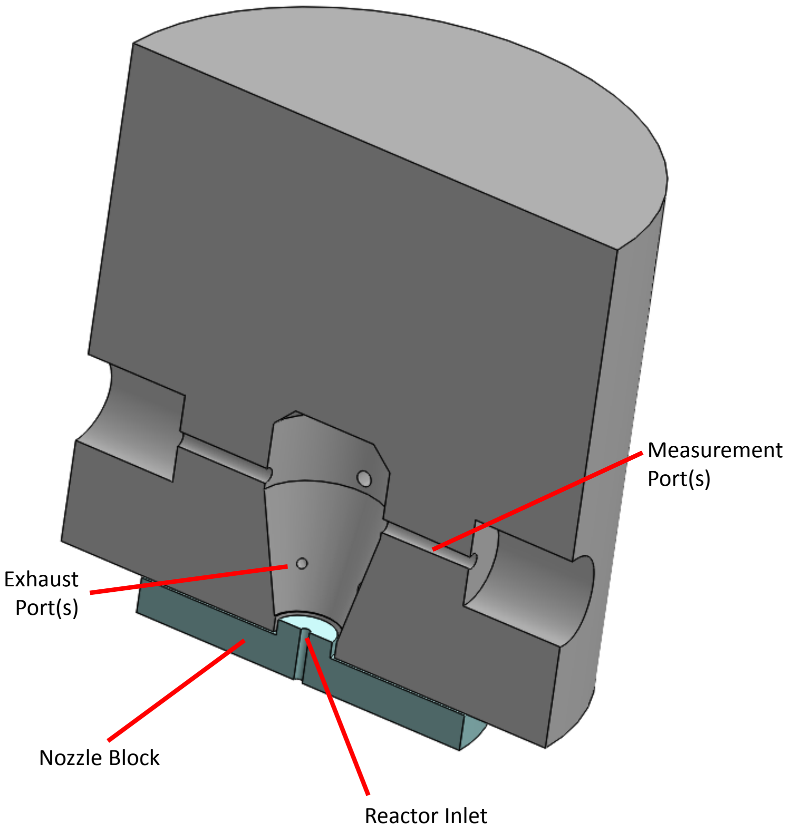

Figure 5.2: JSR solid model (section view at mid-plane)

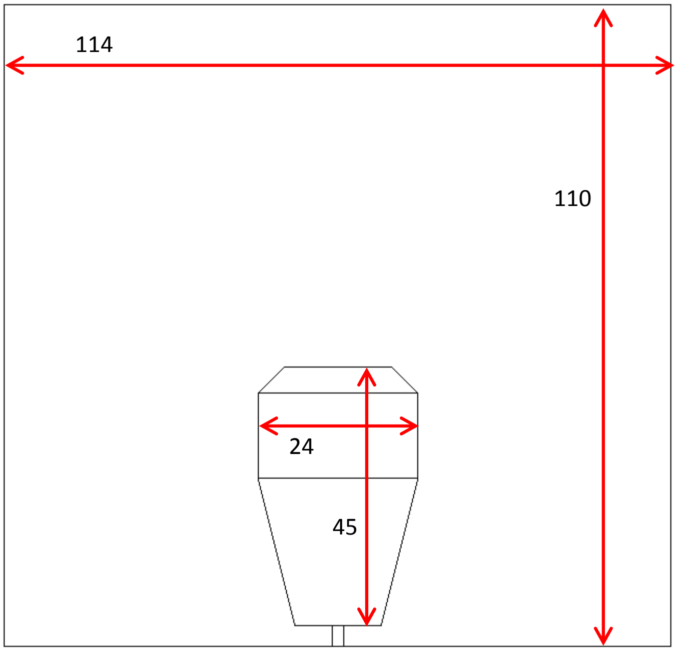

Figure 5.3: Important JSR dimensions (in millimeters)

The premixed fuel and oxidant (henceforth called 'premix') enter the reactor via the Inconel™ nozzle block through a single 2 mm (0.079 in) diameter jet. There are a total of four measurement access ports in the reactor as shown in Figure 5.2, but two are closed during testing. The two remaining measurement ports are used for a Type R thermocouple and for the gas sampling probe. There are four reactor exit exhaust ports, but only one can be seen from the view shown in Figure 5.2.

Unlike the TSR, the flow path in this reactor is reasonably two-dimensional (2D) as shown in the cross-sectional view of Figure 5.4. In the cross-section, the premix enters and is ignited by the entrainment of the recirculating flow. The flow exits through the exhaust ports. This view also shows the location of the Type R thermocouple used to measure temperature inside the reactor at 10 mm from the center of the reactor (which is roughly 2 mm from the wall) at 2/3 of the reactor height. The thermocouple bead is coated with ceramic to prevent exothermic catalytic surface reactions.

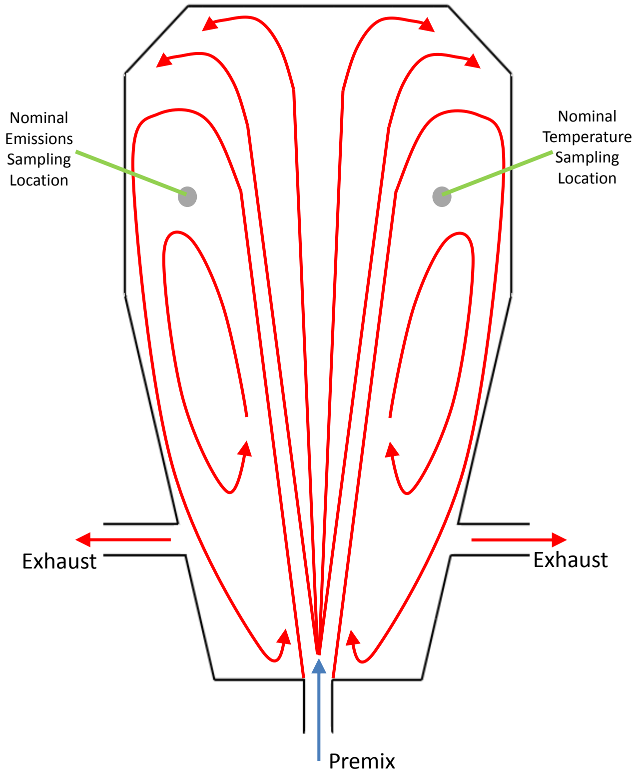

Figure 5.4: JSR cross-section with generic flow paths

Table 5.1: JSR characteristics

	JSR
Volume [cm^3]	15.8
Reactor Material	Alumina
Nozzle Block Material	Inconel™
Jet Diameter [mm]	2.0
Number of Jets	1
Surface Area to Volume Ratio [1/cm]	2.4
Reactor Mass (kg)	4.4

The remainder of the system provides fuel/air delivery, sampling, controls/data acquisition, and procedures.

The TSR system mixed fuels 'on the fly'. The JSR system has one liquid fuel delivery system, so the blends are manually mixed before testing. The method for determining the blended fuel properties is described in Appendix A. The fuel is stored in a reservoir of roughly 800 mL that is pressurized to 60 psig with nitrogen. The pressurized reservoir replaces the need for a pump. The fuel first passes through a 15μm filter (Swagelok Part No. SS-4F-15) before passing through the fuel rotameter and metering valve which are the same as those used by Lee [86]. The liquid fuel enters the atomizer and finally the staged prevaporizer premixer (SPP), which are both described below.

Simultaneously, air is delivered to the system from facility services compressed air in three separate streams through the same system used by Lee [86]. The first stream is unheated and delivered at 40 psig for use in the atomizer. The flow rate is approximately 4.5 SLPM through the rotameter.

The atomizer was originally designed by Lee [24], and then used and described by Edmonds [87] and Lee [86]. It is a Nukiyama/Tanasawa type plain jet airblast atomizer described in detail in the work of Lefebvre [88]. According to Lee *et al.* [49] and Lee [86] the Sauter mean diameter (SMD) is approximately 10 to 20μm which should allow the fuel droplets to vaporize in less than 10 ms. The atomized fuel and air mixture enters the first stage of the SPP.

The second and third air streams are unheated and delivered at 30 psig through rotameters for use in the SPP. The SPP was designed by Lee [24] as a means of reducing NO_X emissions, and then used and described by Edmonds [87] and Lee [86]. It is protected by US Patent US6174160 B1 [89]. The first stage air is heated and introduced just downstream of the atomizer at 30 SLPM and approximately 325^oC. The hot air in the first stage promotes fuel vaporization and has a residence time of approximately 9 ms. The second stage air is introduced just downstream of the first stage at roughly 25 SLPM and 325^oC. The hot air in the second stage completes fuel vaporization and has a residence time of approximately 8 ms. The last stage, which was not included in the original design, is a mixing tube that was implemented for gaseous fuel studies. The mixing tube has a residence time of approximately 5 ms. The premix temperature is approximately 350^oC (625K) as measured at the exit of the mixing tube which is just before the reactor inlet.

The gaseous emissions samples are extracted from the JSR using a warm water-cooled quartz probe that was also used by Fackler *et al.* [26] and Karalus *et al.* [27]. The probe has an orifice of roughly 0.03 inch (0.76 mm) diameter with a short (~1cm) uncooled portion at the tip. The sample is taken at roughly 2 mm from the wall (10 mm from the center) of the reactor. The samples are taken from reacting, non-equilibrium gases that contain a significant concentration of free radicals, so some reactions driven by radical recombination will continue inside the probe. The cooled probe aims to minimize these effects. The sample leaves the probe and is sent via heated lines to two quartz impingers in series that are housed in an ice-bath to remove the water vapor. The sample then passes into a multi-gas analyzer that measures CO, O_2, and CO_2 concentration. The CO and CO_2 analyzers are NDIR and the O_2 analyzer is paramagnetic (PM). In parallel, the sample passes through a chemiluminescent (CL) NO_X analyzer. Table 5.2 summarizes the JSR gas analyzer system.

Table 5.2: Summary of gas analyzer system for JSR

Emission	Method	Analyzer Make/Model	Zero Gas [Volume %]	Span Gas[1] [Volume %]
CO	NDIR	Horiba VA-3000	100% N_2	1.512% CO 7.195% CO_2
CO_2				
O_2	PM			Air
NO_X	CL	Thermo Electron 10		10.1 ppm NO_X

1. Balance N2

The JSR system is controlled manually. The first stage, second stage, and atomizing air flows are metered via rotameters and control valves. The liquid fuel flow rate is also metered via a rotameter and control valve. A Personal DaqView [90] data acquisition (DAq) system is used to monitor all temperatures and emissions every three seconds. The air and fuel flow rates are periodically manually recorded, which means that the inlet equivalence ratio was only determined occasionally. This affects the data analysis methods discussed below.

Table 5.3 presents the primary quantities measured that are used in the data analysis presented in Section 5.1.2.

Table 5.3: Important recorded experimental quantities for NO_X tests

Description		Symbol	Units	Used For:
Flow Rates	Liquid Fuel	$\dot{\forall}_{LF}$	mL/min	Inlet Equivalence Ratio, ϕ_{in} Residence Time, τ
	Air	$\dot{\forall}_{A}$	SLPM	
Temperatures	Premix	T_{premix}	°C	Product Temperature, $T_{product}$
	Reactor	$T_{reactor}$	°C	
Emissions	CO	-	[%V dry]	Exhaust Equivalence Ratio, $\phi_{exhaust}$ NO_X Emissions/Rates
	CO_2	-	[%V dry]	
	O_2	-	[%V dry]	
	NO_X	-	[ppm]	

Testing begins by heating the reactor with a gaseous fuel until all temperatures reach steady state. During this time the gas analyzers are calibrated. After reaching steady state, the reactor is slowly switched to the liquid test fuel. Once the reactor is running on a liquid fuel, the flow rate is adjusted to reach a nominal corrected temperature of 1900K. The reactor is allowed to rest at this condition for roughly 25 minutes. After that time, the fuel flow rate is decreased to reach a new nominal temperature (first 1850K and then 1800K). Data are automatically recorded by the DAq every three seconds.

A summary of the experimental conditions for the NO_X tests is provided in Table 5.4. The flow rates used here in conjunction with the reactor/nozzle block dimensions are based on the conditions suggested by Fackler [25] and Karalus [28] to produce sonic velocities for the jet and to ensure turbulent mixing is present throughout the reactor.

Table 5.4: Nominal values of experimental conditions for liquid fuel NO_X tests

Parameter	Nominal Value			Units
Product Temperature[1]	1900	1850	1800	K
Reactor Pressure	1			atm
Premix Temperature	625			K
Air Flow Rate	1.16			g/s
Fuel Flow Rate	0.053	0.049	0.045	g/s
Equivalence Ratio[2]	0.71	0.67	0.64	-
Residence Time[2]	2.43	2.52	2.60	ms

1. Corrected temperature as described in Appendix C
2. Calculated as presented in Section 5.1.2

5.1.2 Data Analysis and Reduction

The NO_X data are characterized by the corrected temperature, equivalence ratio, concentration, and rate of production. Appendix D presents the details of the analysis, but these parameters are briefly mentioned here.

The first step in data analysis is the temperature correction for thermocouple heat loss, which is described in Appendix C. Equation 5.1 provides the temperature correction correlation.

5.1 $$T_{\text{corrected}} = 1.0621T_{\text{measured}} - 66.55 \qquad \text{K}$$

The inlet equivalence ratio is only calculated occasionally (because of the manual flow control/recording), so the outlet exhaust measurements are used to characterize the conditions at every data point. The equivalence ratio based on both the measured fuel and air flow rates and on the exhaust composition match closely (approximately 5% difference). The calculated equivalence ratio is extremely sensitive to the fuel properties and calibration curves. The sensitivity to fuel properties is discussed in Appendix A. The exhaust equivalence ratio is discussed in detail in Appendix D, but is given here as Equations 5.2 and 5.3, where χ is the moles of fuel and α is the moles of air as determined from the measured emissions.

5.2 $$\left.\frac{\dot{m}_F}{\dot{m}_A}\right|_{\text{exhaust}} = \frac{\chi MW_{\text{fuel}}}{4.76\alpha MW_{\text{air}}} \qquad -$$

5.3 $$\phi_{\text{exhaust}} = \frac{\dot{m}_F/\dot{m}_A|_{\text{exhaust}}}{\dot{m}_F/\dot{m}_A|_{\text{stoich}}} \qquad -$$

In general, the NO_X values presented below are shown as directly measured in parts per million (ppm) on a dry volume basis with the actual O_2 concentration in the exhaust. However, NO_X concentration is sometimes presented on a wet volume basis and/or with a standardized 15% exhaust O_2 concentration. These unit bases are calculated as described in Appendix D based on the exhaust emissions that were measured directly.

The NO_X rate of production (ROP) is calculated from the NO_X emissions and the reactor residence time, τ (Equations 5.4 and 5.5). It can be determined for any of the unit bases previously mentioned (dry/wet and actual/15% O_2).

5.4 $$NO_X\ ROP = \frac{NO_X[\text{ppm, dry/wet, actual/15\% } O_2]}{\tau\ [\text{ms}]} \qquad \text{ppm/ms}$$

5.5 $$\tau = \frac{\rho \forall}{\dot{m}} \qquad \text{ms}$$

To illustrate the data analysis process, we use a single fuel (JP8) as an example. First, Figure 5.5 shows the exhaust equivalence ratio, temperature, and NO_X emissions versus time. As mentioned previously the fuel rotameter was first set to a value that resulted in a temperature of approximately 1900K. However, the fuel flow oscillated consistently a small amount over a roughly five minute period. This oscillation in the fuel flow rate resulted in synced oscillations in the equivalence ratio, temperature, and NO_X emissions. These variations resulted in data bands as shown in Figure 5.6 for NO_X versus temperature. The data bands present the fortunate opportunity to obtain an expression for NO_X production as a function of temperature for each fuel.

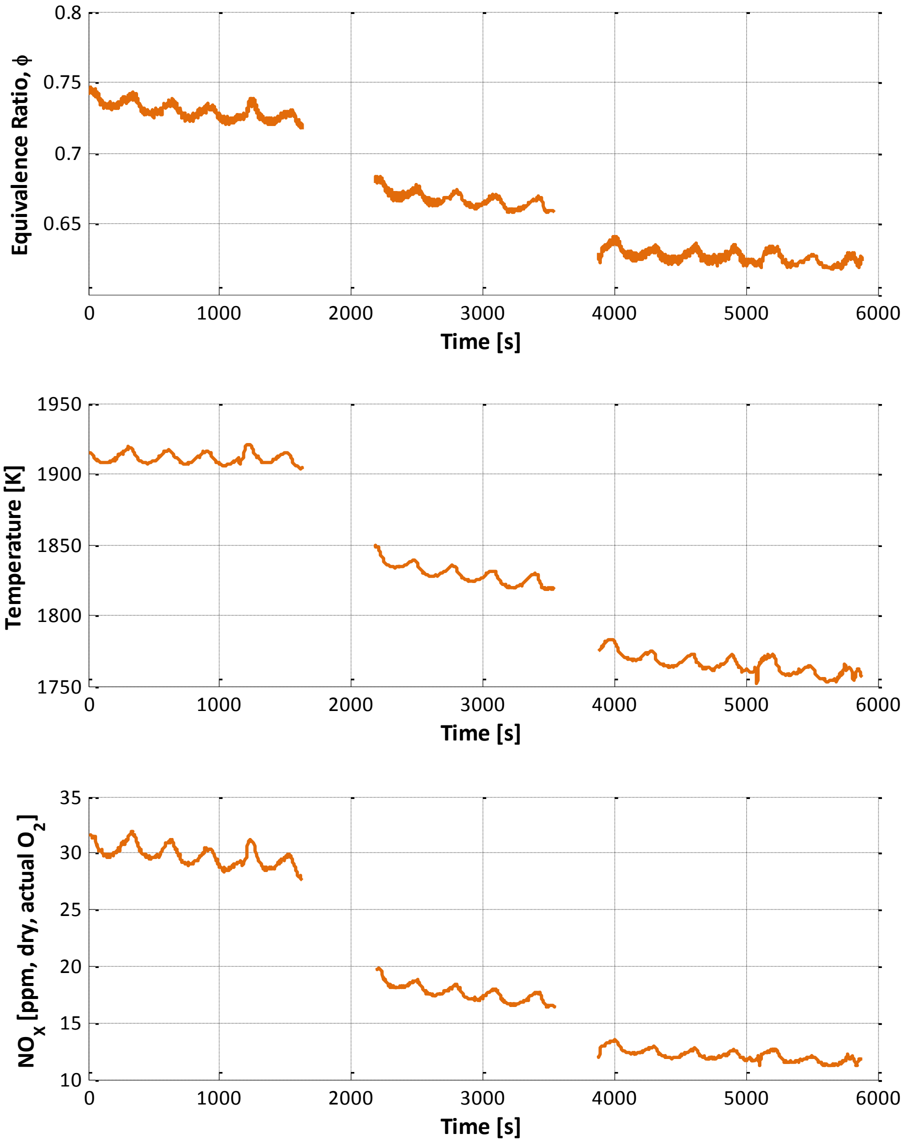

Figure 5.5: ϕ, T, and NO$_X$ versus time for JP8

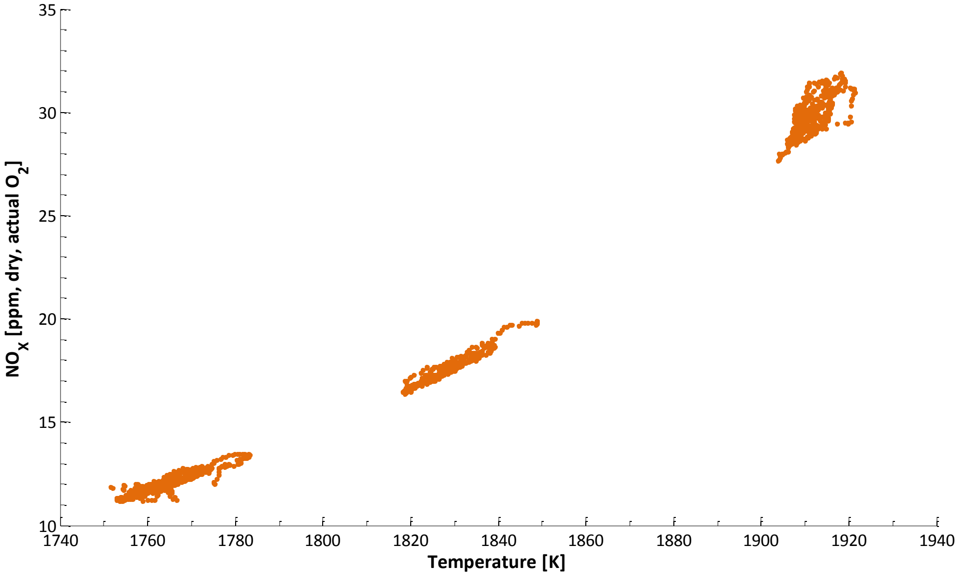

Figure 5.6: NO_X versus T for JP8

The data appear to follow the expected exponential, Arrhenius relationship between temperature and NO_X emissions. This relationship is at the crux of this investigation, so the data from each fuel are analyzed to determine these correlations. Figure 5.7 shows the results for JP8 as an example of NO_X emissions (ppm, dry, actual O_2) versus the inverse of the absolute temperature (K^{-1}). Notice that on a semi-log scale, the emissions fall on a straight line. The 'curve fit' for this data set results in the exponential, Arrhenius relationship between NO_X emissions and temperature (Equation 5.6).

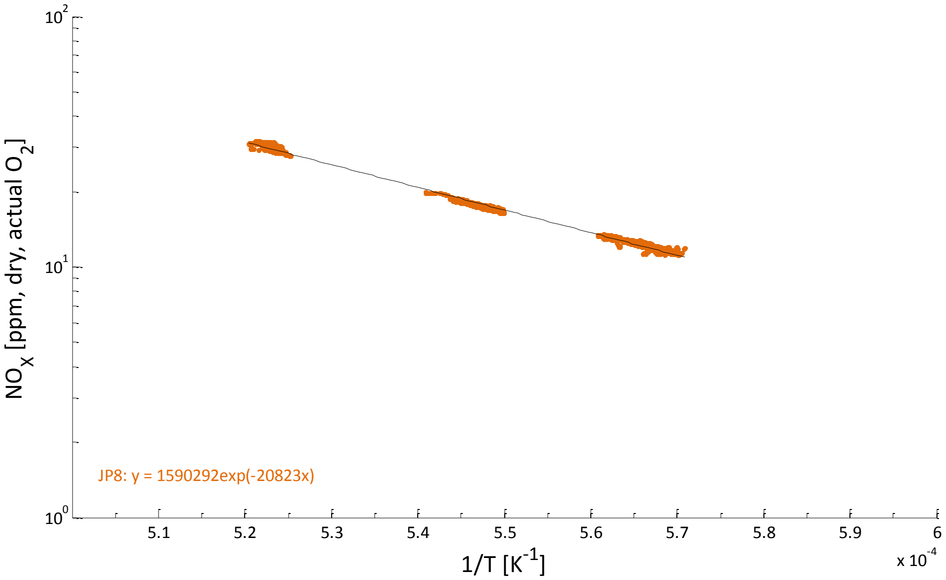

Figure 5.7: NO_X concentration vs. 1/T for JP8

5.6 $$NO_X[\text{ppm, dry, actual } O_2] = 1590292\exp\left(\frac{-20823}{T\ [K]}\right)$$ JP8

Similar relationships are determined for each of the fuel/fuel blends with the various unit bases. Table 5.5 shows the correlation coefficients for NO_X emissions (ppm, dry, actual O_2) as a function of temperature (K). Appendix B contains all the correlation coefficients for NO_X emissions and NO_X production rates in the four unit basis combinations (dry/wet and actual/15% O_2). These relationships enable direct comparisons of NO_X emissions, temperature, and fuel.

Table 5.5: NO_X concentration curve fit coefficients [ppm, dry, actual O_2]

Fuel	**Aromatic**	**$NO_X = A\exp\left(B/T\right)$**		**Experimental Range**
		A	**B**	
		[ppm, dry, actual O_2]	**[K]**	**[K]**
JP8	18.7% Natural	1590292	-20823	1750-1920
FT Natural Gas	0% Natural	2451997	-21837	1770-1900
	20% Pet-Aromatic	582109	-19238	1780-1900
FT Coal	0% Natural	2225160	-21542	1750-1900
	20% Pet-Aromatic	1312136	-20803	1780-1910
HP Camelina	0% Natural	3106551	-22083	1790-1900
	20% Pet-Aromatic	1480137	-20743	1780-1900
HP Tallow	0% Natural	2141829	-21717	1790-1915
	20% Pet-Aromatic	2548759	-21812	1770-1890
Pet-Aromatic	100% Natural	781508	-19568	1780-1900
135-TMB	100% Natural	2856655	-21738	1790-1910

The results sections below will utilize these raw data and the NO_X/temperature correlations to look at fuel-based differences in NO_X.

5.2 Experimental Results

5.2.1 Unmodified Fuels

Figure 5.8 presents the complete NO_X data set for the unmodified fuels versus temperature. However, the data in this view leave the trends difficult to discern. The unmodified fuels are JP8, Pet-Aromatic, 135-TMB, and the four synthetic fuels without any additive.

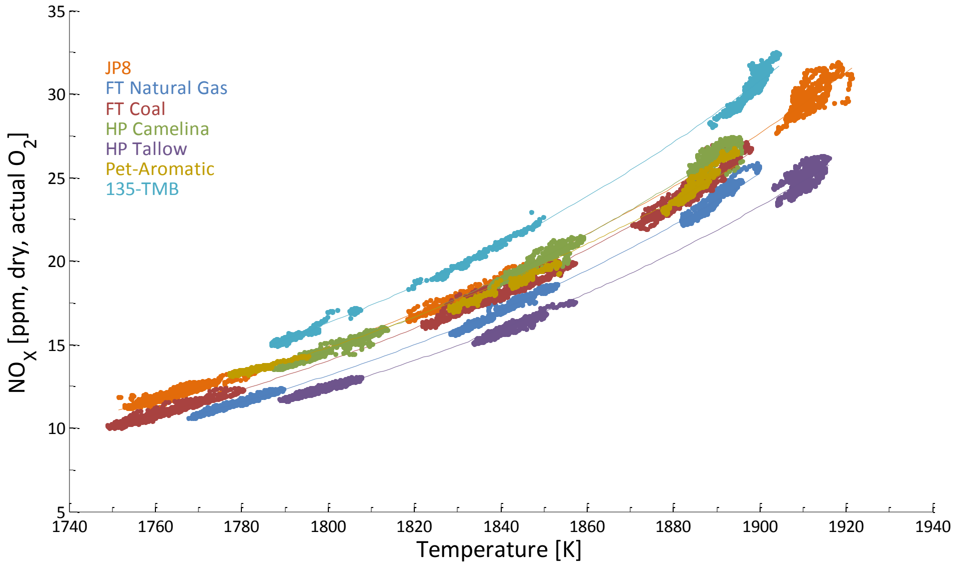

Figure 5.8: NOx vs. temperature for unmodified fuels

The correlations from Table 5.5 are used to determine the NOx emissions at a given temperature. Figure 5.9 shows the results for 1900K, Figure 5.10 shows the results for 1850K, and Figure 5.11 shows the results for 1800K. In general, the 135-TMB forms the most NOx. The three fuels with aromatics are in the same order in each case (135-TMB > JP8 > Pet-Aromatic).

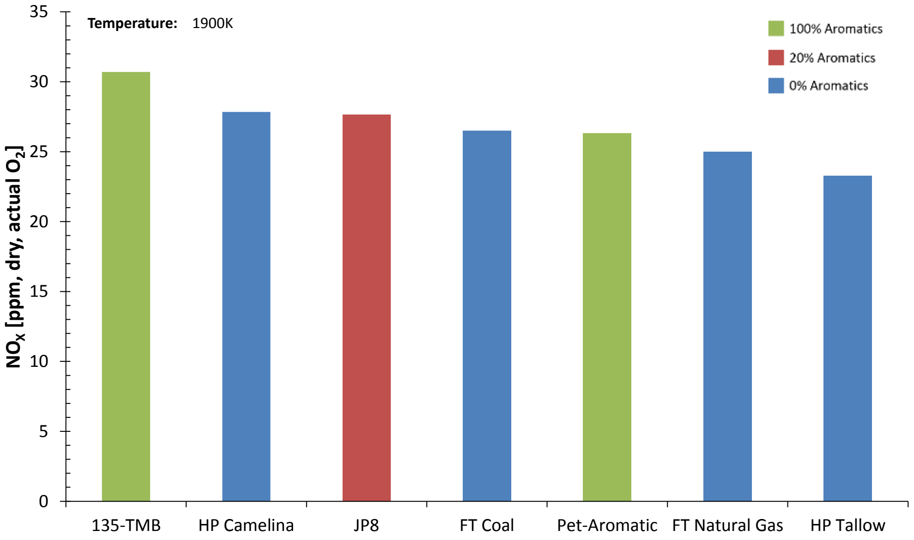

Figure 5.9: NOx for each unmodified fuel at 1900K

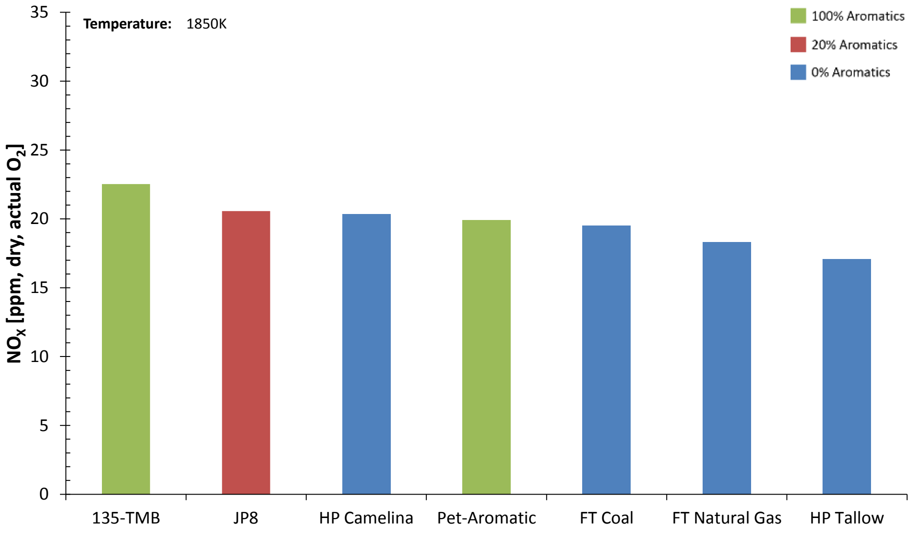

Figure 5.10: NO_X for each unmodified fuel at 1850K

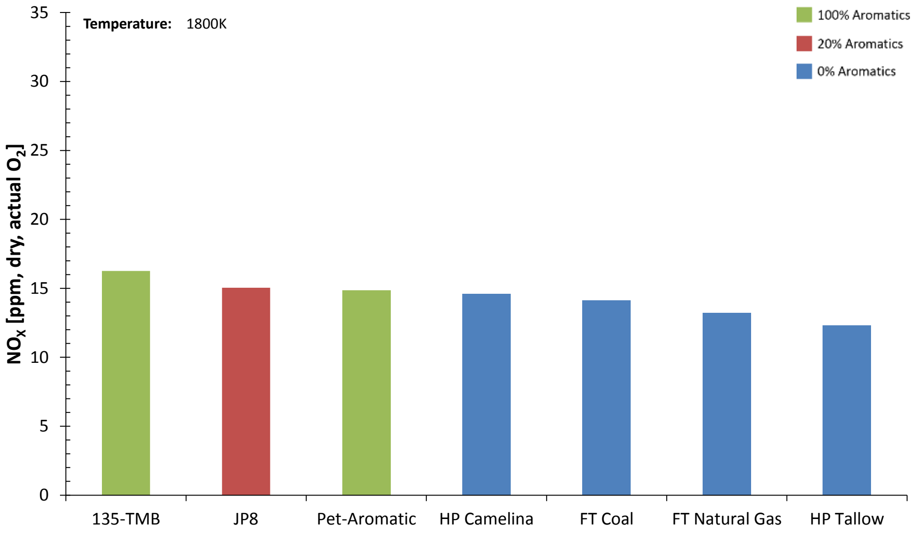

Figure 5.11: NO_X for each unmodified fuel at 1800K

The plots above are reconfigured (Figure 5.12) to look at the four synthetic jet fuels at 1900K, 1850K, and 1800K. Notice, these are in the same order in each case (HP Camelina > FT Coal

> FT Natural Gas > HP Tallow). Focusing on these synthetic fuels, the NOx emissions can then be compared to the fuel component concentrations presented in Chapter 2 and Appendix A. There was only one comparison that showed a discernable trend (Figure 5.13), which shows that NOx emissions appear to increase with cycloalkane concentration in the fuel. Blust *et al.* [16,17] found that cycloalkanes and aromatic HCs produce more NOx than aliphatic HCs. Note, the cycloalkane concentration in these fuels is very small (less than 3.0% by weight), so their effect is difficult to determine. Kinetic models with cycloalkanes are included below, but future experimental studies with surrogate fuels should help to understand their effects.

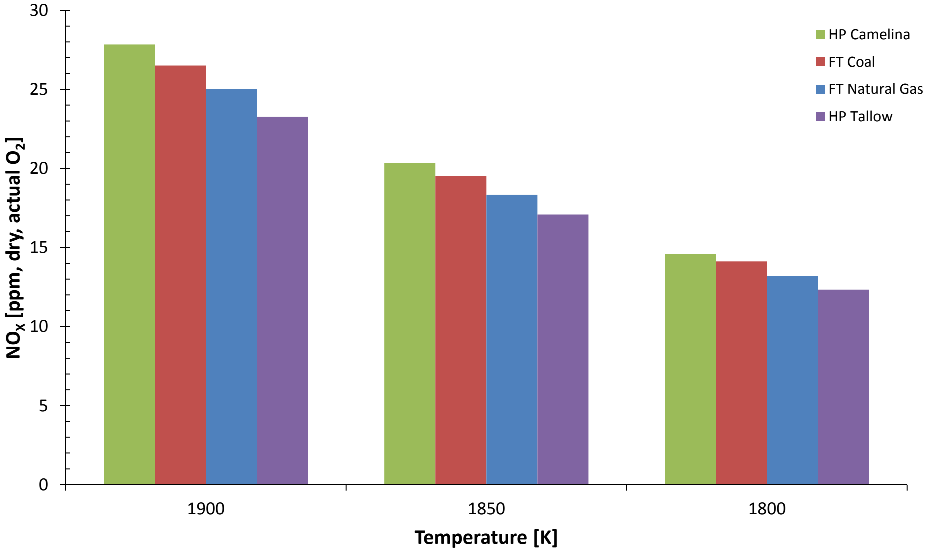

Figure 5.12: NOx for unmodified synthetic fuels

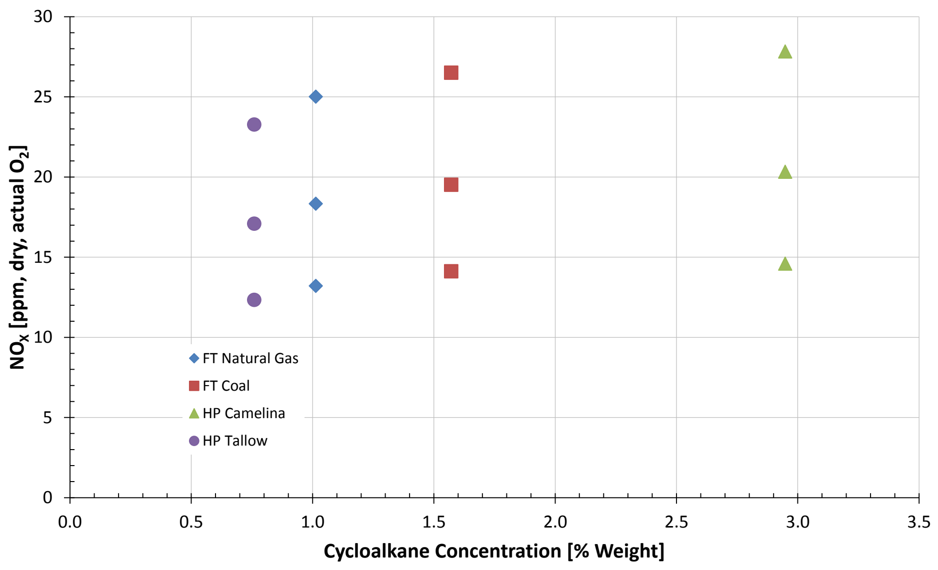

Figure 5.13: NO_X vs. cycloalkane concentration for unmodified synthetic fuels

5.2.2 Synthetic Fuels Blended with 20% Pet-Aromatic

The Pet-Aromatic fuel was blended into the four synthetic jet fuels and tested for NO_X emissions. Figure 5.14 shows the raw data, which is so plentiful that trends are difficult to discern.

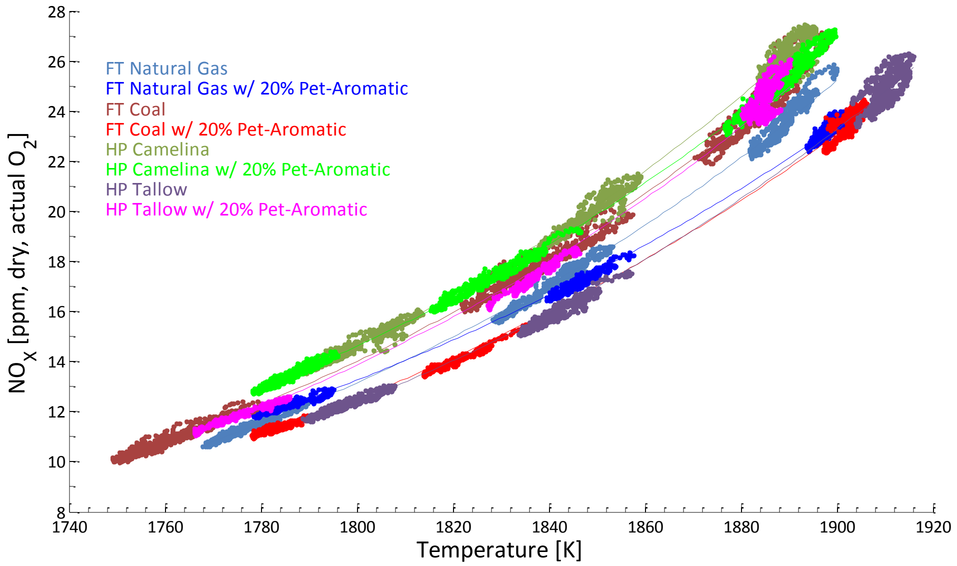

Figure 5.14: NO_X vs. T for synthetic fuels and blends with 20% Pet-Aromatic

The NO_X-temperature correlations from Table 5.5 determine unique values of NO_X emissions for each fuel at any temperature for direct comparison. Figure 5.15 shows the results for 1900K, Figure 5.16 shows the results for 1850K, and Figure 5.17 shows the results for 1800K. In general, combustion fueled by 135-TMB and JP8 forms the most NO_X. The Pet-Aromatic fuel appears to have an inconsistent trend when compared to the synthetic fuel blends. Notice, however that Figure 5.18 shows that the four synthetic fuels with Pet-Aromatic are always in the same order (HP Camelina > HP Tallow > FT Natural Gas > FT Coal). This ordering is different from the unmodified fuels presented above which indicates that the Pet-Aromatic fuel causes NO_X emissions to increase or decrease with different fuels.

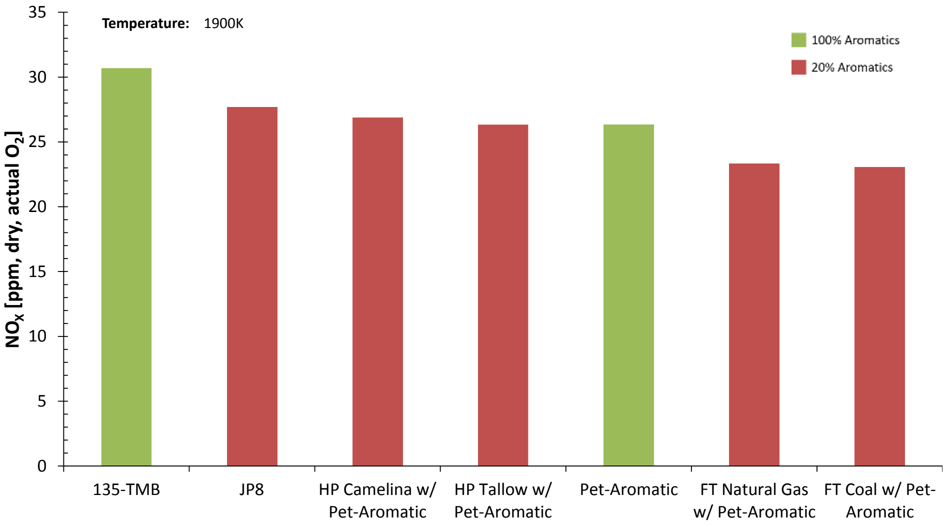

Figure 5.15: NO_X for all fuels with aromatic HCs at 1900K

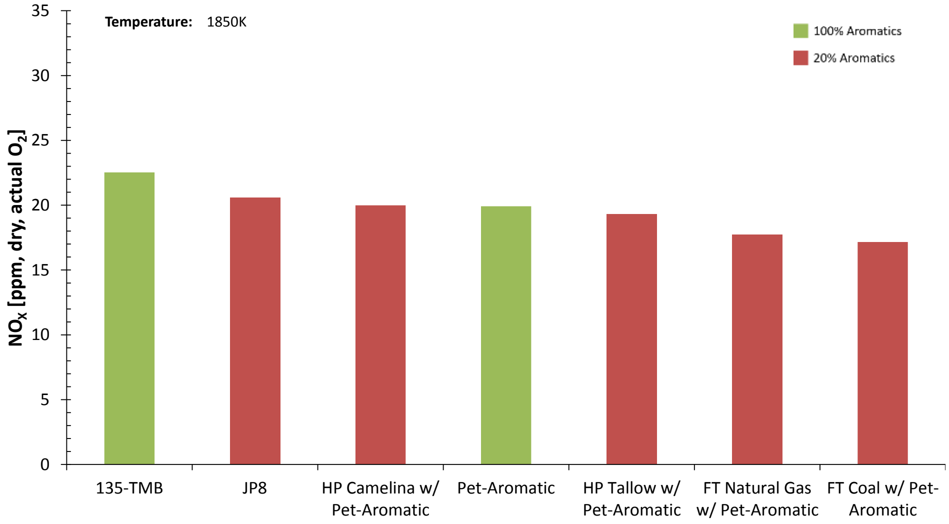

Figure 5.16: NO_X for all fuels with aromatic HCs at 1850K

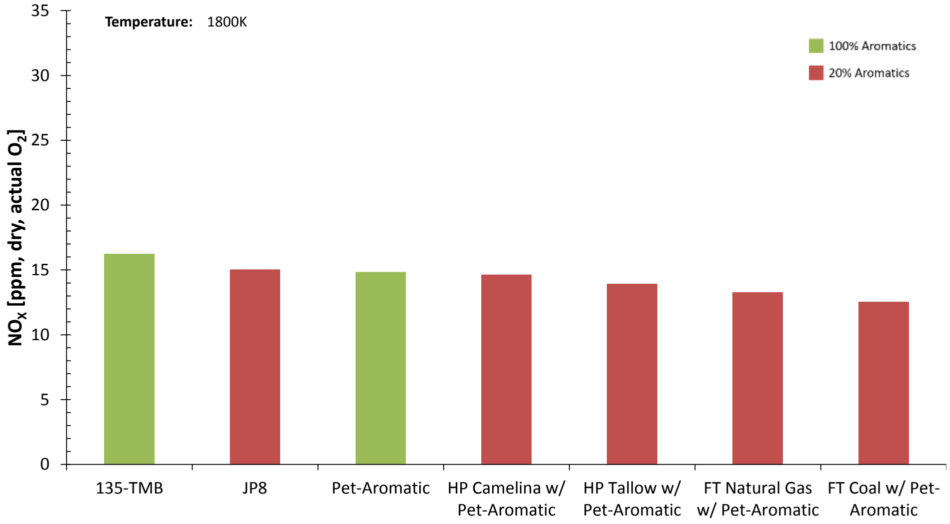

Figure 5.17: NO_X for all fuels with aromatic HCs at 1800K

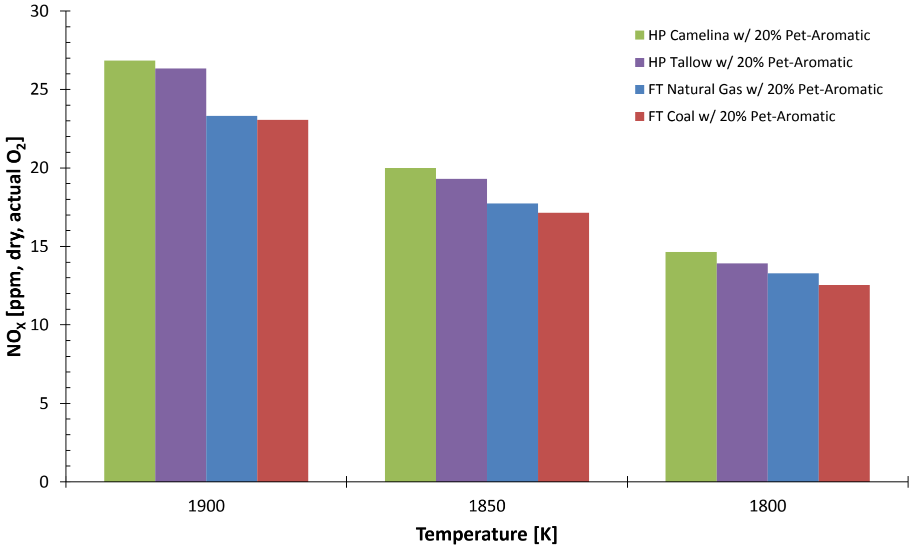

Figure 5.18: NOx for synthetic fuels blended with 20% Pet-Aromatic

Figure 5.19 presents the change in NOx emissions due to the Pet-Aromatic addition. In general, the NOx emissions increase for HP Tallow with 20% Pet-Aromatic and decrease for FT Coal with 20% Pet-Aromatic. The NOx emissions for the other two fuel blends (FT Natural Gas and HP Camelina) decrease at 1900K and 1850K, but increase slightly at 1800K.

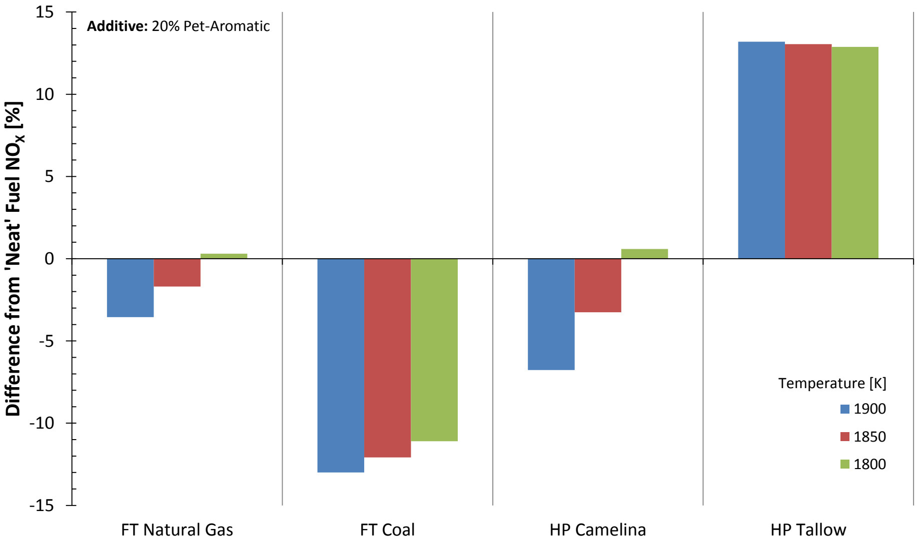

Figure 5.19: Change in NOx emissions with 20% blended Pet-Aromatic

The Pet-Aromatic fuel affects the NOx emissions from the four synthetic fuels. However, the fuel compositions are so complex that it is impractical to attribute the behavior to a single fuel-specific reason. Sections 5.3 and 5.4 use kinetic models with surrogate fuels to attempt to explain these trends.

5.2.3 Comparison to Previous Work

Lee *et al.* [49] showed that NOx emissions increase with fuel carbon to hydrogen (C/H) ratio (Figure 5.20). They also found that the aromatic fuels (toluene and benzene) do not follow the same linear trend.

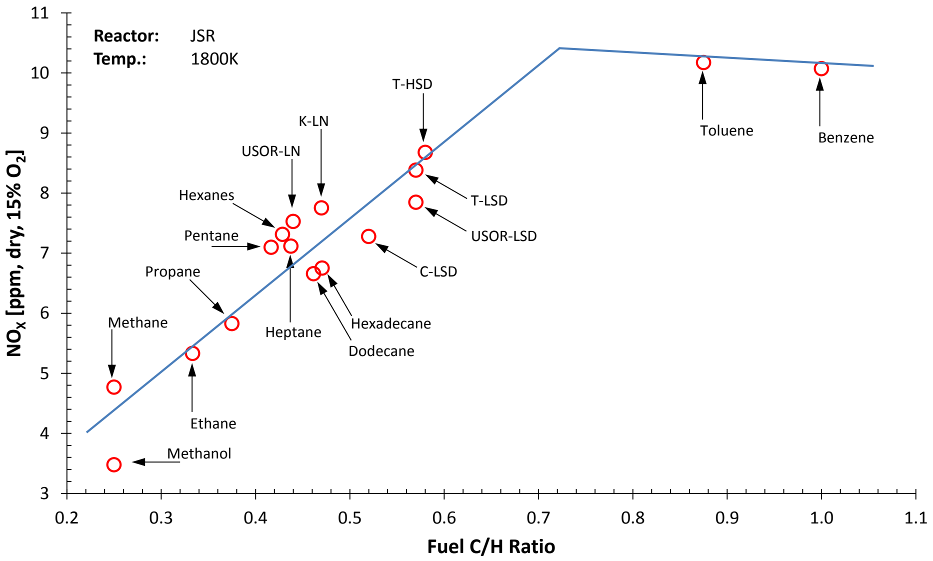

Figure 5.20: NOx emissions vs. fuel C/H ratio from Lee *et al.* [49]

Figure 5.21 shows the NOx emissions for the fuels in the current study as compared to Lee *et al.* [49]. The synthetic fuels without any aromatic additive have a relatively low C/H ratio (~0.46) and a range of NOx emissions. JP8 and the synthetic fuels with 20% Pet-Aromatic blend have a slightly higher C/H ratio (~0.51). The two aromatic fuels have higher C/H ratios (~0.76).

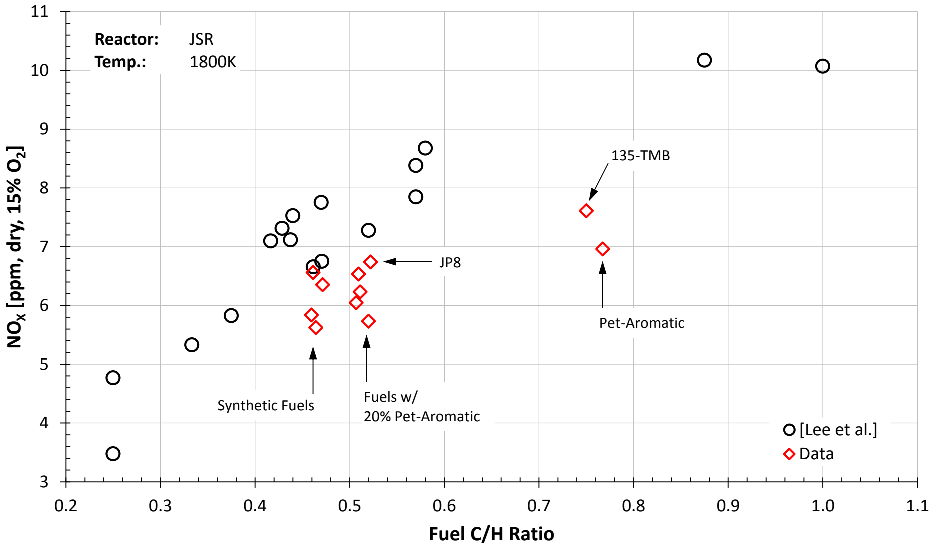

Figure 5.21: NO$_X$ emissions vs. fuel C/H ratio compared to Lee *et al.* [49]

The current data agree reasonably well for the fuels with C/H ratio near 0.5. However, the aromatic fuels with high C/H ratio appear to be well below the data of Lee *et al.* [49] for toluene and benzene. On the surface, this variation may seem to be inconsistent, but in reality, these fuels are very different in chemical structure. The fuel composition data from Chapter 2 show that the Pet-Aromatic fuel contains no benzene or toluene. The Pet-Aromatic fuel consists mostly (~75%) of C_3-C_5 benzene derivatives, which make the fuel much more like 135-TMB than toluene or benzene. The additional groups substituted onto the benzene ring take many forms, and the manner in which the fuel molecule decomposes during reaction will alter the radical pool and ultimately the NO$_X$ formation. The modeling effort of Sections 5.3 and 5.4 investigates this phenomenon.

The TSR system at Wright Patterson Air Force Base was used in a separate study on NO$_X$ emissions from JP8 and FT Natural Gas. Ballal [20] presented a low-temperature NO$_X$ study (Figure 5.22), which agrees well with the data from the current effort even though the temperatures are slightly out of the experimental range of the temperature correlations.

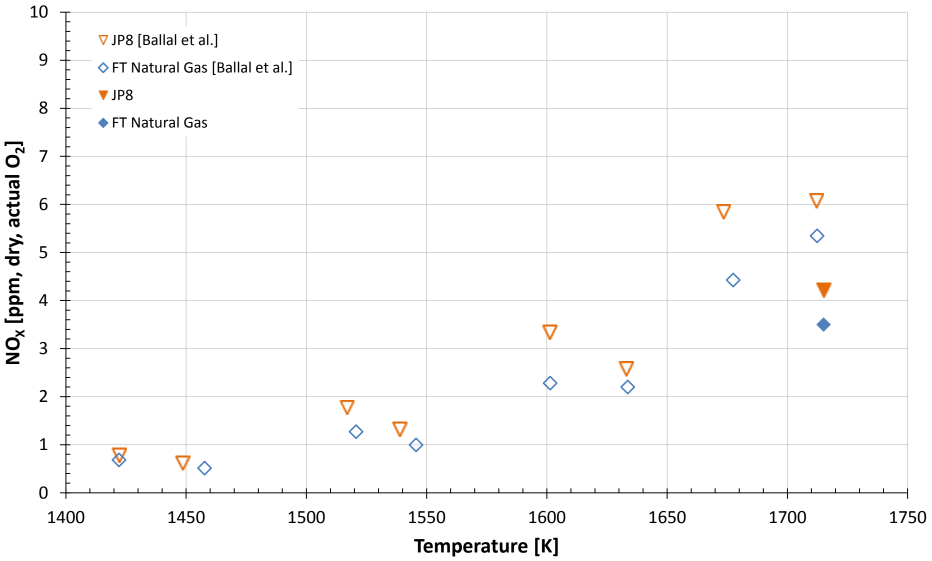

Figure 5.22: NOx emissions vs. temperature with Ballal *et al.* [20]

Not surprisingly, NOx emissions are affected by fuel composition. These real, complex fuels include hundreds of chemical constituents making it impractical to attempt to attribute NOx behavior to a single fuel compound or class of compounds. As an alternative, modeling analysis utilizes single fuel 'surrogate' components to investigate the chemical kinetic pathways that give rise to differences in NOx production.

5.3 Modeling Methods

A single PSR model is used as the tool to understand the chemical kinetic pathways that give rise to the differing amounts of NOx produced by the various fuels. The PSR model does represent something of a compromise in the present application. The advantage is that the model can easily accommodate the very large published chemical kinetic mechanisms that are used to simulate fuel behavior. Such mechanisms contain the order of one thousand species and several thousand chemical reactions. These mechanisms cannot realistically be run in advanced models, but can be easily used in PSR models. The disadvantage is that the PSR model does not resolve the reacting structure in the combustor. We feel that the chemistry responsible for the differences between the fuels will be essentially the same in both the actual reactor and the PSR model. Thus, the PSR model should be able to highlight the differences in fuel chemistry without needing to fully replicate the reactor structure or compromise the detailed chemical kinetic mechanisms. The model used in this kinetic interpretation is similar to the one described in Section 4.3.1. The PSR is implemented in CHEMKIN-PRO 15113 from Reaction Design [6].

Figure 5.23 shows a schematic of the PSR model. The model inputs are generally based on the experimental conditions of the JSR. The fuel of interest and air enter the reactor at a given premix temperature (625K). The total flow rate is 1.25 g/s. The equivalence ratio and temperature are fixed to isolate the fuel chemical effects. The reactor pressure is 1 atm. The reactor volume is 15.8 mL.

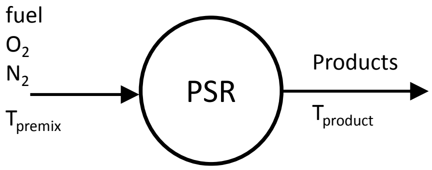

Figure 5.23: PSR schematic for fuel effects NO_X analysis

First, the PSR models will be used to identify any differences in NO_X behavior for the fuels of interest. Then, the NO_X production reactions will be analyzed to determine the reason for those differences.

The kinetic mechanisms for each study are discussed below, and the details for all of the mechanisms are presented in Appendix F. Published mechanisms were found for several jet fuel surrogates and modified to include NO_X formation by including the 27 unique reactions for NO_X formation from the GRI 3.0 mechanism (listed in Section 1.2.2) [4].

5.4 Modeling Results

5.4.1 Toluene and iso-Octane

The fuel comparison focuses on an aliphatic fuel and an aromatic fuel, specifically iso-octane and toluene. Dooley *et al.* [85] published a jet fuel mechanism that contains the kinetics for both iso-octane and toluene oxidation. The 27 unique NO_X reactions (presented in Section 1.2.2) from GRI 3.0 [4] are imported into the mechanism to include NO_X production behavior.

Figure 5.24 shows that toluene produces more NO than iso-octane at three temperature/equivalence ratio combinations (1900K/0.70, 1850K/0.68, 1800K/0.66). The production rates will help identify the reasons.

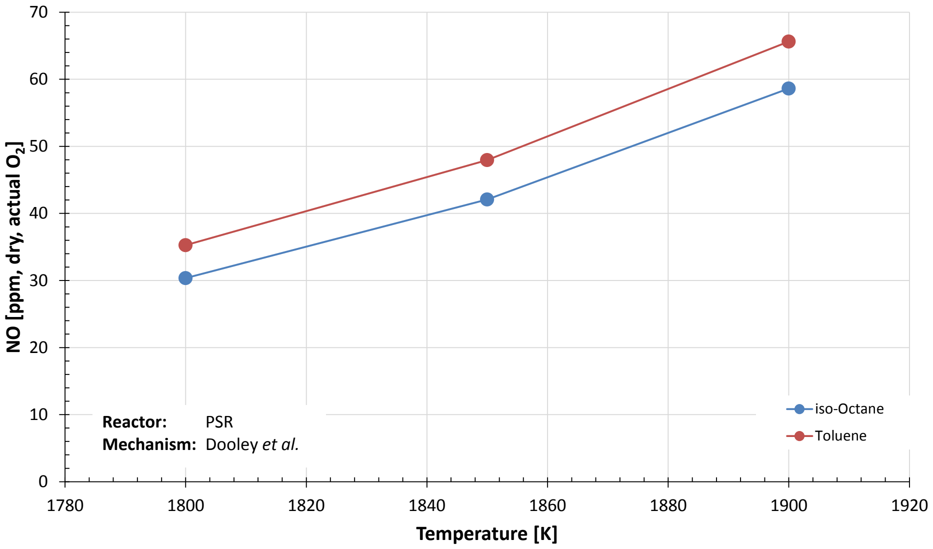

Figure 5.24: PSR NO_X emissions vs. temperature for iso-octane and toluene

Figure 5.25 shows the NO Rates of Production (ROP) for the 1900K/0.7 case by reaction. The increased NO_X from toluene appears to be due primarily to the four highlighted reactions (1, 2, 17, and 19). All four of these are driven by O radical, suggesting that the toluene flame has a higher concentration of O radical. Table 5.6 shows the concentrations of the major species for both fuels. Notice that iso-octane has more hydrogen (H_2) and water vapor (H_2O) which is expected as it has a higher H/C ratio. Notice that toluene has more O radical, but less H and OH radical. More importantly, notice that toluene shows approximately 16% higher NO concentration and 15% higher O radical concentration.

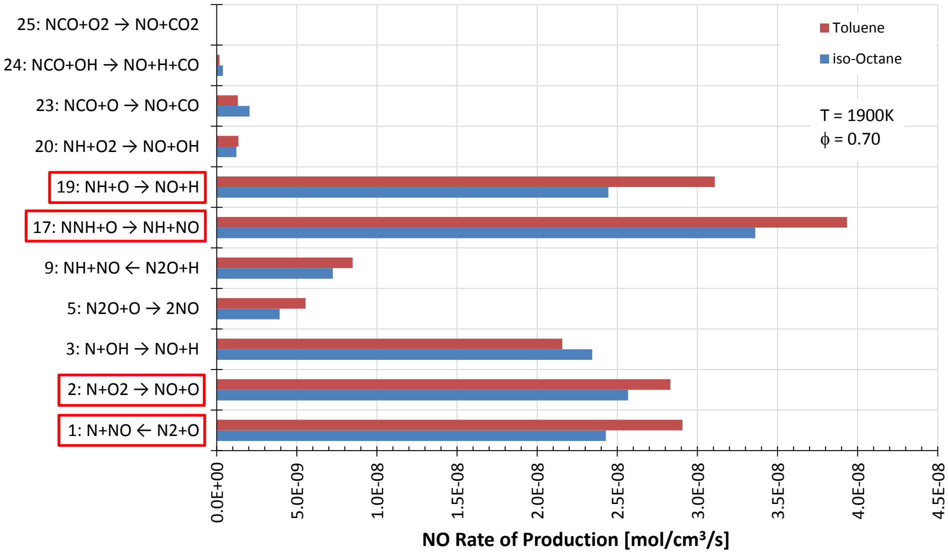

Figure 5.25: NO ROP (per reaction) for iso-octane and toluene

Table 5.6: Species mole fractions from PSR

Species	Toluene	iso-Octane
NO	6.18E-05	5.32E-05
N	3.6E-09	3.3E-09
N_2O	2.8E-07	2.3E-07
NH	4.9E-09	4.6E-09
NNH	3.56E-09	3.58E-09
HCN	7.3E-09	1.5E-08
NCO	3.6E-10	6.5E-10
O_2	6.5E-02	6.4E-02
N_2	7.6E-01	7.4E-01
CO	1.3E-02	9.2E-03
CO_2	9.6E-02	7.8E-02
H_2O	5.8E-02	9.3E-02
CH	9.7E-09	1.7E-08
H	1.59E-03	1.63E-03
H_2	1.6E-03	2.2E-03
O	3.8E-03	3.3E-03
OH	5.0E-03	5.9E-03
HO_2	4.9E-06	6.6E-06
CH_4	3.3E-08	5.1E-07
CH_3	4.3E-07	5.4E-06

1. T = 1900 K and ϕ = 0.70

The next question then asks why the toluene flame produces more O radical. Table 5.7 shows that iso-octane has a lower *net* production rate of O radical than toluene. Notice that the *gross* production rate of O radical for iso-octane is slightly greater than for toluene, but the iso-octane also consumes O radical at a greater rate than toluene. The result is that the net production of O radical is greater for toluene. This suggests that O radical consumption is the ultimate cause for its decreased concentration in the iso-octane flame.

Table 5.7: Concentrations and rates of O radical

		Toluene	**iso-Octane**
Concentration [mol frac.]		3.8E-03	3.3E-03
Rates [mol/cm^3/s]	**Production**	3.165E-04	3.273E-04
	Consumption	3.062E-04	3.183E-04
	Net	1.03E-05	9.00E-06

1. T = 1900 K and ϕ = 0.70

Figure 5.26 shows the O ROP for many reactions for iso-octane and toluene. One reaction (28: H + O_2 → OH + O) is primarily responsible for producing O radical, and this reaction is more active for iso-octane. However, the highlighted reaction (83: CH_3 + O → CH_2O + H) shows a significantly higher consumption of O radical for iso-octane flames. The temperature is constant, which means the rate coefficient is the same. The different rates can only be due to differences in CH_3 radical concentration between the two fuels. Table 5.8 shows much larger (by an order of magnitude) CH_3 radical concentration and net rates of production for the iso-octane flame.

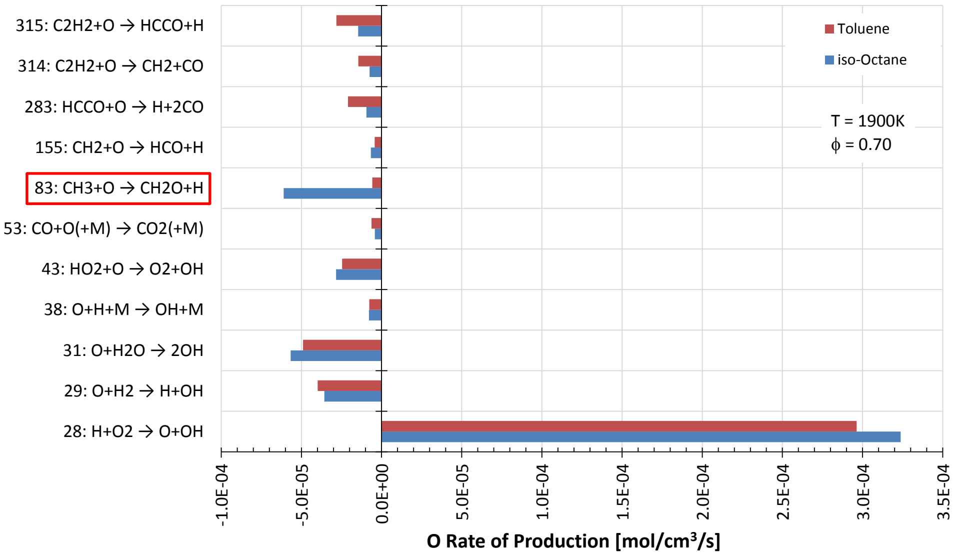

Figure 5.26: O ROP (per reaction) for iso-octane and toluene

Table 5.8: Concentrations and rates of CH_3 radical

		Toluene	iso-Octane
Concentration [mol frac.]		4.3E-07	5.4E-06
Rates [mol/cm^3/s]	**Production**	8.054E-06	1.0353E-04
	Consumption	8.053E-06	1.0352E-04
	Net	1.16E-09	1.48E-08

1. T = 1900 K and ϕ = 0.70

The largest CH_3 radical production reaction for iso-octane is the unimolecular fuel decomposition of Reaction 5.7. The products of the reaction are an iso-heptyl radical (C_7H_{15}) and a methyl radical (CH_3). The iso-heptyl radical is of the form shown in Figure 5.27 [91].

$$iC_8H_{18} \longrightarrow C_7H_{15} + CH_3 \tag{5.7}$$

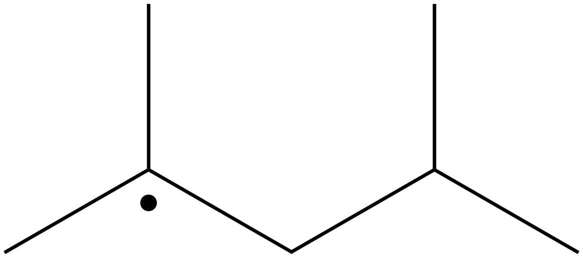

Figure 5.27: iso-heptyl radical (C_7H_{15}) [91]

This model shows that the NO_X emissions are increased for toluene when compared to iso-octane because of the increased O radical. The O radical is greater for toluene because it is consumed by CH_3 radical to a much smaller degree than it is in iso-octane flames. The large quantities of CH_3 radical in iso-octane flames are due to this primary unimolecular fuel decomposition reaction that is absent in the toluene flames.

Therefore, the chemical kinetic mechanism suggests that the reason for higher NO_X production in the toluene flame (relative to iso-octane) is the presence of a higher O radical concentration, and that the O radical concentration is greater because less CH_3 radical is generated by the primary fuel molecule decomposition reactions.

5.4.2 Comparison of Several Fuel Classes

As just noted, the relation between fuel type and NO_X production appears to be directly tied to O radical and CH_3 radical production. The kinetic models can be used to investigate fuels from various fuel classes to further test this hypothesis.

The first comparison uses two mechanisms from the Fuels and Combustion Research Laboratory at Princeton University [92]. The Dooley *et al.* [85] jet fuel mechanism calculates the kinetic behavior for iso-octane, toluene, and n-octane. The Diévart *et al.* [93] mechanism calculates the kinetic behavior for 135-TMB.

Firstly, Figure 5.28 shows the model prediction of NO emissions for the four fuels. Notice that the model shows reduced NO emissions for 135-TMB when compared to toluene, which is consistent with the experimental results from Figure 5.21 above. Also, n-octane produces slightly more NO emissions than iso-octane. Figure 5.29 shows that the modeled NO emissions are positively correlated with O radical concentration and Figure 5.30 shows that the modeled O radical concentration decreases with increased CH_3 radical concentration for the four fuels. Thus, the model trends are consistent with the hypothesis.

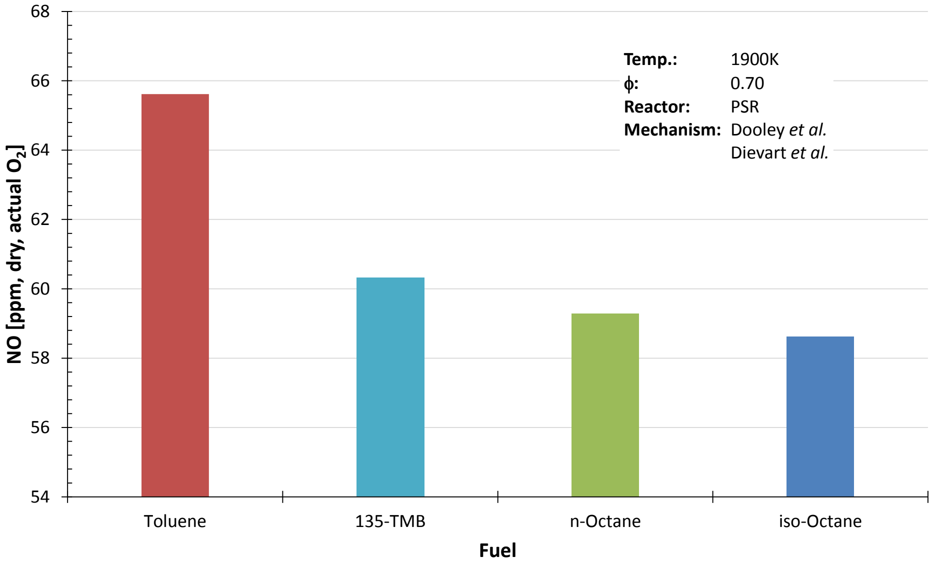

Figure 5.28: PSR NO concentration for toluene, 135-TMB, n-octane, and iso-octane

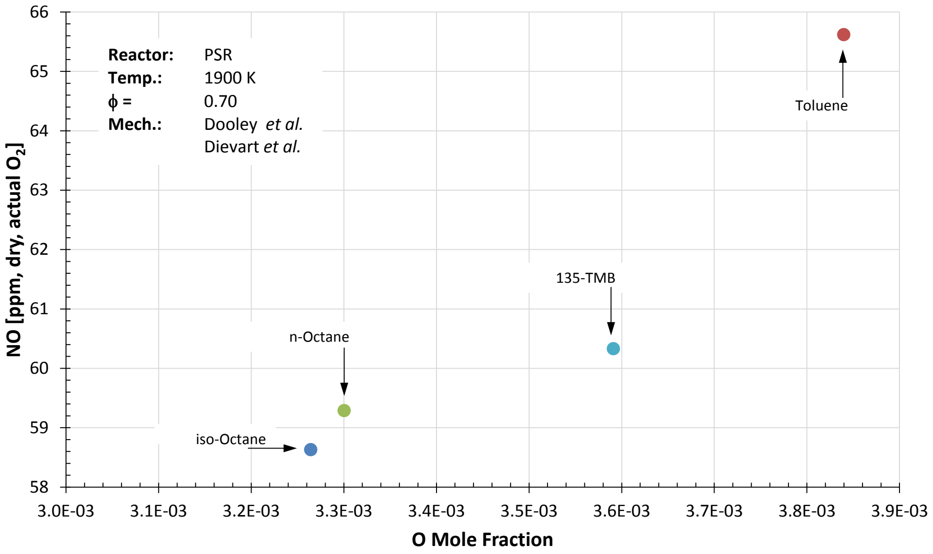

Figure 5.29: PSR NO vs. O for toluene, 135-TMB, n-octane, and iso-octane

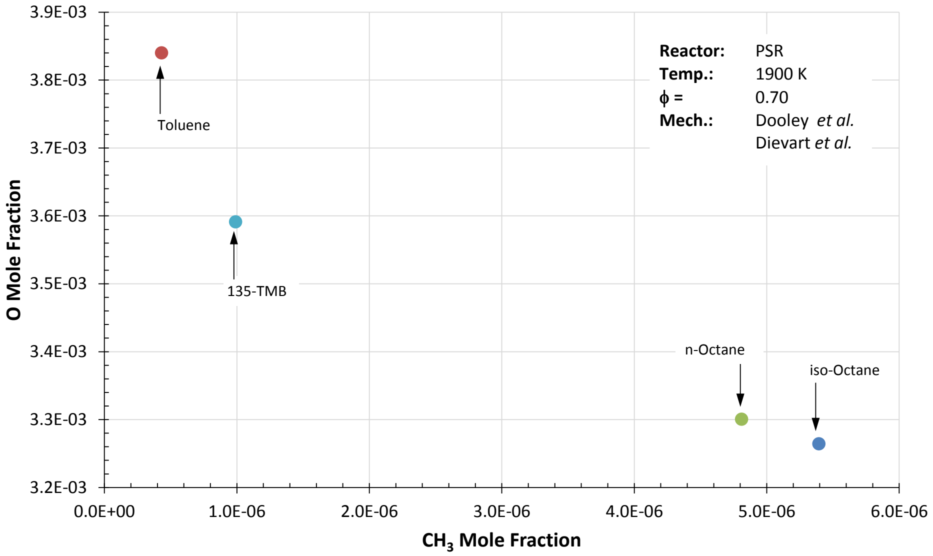

Figure 5.30: PSR O vs. CH_3 for toluene, 135-TMB, n-octane, and iso-octane

The net reaction rates for CH_3 and O radical also follow the expected trend, as shown in Figure 5.31. Finally, the rates of destruction for the specific reaction ($CH_3 + O \rightarrow H + CH_2O$) show the same trend with fuel type.

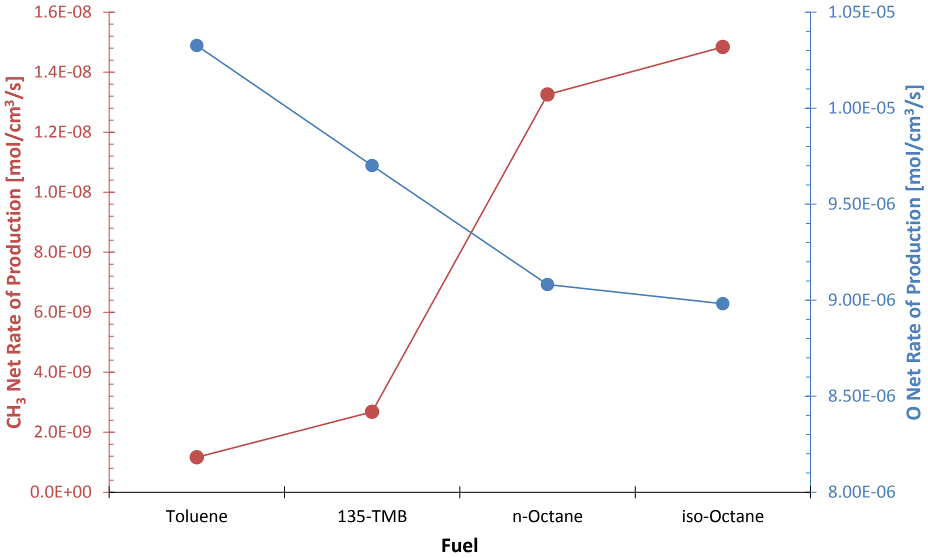

Figure 5.31: PSR CH_3 and O net prod. rates for toluene, 135-TMB, n-octane, and iso-octane

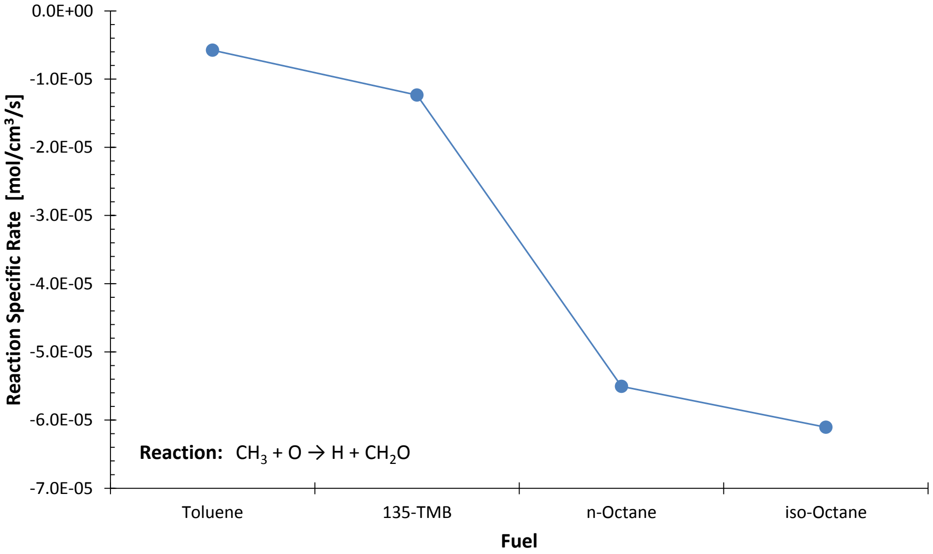

Figure 5.32: PSR specific reaction rates for toluene, 135-tmb, n-octane, and iso-octane

A second comparison uses a different chemical kinetic mechanism to help test the hypothesis that NO_X is reduced with increased CH_3 production. The Mzé-Ahmed *et al.* [94] mechanism is designed for surrogate fuels including iso-octane, toluene, and propylcyclohexane (PCH).

The model results follow the same pattern as that from the previous mechanism. First, Figure 5.33 shows that NO is highest for toluene, followed by PCH, and then iso-octane. This appears consistent with the experimental result that the cycloalkane content of the fuel tends to increase NO_X production. Figure 5.34 and Figure 5.35 show, once again, that NO decreases with decreased O radical and O radical decreases with increased CH_3 radical. Finally, Figure 5.36 and Figure 5.37 present the net rates of production and reaction specific consumption rates for CH_3 and O radicals. Notice, this mechanism utilizes two reactions for the destruction of CH_3 and O ($CH_3 + O \rightarrow H + CH_2O$ and $CH_3 + O \rightarrow H + H_2 + CO$), which is one reason the two mechanisms cannot be compared to one another.

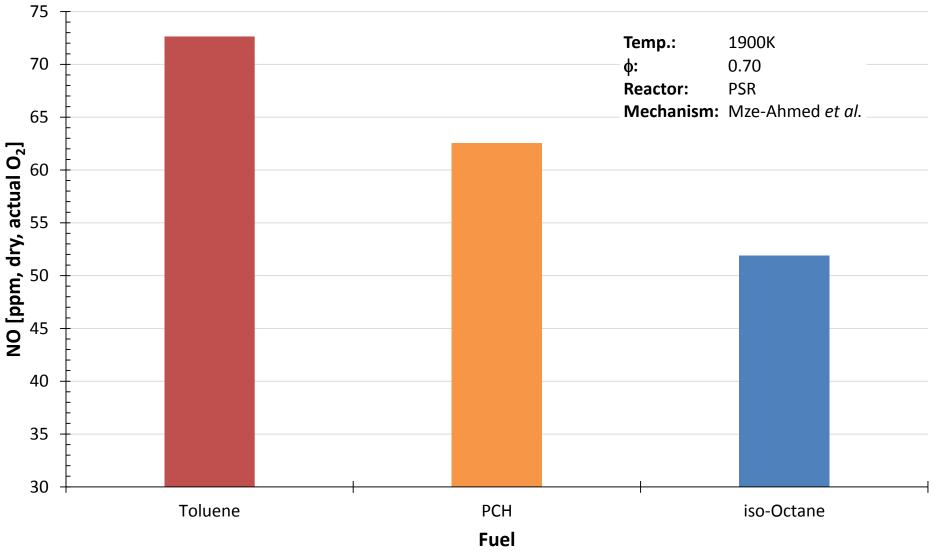

Figure 5.33: PSR NO concentration for toluene, PCH, and iso-octane

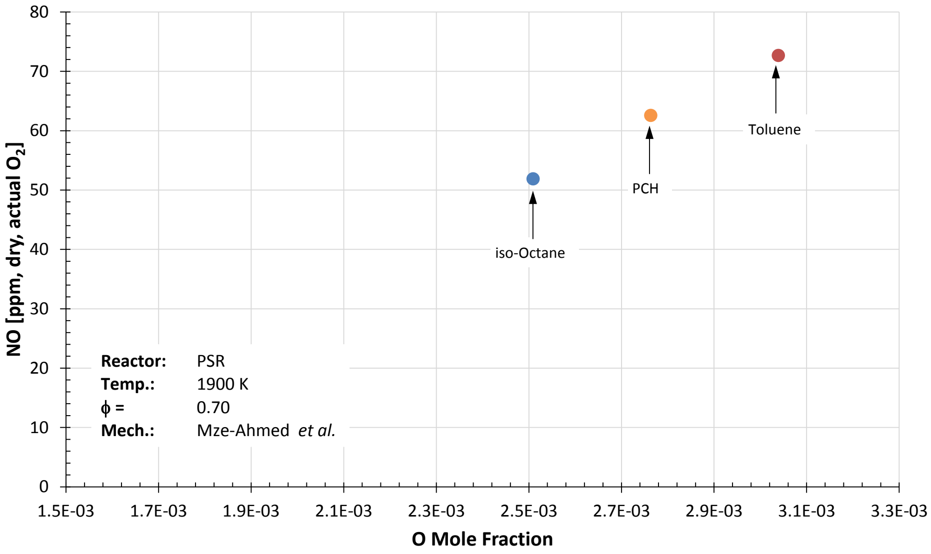

Figure 5.34: PSR NO vs. O for toluene, PCH, and iso-octane

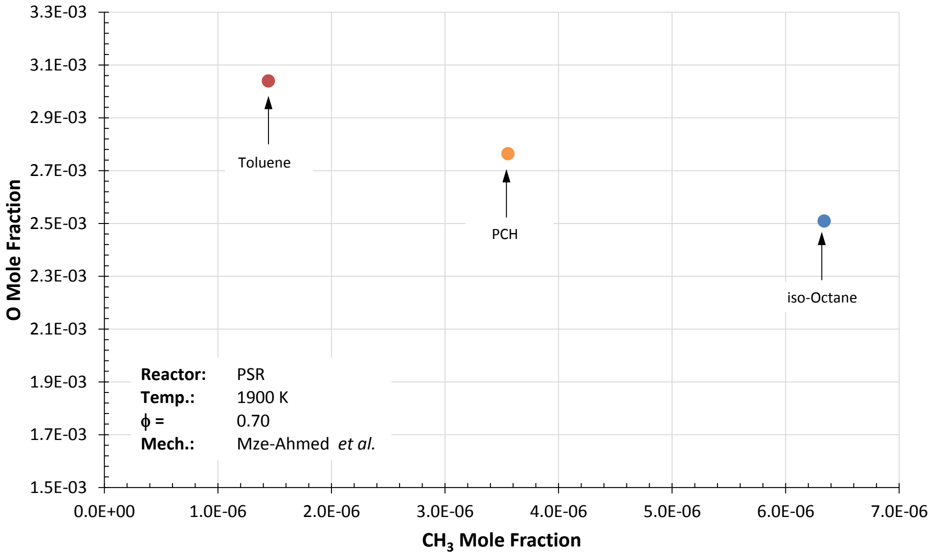

Figure 5.35: PSR O vs. CH_3 for toluene, PCH, and iso-octane

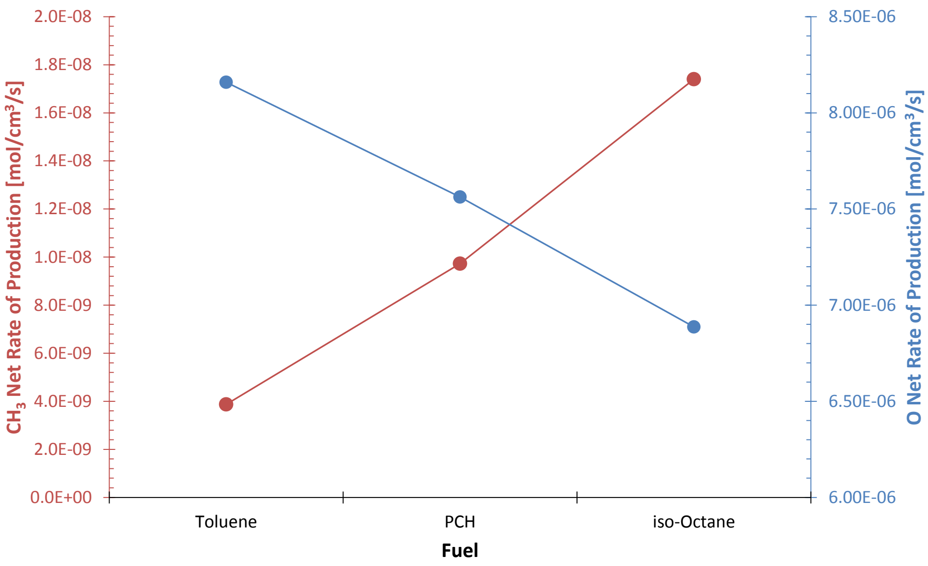

Figure 5.36: PSR CH_3 and O net prod. rates for toluene, PCH, and iso-octane

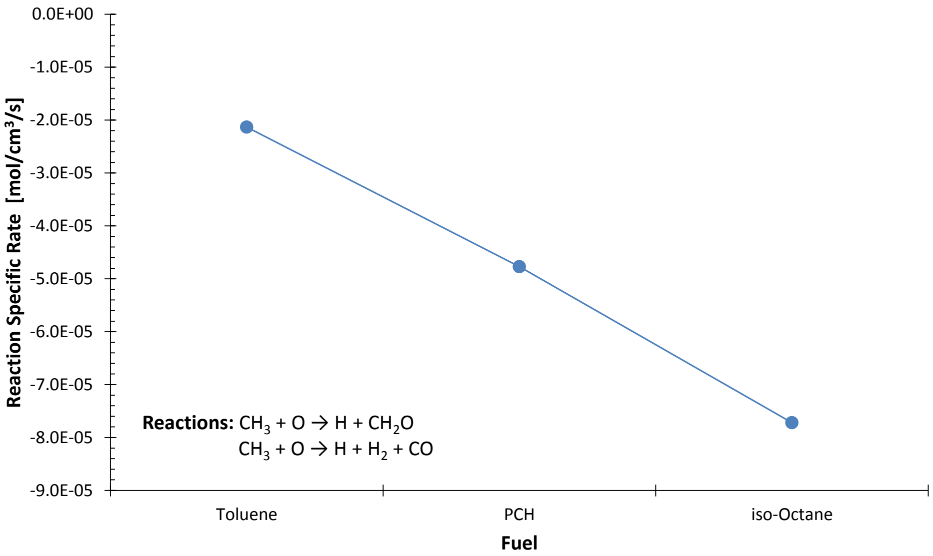

Figure 5.37: PSR specific reaction rates for toluene, PCH, and iso-octane

5.4.3 Formation of Methyl Radical

The methyl radical concentration appears to be the cause for the differences in NO_X between these surrogate fuels, so the next step is to understand the manner in which the methyl radicals are formed. The methyl radical formation process depends largely on the manner with which the fuel molecule is destroyed. Turns [5] provides a very detailed description of the destruction of higher alkanes based on the differences in bond dissociation energy of C-C bonds (approximately 370 kJ/mol) and C-H bonds (approximately 435 kJ/mol) [95].

The initial reactions for fuels are primarily via H abstraction from H, O, or OH attack. A bimolecular collision between the fuel molecule and a radical cause one of the hydrogen atoms to be removed and the fuel molecule to be converted to a free radical. Increased radical concentration will increase the reaction rates associated with radical collisions. However, other fuel destruction reactions are possible, and those involving methyl radical are particularly important here. The large fuel molecules present in jet fuel can decompose to form methyl radicals in many ways, and the chemical kinetic mechanisms provide some insight into the possibilities.

Figure 5.38 shows the three alkane fuels. Notice that the iso-octane has five methyl groups present on the molecule, while n-octane only has two. Any of these methyl groups could be abstracted from the primary molecule. The kinetic mechanisms of Dooley *et al.* [85] and Mzé-Ahmed *et al.* [94] both consider the unimolecular decomposition of the fuel molecule to be relatively important. A collision with an arbitrary species (M) generates either heptyl radical (C_7H_{15} and methyl radical (CH_3) or two butyl radicals (C_4H_9). The alkyl radicals collide with other species and can generate methyl radicals. For example, the butyl radicals decompose into a methyl radical and propylene (C_3H_6). However, in the n-octane case, ethylene (C_2H_4) forms readily when the chain is broken. The ethylene produces methyl radical via the reaction: $C_2H_4 + O \rightarrow CH_3 + HCO$. The propylcyclohexane (PCH) molecule produces a propyl (C_3H_7) radical and a cyclohexyl radical (C_6H_{11}). The methyl group could also be abstracted. Once the cyclohexane ring is broken, ethylene (C_2H_4) is produced readily, and ethylene forms CH_3 in the same manner as n-octane ($C_2H_4 + O \rightarrow CH_3 + HCO$).

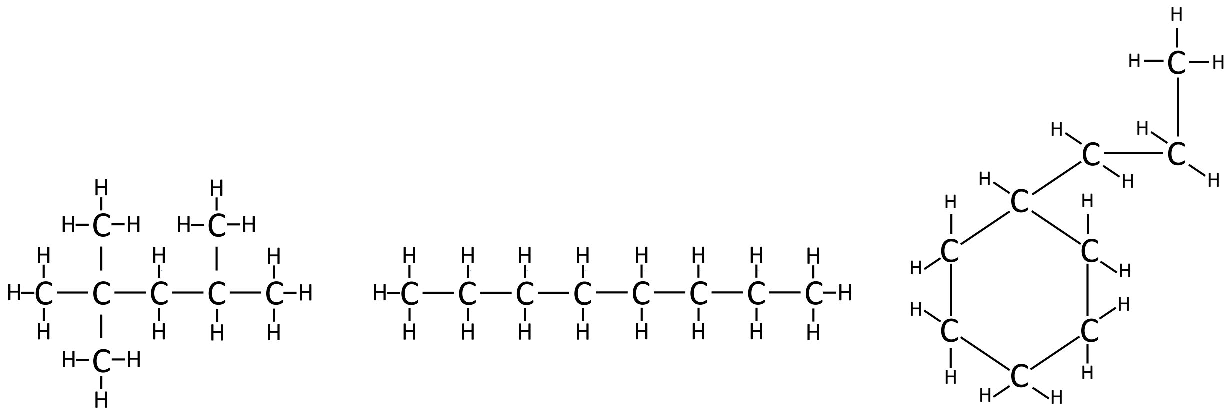

iso-Octane n-Octane PCH

Figure 5.38: 2,2,4-trimethylpentane (iso-octane), n-octane, and PCH

Figure 5.39 shows the two aromatic fuels. Notice that the toluene has one methyl group present on the molecule, while 135-TMB has three. Any of these methyl groups could be abstracted from the primary molecule. When toluene experiences unimolecular decomposition, the result is two radicals – a phenyl (C_6H_5) and a methyl (CH_3). When toluene collides with OH or H radicals, the methyl group is abstracted and the products will be phenol (C_6H_5OH) and benzene (C_6H_6), respectively. Similarly, 135-TMB can undergo methyl abstraction by unimolecular decomposition from either the first, third, or fifth carbon locations. If 135-TMB collides with an H radical, the result will be a methyl group and stable dimethylbenzene molecule. Aromatic rings (like toluene or 135-TMB) decompose to form acetylene (C_2H_2) [96], and that pathway consists of several alkyl radical steps. The toluene mechanism from Dooley et al. [85]shows a significant contribution of methyl radicals via the reaction of propadiene (C_3H_4) and H radical ($C_3H_4 + H \rightarrow C_2H_2 + CH_3$).

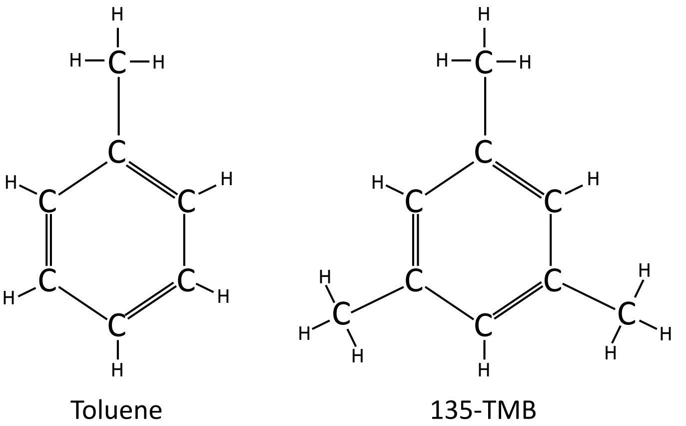

Figure 5.39: 1,3,5-trimethylbenzene (135-TMB) and methylbenzene (toluene)

The formation of methyl radical from different fuel species can take many paths, and the qualitative discussion above presents some information about the differences. It appears that unimolecular decomposition plays a significant role in methyl abstraction from the fuel molecule [97]. After the first methyl abstraction, the β-scission rule helps to identify which bonds will be preferentially broken. The rule states that the location of the free electron strengthens the bonds from the same carbon atom, so the bonds that are one-atom removed from the radical location will be preferentially broken [5].

The reactions and kinetic rates that model fuel decomposition (and methyl formation) are typically determined via experiments and analogies. These large, complex, and polyatomic fuel molecules are not spherically symmetric, so the reaction behavior also depends on the geometrical orientation of the molecules upon collision [2]. Mechanism developers consider these configurational influences, which bonds are preferentially broken, and which of the possible kinetic pathways need inclusion. In this study, the mechanisms are used to provide insight, making these considerations beyond the scope of this work.

5.5 Conclusions

The objective of the work reported in this chapter is to understand the chemical kinetic basis for the differences in NO_X production between real jet fuels and alternative jet fuels using the experimental JSR and idealized PSR models. The conclusions drawn from this portion of the study can be summarized as follows:

- NO_X formation for the unmodified synthetic fuels followed the same order regardless of temperature (HP Camelina > FT Coal > FT Natural Gas > HP Tallow)

- NO_X formation for the synthetic fuels blended with 20% Pet-Aromatic followed the same order regardless of temperature (HP Camelina > HP Tallow > FT Natural Gas > FT Coal)

- The Pet-Aromatic appears to have inconsistent effects when blended with the synthetic fuels (in some cases it increases NO_X production and in some cases it decreases NO_X production).

- A PSR model with chemical kinetics for iso-octane and toluene shows that the NO production is correlated with O radical concentration. The O radical concentration is depressed due to reaction with CH_3 radical, which in turn indicates that fuels which produce more CH_3 during combustion will generate less NO_X. Simply put, increased CH_3 → decreased O → decreased NO_X.

- PSR models for several fuels (iso-octane, toluene, 135-TMB, n-octane, and PCH) using multiple kinetic mechanisms show the NO_X – O – CH_3 relationship noted above to be consistently true for all cases.

- The production of CH_3 for the real, complex experimental fuels is unfortunately impossible to determine as they are composed of hundreds of different species. The fuel composition analysis presented in Chapter 2 is not detailed enough to fully determine the species present in the fuels and consequently the pathway to CH_3 production.

Ultimately, the only way to really determine the manner in which fuel composition affects NO_X formation is to use surrogate fuels for experiments and models. A possible plan is described near the end of Chapter 6 as this work draws to a conclusion and proposes some potential future work.

Chapter 6
Summary and Conclusions

The three objectives addressed by this work are the subject of the three primary chapters (Chapter 3, Chapter 4, and Chapter 5), and important highlights and conclusions of each of these are summarized here. Finally, we present directions for future work before summarizing the significant contributions.

As a reminder, six 'real', complex fuels are studied as part of this work. Two of the fuels tested are derived via Fischer Tropsch (FT) synthesis from natural gas and coal. Two of the fuels are derived via hydroprocessing (HP) of the biological feedstocks of Camelina oil and tallow. The baseline petroleum-based fuel is JP8, which is the standard fuel for United States military aircraft. The sixth fuel, Pet-Aromatic, is a blend of many aromatic compounds and is used to study the effect of aromatic additives to synthetic fuels. Several single component fuels (methane, 1,3,5-trimethylbenzene, iso-octane, n-octane, toluene, and propylcyclohexane) are studied via experiments and/or models to aid in understanding underlying behavior.

6.1 Objective 1: Fuel Effects on Combustion Stability

6.1.1 Task Summary

The first part of Chapter 3 describes the experimental study of blowout from real fuels. A Toroidal Stirred Reactor (TSR) is used to perform lean extinction tests. The prevaporized, premixed fuel and air enter the reactor and the fuel flow is slowly decreased throughout the test to vary the equivalence ratio towards extinction. The test data is analyzed and characterized by an equivalence ratio (ϕ), loading parameter (LP), residence time (τ), and corrected temperature (T).

The second part of Chapter 3 presents the results of the extinction studies. At low aromatic concentrations (0%, 10%, and 20% Pet-Aromatic additive) the four synthetic fuels (FT Natural Gas, FT Coal, HP Camelina, and HP Tallow) showed no appreciable difference in temperature or equivalence ratio at extinction. JP8 (with 18.7% aromatic content) also showed no appreciable difference. The FT Natural Gas fuel was blended with the Pet-Aromatic additive at concentrations ranging from 0% to 80%, and the extinction behavior of these blends was compared to JP8 and pure Pet-Aromatic. In this case, the purely aromatic fuel showed an increase in temperature and equivalence ratio at extinction, indicating less resistance to lean blowout. However, the high aromatic content fuels tended to increase carbon deposits in the fuel delivery system which could lead to difficulties for implementation in realistic systems.

6.1.2 Conclusions

The first objective was to determine, via experimental measurements, the influence of fuel composition on extinction behavior in the toroidal stirred reactor. The conclusions drawn from this study can be summarized as follows:

- The various base fuels (feedstock) all exhibited statistically identical lean blowout limits. When these fuels were blended with aromatic species to 0%, 10%, or 20% by volume, the blowout limits remained indistinguishable between all the fuels as a group.

- Aromatic content from 20% to 100% does have a significant effect on blowout behavior for FT Natural Gas.

- High aromatic content fuels (40% and above) exhibited inconsistent behavior that could be attributed to carbon deposition in the premix filter and jet ring, so carbon deposition could be an issue for high aromatic content fuels.

- There is a difference in behavior between a highly aliphatic fuel and the highly aromatic fuel, and that difference was explored while addressing the second objective, specifically the mechanism of flame stabilization.

6.2 Objective 2: TSR Flame Stabilization

6.2.1 Task Summary

The first part of Chapter 4 describes the methodology for modeling the mechanism of flame stabilization in the Toroidal Stirred Reactor (TSR) using CFD and Chemical Reactor Models (CRMs). There are several chemical kinetic mechanisms available for methane, but realistically only the Reduced GRI [78] mechanism is feasible within the computational constraints imposed by CFD. The reactor domain was modeled as a single $1/48^{th}$ (7.5^{o}) slice of the TSR (because of the recurring symmetry associated with the 48 jets).

The second part of Chapter 4 presents the results of the CFD model and explores the mechanism for flame stabilization in the TSR. The stable condition results ($\phi = 0.55$) show that the reactor is asymmetric about the horizontal midplane, and that the jet from upstream slices enter the current slice. The jets cause the bulk toroidal flow and generate the radical pool that interacts with the jet to stabilize combustion via recirculation of products. CFD runs at progressively decreasing equivalence ratios show how the reactor behavior changes as it approaches blowout. In general, the reactor has a recirculation region that transports OH radical around the reactor to interact with the jet. This OH radical is generated in a shear region between the recirculation region and the 'eye' region. At incipient blowout, the OH radical is diffused into the 'eye' region instead of the recirculation region and there is a very low OH concentration in the stream that is entrained into the jet. The PSR model predicts that the minimum volume for sustaining combustion is approximately the same as the volume of the CFD model that is reacting (as defined by a minimum OH reaction rate). This shows that blowout occurs when a subset of the total volume that is associated with active reaction reaches essentially a PSR blowout point. The remainder of the volume is passive in the sense that it either contains non-reacted fuel and oxidizer (e.g., inside the inlet jet), or it contains near equilibrium products (e.g., the "eye" of the recirculation zone).

6.2.2 Conclusions

The second objective focused on the mechanism by which flames are stabilized inside the toroidal stirred reactor (TSR). The primary tools are CFD models in conjunction with CRM interpretation and experimental comparison. The conclusions drawn from this study are summarized as given below:

- The reactor can be separated into segments for each jet, but the jets interact with each other (in the model this is achieved via periodic boundary conditions). If we focus on a single segment of the reactor, the jets from the two upstream segments enter the current segment. This flow field creates a bulk flow in the toroidal direction and also plays a role in flame stabilization.

- During stable combustion, the chain-branching radical OH is generated during CO oxidation and is transported around the reactor in the recirculation zone where it eventually interacts with the incoming jet and acts to initiate combustion.

- As equivalence ratio is decreased, and blowout becomes imminent, the OH production in the shear region is diffused toward the 'eye' of the reactor instead of the recirculation region. Now, there is a reduced concentration of OH radical that is recirculating around the reactor and interacting with the incoming jet. This effectively causes the reactor to blow out.

- The reactor is quite homogeneous at high equivalence ratios, but does experience significant inhomogeneity as it approaches blowout. The reacting volume (and effectively residence time) decreases to a point that cannot sustain combustion. This volume prediction is similar for the PSR and CFD models.

- The difference in blowout for a highly aliphatic fuel (represented by iso-octane) and a highly aromatic fuel (represented by toluene) can be attributed to the rate at which the fuel is destroyed by radical species. The initial reaction step of toluene with free radicals is slower than it is for iso-octane, thus requiring a higher temperature to maintain a stable rate of combustion. Thus, the toluene undergoes blowout at a higher flame temperature and a higher equivalence ratio.

6.3 Objective 3: Fuel Effects on NO_X Emissions

6.3.1 Task Summary

The first part of Chapter 5 describes the experimental study of NO_X formation from real fuels. A Jet Stirred Reactor (JSR) is used to perform emissions tests. The prevaporized, premixed fuel and air enter the reactor and the fuel flow is adjusted throughout the test to vary the equivalence ratio such that temperature is held roughly constant. The data are analyzed and used to develop correlations of NO_X as function of temperature for each fuel. The experimental study found inconsistent trends in the NO_X emissions for these fuels, especially with the addition of 20% Pet-Aromatic. In general, these real, complex fuels have so many components that it is difficult to extract a chemical kinetic interpretation for the observed NO_X formation behavior.

The second part of Chapter 5 presents surrogate fuel modeling that aims to understand how NO_X formation characteristics vary with the different fuel classes. A single PSR model is utilized at constant temperatures and equivalence ratios for several fuels with multiple kinetic mechanisms. The list of fuels includes iso-octane, n-octane, toluene, propylcyclohexane, and 1,3,5-trimethylbenzene. In all cases, the NO_X production rate is correlated with O radical concentration. The O radical concentration is reduced for fuels which produce more CH_3 radical during combustion because of a fast reaction between CH_3 and O radicals. In the present case, aliphatic fuels tended to produce more CH_3 during the initial fuel molecule reaction, which in turn reduced O radical and finally reduced NO_X formation.

6.3.2 Conclusions

The third objective was to understand the mechanistic reasons behind differences in NO_X production for real jet fuels are they were burned at constant temperatures. The work used the experimental JSR and idealized PSR model. The conclusions drawn from this study are summarized as follows:

- NO_X formation for the unmodified synthetic fuels followed the same order regardless of temperature (HP Camelina > FT Coal > FT Natural Gas > HP Tallow)

- NO_X formation for the synthetic fuels blended with 20% Pet-Aromatic followed the same order regardless of temperature (HP Camelina > HP Tallow > FT Natural Gas > FT Coal)

- The Pet-Aromatic appears to have inconsistent effects when blended with the synthetic fuels (in some cases it increases NO_X production and in some cases it decreases NO_X production).

- A PSR model with chemical kinetics for iso-octane and toluene shows that the NO_X production correlates with O radical concentration, and that O radical concentration is decreased due to reaction with CH_3 radical. Thus, NO_X formation is reduced for those fuels that create more CH_3 radical during their initial decomposition reactions.

- PSR models for several fuels (iso-octane, toluene, 135-TMB, n-octane, and PCH) using multiple kinetic mechanisms shows the NO_X – O – CH_3 relationship noted above to be consistent for all cases.

- The production of CH_3 for the experimental fuels is unfortunately impossible to determine as they are composed of hundreds of different species. The fuel composition analysis presented in Chapter 2 is not detailed enough to fully determine the species present in the fuels and consequently the pathway to CH_3 production. However, this issue can be approached experimentally via surrogate fuel studies.

6.4 Future Work

Possible continuing work could focus on the TSR CFD model and/or NO_X emissions from surrogate fuels.

Firstly, the TSR CFD model predicted blowout reasonably well, but that prediction could be improved by including more detailed heat loss treatment. The model could be expanded beyond the reactor domain to include the alumina solid. The expanded domain enables the model to computationally determine conductive heat loss. Currently the model assumes a uniform heat flux out of the reactor wall, but the improved model would calculate a realistic heat loss including non-uniform behavior. The non-uniform heat loss will certainly affect the temperature and species behavior inside the reactor, which will also change the blowout prediction. Essentially, improved heat loss modeling should improve the ability of the model to match the experimental data.

Secondly, the NO_X emission results showed varying behavior for the real fuels, but a very consistent trend for the surrogate fuel models. More surrogate fuel studies could help to better identify fuel structure characteristics that affect NO_X emissions. Experimental JSR data could be obtained on fuels with few methyl branches (i.e., n-octane and benzene) and these data compared to fuels with several methyl branches (i.e., 2,2,4-trimethylpentane and 1,3,5-trimethylbenzene). According to the hypothesis, the NO_X emissions should be reduced for the fuels with more methyl branches. Alternatively, an experiment with an open flame (e.g., a Bunsen or McKenna type burner) provides optical access to the flame. Optical access enables direct measurement of radical species for the different fuels. Wu *et al.* [98] recently developed a method to measure relative amounts of methyl radical using Rayleigh scattering from resonance enhanced multi-photon ionization. The amount of methyl radical from different fuels should provide some insight into the fuel decomposition pathways. Also, the detailed chemical kinetic modeling of different fuels can be continued to understand the pathways for NO_X formation, similar to the methods outlined by Fackler [25,26].

Choosing surrogate fuels depends largely on the parameter being studied, and the scientific literature provides some guidance. Colket *et al.* [99] presented JP8 surrogates as an analogy to the gasoline industry, which uses octane number as a way to compare fuels to a single reference fuel. Such a reference fuel would make it easier to classify fuels, but determining what fuel it is (via surrogate fuel studies) depends on what phenomenon is being studied. Edwards and Maurice [65] review surrogate fuel mixtures to aid in modeling. The first category is for physical surrogates, which match physical properties like density, lubricity, specific heat, volatility, etc. The second category is for chemical surrogates, which match the chemical classes and will be the only way to match combustion phenomenon (like stability and emissions). Later, Edwards *et al.* [51] used surrogate methodology to study autoignition of different fuel types that could serve as jet fuel surrogates. The focus is not only the surrogate fuels, but also on mixing rules.

Hopefully these studies can be expanded to focus on other effects of fuel molecular arrangement. For example, preliminary data suggest that fuel composition has an effect on black carbon (soot) emissions.

Knowledge of how fuels disintegrate and how NO_X and soot emissions are made could help design new fuels. Eventually, it is possible that fuels could be designed with specific molecular arrangements that reduce certain emissions.

6.5 Significance

The ultimate goal has been to assess the viability of synthetic alternatives to jet fuel, while providing improvements in the understanding of the mechanisms that give rise to the observed global lean blowout and NO_X emission behavior. Three broad significant findings resulted from our work.

1. This has been the first comprehensive experimental study to investigate the flame stability characteristics of so many fuels, including the effects of aromatic content. In general, the flame stability of the alternative fuels compare well with the baseline fuels and they can thus be considered good alternatives. The highly aromatic fuel did show less resistance to blowout relative to the alternative fuels and the highly aliphatic surrogate fuel, and that behavior necessitated detailed modeling for interpretation.

2. The detailed modeling study of flame stabilization in the TSR is also a novel contribution. There has been only one TSR CFD study prior to this one, but it utilized assumptions regarding symmetry that appear to have compromised the three-dimensional structure of the flame. This in turn compromised the conclusions regarding the mechanism of flame stabilization. The present work found that the key to flame stabilization is the manner in which the radical species are transported around the reactor to interact with the fuel. The radical concentration and production rates also explained the differences in blowout for toluene and iso-octane, and thus provided a plausible explanation for the reduced resistance of the aromatic fuels to blowout.

3. This is the first comprehensive study of NO_X formation from so many alternative jet fuels in a stirred reactor. Previous studies found little or no differences as they were generally performed in real engines that do not separate the effects of temperature and chemistry. The present experimental data resulted in correlations that allowed for direct comparison of fuel type, temperature, and NO_X emissions. The detailed chemical kinetic models found a critical role for methyl radical formation in which the methyl radical acted as a sink for O radical, and this in turn reduced NO_X formation. Thus, the relative propensity of the fuel to produce methyl radical during the initial fuel destruction was a critical step in correlating NO_X behavior.

The potential for these fuels as alternatives is promising. Flame stability is a non-issue for fully formulated fuels, and NO_X differences are not present in real engines. However, the fuel decomposition pathway appears to affect emissions. Ultimately, the molecular arrangement of the fuel could be controlled such that certain emissions are reduced, and these 'designer' fuels could then be much more viable alternatives.

Bibliography

[1] Zelina J., and Ballal D., 1994, "Combustion Studies in a Well Stirred Reactor (AIAA 94-0114)," 32nd AIAA Aerospace Sciences Meeting & Exhibit, AIAA, Reno, NV.

[2] Law C., 2006, Combustion Physics, Cambridge University Press.

[3] Shan R., and Lu T., 2012, "Ignition and Extinction in Perfectly Stirred Reactors with Detailed Chemistry," Combust. Flame, **159**(6), pp. 2069–2076.

[4] Smith G., Golden D., Frenklach M., Moriarty N., Eiteneer B., Goldenberg M., Bowman C., Hanson R., Song S., Gardiner W., Lissianski V., and Qin Z., 2010, "GRI-Mech 3.0," **2010** [Online]. Available: http://www.me.berkeley.edu/gri_mech/.

[5] Turns S., 2000, An Introduction to Combustion: Concepts and Applications, McGraw-Hill Higher Education, New York, N.Y.

[6] Reaction Design, 2013, "CHEMKIN-PRO (Version 15113)."

[7] Zeldovich Y., 1946, "The Oxidation of Nitrogen in Combustion and Explosions," Acta Physicochim. URSS, **21**(4), pp. 577–628.

[8] Malte P., and Pratt D., 1974, "The Role of Energy-Releasing Kinetics in NOx Formation: Fuel-Lean, Jet-Stirred CO-Air Combustion," Combust. Sci. Technol., **9**(5-6), pp. 221–231.

[9] Bozzelli J. W., and Dean A. M., 1995, "O + NNH: A Possible New Route for NOX Formation in Flames," Int. J. Chem. Kinet., **27**(11), pp. 1097–1109.

[10] Fenimore C., 1971, "Formation of nitric oxide in premixed hydrocarbon flames," Symp. Combust., **13**(1), pp. 373–380.

[11] Longwell J., and Weiss M., 1955, "High Temperature Reaction Rates in Hydrocarbon Combustion," Ind. Eng. Chem., **47**(8), pp. 1634–1643.

[12] Weiss M., Lang R., and Longwell J., 1958, "Combustion Rates in Spherical Reactors," J. Ind. Eng. Chem., **50**(2), pp. 257–264.

[13] Sturgess G., Heneghan S., Vangsness M., Ballal D., and Lesmerises A., 1996, "Lean Blowout in a Research Combustor at Simulated Low Pressures," J. Eng. Gas Turbines Power, **118**(4), p. 773.

[14] Nenniger J., Kridiotis A., Chomiak J., Longwell J., and Sarofim A., 1984, "Characterization of a Toroidal Well Stirred Reactor," 20th Symp. Combust., **20**(1), pp. 473–479.

[15] Zelina J., and Ballal D., 1997, "Combustor Stability and Emissions Research Using a Well-Stirred Reactor," J. Eng. Gas Turbines Power, **119**(1), p. 70.

[16] Blust J., Ballal D., and Sturgess G., 1997, "Emissions Characteristics of Liquid Hydrocarbons in a Well Stirred Reactor (AIAA-97-2710)," 33rd AIAA/ASME/SAE/ASEE Joint Propulsion

Conference & Exhibit, AIAA, Seattle, WA.

[17] Blust J., Ballal D., and Sturgess G., 1999, “Fuel Effects on Lean Blowout and Emissions from a Well-Stirred Reactor,” J. Propuls. Power, **15**(2), pp. 216–223.

[18] Ballal D., 2004, “Combustor Stability & Lean Blowout (AIAA-2004-3546),” 40th AIAA/ASME/SAE/ASEE Joint Propulsion Conference & Exhibit, AIAA, Fort Lauderdale, FL, pp. 1–10.

[19] Moses C. A., and Roets P. N. J., 2009, “Properties, Characteristics, and Combustion Performance of Sasol Fully Synthetic Jet Fuel,” J. Eng. Gas Turbines Power, **131**(4), p. 041502.

[20] Ballal D., 2008, Intelligent Engine Systems Alternate Fuels Evaluation, Dayton, Ohio.

[21] Stouffer S., Pawlik R., Justinger G., Heyne J., Zelina J., and Ballal D., 2007, “Combustion Performance and Emissions Characteristics for a Well Stirred Reactor for Low Volatility Hydrocarbon Fuels (AIAA-2007-5663),” 43rd AIAA/ASME/SAE/ASEE Joint Propulsion Conference & Exhibit, Cincinnati, OH.

[22] Kumar K., Sung C.-J., and Hui X., 2011, “Laminar flame speeds and extinction limits of conventional and alternative jet fuels,” Fuel, **90**(3), pp. 1004–1011.

[23] Hui X., Kumar K., Sung C.-J., Edwards T., and Gardner D., 2012, “Experimental studies on the combustion characteristics of alternative jet fuels,” Fuel, **98**, pp. 176–182.

[24] Lee J., 2000, “Reduction of NOx Emission for Lean Prevaporized-Premixed Combustors,” University of Washington.

[25] Fackler K., 2011, “A Study of Pollutant Formation from the Lean Premixed Combustion of Gaseous Fuel Alternatives to Natural Gas,” University of Washington.

[26] Fackler K., Karalus M., Novosselov I., Kramlich J., and Malte P., 2011, “Experimental and Numerical Study of NOx Formation From the Lean Premixed Combustion of CH4 Mixed With CO2 and N2,” J. Eng. Gas Turbines Power, **133**(December).

[27] Karalus M., Fackler K., Novosselov I., Kramlich J., and Malte P., 2012, “Characterizing the Mechanism of Lean Blowout for a Recirculation-Stabilized Premixed Hydrogen Flame (GT2012-68060),” Proceedings of the ASME Turbo Expo, ASME, Copenhagen, Denmark.

[28] Karalus M., 2013, “An Investigation of Lean Blowout of Gaseous Fuel Alternatives to Natural Gas,” University of Washington.

[29] Peters N., 2000, Turbulent Combustion, Cambridge University Press.

[30] Longwell J., and Bar-Ziv E., 1989, “Modeling of Inhomogeneities in the Toroidal Jet-Stirred Reactor,” Combust. Flame, **78**, pp. 99–119.

[31] Barat R., 1992, “Jet-Stirred Combustor Behavior Near Blowout: Observations and Implications,” Combust. Sci. Technol., **84**(1965), pp. 187–197.

[32] Bass C., and Barat R., 2003, "Simulation of a Toroidal Jet-Stirred Combustor Using a Partially Stirred Reactor Model with Detailed Kinetic Mechanisms," Combust. Flame, **135**(3), pp. 249–259.

[33] Briones A., Sekar B., Zelina J., Pawlik R., and Stouffer S., 2008, "Numerical Modeling of Combustion Performance for a Well-Stirred Reactor for Aviation Hydrocarbon Fuels (AIAA-2008-4565)," 44th AIAA/ASME/SAE/ASEE Joint Propulsion Conference & Exhibit, Hartford, CT, pp. 1–19.

[34] Monroig O., Corporan E., DeWitt M., Mortimer B., Ostdiek D., and Wagner M., 2005, "Effect of Jet Fuel Aromatic Concentration on the Emissions of a T63 Engine," Am. Chem. Soc. Div. Fuel Chem., **50**(1), pp. 335–337.

[35] Cain J., DeWitt M. J., Blunck D., Corporan E., Striebich R., Anneken D., Klingshirn C., Roquemore W. M., and Vander Wal R., 2013, "Characterization of Gaseous and Particulate Emissions From a Turboshaft Engine Burning Conventional, Alternative, and Surrogate Fuels," Energy & Fuels, **27**(4), pp. 2290–2302.

[36] DeWitt M., Corporan E., Graham J., and Minus D., 2008, "Effects of Aromatic Type and Concentration in Fischer−Tropsch Fuel on Emissions Production and Material Compatibility," Energy & Fuels, **22**(4), pp. 2411–2418.

[37] Corporan E., DeWitt M. J., Belovich V., Pawlik R., Lynch A. C., Gord J. R., and Meyer T. R., 2007, "Emissions Characteristics of a Turbine Engine and Research Combustor Burning a Fischer−Tropsch Jet Fuel," Energy & Fuels, **21**(5), pp. 2615–2626.

[38] Corporan E., Edwards T., Shafer L., DeWitt M. J., Klingshirn C., Zabarnick S., West Z., Striebich R., Graham J., and Klein J., 2011, "Chemical, Thermal Stability, Seal Swell, and Emissions Studies of Alternative Jet Fuels," Energy & Fuels, **25**(3), pp. 955–966.

[39] Klingshirn C. D., DeWitt M. J., Striebich R. C., Anneken D., Shafer L., Corporan E., Wagner M., and Brigalli D., 2012, "Hydroprocessed Renewable Jet Fuel Evaluation, Performance, and Emissions in a T63 Turbine Engine," J. Eng. Gas Turbines Power, **134**(5), p. 051506.

[40] Timko M., Yu Z., Onasch T., Wong H., Miake-Lye R., Beyersdorf A., Anderson B., Thornhill K., Winstead E., Corporan E., DeWitt M., Klingshirn C., Wey C., Tacina K., Liscinsky D., Howard R., and Bhargava A., 2010, "Particulate Emissions of Gas Turbine Engine Combustion of a Fischer−Tropsch Synthetic Fuel," Energy & Fuels, **24**(11), pp. 5883–5896.

[41] Timko M., Herndon S., de la Rosa Blanco E., Wood E., Yu Z., Miake-Lye R., Knighton W., Shafer L., Dewitt M., and Corporan E., 2011, "Combustion Products of Petroleum Jet Fuel, a Fischer–Tropsch Synthetic Fuel, and a Biomass Fatty Acid Methyl Ester Fuel for a Gas Turbine Engine," Combust. Sci. Technol., **183**(10), pp. 1039–1068.

[42] Lobo P., Rye L., Williams P. I., Christie S., Uryga-Bugajska I., Wilson C. W., Hagen D. E., Whitefield P. D., Blakey S., Coe H., Raper D., and Pourkashanian M., 2012, "Impact of alternative fuels on emissions characteristics of a gas turbine engine - part 1: gaseous and particulate matter emissions.," Environ. Sci. Technol., **46**(19), pp. 10805–11.

[43] Khandelwal B., Ubogu E., Akram M., Blakey S., and Wilson C. W., 2013, "Experimental

Analysis on Emission Production and Performance of Stressed 100 % SPK, Stressed Fully Formulated Synthetic Jet Fuel, Jet A-1 in a Small Gas Turbine Engine (AIAA 2013-3936)," 11th International Energy Conversion Engineering Conference, American Institute of Aeronautics and Astronautics, San Jose, CA, pp. 1–9.

[44] Zelina J., and Ballal D., 1996, "Emissions Studies in a Well-Stirred Reactor and Applications to Combustion Modeling," International Joint Power Generation Conference, Part 1, ASME, pp. 255–263.

[45] Zelina J., and Ballal D., 1994, "Combustion and Emissions Studies Using a Well Stirred Reactor (AIAA 94-2903)," 30th AIAA/ASME/SAE/ASEE Joint Propulsion Conference, Indianapolis, IN.

[46] Zelina J., Blust J., and Ballal D., 1996, "Combustion of Liquid Fuels in the Well Stirred Reactor (96-GT-47)," 41st International Gas Turbine and Aeroengine Congress & Exposition, ASME, Birmingham, UK.

[47] Meeks E., Naik C., Puduppakkam K., Modak A., Egolfopoulos F., Tsotsis T., and Westbrook C., 2011, Experimental and Modeling Studies of Combustion Characteristics of Conventional and Alternative Jet Fuels, Cleveland, OH.

[48] Han X., Aggarwal S. K., and Brezinsky K., 2013, "Effect of Unsaturated Bond on NOx and PAH Formation in n -Heptane and 1-Heptene Triple Flames," Energy & Fuels, **27**(1), pp. 537–548.

[49] Lee J. C. Y., Malte P. C., and Benjamin M. a., 2003, "Low NOX Combustion for Liquid Fuels: Atmospheric Pressure Experiments Using a Staged Prevaporizer-Premixer," J. Eng. Gas Turbines Power, **125**(4), p. 861.

[50] Rutar T., Lee J., Dagaut P., Malte P., and Byrne A., 2007, "NOx formation pathways in lean-premixed-prevapourized combustion of fuels with carbon-to-hydrogen ratio between 0.25 and 0.88," Proc. Inst. Mech. Eng. Part A J. Power Energy, **221**(3), pp. 387–398.

[51] Edwards T., Moses C., and Dryer F., 2010, "Evaluation of Combustion Performance of Alternative Aviation Fuels," 46th AIAA/ASME/SAE/ASEE Joint Propulsion Conference & Exhibit, Nashville, TN.

[52] Kinder J., 2010, Evaluation of Bio-Derived Synthetic Paraffinic Kerosenes (Bio-SPKs).

[53] Energy Information Administration, "Crude Oil Distillation and the Definition of Refinery Capacity," Today In Energy [Online]. Available: http://www.eia.gov/todayinenergy/detail.cfm?id=6970#. [Accessed: 20-Nov-2013].

[54] Wikimedia Foundation, "Wikipedia: The Free Encyclopedia" [Online]. Available: http://en.wikipedia.org/.

[55] Babu M. K. G., and Subramanian K. A., 2013, Alternative Transportation Fuels: Utilisation in Combustion Engines, CRC Press.

[56] Speight J., 2008, Synthetic Fuels Handbook: Properties, Process, and Performance, McGraw Hill.

[57] Dahlquist E., ed., 2013, Biomass as Energy Source: Resources, Systems and Applications, CRC Press.

[58] Aresta M., Dibenedetto A., and Dumeignil F., eds., 2012, Biorefinery: From Biomass to Chemicals and Fuels, De Gruyter.

[59] Vertes A., Qureshi N., Blaschek H., and Yukawa H., eds., 2011, Biomass to Biofuels: Strategies for Global Industries, John Wiley & Sons.

[60] Nag A., 2007, Biofuels Refining and Performance, McGraw Hill Professional.

[61] Lee S., 1996, Alternative Fuels, Taylor & Francis.

[62] Shafer L., Striebich R., West Z., and Cook R., 2010, "Fuel Properties."

[63] Naik C., Puduppakkam K., Modak A., Meeks E., Wang Y., Feng Q., and Tsotsis T., 2011, "Detailed Chemical Kinetic Mechanism for Surrogates of Alternative Jet Fuels," Combust. Flame, **158**(3), pp. 434–445.

[64] Ryder R., Hendricks R., Huber M., and Shouse D., 2010, "Computational Analysis of Dynamic SPK(S8)-JP-8 Fueled Combustor-Sector Performance," Proceedings of the 13th International Symposium on Transport Phenomena and Dynamics of Rotating Machinery, Honolulu, HI, pp. 1–13.

[65] Edwards T., and Maurice L. L. Q., 2001, "Surrogate mixtures to represent complex aviation and rocket fuels," J. Propuls. Power, **17**(2), pp. 461–466.

[66] "JSMol Virtual Molecular Modeling Kit" [Online]. Available: http://chemagic.com/JSmolVMK2.htm.

[67] Longwell J., 1977, "Synthetic Fuels and Combustion," Prog. Energy Combust. Sci., **3**, pp. 127–138.

[68] Zabarnick X., Phelps D., West Z., Shafer L., Ervin J., DeWitt M., Binns K., Williams T., Dieterle G., Balster L., and Harrison W., 2008, Evaluation and Testing of the Suitability of a Coal-Based Jet Fuel, Dayton, OH.

[69] Zelina J., 1995, "Combustion Studies in a Well-Stirred Reactor," University of Dayton.

[70] Blust J., Getz M., and Zabarnick S., 1997, "Probe Design Optimization for the Well Stirred Reactor (AIAA-97-0907)," 35th AIAA Aerospace Sciences Meeting & Exhibit, Reno, NV.

[71] National Instruments, 2010, "LabView."

[72] Dean R., and Dixon W., 1951, "Simplified Statistics for Small Numbers of Observations," J. Anal. Chem., **23**(4), pp. 636–638.

[73] Rorabacher D., 1991, "Statistical Treatment for Rejection of Deviant Values: Critical values of Dixon's 'Q' Parameter and Related Subrange Ratios at the 95% Confidence Level," Anal. Chem., **63**(2), pp. 139–146.

[74] Won S. H., Sun W., and Ju Y., 2010, “Kinetic effects of toluene blending on the extinction limit of n-decane diffusion flames,” Combust. Flame, **157**(3), pp. 411–420.

[75] Hui X., Das A. K., Kumar K., Sung C.-J., Dooley S., and Dryer F. L., 2012, “Laminar flame speeds and extinction stretch rates of selected aromatic hydrocarbons,” Fuel, **97**, pp. 695–702.

[76] Kumar K., and Sung C.-J., 2010, “Flame Propagation and Extinction Characteristics of Neat Surrogate Fuel Components,” Energy & Fuels, **24**(7), pp. 3840–3849.

[77] ANSYS, 2013, “Fluent 14.5.”

[78] Karalus M., Fackler K., Novosselov I., Kramlich J., and Malte P., 2013, “A Skeletal Mechanism for the Reactive Flow Simulation of Methane Combustion (GT2013-95904),” Proceedings of the ASME Turbo Expo, ASME, San Antonio, TX.

[79] Launder B. E., Reece G. J., and Rodi W., 1975, “Progress in the development of a Reynolds-stress turbulence closure,” J. Fluid Mech., **68**(3), p. 537.

[80] ANSYS, 2013, “Fluent 14.5 Theory Guide.”

[81] ANSYS, 2013, “Fluent 14.5 User’s Guide.”

[82] Magnussen B., 1981, “On the structure of turbulence and a generalized eddy dissipation concept for chemical reaction in turbulent flow,” 19h AIAA Aerospace Sciences Meeting, St. Louis, MO.

[83] McBride B., and Gordon S., 1994, “Chemical Equilibrium with Applications.”

[84] Gordon S., and McBride B., 1994, Computer Program for Calculation of Complex Chemical Equilibrium Compositions and Applications, Cleveland, Ohio.

[85] Dooley S., Won S. H., Chaos M., Heyne J., Ju Y., Dryer F. L., Kumar K., Sung C.-J., Wang H., Oehlschlaeger M. A., Santoro R. J., and Litzinger T. A., 2010, “A jet fuel surrogate formulated by real fuel properties,” Combust. Flame, **157**(12), pp. 2333–2339.

[86] Lee A. C., 2003, “Experimental Investigation of Liquid Fuel Vaporization and Mixing in Steam and Air,” University of Washington.

[87] Edmonds R. G., 2002, “Prevaporized Premixed Combustion at Short Residence Times,” University of Washington.

[88] Lefebvre A., 1989, Atomization and Sprays, Hemisphere Publishing Corporation, New York, N.Y.

[89] Lee J., and Malte P., 2001, “Staged prevaporizer-premixer.”

[90] Measurement Computing, 2013, “Personal DaqView.”

[91] Dooley S., 2014, “Personal Communication.”

[92] Dryer F. L., “Fuels and Combustion Research Laboratory (Princeton University)” [Online]. Available: http://www.princeton.edu/mae/people/faculty/dryer/homepage/combustion_lab/.

[93] Diévart P., Kim H. H., Won S. H., Ju Y., Dryer F. L., Dooley S., Wang W., and Oehlschlaeger M. a., 2013, “The combustion properties of 1,3,5-trimethylbenzene and a kinetic model,” Fuel, **109**, pp. 125–136.

[94] Mzé-Ahmed A., Dagaut P., Hadj-Ali K., Dayma G., Kick T., Herbst J., Kathrotia T., Braun-Unkhoff M., Herzler J., Naumann C., and Riedel U., 2012, “Oxidation of a Coal-to-Liquid Synthetic Jet Fuel: Experimental and Chemical Kinetic Modeling Study,” Energy & Fuels, **26**(10), pp. 6070–6079.

[95] Carey F., 2006, Organic Chemistry, McGraw-Hill Higher Education, New York, N.Y.

[96] Glassman I., 1996, Combustion, Academic Press.

[97] Curran H., Gaffuri P., Pitz W., and Westbrook C., 2002, “A Comprehensive Modeling Study of Iso-octane Oxidation,” Combust. Flame, **129**(3), p. 253.

[98] Wu Y., Bottom A., Zhang Z., Ombrello T. M., and Katta V. R., 2011, “Direct measurement of methyl radicals in a methane/air flame at atmospheric pressure by radar REMPI.,” Opt. Express, **19**(24), pp. 23997–4004.

[99] Colket M., Edwards T., Cernansky N., Dryer F., Egolfopoulos F., Friend D., Law E., Lenhert D., Lindstedt P., Pitsch H., Sarofim A., Seshadri K., Smooke M., Tsang W., and Williams S., 2007, “Development of an Experimental Database and Kinetic Models for Surrogate Jet Fuels (AIAA 2007-770),” 45th AIAA Aerospace Sciences Meeting and Exhibit, American Institute of Aeronautics and Astronautics, Reno, NV, pp. 1–21.

[100] NIST, 2007, “Thermophysical Properties of Hydrocarbon Mixtures Database (SUPERTRAPP).”

[101] ASTM, 2012, Standard Test Method for Density , Relative Density , or API Gravity of Crude Petroleum and Liquid Petroleum Products by Hydrometer Method (D1298-12b), West Conshohocken, PA.

[102] ASTM, 2009, Standard Test Method for Estimation of Net Heat of Combustion of Aviation Fuels (D3338), West Conshohocken, PA.

[103] Brankovic A., Ryder R., Hendricks R., and Huber M., 2008, A Step Towards CO2 Neutral Aviaton.

[104] ASTM, 2011, Standard Test Method for Distillation of Petroleum Products at Atmospheric Pressure (D86), West Conshohocken, PA.

[105] Cengel Y., and Boles M., 2006, Thermodynamics: An Engineering Approach, McGraw-Hill Higher Education, New York, N.Y.

[106] Kelly F. J., and Stokes R. H., 1959, “Diffusion coefficients and densities for the systems carbon

tetrachloride + m-xylene and carbon tetrachloride + mesitylene at 25o," Trans. Faraday Soc., **55**, p. 388.

[107] Rossini F., and American Petroleum Institute, 1953, Selected values of physical and thermodynamic properties of hydrocarbons and related compounds, Carnegie Press, Pittsburgh, PA.

[108] Incropera F., and Dewitt D., 2001, Fundamentals of Heat and Mass Transfer, Wiley.

[109] ANH Refractories, 2013, Greencast 94 Data Sheet, AP Green.

[110] COMSOL, 2013, "COMSOL Multiphysics."

[111] Lefebvre A., and Ballal D., 2010, Gas turbine combustion: alternative fuels and emissions, CRC Press/Taylor & Francis Group.

[112] Dagaut P., "Institut de Combustion Aerothermique Reactivite et Environment (French National Center for Scientific Research)" [Online]. Available: http://www.icare.cnrs-orleans.fr/?lang=fr.

Appendix A
Fluid Details and Properties

The multiple component liquid fuels tested in this work were somewhat unique for this kind of effort. Considerable effort went into characterizing the fuels, and some of these details may be useful to some readers. Properties of all the fuels and fluids are summarized here.

A.1 Fuel Identification

Firstly, a small subset of readers may be interested in detailed identification of the fuels as assigned by AFRL. These identification numbers are known as POSF numbers, and are given in Table A.1 along with manufacturers.

Table A.1: AFRL identification for liquid fuels tested

Fuel	POSF #	Manufacturer
FT Natural Gas	5018	Syntroleum
FT Coal	5959/5642/7280/7629	Sasol
HP Camelina	6152	UOP
HP Tallow	6308	UOP
JP8	3773	Marathon
Pet-Aromatic	6871/10240	Exxon Mobil
135-TMB	6898	Swift

A.2 Detailed Fuel Composition

The graphs of fuel composition presented in Section 2.3 were created from the data in Table A.2, which was obtained from the two-dimensional gas chromatography analysis.

Table A.2: Detailed fuel composition in weight percent

	FT Natural Gas	FT Coal	HP Camelina	HP Tallow	JP8	Pet-Aromatic
Total	100.00	100.00	100.00	100.00	100.00	100.00
Total Alkanes	99.57	99.49	99.69	99.76	80.03	0.73
n-Alkanes	23.29	2.83	11.39	11.67	19.74	0.07
C7	0.02	0.00	0.02	0.00	0.07	0.00
C8	1.44	0.01	0.75	0.11	0.39	0.00
C9	3.12	0.21	3.08	1.79	2.14	0.01
C10	3.94	1.66	2.68	1.81	3.66	0.04
C11	4.23	0.35	1.32	1.75	4.01	0.01
C12	3.87	0.46	1.13	1.72	3.32	0.00
C13	3.14	0.10	0.97	1.35	2.74	0.00
C14	2.18	0.05	0.78	2.75	2.01	0.00
C15	1.21	0.01	0.55	0.39	1.05	0.00
C16	0.14	0.00	0.10	0.01	0.34	0.00
iso-Alkanes	75.26	95.08	85.36	87.33	32.01	0.48
C7 and less	0.08	0.05	0.10	0.02	0.14	0.01
C8	1.55	0.78	0.68	0.07	0.35	0.01
C9	6.43	15.13	14.86	6.13	1.68	0.00
C10	8.32	28.16	19.97	12.50	6.33	0.27
C11	10.08	31.97	15.82	13.34	6.86	0.11
C12	11.52	13.16	10.35	14.24	5.95	0.07
C13	11.72	4.79	8.77	11.96	4.46	0.01
C14	10.99	0.85	6.12	13.91	3.38	0.00
C15	9.83	0.12	6.18	14.74	1.86	0.00
C16	4.47	0.03	2.12	0.42	0.68	0.00
C17 and more	0.28	0.04	0.38	0.01	0.32	0.00
Cycloalkanes	1.01	1.57	2.95	0.76	28.28	0.19
Mono-cycloalkanes	0.78	1.57	2.65	0.66	22.22	0.12
Di-cycloalkanes	0.24	0.00	0.30	0.10	6.05	0.07
Total Aromatics	0.43	0.51	0.31	0.24	19.97	99.27
Alkylbenzenes	0.36	0.44	0.28	0.21	15.16	76.56
Benzene	0.00	0.00	0.00	0.00	0.00	0.00
Toluene	0.00	0.00	0.00	0.00	0.06	0.00
C2 Benzene	0.01	0.00	0.02	0.01	0.69	0.54
C3 Benzene	0.09	0.09	0.08	0.03	3.64	28.14
C4 Benzene	0.07	0.16	0.07	0.06	3.48	36.85
C5 Benzene	0.08	0.08	0.03	0.04	2.31	9.97
C6+ Benzenes	0.10	0.10	0.08	0.08	4.98	1.07
Indans and Tetralins	0.06	0.07	0.03	0.02	2.47	7.16
Alkylnaphthalenes	0.02	0.00	0.00	0.00	2.34	15.55
Naphthalene	0.00	0.00	0.00	0.00	0.15	7.02
C1 Naphthalene	0.01	0.00	0.00	0.00	0.61	3.76
C2-C4 Naphthalenes	0.01	0.00	0.00	0.00	1.58	4.77

A.3 Fluid Properties

This section is a centralized location of all of the properties used in the analysis performed for this study. The gaseous fuels, liquid fuels, and non-fuel gases are presented separately. Also, there is a brief discussion on how some properties are determined for the complex liquid fuels.

A.3.1 Complex Fuel Properties

Table A.3: Complex liquid fuel properties

Fuel	**Global Formula**[1]	**Enthalpy of Formation**[2]	**Specific Heat**[3]	**Molecular Weight**[1]	**Density**[4]	**Heat of Combustion**[5]	$\left.\frac{\dot{m}_F}{\dot{m}_A}\right\rvert_{stoich}$
		[kJ/kmol]	**[kJ/kg K]**	**[kg/kmol]**	**[kg/m^3]**	**[MJ/kg]**	
FT Natural Gas	$C_{11.9}H_{25.9}$	-322,560	1.63-2.00	169.5	755	44.2	0.066894
FT Coal	$C_{10.7}H_{22.7}$	-271,720	1.57-1.96	151.9	760	44.0	0.067270
HP Camelina	$C_{11.3}H_{24.5}$	-294,490	1.60-1.99	160.6	751	44.3	0.066837
HP Tallow	$C_{12.3}H_{26.5}$	-335,730	1.63-1.99	174.8	758	44.1	0.066981
JP8	$C_{11.9}H_{22.8}$	-256,170	1.49-1.85	165.9	800	43.3	0.068356
Pet-Aromatic	$C_{9.9}H_{12.9}$	-69,057	1.22-1.60	131.7	901	40.9	0.072766

1. Obtained from tests performed at AFRL [62]
2. Calculated as shown below
3. Obtained from NIST SUPERTRAPP [100]; inputs were the 50% boiling point from Figure A.2 and API gravity from the density
4. Obtained per ASTM D1298-12 [62,101] at 70oF and 1 atm,
5. Obtained per ASTM D3338-09 [62,102] as the Net Heat of Combustion

The thermodynamic properties for the liquid fuels require a specific heat polynomial. The one proposed by Ryder *et al.* [64] and Brankovic *et al.* [103] was selected and given in Equation A.1. Strictly speaking, this polynomial is meant for FT Natural Gas, but since the fuels are similar, the polynomial has been assumed for all the liquid fuels.

$$\bar{c_p} = -15202T^{-0.5} + 1097.8 \qquad \text{kJ/kmol K} \tag{A.1}$$

Certain studies (especially sooting) using laminar premixed flames require knowledge of specific combustion properties for these alternative fuels. Kumar *et al.* [22] provided laminar flame speeds for Jet A and FT Natural Gas as a function of premix temperature and equivalence ratio. Later, Hui *et al.* [23] presented laminar flame speeds for Jet A, FT Natural Gas, FT Coal, HP Camelina, and HP Tallow.

Enthalpy of Formation for Complex Liquid Fuels

The enthalpy of formation shown in Table A.3 is really just an effective enthalpy of formation that is used to calculate the heat loss from the reactor. Since these fuels are made up of many species, there really is not an enthalpy of formation, so this alternative is calculated from an energy balance on the system shown schematically in Figure A.1.

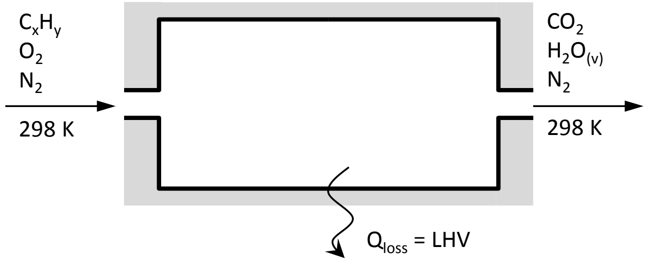

Figure A.1: Schematic used for calculating enthalpy of formation

Setting up the energy balance around this system results in Equation A.2 where the LHV is the same as the heat of combustion given in Table A.3 (i.e., LHV is 44,200 kJ/kg for FT Natural Gas). Using the global reaction for FT Natural Gas as an example (repeated here as Reaction A.3), Table A.4 helps calculate H_R and H_P.

A.2 $$\mathrm{LHV} = \mathrm{H_R} - \mathrm{H_P}$$ kJ/kmol

A.3 $$C_{11.9}H_{25.9} + 18.375[O_2 + 3.76N_2] \longrightarrow 11.9CO_2 + 12.95H_2O + 69.09N_2$$ FT Natural Gas

Table A.4: Calculating the enthalpy of formation for complex fuels

	Species	**Amount**	**h_f**	**h_T-h_{298}**	**H**	**∑H**
		[kmol]	**[kJ/kmol]**	**[kJ/kmol]**	**[kJ]**	**[kJ/kmol$_{fuel}$]**
Reactants	$C_{11.9}H_{25.9}$	1	$h_{f,fuel}$	0	$h_{f,fuel}$	$H_R = h_{f,fuel}$
	O_2	18.375	0	0	0	
	N_2	69.09	0	0	0	
Products	CO_2	11.9	-393,520	0	-4,682,888	H_P = -7,814,457
	$H_2O_{(v)}$	12.95	-241,820	0	-3,131,569	
	N_2	69.09	0	0	0	

The only unknown is $h_{f,fuel}$, which is determined for FT Natural Gas to be -322,560 kJ/kmol as shown in Table A.3. This same process was performed for each fuel.

Boiling Point Distribution

Burning liquid fuels first requires vaporization. The vaporization system on the TSR was designed for the most common fuel of FT Natural Gas, but the system often runs with other fuels. One way to compare the ability of a fuel to vaporize is to compare the boiling point distributions as determined by AFRL using the ASTM D86 Standard [62,104] and shown in Figure A.2.

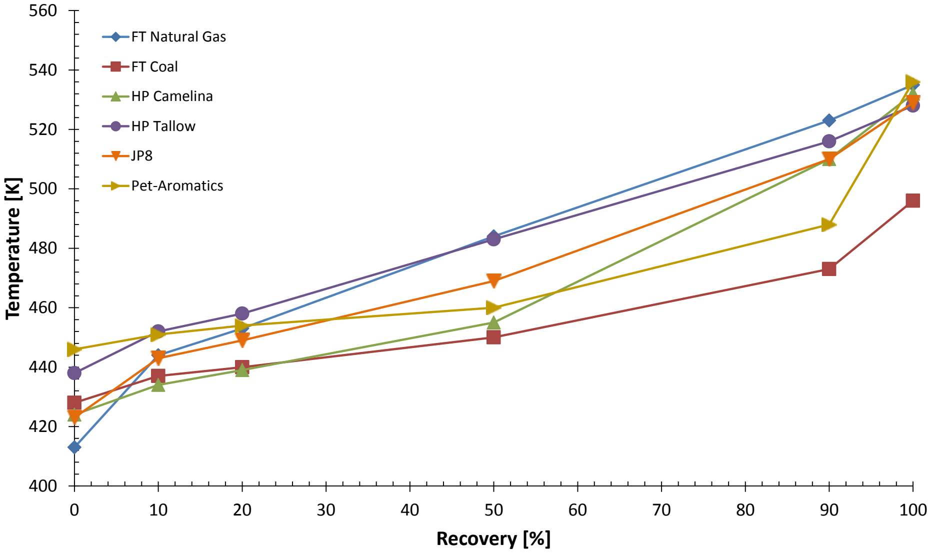

Figure A.2: Boiling point distributions for liquid fuels [62,104]

Properties for Blends of Fuels

The TSR system utilized two separate fuel delivery systems, so the relevant properties were calculated from individual flow rates. The JSR system had only one fuel delivery system, so the fuels were blended in a beaker before being poured into the fuel container. The blended fuel will have a different global formula, molecular weight, and density. The values from Table A.3 were used to calculate the new properties, which are presented in Table A.5.

In order to calculate the global formula, molecular weight, and density, first assume a 1000 mL sample of fuel that consisted of 800 mL of the primary fuel and 200 mL of the secondary fuel. The density of each fuel was used to convert the volume into mass. The ratio of the total mass to the 1000 mL gives the density of the fuel blend.

Table A.5: Fuel blend properties

Fuel #1	**%**	**Fuel #2**	**%**	**Global Formula**	**Molecular Weight**	**Density**	$\left.\frac{\dot{m}_F}{\dot{m}_A}\right\vert_{stoich}$
					[kg/kmol]	**[kg/m^3]**	
FT Natural Gas	80	Pet-Aromatic	20	$C_{11.3}H_{22.3}$	159.0	784	0.068158
FT Coal				$C_{10.5}H_{20.2}$	146.8	788	0.068452
HP Camelina				$C_{10.9}H_{21.4}$	152.9	781	0.068118
HP Tallow				$C_{11.6}H_{22.7}$	162.6	767	0.068223

The mass and molecular weight of each individual fuel determine the moles of each fuel in the blend and the total moles of fuel, which give mole fractions. The molecular weight of the fuel blend is calculated as a mole-weighted average. The global formula of the fuel blend is determined by taking a mole-weighted average of the number of carbon atoms and the number of hydrogen atoms in the original fuels.

Sensitivity Analysis of Measured Fuel Properties

The complex fuels properties listed in Table A.3 are all measured and contain some uncertainty. The uncertainty was not quantified by the personnel at AFRL, but is important when used in combustion calculations. The global formula (C_xH_y), density (ρ), and molecular weight (MW) all go into determining the equivalence ratio that defines the stoichiometry of the system.

A very simplified sensitivity analysis was performed by varying each of the four parameters (x, y, ρ, and MW) by a given percentage independently and calculating the variation in the equivalence ratio. For example, the properties of FT Natural Gas could vary as seen in Table A.6. Each of the four properties has three possibilities which results in 81 ($=3^4$) possible combinations. One of those possible combinations is the as measured (0% uncertainty) case which results in an equivalence ratio of $\phi = 0.5626$ for typical air and fuel flow rates.

Table A.6: Example uncertainty possibilities in FT Natural Gas properties

Parameter	Uncertainty		
	-5%	0%	5%
x	11.31	11.90	12.50
y	24.61	25.90	27.20
MW [g/mol]	161.0	169.5	178.0
ρ [g/mL]	0.7173	0.7550	0.7928

The equivalence ratio was calculated for each of the other 80 possibilities for ±5% uncertainty in the four parameters. The maximum equivalence ratio was $\phi = 0.6530$, which is 16% larger than the base case. The minimum equivalence ratio was $\phi = 0.4836$, which is 14% smaller than the base case. Considering a possible uncertainty of ±10% the cascading uncertainty causes a 34% larger or 26% smaller equivalence ratio when compared to the base case.

A small uncertainty in the measured fuel properties could result in a moderate uncertainty in the equivalence ratio. When comparing the equivalence ratio based on flow rates to the equivalence ratio from the exhaust this uncertainty should be considered.

A.3.2 Simple Fuel Properties

Table A.7: Simple gaseous fuel properties [105]

Fuel	Formula	Molecular Weight	Standard Density[1]	Higher Heating Value	Enthalpy of Formation	$\left.\frac{\dot{m}_F}{\dot{m}_A}\right\|_{stoich}$
		[kg/kmol]	[kg/m³]	[MJ/kg]	[kJ/kmol]	
Methane	CH_4	16.043	0.663	55.53	-74,850	0.058170
Ethane	C_2H_6	30.070	1.242	51.90	-84,680	0.062303
Propane	C_3H_8	44.097	1.882	50.33	-103,850	0.063956

1. Standard Density is calculated at 70oF and 1 atm via the Ideal Gas Law

Table A.8: Simple liquid fuel properties [54,106,107]

Fuel	Global Formula	Boiling Point[1]	Molecular Weight	Density[2]	Heat of Combustion[3]	$\left.\frac{\dot{m}_F}{\dot{m}_A}\right\|_{stoich}$
		[K]	[kg/kmol]	[kg/m³]	[MJ/kg]	
135-TMB	C_9H_{12}	437.9	120.2	861	41.0	0.072639

1. At 1 atm
2. At 25oC
3. For liquid fuel and gaseous H_2O

Table A.9: Specific heat polynomials for gaseous fuels [105]

Fuel	**Formula**	**Specific Heat Polynomial, $\overline{c_p} = a + bT + cT^2 + dT^3$ T in [K] and $\overline{c_p}$ in [kJ/kmol K]**			
		a	**b**	**c**	**d**
Methane	CH_4	19.89	5.024×10^{-2}	1.269×10^{-5}	-11.01×10^{-9}
Ethane	C_2H_6	6.90	17.27×10^{-2}	-6.406×10^{-5}	7.285×10^{-9}
Propane	C_3H_8	-4.04	30.48×10^{-2}	-15.72×10^{-5}	31.74×10^{-9}

A.3.3 Non-Fuel Gas Properties

Table A.10: Non-fuel gas properties [105]

Fluid	**Formula**	**Enthalpy of Formation**	**Molecular Weight**	**Standard Density[1]**
		[kJ/kg]	**[kg/kmol]**	**[kg/m^3]**
Oxygen	O_2	0	31.999	1.3253
Nitrogen	N_2	0	28.013	1.1602
Carbon Monoxide	CO	-110,530	28.011	1.1601
Carbon Dioxide	CO_2	-393,520	44.01	1.8227
Water Vapor	H_2O	-241,820	18.015	0.7461
Air	-	-	28.97	1.1998

1. Density is calculated at 70oF and 1 atm via the Ideal Gas Law

Table A.11: Specific heat polynomials for non-fuel gases [105]

Fluid	**Formula**	**Specific Heat Polynomial, $\overline{c_p} = a + bT + cT^2 + dT^3$ T in [K] and $\overline{c_p}$ in [kJ/kmol K]**			
		a	**b**	**c**	**d**
Oxygen	O_2	25.48	1.520×10^{-2}	-0.7155×10^{-5}	1.312×10^{-9}
Nitrogen	N_2	28.90	-0.1571×10^{-2}	0.8081×10^{-5}	-2.873×10^{-9}
Carbon Monoxide	CO	28.16	0.1675×10^{-2}	0.5372×10^{-5}	-2.222×10^{-9}
Carbon Dioxide	CO_2	22.26	5.981×10^{-2}	-3.501×10^{-5}	7.469×10^{-9}
Water Vapor	H_2O	32.24	0.1923×10^{-2}	1.055×10^{-5}	-3.595×10^{-9}

Appendix B
Complete Experimental Conditions and Results

This portion of the work presents the results of each test for each fuel and fuel blend. The data presented in the tables below are the results of the analysis described in Chapter 3, Chapter 4, and Chapter 5. The NO_X results present the correlation plots for one unit basis, and all the correlations in tables.

In some cases the tests were performed in different years (2010, 2011, 2012, or 2013), which is indicated by the first two digits of the test number. In some cases, the test numbers are non-sequential which indicates that the missing tests were discarded for some reason. The data files contain the complete details.

B.1 Blowout Tests

Table B.1: Extinction results for JP8

Fuel	**Aromatic**	**Reactor**	**Test**	**ϕ**	**$T_{product}$**	**LP**	**τ**
				[-]	**[K]**	**$\left[\frac{mol}{L\ s\ atm^{1.8}}\right]$**	**[ms]**
JP8	18.7% (Natural)	TSR	10-1	0.397	1365.1	1.11	7.91
			10-2	0.399	1355.0		7.97
			10-3	0.399	1355.4		7.97
			10-4	0.398	1359.0		7.94
			10-5	0.398	1358.5		7.95
			Median	0.398	1358.5		7.95
		JSR	13-1	0.428	1350.6	2.52	3.55

Table B.2: Extinction results for FT Coal

Fuel	**Aromatic**	**Reactor**	**Test**	**ϕ**	**$T_{product}$**	**LP**	**τ**
				[-]	**[K]**	**$\left[\frac{mol}{L\ s\ atm^{1.8}}\right]$**	**[ms]**
FT Coal	0% (Unmodified)	TSR	10-1	0.397	1364.1	1.11	7.91
			10-2	0.401	1365.7		7.90
			10-3	0.402	1362.9		7.92
			10-4	0.403	1367.8		7.89
			10-5	0.403	1360.5		7.93
			10-6	0.403	1364.8		7.91
			10-7	0.404	1365.8		7.91
			Median	0.403	1364.8		7.91
	10% Pet-Aromatic	TSR	10-1	0.401	1365.9	1.11	7.90
			10-2	0.401	1366.9		7.90
			10-4	0.400	1365.7		7.91
			Median	0.401	1365.9		7.90
	20% Pet-Aromatic	TSR	10-3	0.399	1372.5	1.11	7.87
			10-4	0.399	1367.1		7.89
			10-5	0.399	1371.2		7.87
			10-7	0.399	1365.5		7.90
			Median	0.399	1369.1		7.88
		JSR	13-1	0.438	1341.5	2.52	3.57

Table B.3: Extinction results for FT Natural Gas

Fuel	**Aromatic**	**Reactor**	**Test**	**ϕ**	**$T_{product}$**	**LP**	**τ**
				[-]	**[K]**	$\left[\frac{\mathrm{mol}}{\mathrm{L\ s\ atm^{1.8}}}\right]$	**[ms]**
FT Natural Gas	0% (Unmodified)	TSR	10-1	0.397	1363.9	1.11	7.92
			10-2	0.393	1362.0		7.93
			10-3	0.400	1357.5		7.96
			11-1	0.404	1358.4		8.00
			11-2	0.403	1353.2		8.03
			11-3	0.404	1358.2		8.00
			Median	0.402	1358.3		7.98
	10% Pet-Aromatic	TSR	10-1	0.395	1356.0	1.11	7.96
			10-2	0.396	1351.6		7.99
			10-3	0.396	1357.1		7.96
			Median	0.396	1356.0		7.96
	20% Pet-Aromatic	TSR	10-1	0.399	1376.0	1.11	7.85
			10-2	0.403	1376.0		7.85
			10-3	0.401	1363.0		7.92
			10-4	0.396	1360.7		7.93
			10-5	0.397	1355.1		7.97
			10-6	0.398	1365.7		7.91
			11-1	0.406	1364.7		7.96
			11-2	0.406	1361.7		7.97
			11-3	0.406	1356.5		8.00
			Median	0.401	1363.0		7.93
		JSR	13-1	0.430	1361.0	2.52	3.53
	40% Pet-Aromatic	TSR	11-1	0.415	1396.5	1.11	7.79
			11-2	0.413	1380.6		7.87
			11-3	0.411	1386.2		7.84
			11-4	0.409	1364.2		7.96
			Median	0.412	1383.4		7.85
	60% Pet-Aromatic	TSR	11-1	0.410	1378.9	1.11	7.88
			11-2	0.417	1383.4		7.86
			11-3	0.414	1375.4		7.90
			Median	0.414	1378.9		7.88
	80% Pet-Aromatic	TSR	11-1	0.411	1389.1	1.11	7.82
			11-2	0.415	1386.5		7.83
			11-3	0.419	1383.3		7.85
			Median	0.415	1386.5		7.83

Table B.4: Extinction results for HP Camelina

Fuel	**Aromatic**	**Reactor**	**Test**	**ϕ**	**$T_{product}$**	**LP**	**τ**
				[-]	**[K]**	$\left[\frac{\mathbf{mol}}{\mathbf{L\ s\ atm^{1.8}}}\right]$	**[ms]**
HP Camelina	0% (Unmodified)	TSR	10-1	0.400	1365.7	1.11	7.91
			10-2	0.400	1348.3		8.00
			10-3	0.400	1355.4		7.96
			10-4	0.401	1358.0		7.95
			10-5	0.401	1353.8		7.97
			Median	0.400	1355.4		7.96
	10% Pet-Aromatic	TSR	10-1	0.400	1357.7	1.11	7.95
			10-2	0.400	1358.0		7.95
			10-3	0.400	1352.2		7.98
			10-4	0.400	1355.5		7.96
			Median	0.400	1356.6		7.96
	20% Pet-Aromatic	TSR	10-1	0.397	1361.8	1.11	7.93
			10-2	0.396	1356.4		7.96
			10-3	0.396	1358.6		7.95
			10-4	0.398	1361.0		7.92
			10-5	0.397	1362.6		7.92
			10-7	0.398	1363.4		7.92
			Median	0.397	1361.4		7.93
		JSR	13-1	0.429	1334.9	2.52	3.59

Table B.5: Extinction results for Pet-Aromatic

Fuel	**Aromatic**	**Reactor**	**Test**	**ϕ**	**$T_{product}$**	**LP**	**τ**
				[-]	**[K]**	$\left[\frac{\mathbf{mol}}{\mathbf{L\ s\ atm^{1.8}}}\right]$	**[ms]**
Pet-Aromatic	100% (Unmodified)	TSR	11-1	0.42	1413.1	1.11	7.69
			11-2	0.42	1409.6		7.71
			11-3	0.41	1396.8		7.77
			11-4	0.41	1396.9		7.77
			Median	0.42	1403.2		7.74

Table B.6: Extinction results for HP Tallow

Fuel	Aromatic	Reactor	Test	ϕ	$T_{product}$	LP	τ
				[-]	[K]	$\left[\frac{mol}{L\ s\ atm^{1.8}}\right]$	[ms]
HP Tallow	0% (Unmodified)	TSR	10-1	0.385	1355.0	1.11	7.97
			10-2	0.388	1351.7		7.99
			10-3	0.388	1349.3		8.00
			10-4	0.394	1353.0		7.98
			10-5	0.397	1352.1		7.99
			10-6	0.397	1351.7		7.99
			10-7	0.394	1352.7		7.98
			Median	0.394	1352.1		7.99
	10% Pet-Aromatic	TSR	10-1	0.397	1359.0	1.11	7.95
			10-2	0.397	1352.9		7.98
			10-3	0.396	1354.7		7.97
			10-4	0.397	1355.8		7.96
			10-5	0.397	1358.8		7.95
			10-6	0.399	1354.5		7.97
			10-7	0.398	1354.2		7.97
			10-8	0.399	1361.0		7.94
			10-9	0.399	1360.6		7.94
			Median	0.397	1355.8		7.96
	20% Pet-Aromatic	TSR	10-1	0.398	1359.7	1.11	7.94
			10-2	0.398	1358.3		7.95
			10-3	0.398	1360.8		7.94
			10-4	0.398	1363.7		7.92
			Median	0.398	1360.2		7.94
		JSR	13-1	0.443 3	1383.8	2.52	3.47

Table B.7: Extinction results for methane

Fuel	Reactor	Test	ϕ	$T_{product}$	LP	τ
			[-]	[K]	$\left[\frac{mol}{L\ s\ atm^{1.8}}\right]$	[ms]
Methane	TSR	11-1	0.501	1528.4	1.11	6.85
		11-2	0.507	1551.8		6.74
		11-3	0.504	1538.1		6.80
		11-4	0.501	1538.5		6.81
		Median	0.503	1538.3		6.81
	JSR	12-1	0.522	1495.6	2.34	3.29
		12-2	0.522	1497.3		3.29
		12-3	0.522	1503.3		3.27
		12-4	0.514	1500.4		3.28
		Median	0.522	1498.8		3.28

Table B.8: Extinction results for ethane

Fuel	Reactor	Test	ϕ	$T_{product}$	LP	τ
			[-]	[K]	$\left[\frac{mol}{L\ s\ atm^{1.8}}\right]$	[ms]
Ethane	TSR	11-1	0.419	1396.8	1.11	7.70
		11-2	0.416	1400.1		7.68
		11-3	0.409	1395.9		7.71
		11-4	0.406	1393.7		7.72
		Median	0.413	1396.4		7.70
	JSR	12-1	0.472	1400.0	2.34	3.61
		12-2	0.463	1389.1		3.64
		12-3	0.463	1391.5		3.63
		Median	0.463	1391.5		3.63

Table B.9: Extinction results for propane

Fuel	Reactor	Test	ϕ	$T_{product}$	LP	τ
			[-]	[K]	$\left[\frac{mol}{L\ s\ atm^{1.8}}\right]$	[ms]
Propane	TSR	11-1	0.462	1419.0	1.11	7.62
		11-2	0.469	1457.6		7.42
		11-3	0.462	1442.2		7.50
		11-4	0.456	1421.0		7.85
		Median	0.462	1431.6		7.56
	JSR	12-1	0.522	1518.4	2.34	3.35
		12-2	0.513	1501.0		3.39
		12-3	0.504	1507.6		3.37
		Median	0.513	1507.6		3.37

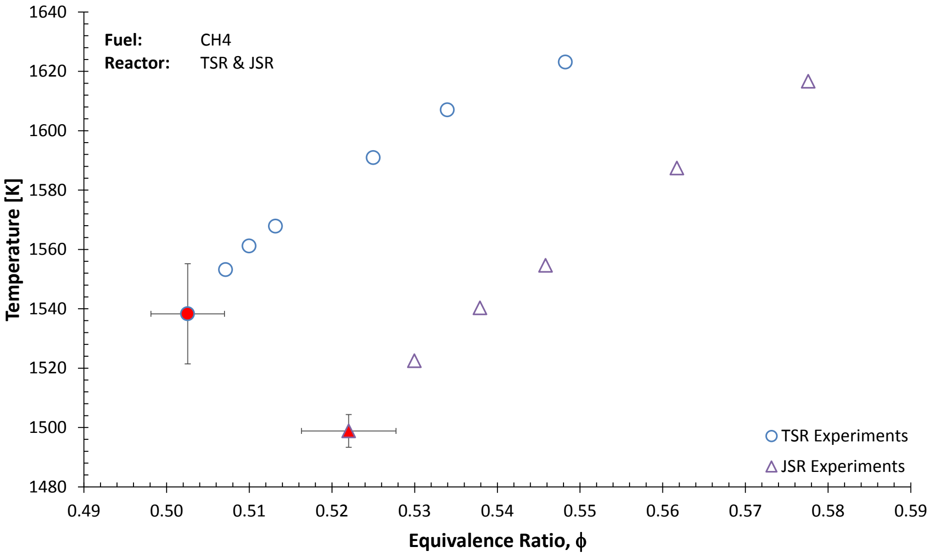

Figure B.1: Comparison of methane on TSR and JSR

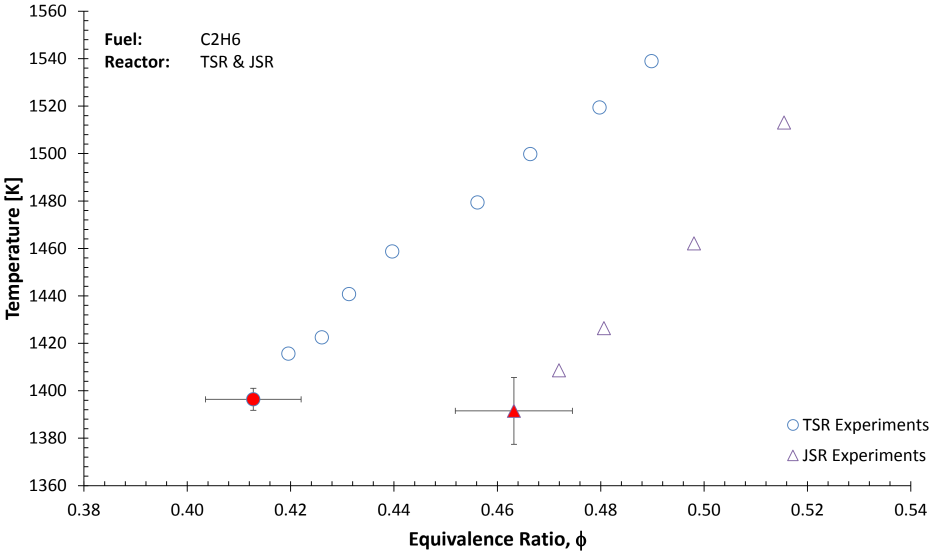

Figure B.2: Comparison of ethane on TSR and JSR

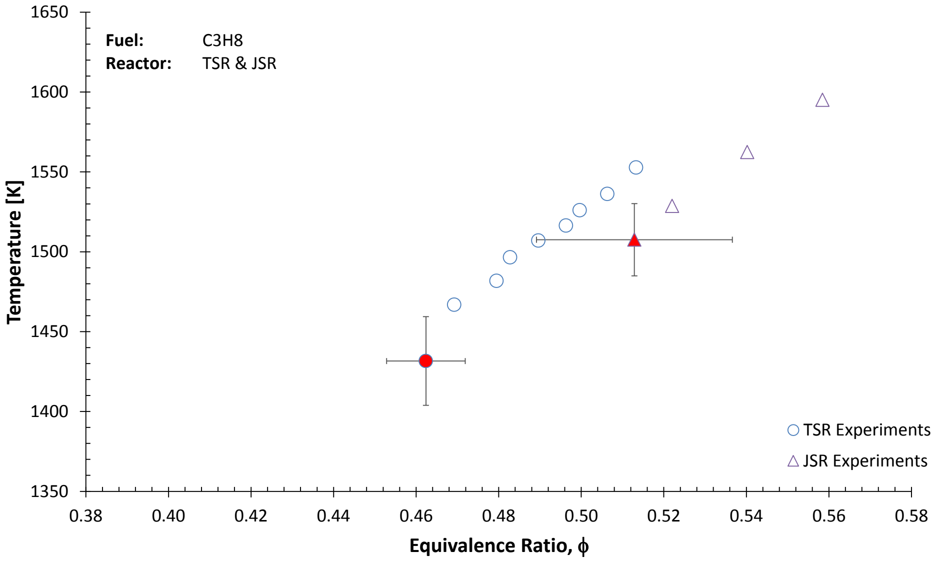

Figure B.3: Comparison of propane on TSR and JSR

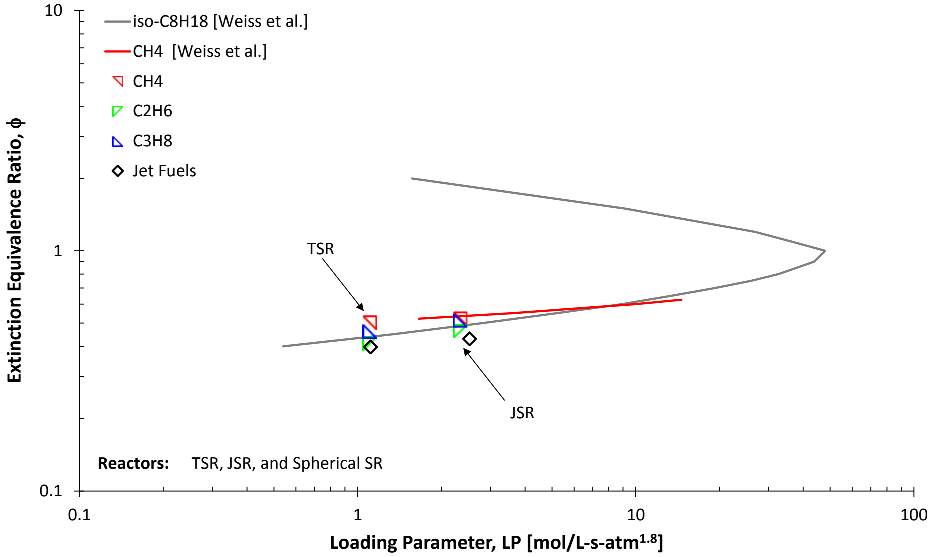

Figure B.4: Comparison of ϕ_{ext} vs. loading parameter with Weiss *et al.* [12]

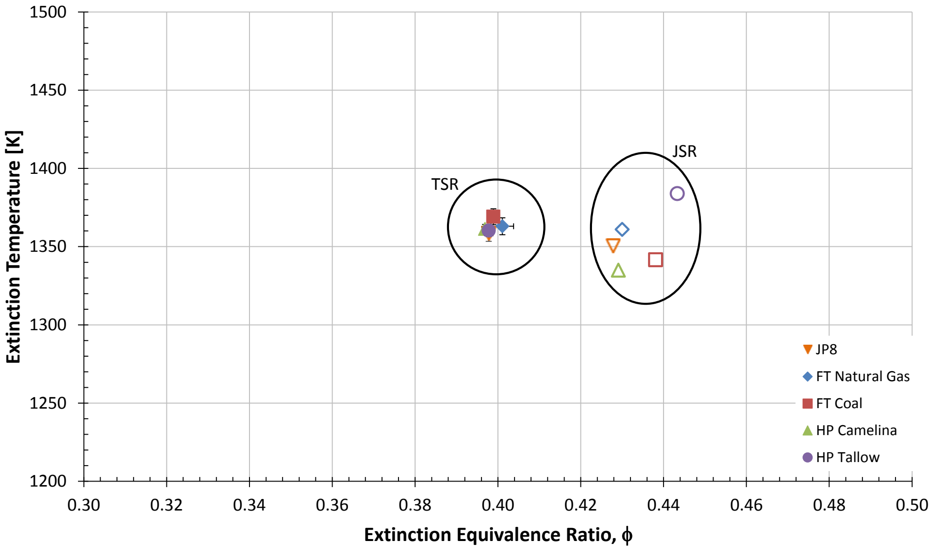

Figure B.5: T_{ext} versus ϕ_{ext} for jet fuels on TSR and JSR

B.2 NO_X Tests

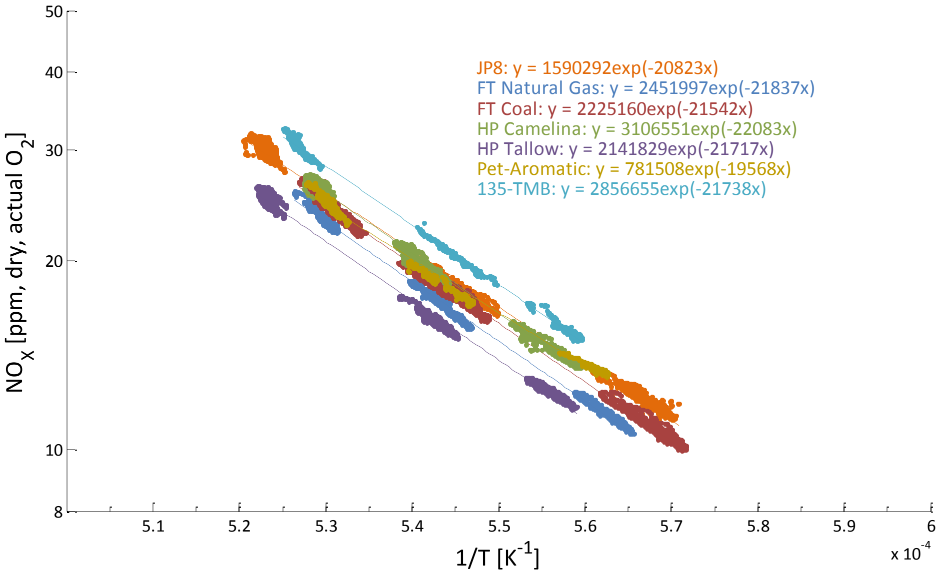

Figure B.6: NO_X vs. 1/T for unmodified fuels

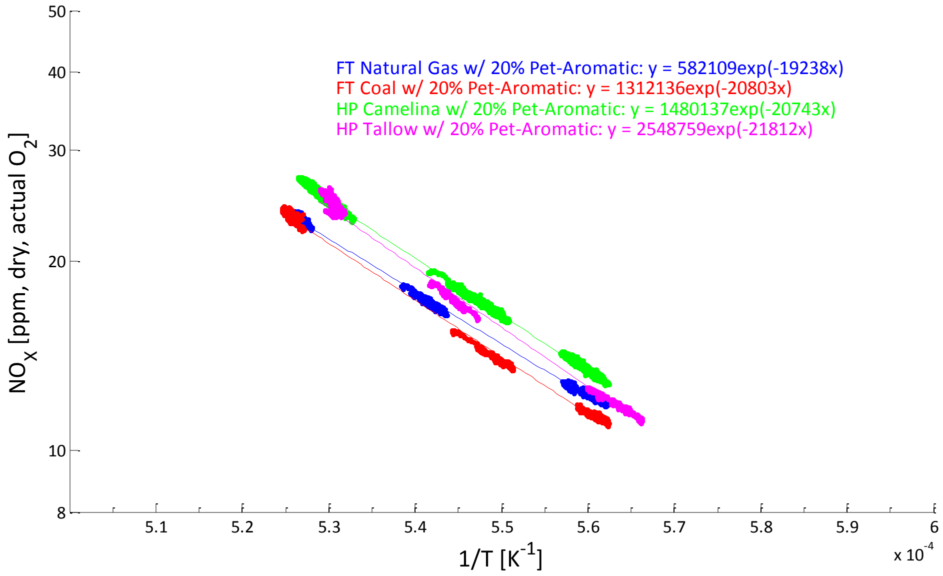

Figure B.7: NO_X vs. 1/T for synthetic fuels blended with 20% Pet-Aromatic

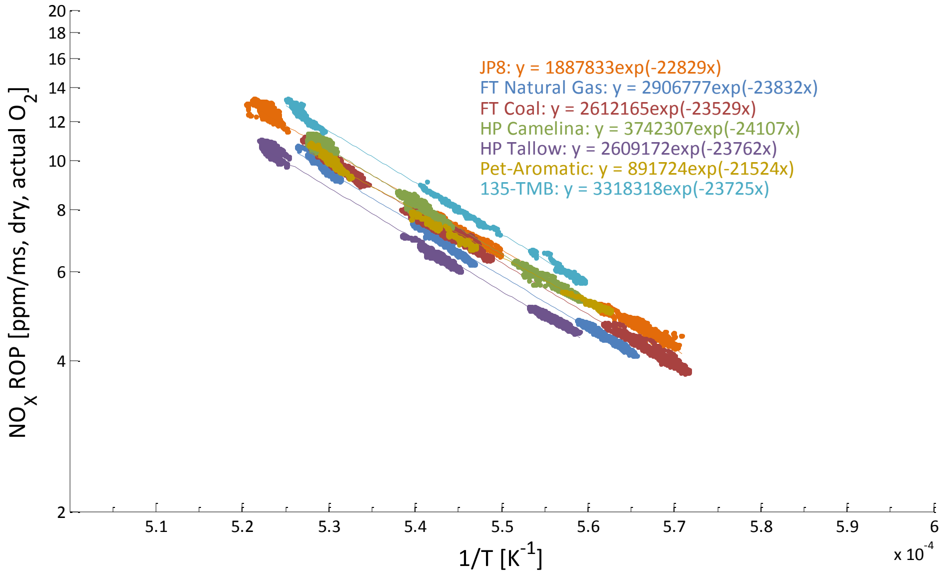

Figure B.8: NO_X ROP vs. 1/T for unmodified fuels

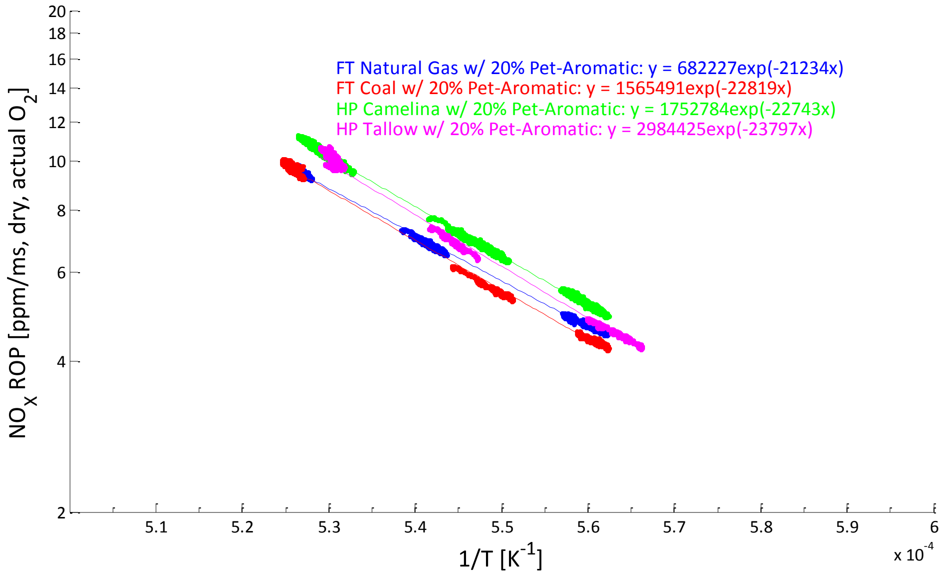

Figure B.9: NO_X ROP vs. 1/T for synthetic fuels blended with 20% Pet-Aromatic

Table B.10: NO_X concentration curve fit coefficients [ppm, dry, actual O_2]

Fuel	**Aromatic**	**$NO_X = A\exp\left(B/T\right)$**		**Experimental Range**
		A	**B**	
		[ppm, dry, actual O_2]	**[K]**	**[K]**
JP8	18.7% Natural	1590292	-20823	1750-1920
FT Natural Gas	0% Natural	2451997	-21837	1770-1900
	20% Pet-Aromatic	582109	-19238	1780-1900
FT Coal	0% Natural	2225160	-21542	1750-1900
	20% Pet-Aromatic	1312136	-20803	1780-1910
HP Camelina	0% Natural	3106551	-22083	1790-1900
	20% Pet-Aromatic	1480137	-20743	1780-1900
HP Tallow	0% Natural	2141829	-21717	1790-1915
	20% Pet-Aromatic	2548759	-21812	1770-1890
Pet-Aromatic	100% Natural	781508	-19568	1780-1900
135-TMB	100% Natural	2856655	-21738	1790-1910

1. This table was originally presented as Table 5.5

Table B.11: NO_X concentration curve fit coefficients [ppm, wet, actual O_2]

Fuel	**Aromatic**	**$NO_X = A\exp(B/T)$**		**Experimental Range**
		A	**B**	
		[ppm, wet, actual O_2]	**[K]**	**[K]**
JP8	18.7% Natural	1679539	-21041	1750-1920
FT Natural Gas	0% Natural	2123642	-21668	1770-1900
	20% Pet-Aromatic	565452	-19303	1780-1900
FT Coal	0% Natural	1976804	-21454	1750-1900
	20% Pet-Aromatic	1480744	-21143	1780-1910
HP Camelina	0% Natural	2748094	-21985	1790-1900
	20% Pet-Aromatic	1568231	-20925	1780-1900
HP Tallow	0% Natural	2166868	-21887	1790-1915
	20% Pet-Aromatic	2442081	-21862	1770-1890
Pet-Aromatic	100% Natural	783079	-19662	1780-1900
135-TMB	100% Natural	2769554	-21780	1790-1910

Table B.12: NO_X concentration curve fit coefficients [ppm, dry, 15% O_2]

Fuel	**Aromatic**	**$NO_X = A\exp(B/T)$**		**Experimental Range**
		A	**B**	
		[ppm, dry, 15% O_2]	**[K]**	**[K]**
JP8	18.7% Natural	88322	-17065	1750-1920
FT Natural Gas	0% Natural	180134	-18606	1770-1900
	20% Pet-Aromatic	37844	-15735	1780-1900
FT Coal	0% Natural	137110	-17963	1750-1900
	20% Pet-Aromatic	68717	-16905	1780-1910
HP Camelina	0% Natural	182686	-18422	1790-1900
	20% Pet-Aromatic	93051	-17215	1780-1900
HP Tallow	0% Natural	107575	-17746	1790-1915
	20% Pet-Aromatic	164133	-18322	1770-1890
Pet-Aromatic	100% Natural	48905	-15943	1780-1900
135-TMB	100% Natural	153920	-17846	1790-1910

Table B.13: NO_X concentration curve fit coefficients [ppm, wet, 15% O_2]

Fuel	Aromatic	$NO_X = A\exp(B/T)$ A	$NO_X = A\exp(B/T)$ B	Experimental Range
		[ppm, wet, 15% O_2]	[K]	[K]
JP8	18.7% Natural	93279	-17283	1750-1920
FT Natural Gas	0% Natural	156012	-18437	1770-1900
	20% Pet-Aromatic	36761	-15799	1780-1900
FT Coal	0% Natural	121807	-17876	1750-1900
	20% Pet-Aromatic	77547	-17245	1780-1910
HP Camelina	0% Natural	161607	-18324	1790-1900
	20% Pet-Aromatic	98590	-17397	1780-1900
HP Tallow	0% Natural	108833	-17916	1790-1915
	20% Pet-Aromatic	157263	-18373	1770-1890
Pet-Aromatic	100% Natural	49003	-16037	1780-1900
135-TMB	100% Natural	149227	-17887	1790-1910

Table B.14: NO_X production rate curve fit coefficients [ppm/ms, dry, actual O_2]

Fuel	Aromatic	$NO_XROP = A\exp(B/T)$ A	$NO_XROP = A\exp(B/T)$ B	Experimental Range
		[ppm/ms, dry, actual O_2]	[K]	[K]
JP8	18.7% Natural	1887833	-22829	1750-1920
FT Natural Gas	0% Natural	2906777	-23832	1770-1900
	20% Pet-Aromatic	682227	-21234	1780-1900
FT Coal	0% Natural	2612165	-23529	1750-1900
	20% Pet-Aromatic	1565491	-22819	1780-1910
HP Camelina	0% Natural	3742307	-24107	1790-1900
	20% Pet-Aromatic	1752784	-22743	1780-1900
HP Tallow	0% Natural	2609172	-23762	1790-1915
	20% Pet-Aromatic	2984425	-23797	1770-1890
Pet-Aromatic	100% Natural	891724	-21524	1780-1900
135-TMB	100% Natural	3318318	-23725	1790-1910

Table B.15: NO_X production rate curve fit coefficients [ppm/ms, wet, actual O_2]

Fuel	**Aromatic**	$\mathbf{NO_XROP = A\exp\left(B/T\right)}$		**Experimental Range**
		A	**B**	
		[ppm/ms, wet, actual O_2]	**[K]**	**[K]**
JP8	18.7% Natural	1993777	-23048	1750-1920
FT Natural Gas	0% Natural	2517521	-23663	1770-1900
	20% Pet-Aromatic	662705	-21299	1780-1900
FT Coal	0% Natural	2320614	-23442	1750-1900
	20% Pet-Aromatic	1766655	-23159	1780-1910
HP Camelina	0% Natural	3310492	-24009	1790-1900
	20% Pet-Aromatic	1857105	-22926	1780-1900
HP Tallow	0% Natural	2639674	-23932	1790-1915
	20% Pet-Aromatic	2859513	-23847	1770-1890
Pet-Aromatic	100% Natural	893517	-21618	1780-1900
135-TMB	100% Natural	3217140	-23766	1790-1910

Table B.16: NO_X production rate curve fit coefficients [ppm/ms, dry, 15% O_2]

Fuel	**Aromatic**	$\mathbf{NO_XROP = A\exp\left(B/T\right)}$		**Experimental Range**
		A	**B**	
		[ppm/ms, dry, 15% O_2]	**[K]**	**[K]**
JP8	18.7% Natural	104847	-19071	1750-1920
FT Natural Gas	0% Natural	213544	-20600	1770-1900
	20% Pet-Aromatic	44353	-17731	1780-1900
FT Coal	0% Natural	160956	-19950	1750-1900
	20% Pet-Aromatic	81985	-18921	1780-1910
HP Camelina	0% Natural	220073	-20446	1790-1900
	20% Pet-Aromatic	110192	-19215	1780-1900
HP Tallow	0% Natural	131048	-19791	1790-1915
	20% Pet-Aromatic	192188	-20307	1770-1890
Pet-Aromatic	100% Natural	55802	-17899	1780-1900
135-TMB	100% Natural	178794	-19833	1790-1910

Table B.17: NO_X production rate curve fit coefficients [ppm/ms, wet, 15% O_2]

Fuel	**Aromatic**	**$NO_XROP = A\exp\left(\frac{B}{T}\right)$**		**Experimental Range**
		A	**B**	
		[ppm/ms, wet, 15% O_2]	**[K]**	**[K]**
JP8	18.7% Natural	110731	-19290	1750-1920
FT Natural Gas	0% Natural	184948	-20432	1770-1900
	20% Pet-Aromatic	43084	-17795	1780-1900
FT Coal	0% Natural	142992	-19863	1750-1900
	20% Pet-Aromatic	92520	-19261	1780-1910
HP Camelina	0% Natural	194680	-20348	1790-1900
	20% Pet-Aromatic	116750	-19398	1780-1900
HP Tallow	0% Natural	132580	-19961	1790-1915
	20% Pet-Aromatic	184144	-20357	1770-1890
Pet-Aromatic	100% Natural	55914	-17993	1780-1900
135-TMB	100% Natural	173343	-19874	1790-1910

Appendix C
Heat Transfer Analyses

The heat transfer behavior of the reactors becomes important for applying the loss of energy to the CFD and CRMs. The heat loss from the TSR has been roughly estimated in previous work to be very small (even negligible). The analyses below estimate the heat loss through various methods. The magnitude of the heat loss from the JSR has been characterized previously, but an analysis presented here estimates the transient nature of the heat loss. In all cases the heat loss will be presented as a percentage of fuel energy input (the product of fuel flow rate and heating value).

C.1 Heat Loss in the Toroidal Stirred Reactor

Firstly, prior to this work the heat loss has been estimated by other researchers utilizing the toroidal stirred reactor in very similar configurations. The original concept came from Nenninger *et al.* [14] who estimated the reactor heat loss to be roughly 5% of energy input. Barat [31] widened the range slightly and estimated heat loss to be between 3-5% of energy input. The only CFD modeling work of this reactor by Briones *et al.* [33] estimated the reactor to be adiabatic.

For this work, the simplest way to estimate heat loss from the TSR is to do an energy balance based on the change in species and temperature between the inlet and the exit of the reactor (see the schematic of Figure C.1). The inlet flow rates of fuel and air are known as is the temperature of the premix entering the reactor. These constitute the reactants (symbolized by 'R') in Equation C.1 for the reactor heat loss. The products (symbolized by 'P') are determined as described in Appendix D based on the measured quantities of CO, CO_2, and O_2. The energy balance method resulted in values of roughly 3% of energy input.

$$\dot{Q} = \sum_{R} \dot{m}h - \sum_{P} \dot{m}h \qquad \text{W} \tag{C.1}$$

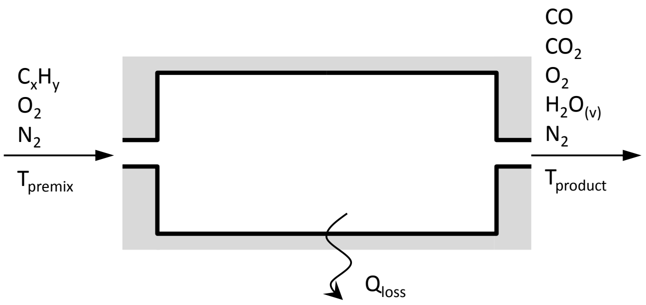

Figure C.1: Schematic used for heat loss calculation

A detailed heat transfer analysis helps to understand the routes the heat loss takes and serves as a way to compare heat loss paths. An analytical process is sufficient for this estimate, and begins with the thermal network shown in Figure C.2. The network assumes the toroid is a cylinder with a small region of the cylinder's circumference for the Inconel™ jet ring (lower branch) and the remainder for the alumina ceramic (upper branch).

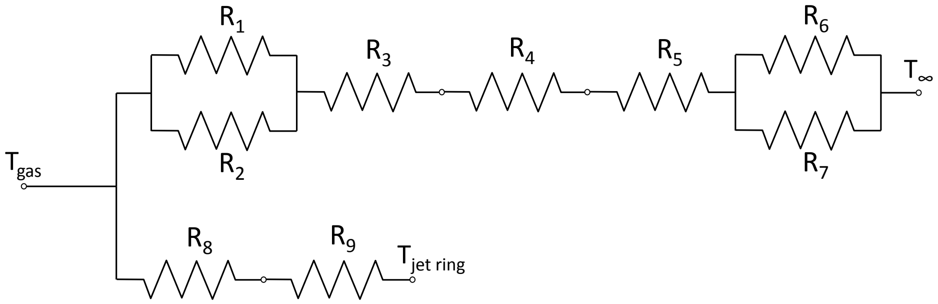

Figure C.2: Thermal network for TSR heat loss analysis

The network begins with the gas temperature at which point the heat can either transfer to the alumina reactor wall (upper branch) or the Inconel™ jet ring (lower branch). For the upper branch, the convection to the walls is assumed to be due to two flow fields in parallel: R_1 is the recirculating jet treated as an impinging jet and R_2 is the bulk flow treated as flow in a pipe. The correlations used to determine the heat transfer coefficient came from Incropera and DeWitt [108]. R_3 is conduction through the cylindrical alumina ceramic with the properties of Greencast® 94 [109]. R_4 is conduction through an insulation material, and R_5 is conduction through a steel housing. R_6 and R_7 are natural convection and radiation, respectively, ending at the room temperature of 300K.

For the lower branch, R_8 is physically the same as R_2 with the smaller area of the Inconel™ jet ring. R_9 is plane wall conduction through the Inconel™ jet ring. This branch ends with the temperature of the Inconel™ jet ring (roughly 560K) measured throughout the test as it was actively cooled by unmetered N_2. This detailed analysis estimates the heat loss to be roughly 8% of the fuel energy input.

As one last check, NASA's CEA [83,84] program was used to determine the equilibrium combustion temperature and enthalpy for an adiabatic reactor at a given equivalence ratio. When compared to the experimental conditions (equivalence ratio and temperature) for methane combustion, the difference amounted to roughly 1% heat loss.

The heat loss analysis results in ranges from roughly adiabatic (0% heat loss) to 8% heat loss based on energy input. Many previous studies using the toroidal reactor (Blust et al. [16], Barat [31], Nenniger et al. [14], Zelina and Ballal [1]) present similar values. The CFD analysis presented in Chapter 4 utilizes a reasonable value of 2.5% heat loss based on nominal energy input.

C.2 Heat Loss in the Jet Stirred Reactor

The heat loss from the JSR has been a critical aspect of previous performed by members of this research group. The analyses are thoroughly described by Fackler [25] and Karalus [28]. In general, they both estimated a heat loss of roughly 20% from the reactor. Karalus parameterized the heat loss to see the importance of the parameter and found that heat loss of 12-15% caused very little change in the results and maintained the same behavioral trends. Karalus performed an analytical transient calculation to estimate the thermal response time of the reactor, and found it to be approximately 10 minutes. The thermal network is shown in Figure C.3. The two network diagrams show that the TSR has greater resistance to heat loss than the JSR which is consistent with the analyses.

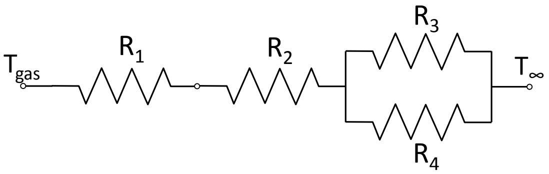

Figure C.3: Thermal network for JSR heat loss analysis [25,28]

The thermal response of the JSR was further investigated with simplified transient finite element modeling implemented in COMSOL [110] by undergraduate/graduate students gaining research experience. The students' analysis found that the region surrounding the reactor cavity reached steady state in roughly 7 minutes, and the whole reactor will near steady state after 20 minutes.

C.3 Thermocouple Correction

Lee [24] presents an extremely thorough description of the thermocouple correction for the JSR, which will be simplified for the discussion below. Considering the assumptions and simplifications that go into the analysis, the same correction correlation is used for both the TSR and JSR. The TSR system uses an S-type (100% platinum and 90%/10% platinum/rhodium) thermocouple. The JSR system uses an R-type (100% platinum and 87%/13% platinum/rhodium) thermocouple. Both thermocouple beads are coated with ceramic to prevent exothermic catalytic surface reactions.

The goal is to determine the actual gas temperature when the known temperature is the tip of the thermocouple. The hot gases are transferring energy to the thermocouple tip via convection, while the tip is losing energy via conduction through the sheath and wires, as well as via radiation to the reactor walls (see Equation C.2).

C.2 $$\dot{Q}_{conv} = \dot{Q}_{cond} + \dot{Q}_{rad} \qquad \text{W}$$

The convection value is determined with Newton's Law of Cooling where the heat transfer coefficient at the tip is determined from the Nusselt number correlation for the conditions inside the reactor. According to Lee [24], the conduction occurs in the thermocouple wire and through the ceramic sheath. The wire heat transfer is determined from a simple 1D conduction, and the sheath is treated as a fin. The radiation is determined assuming the thermocouple tip interacts with both the hot wall and with small cold-spots that are due to the ports in the reactor (for exhaust and measurement).

The analysis equations with the relevant assumptions were implemented in MS Excel to utilize the built-in Solver routine. The tip temperature is input and the MS Excel Solver determines the gas temperature causing Equation C.2 to be true. That is, the analysis determines the gas temperature that causes convective heating to be equal to the heat lost from the thermocouple tip due to conduction and radiation.

The analysis developed by Lee [24] was carried out for several values of thermocouple temperature from 1000°C to 1600°C (1273K to 1873K), which resulted in correction values between 15K and 52K. The corrected temperature was compared to the thermocouple temperature to obtain a simple linear correlation as shown in Figure C.4.

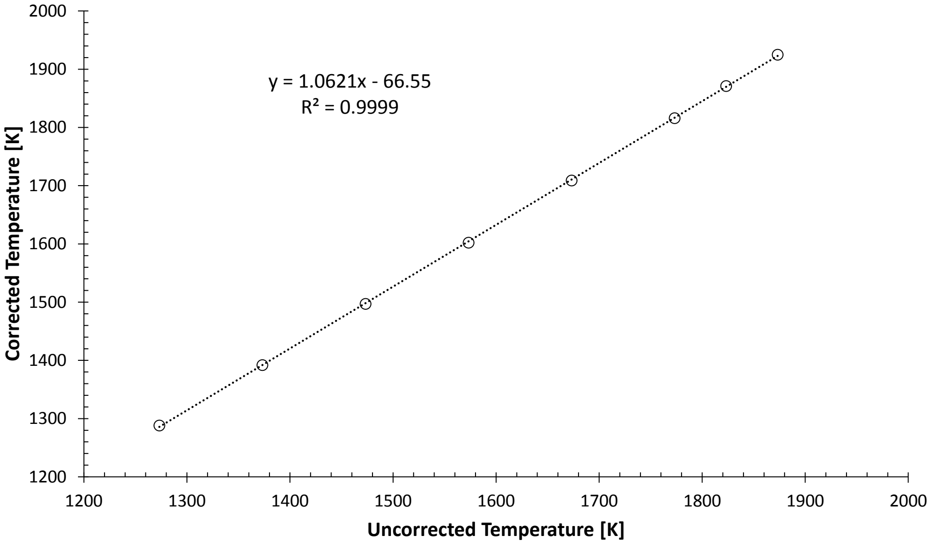

Figure C.4: Thermocouple temperature correction correlation

Appendix D
Data Analysis Details

The analysis methods for the combustion stability study (Chapter 3) and the NO_X study (Chapter 5) are slightly different. The relevant differences were highlighted in the respective chapters. The similar methods are described here as well as some details the reader may find useful.

The following parameters help characterize the emissions, chemistry, intensity, etc.

D.1 Wet-Basis Emissions

The experimental CO, O_2, and CO_2 emissions values are all on a dry basis since the water was condensed out of the exhaust stream before measurement. However, the fuel composition enables us to calculate the water emissions and determine the wet emissions from the reactor. These are useful for comparing to models and calculating other parameters.

If an operating point is chosen far from extinction conditions (which is roughly $\phi = 0.4$), then hydrocarbon emissions are sufficiently low and H_2O emissions can be calculated based on the measured values of CO, CO_2, and O_2 with an assumed balance of N_2. The following sample calculation is for ethane combustion, with measured exhaust gas concentrations shown in Table D.1.

Table D.1: Dry emissions for ethane ($\phi_{inlet} = 0.444$)

Species	Concentration	Symbol
	[%V_{dry}]	
O_2	12.53	ϵ
CO_2	5.21	β
CO	0.32	δ

The calculations begin with the generic chemical reaction for a hydrocarbon, shown in Equation D.1. At this point, the mole numbers of some of the products are unknown, so they are replaced with generic symbols. The mole numbers for the three known species (CO, O_2, and CO_2) are given the symbols from Table D.1.

$$\text{D.1}\qquad \chi C_xH_y + \alpha[O_2 + 3.76N_2] \longrightarrow \beta CO_2 + \gamma H_2O + \delta CO + \epsilon O_2 + \zeta N_2 \qquad -$$

The atom balances for carbon, hydrogen, and oxygen, are given in Equations D.2, D.3, and D.4, respectively. The values of β, δ, and ϵ are measured, so the values of χ, γ, and α can be calculated as shown.

$$\text{D.2}\qquad \chi x = \beta + \delta \Longrightarrow \chi = \frac{\beta + \delta}{x} \qquad -$$

$$\text{D.3}\qquad \chi y = 2\gamma \Longrightarrow \gamma = \frac{y}{2}\chi \qquad -$$

$$\text{D.4}\qquad 2\alpha = 2\beta + \gamma + \delta + 2\epsilon \Longrightarrow \alpha = \beta + {}^{\gamma}/_{2} + {}^{\delta}/_{2} + \epsilon \qquad -$$

The nitrogen in the exhaust was assumed to be the balance after drying, so the value of ζ is found from Equation D.5.

$$\text{D.5}\qquad \zeta = 100 - (\beta + \epsilon + \delta) \qquad -$$

Now, everything on the right side of Equation D.1 is known, and the wet emissions can be determined by determining how much each species is as a percent of the total exhaust based on the mole numbers. As an example, for this specific case, the wet emissions are given in Table D.2.

Table D.2: Wet emissions for ethane ($\phi_{inlet} = 0.444$)

Species	**Concentration**
	[%V_{wet}]
O_2	11.6
CO_2	4.8
CO	0.29
H_2O	7.7
N_2	75.7

In the case of two fuels blended together, the wet emissions calculations are slightly more complicated. The process begins again with a generic chemical equation (Equation D.6) where one fuel is C_xH_y and the second is C_mH_n. Again, in this case the values of β, δ, and ϵ are all measured directly.

D.6 $$\chi C_x H_y + \omega C_m H_n + \alpha[O_2 + 3.76N_2] \longrightarrow \beta CO_2 + \gamma H_2O + \delta CO + \epsilon O_2 + \zeta N_2$$ -

Just as before, the nitrogen in the exhaust was assumed to be the balance after drying, so the value of ζ is found from Equation D.7 (same as Equation D.5). The nitrogen atom balance in Equation D.8 determines α, which is used in the oxygen atom balance (Equation D.9) to determine γ. At this point all of the emissions are determined, so new wet emissions can be calculated.

D.7 $$\zeta = 100 - (\beta + \epsilon + \delta)$$ -

D.8 $$3.76\alpha = \zeta \Longrightarrow \alpha = \frac{\zeta}{3.76}$$ -

D.9 $$2\alpha = 2\beta + \gamma + \delta + 2\epsilon \Longrightarrow \gamma = 2\alpha - 2\beta - \delta - 2\epsilon$$ -

Now, the two atom balance equations for carbon and hydrogen result in Equations D.10 and D.11. This is a system of two equations with two unknowns, which can be solved to determine χ and ω as the moles of each fuel. These will be used to determine the equivalence ratios.

D.10 $$\chi x + \omega m = \beta + \delta$$ -

D.11 $$\chi y + \omega n = 2\gamma$$ -

D.2 Equivalence Ratios

The inlet equivalence ratio (Equation D.12) is the most common way to define the chemistry of the combustion, and is calculated with the total air mass flow rate and total fuel mass flow rates (so all fuel flow rates are combined to determine the total fuel flow rate). As mentioned previously, everything here is based on the fuel-air equivalence ratio. The stoichiometric fuel air ratio is specific to a fuel, and is tabulated for each fuel along with its properties in

Appendix A.

D.12 $$\phi_{\text{inlet}} = \frac{\dot{m}_F/\dot{m}_A|_{\text{inlet}}}{\dot{m}_F/\dot{m}_A|_{\text{stoich}}}$$ -

The exhaust equivalence ratio is used as a cross-check for the inlet equivalence ratio. It is calculated from the exhaust emissions data that were used to determine the emissions on a wet basis above. Using the results of the wet emissions analysis above the exhaust equivalence ratio can be easily determined with the newly found values of χ and α for the fuel and air mole numbers, respectively. Those can be turned into the masses with the molecular weights and into a ratio as shown in Equation D.13. The equivalence ratio simply uses this as the numerator and the stoichiometric value as the denominator (Equation D.14). For the specific case used as an example, the inlet equivalence ratio was 0.444 which compares well with the exhaust equivalence ratio which is calculated to be 0.439. For the case of two fuels, the mass flow rate for fuel is simply the total mass flow rate.

D.13 $$\left.\frac{\dot{m}_F}{\dot{m}_A}\right|_{\text{exhaust}} = \frac{\chi MW_{\text{fuel}}}{4.76\alpha MW_{\text{air}}}$$ -

D.14 $$\phi_{\text{exhaust}} = \frac{\dot{m}_F/\dot{m}_A|_{\text{exhaust}}}{\dot{m}_F/\dot{m}_A|_{\text{stoich}}}$$ -

D.3 Reactor Loading

The reactor loading is described by the loading parameter (LP) and the residence time (τ) as described below.

The loading parameter (Equation D.15) is a classic combustor parameter and is particularly useful for extinction characterization. It was used by Longwell and Weiss [11] to characterize the blowout of multiple fuels in multiple reactors. Stouffer *et al.* [21] used a slightly different exponential term on the pressure based on information from Lefebvre *et al.* [111], which is used here, since that work was performed on the same reactor and is the basis of the current investigation.

D.15 $$LP = \frac{\dot{n}_A}{\forall p^{1.8}} \qquad \frac{\text{mol}}{\text{s L atm}^{1.8}}$$

Interestingly the loading parameter only has two values in this study since it is based on the air flow rate and reactor volume. One value is for the TSR (1.11 mole/sec L atm$^{1.8}$) and the second is for the JSR (2.52 mole/sec L atm$^{1.8}$).

The bulk residence time, τ, is also used as a way to characterize the reactor loading (Equation D.16). It uses the reactor gas density (ρ) which depends on temperature in the reactor, reactor volume (∀) and mass flow rate ($\dot{m}$).

D.16 $$\tau = 1000\frac{\rho\forall}{\dot{m}} \qquad \text{ms}$$

D.4 NO$_X$ Concentrations and Rates of Production

The NO$_X$ values are directly measured as parts per million (ppm) on a dry volume basis with the actual O$_2$ concentration in the exhaust. Often these values are quoted in terms of wet emissions or with a standardized O$_2$ concentration. The first step is to convert the primary emissions (CO, CO$_2$, and O$_2$) to an absolute basis as described above. Once the emissions are known in absolute units of kmol, the absolute NO$_X$ emissions are determined in kmol by the ratio absolute to relative CO$_2$ emissions (Equation D.17).

D.17 $$NO_X\ [\text{kmol}] = \frac{CO_2\ [\text{kmol}]}{CO_2[\text{ppm, dry}]} NO_X[\text{ppm, dry}] \qquad \text{kmol}$$

The total, absolute amounts (in kmoles) of each species (CO, CO$_2$, O$_2$, H$_2$O, N$_2$, and NO$_X$) are now known, so the relative concentration of NO$_X$ can be re-determined for a wet basis (Equation D.18).

D.18 $$NO_X\ [\text{ppm, wet}] = 1x10^6 \frac{NO_X\ [\text{kmol}]}{\text{Total Emissions [kmol]}} \qquad \text{kmol}$$

Both of the NO$_X$ measurements discussed so far (ppm dry or ppm wet) are based on the actual O$_2$ concentrations found in the exhaust. Since this could change based on the stoichiometry of the system, these emissions are sometimes reported on a standardized O_2 exhaust concentration of 15% (Equation D.19). The linear conversion uses the O_2 concentration as measured, the standard O_2 concentration in air (20.95% by volume), and the desired standard value (15% by volume).

$$\text{D.19} \qquad \mathrm{NO_X}\,[15\%\ \mathrm{O_2}] = \mathrm{NO_X}[\text{Actual } \mathrm{O_2}]\,\frac{(20.95 - 15)}{(20.95 - \mathrm{O_2}[\%\ \text{vol, dry}])} \qquad \text{ppm}$$

The NO_X emissions now are available in four different emissions bases: 1) dry/actual O_2; 2) wet/actual O_2; 3) dry/15% O_2; and 4) wet/15% O_2. Any of these can be converted to a rate of production (ROP) by dividing the concentration by the residence time in the reactor, which was discussed earlier. The expression is shown in Equation D.20.

$$\text{D.20} \qquad \mathrm{NO_X}\ \text{ROP} = \frac{\mathrm{NO_X}[\text{ppm, dry/wet, actual/15\% } \mathrm{O_2}]}{\tau\ [\text{ms}]} \qquad \text{ppm/ms}$$

D.5 Data Reduction

D.5.1 Blowout Studies

In general, the parameters mentioned above were calculated for each data point and were tracked throughout the test. As described in Chapter 3, the equivalence ratio was held constant for a significant duration to allow for the experiment to stabilize. During this time there was some change in the temperature, residence time, and emissions.

For the liquid fuels, the extinction point was the only point of interest. However, to assist in the CFD modeling of Chapter 4, the methane tests were monitored through stable and unstable conditions. It made the most sense to characterize the conditions by the last few data points before changing equivalence ratio as that was when the reactor was stabilized at a condition. This data reduction resulted in a few data points that represented 'conditional averages' and 'extinction averages'.

Figure D.1 helps to understand the data reduction process via a pictorial representation. As an example, see that Test 2 in Figure 3.5 on page 52 is divided into four conditions. Each condition is held at constant flow rates (hence equivalence ratio), but the temperature and emissions stabilize over time. Each condition will result in a stabilized average as calculated by an average of the last 30 seconds at a condition. This is called a condition average. As discussed in Chapter 3, the blowout point is the average of the 30 seconds before the precipitous drop in temperature.

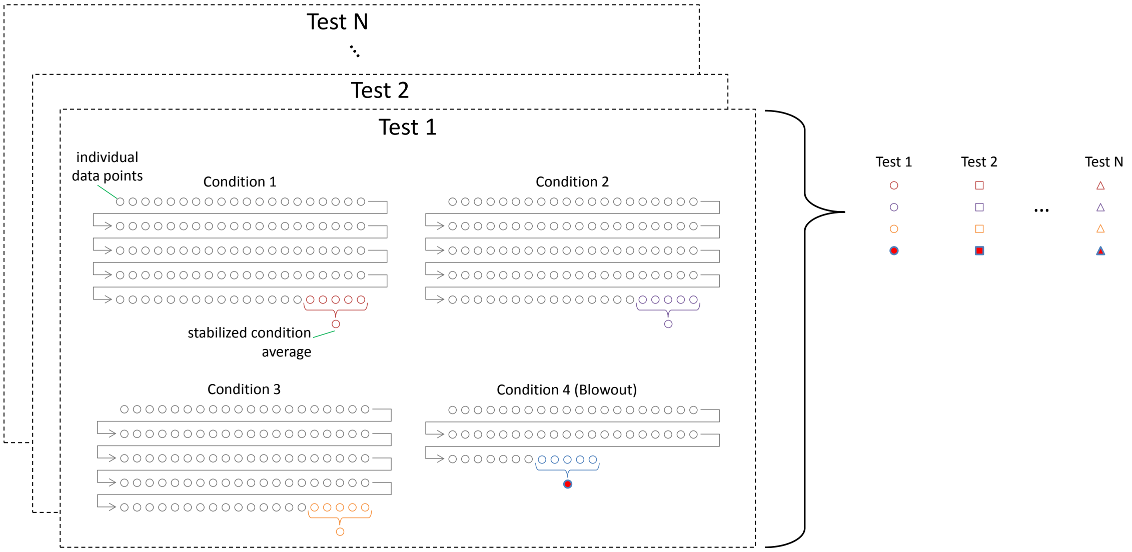

Figure D.1: Data reduction process

D.5.2 NO_X Studies

The exponential nature of NO_X-temperature data enables correlations for reduced data. The first step is to take the natural logarithm of the NO_X data in any of the unit bases (dry/wet and actual/15% O_2). The same method applies to the NO_X ROP data.

The data set is subjected to a first-order linear least squares fit to determine the coefficients for a first-order polynomial that characterizes the NO_X data. The result is two coefficients (p_1 and p_2) for the linear relationship between $\ln(NO_X)$ and $1/T$ (Equation D.21). The relationship is transformed to an exponential relationship by Equations D.22 and D.23. The final relationship takes the form of Equation D.24.

D.21 $$\ln NO_X = \frac{p_1}{T} + p_2$$

D.22 $$A = \exp(p_2)$$ ppm

D.23	$B = p_1$	K
D.24	$NO_X = A\exp\left({}^{B}/_{T}\right)$	ppm

Appendix E
Additional CFD Results

The first four figures (Figure E.1 to Figure E.4) show the difference between stable combustion (ϕ = 0.55) and incipient blowout (ϕ = 0.44) for temperature and the three products for lean, complete combustion (O_2, CO_2, and H_2O). Notice that for the stable conditions, the reactor is very homogenous. In general, the only real variations are in the jet region. The CO_2 is somewhat less homogeneous as it depends also on the time allowed for CO oxidation to CO_2. At incipient blowout, the reactor is very inhomogeneous. The temperature and species contours all show large regions of high variation.

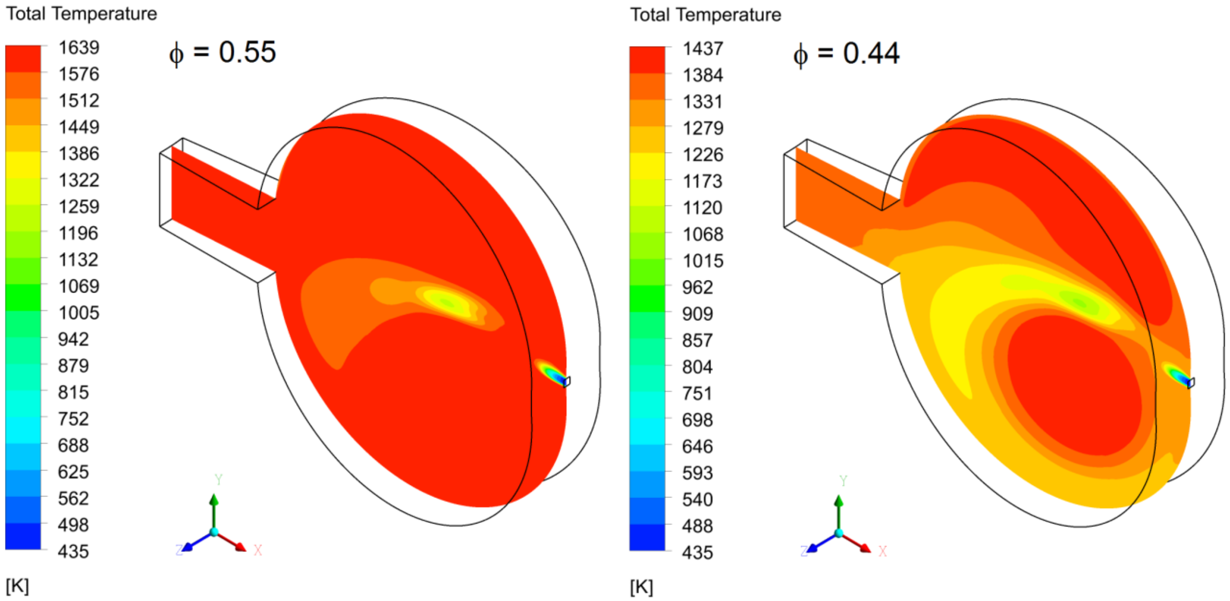

Figure E.1: Contours of temperature at ϕ=0.55 and ϕ=0.44

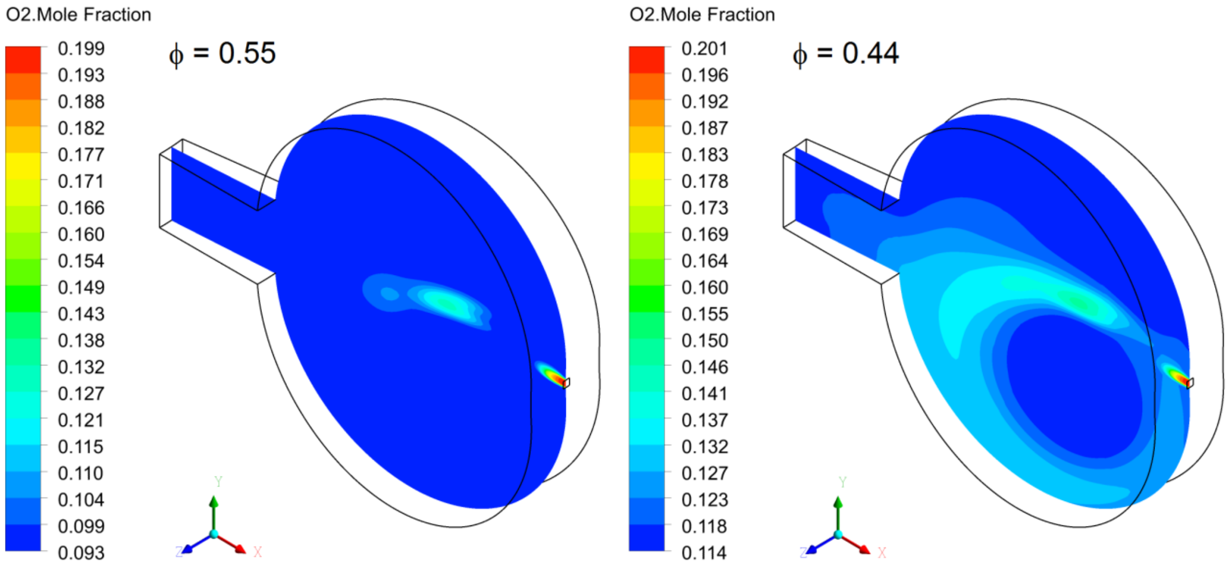

Figure E.2: Contours of O_2 mole fraction at ϕ=0.55 and ϕ=0.44

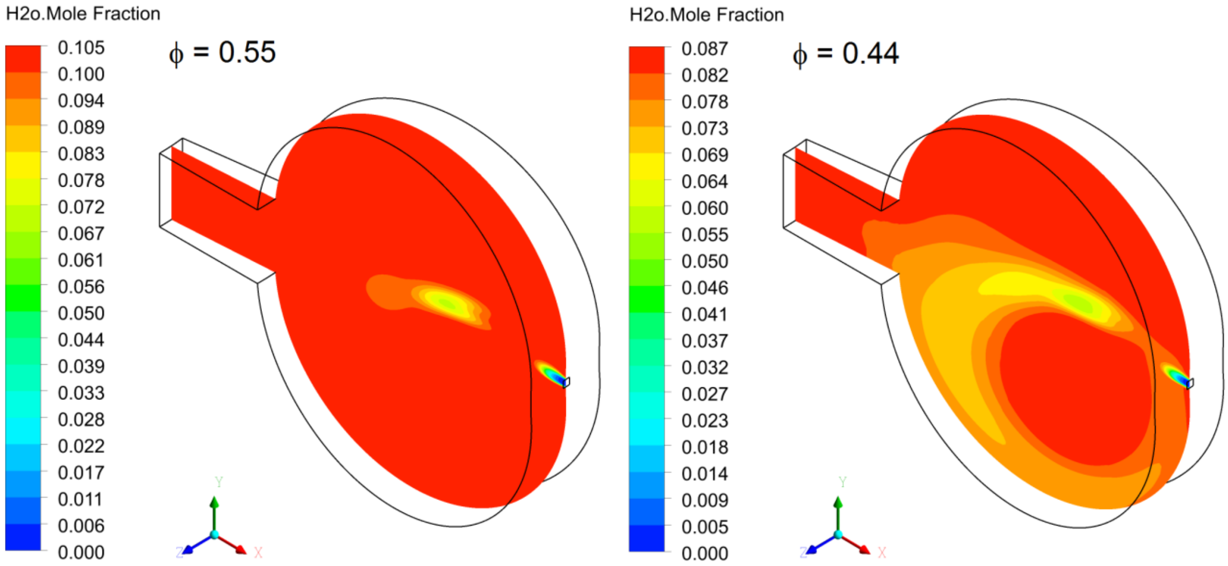

Figure E.3: Contours of H_2O mole fraction at ϕ=0.55 and ϕ=0.44

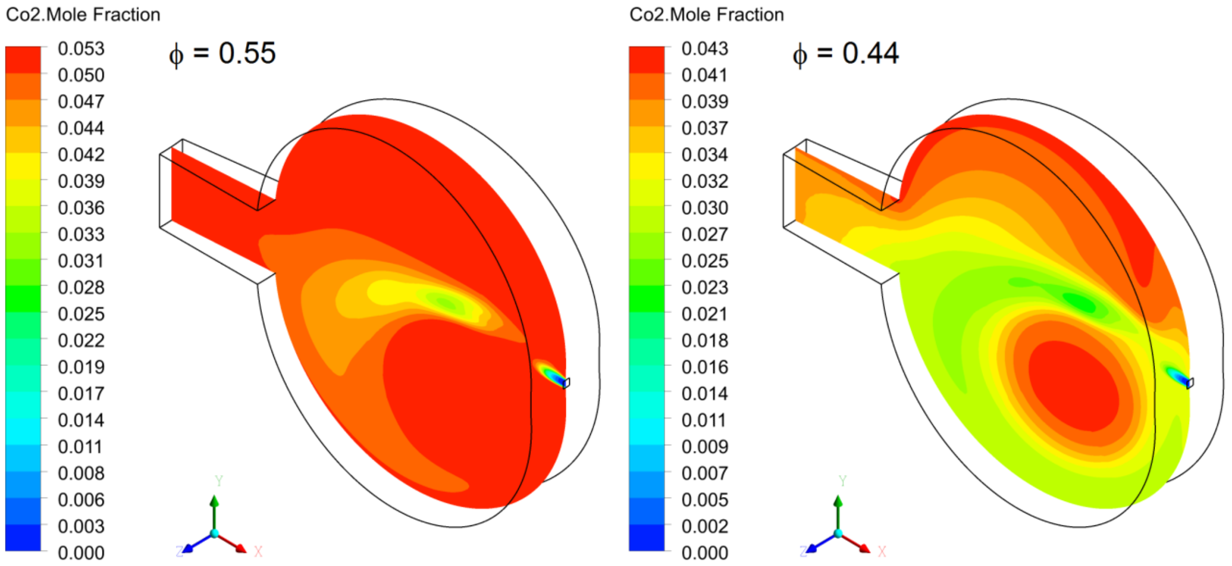

Figure E.4: Contours of CO_2 mole fraction at ϕ=0.55 and ϕ=0.44

The CFD model is able to determine quantities within the reactor that help classify the system, and get an estimate of what regime the reactor operates under given average conditions. The CFD model determined a volume averaged turbulent kinetic energy, k, of 161 J/kg and a volume averaged turbulent dissipation rate, ϵ, of $1.96\text{x}10^6$ m^2/s^3. According to Law [2], the integral velocity fluctuations, u_o', and integral length scale, L_o, are given as in Equations E.1 and E.2. The flame thickness is given as $L_L = \alpha/s_L$ where s_L is the flame speed and α is the thermal diffusivity based on the inlet conditions.

E.1 $$u_o' = \sqrt{{}^2/_3\,k}$$ m/s

E.2 $$L_o = \frac{(u_o')^3}{\epsilon}$$ m

The model calculated values of k and ϵ are used to calculate u_o' and L_o, then the values are normalized and plotted on the premixed turbulent combustion regime diagram (Figure E.5). Interestingly, the TSR averaged quantities lie on the border between the Well Stirred Reactor and Reaction Sheet regimes. Similarly, the non-averaged analysis performed on the JSR by Karalus [28] showed that the reactor is divided into one zone in the Well Stirred Reactor regime and a second zone in the Reaction Sheet regime.

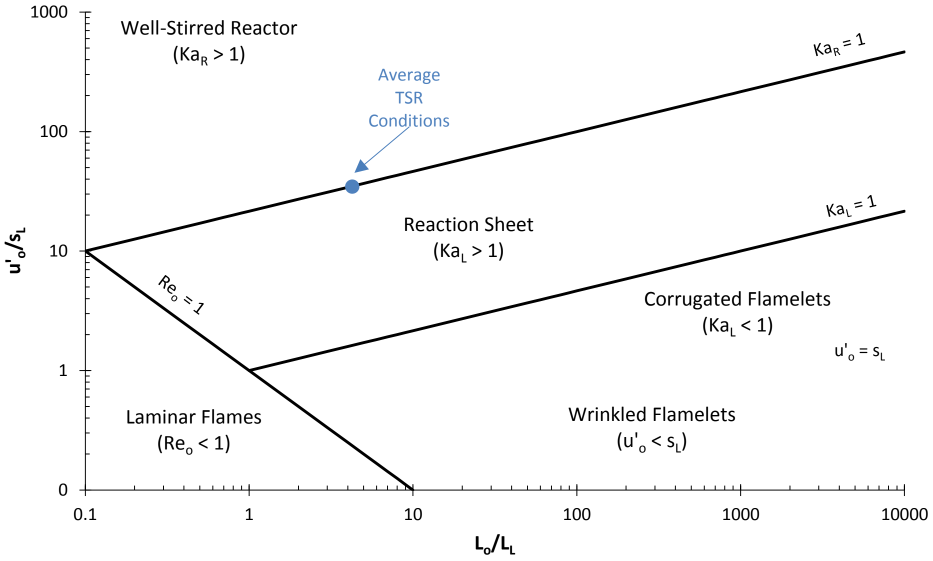

Figure E.5: Average TSR conditions on premixed combustion regime diagram [2]

Figure E.6 shows how the temperature varies in the toroidal direction along sixteen planes at different angles. The back face of this reactor segment is at 7.5°, which corresponds to the first plot in the series. The angle of the plane decreases in increments of 0.5° with very little change except for the location of the low temperature spot moving further away from the jet slightly. At 4.0° the incoming jet begins to emerge. As the plane angle continues to decrease in increments of 0.5°, the low temperature incoming jet grows, evolves, and moves away from the inlet. Finally, at 0.0°, the low temperature location is the same as the 7.5° plane, which indicates that the jet from the previous segment is entering this reactor segment and interacting with the jet from this segment. In general, the variation within the reactor is slight along the toroidal plane, so a single plane at the center of the segment (3.75°) is used for the results presented in Chapter 4.

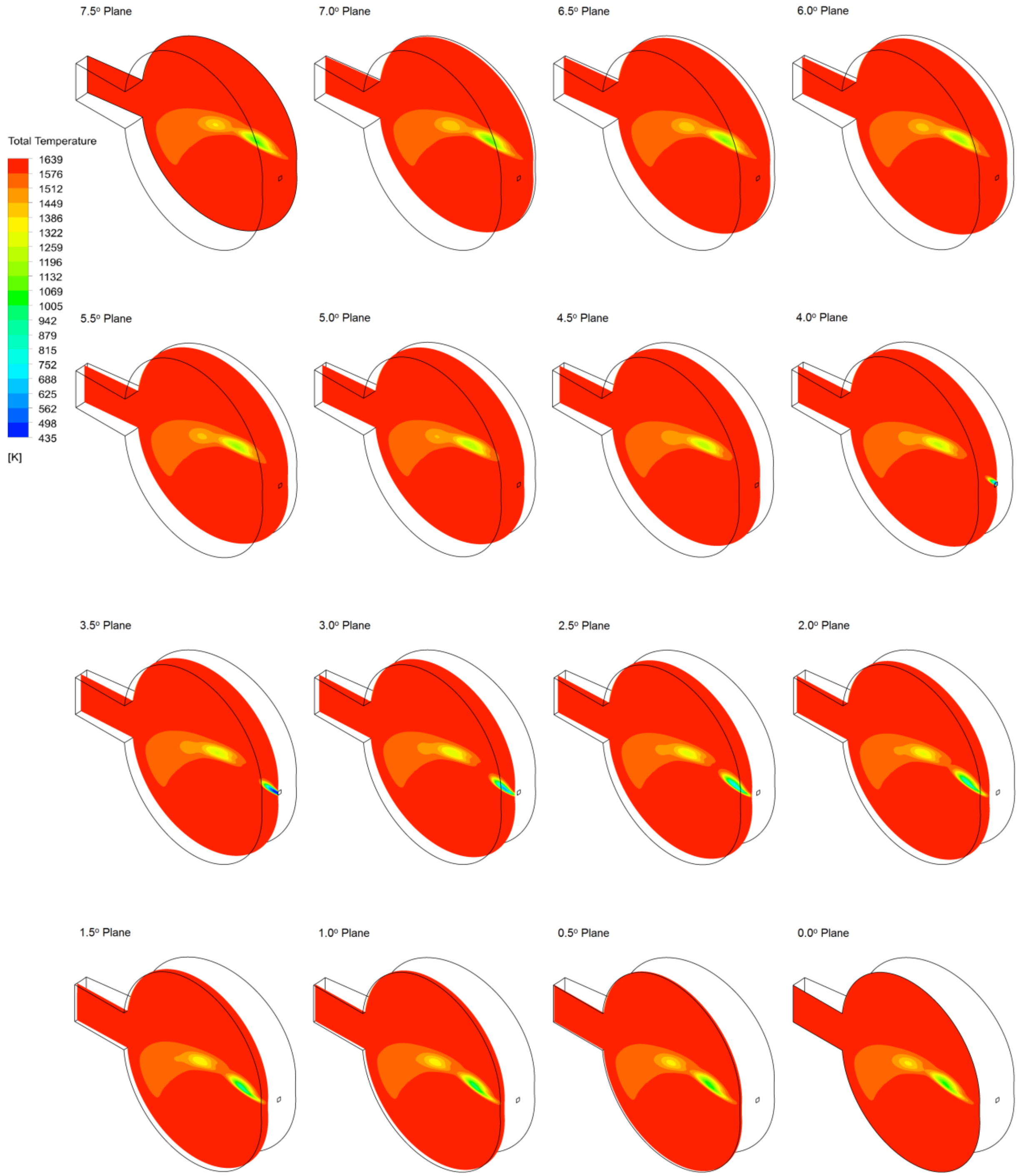
7.5° Plane
7.0° Plane
6.5° Plane
6.0° Plane
5.5° Plane
5.0° Plane
4.5° Plane
4.0° Plane
3.5° Plane
3.0° Plane
2.5° Plane
2.0° Plane
1.5° Plane
1.0° Plane
0.5° Plane
0.0° Plane

Figure E.6: Contours of temperature at ϕ=0.55 on various toroidal planes

Appendix F
Kinetic Mechanisms

Chemical kinetics uses dozens, hundreds, or even thousands of chemical reactions to model the rate at which species are created and destroyed during a combustion study. The chemical reactions are assembled into kinetic mechanisms and used to model the reaction chemistry for various fuels.

F.1 Methane

The GRI 3.0 Mechanism (GRI) is very commonly used for methane combustion [4]. GRI is well-established and is often used to study natural gas combustion, but is generally not recommended for modeling single hydrocarbons above methane. Karalus *et al.* [78] presented a form of GRI based on a methodological reduction method (Reduced GRI). A short summary of these mechanisms is included in Table F.1.

Table F.1: Kinetic mechanisms for methane

Mechanism	Designed For:	# of Species	# of Reactions	Reference
GRI 3.0	Natural Gas	53	325	Smith *et al.* [4]
Reduced GRI	CH_4	22	123	Karalus *et al.* [78]

Ultimately, the number of species should be as small as possible for the CFD models to be tractable. The Reduced GRI performed well in the CFD studies by Karalus [28], and is selected for this study. In some cases, the full GRI 3.0 mechanism is used for comparison, but differences are very small.

F.2 Jet Fuel and Components

Modeling jet fuel chemistry is difficult because it is not a pure fuel. It consists of dozens, hundreds, or thousands of different hydrocarbons species. Typically, surrogate fuels are used to approximate the chemical or physical properties of the fuel. Table F.2 lists the mechanisms used in this study for blowout and NO_X studies.

Table F.2: Kinetic mechanisms for jet fuel and components

Designed For:	**Species**	**Original**		**Modified for NO_X**		**Reference**
		# of Species	**# of Reactions**	**# of Species**	**# of Reactions**	
Jet Fuel	n-octane iso-octane toluene	1599	6633	1606	6660	Dooley *et al.* [85]
135-TMB	135-TMB	450	2569	457	2596	Diévart *et al.* [93]
Synthetic Jet Fuel from Coal	iso-octane PCH toluene	2185	8217	2192	8240	Mzé-Ahmed *et al.* [94]

Dooley *et al.* [85] presented a mechanism for jet fuel that combined mechanisms for normal alkanes, iso-octane, and toluene. It is used to study the blowout and NO_X emissions for flames of n-octane, iso-octane, and toluene. Diévart *et al.* [93] presented a kinetic mechanism for 1,3,5-trimethylbenzene. Both of these mechanisms were developed by the Fuels and Combustion Research Laboratory at Princeton University [92], so they can be reasonably compared.

Mzé-Ahmed et al. [94] presented a kinetic mechanism for a fully formulated synthetic jet fuel from coal. The surrogate fuels included iso-octane, propylcyclohexane (PCH), and toluene. This mechanism was developed by the *Institut de Combustion Aérothermique Réactivité et Environnement* at the French National Center for Scientific Research [112].

The NO_X sub-mechanism is taken from GRI 3.0 [4] and included with the appropriate surrogate fuel mechanism. It consisted of the 27 unique reactions presented in Section 1.2.2. There are 20 associated species, but typically only seven needed to be added to the mechanism.